A PDZ-3 MEDIATED PHYSICAL AND FUNCTIONAL INTERACTION BETWEEN THE $Ca_V3.2$ T-TYPE CALCIUM CHANNEL AND NEURONAL NITRIC OXIDE SYNTHASE

by

Kirk James Mulatz

B.Sc., University of Saskatchewan, 2001

A THESIS SUBMITTED IN PARTIAL FULFILLMENT OF
THE REQUIREMENTS FOR THE DEGREE OF

DOCTOR OF PHILOSOPHY

in

The Faculty of Graduate Studies

(Experimental Medicine)

THE UNIVERSITY OF BRITISH COLUMBIA

(Vancouver)

January 2013

© Kirk James Mulatz, 2013

Abstract:

T-type voltage-gated calcium channels are expressed throughout the central and peripheral nervous systems as well as in several non-neuronal tissues and contribute to variety of functions such as neuronal excitability, intracellular calcium influx, shaping action potentials, pace-making activity, hormone secretion, and neurotransmitter release. Of the three T-type channel isoforms, $Ca_v3.2$ is uniquely sensitive to redox modulation with oxidizing reagents inhibiting and reducing compounds enhancing channel activity. This modulation has been shown to alter firing patterns of reticular thalamic neurons and to affect the nociceptive threshold *in vivo* suggesting that redox modulation of $Ca_v3.2$ may play an important role in regulating neuronal activity.

A potential source of oxidizing molecules *in vivo* is neuronal nitric oxide synthase (nNOS), a calcium dependent enzyme which synthesizes nitric oxide (NO) from arginine. Interestingly, the carboxyl terminus of $Ca_v3.2$ possesses a putative PDZ-3 binding ligand which is compatible with the PDZ-3 domain of nNOS. I hypothesize that $Ca_v3.2$ and nNOS physically interact via the PDZ-3 binding ligand of $Ca_v3.2$ and that this physical interaction mediates a functional interaction whereby $Ca_v3.2$ activity stimulates nNOS to produce NO which, in turn, inhibits $Ca_v3.2$ activity.

$Ca_v3.2$ and nNOS were expressed in a heterologous system which allowed us to examine the putative PDZ-3 mediated interactions between the two proteins. Immunoprecipitation experiments using $Ca_v3.2$ specific antibodies demonstrate that $Ca_v3.2$ and nNOS can interact via the carboxyl PDZ-3 ligand of $Ca_v3.2$ and that this interaction is disrupted when the PDZ-3 ligand is mutated. Utilizing a NO sensitive fluorometric assay we show that $Ca_v3.2$ activity can stimulate nNOS to produce NO and that disruption the PDZ-3

interaction precludes nNOS activation. We also demonstrate that the PDZ-3 mediated physical interaction facilitates the inhibition of $Ca_v3.2$ by nNOS derived NO. Disruption of the $Ca_v3.2$/nNOS interaction *in vivo* using intraperitoneal injection of membrane permeable peptides designed to competitively disrupt the PDZ-3 interaction produces an exaggerated respiratory response to changes in available oxygen and a blunted response in the hyperoxic response test. These results indicate that $Ca_v3.2$ and nNOS physically and functionally interact to contribute to normal physiological processes.

Preface:

I designed all experiments and analyzed all experimental results with input and feedback from other researchers. I performed all experiments except for the PSD-95 co-immunoprecipitation and the glossopharyngeal nerve immunohistochemistry experiments. The PSD-95 co-immunoprecipitation experiments were performed by Zeina Waheed who also assisted in the preparation for the $Ca_v3.2$/nNOS/PSD-95 current density experiments. I performed the dissections to harvest the glossopharyngeal nerves and Karen Jones performed the staining, mounting and imaging for the immunohistochemistry experiments. Dr. Anamika Singh collected the initial current density measurements and provided valuable guidance in optimizing the electrophysiological experiments.

All experimental procedures involving animals and their care were performed in accordance with recommendations of the Canadian Council on Animal Care and the regulations and policies of the University of British Columbia Animal Care Facility and the University Animal Care Committee (Animal care certificate number: A10-0286).

I participated in the molecular portion of Appendix 1 (Hildebrand, M.E., David, L.S., Hamid, J., Mulatz, K., Garcia, E., Zamponi, G.W., Snutch, T.P. 2007. Selective inhibition of Cav3.3 T-type calcium channels by Gαq/11-coupled muscarinic acetylcholine receptors. *Journal of Biological Chemistry*. 282(29), 21043-21055) and Appendix 2 (Adams, P.J., Garcia, E., David, L.S., Mulatz, K.J., Spacey, S.D., Snutch, T.P. 2009. Cav2.1 P/Q-type calcium channel alternative splicing affects the functional impact of familial hemiplegic migraine mutations: Implications for calcium channelopathies. *Channels* (Austin). 3(2):110-121) generating clones which were used for the experimental procedures. In Appendix 3 (Gonzalez, L.E., Kotler, M.L., Vattino, L.G., Conti, E., Reisin, R.C., Mulatz, K.J., Snutch, T.P., Uchitel, O.D. 2011. Amyotrophic lateral sclerosis-immunoglobulins selectively interact

with neuromuscular junctions expressing P/Q-type calcium channels. *Journal of Neurochemistry*. 119(4),826-38) I participated in the design and analysis of the $Ca_v2.1$ immunoprecipitation experiments.

Table of Contents:

Abstract ii

Preface iv

Table of Contents vi

List of Tables xii

List of Figures xiii

List of Abbreviations xv

Acknowledgements xxi

Dedication xxii

Chapter 1 1

1. Introduction 1

1.1. Calcium channel overview 1

1.1.1. Brief history of calcium channels – Discovery of calcium currents 1

1.1.2. Brief history of calcium channels – Classes and nomenclature 2

1.1.3. Molecular structure and composition 9

1.2. Ca_v3 calcium channels 12

1.2.1. Ca_v3 calcium channel expression 12

1.2.2. Biophysical properties of Ca_v3 channels 16

1.2.3. Physiological roles of T-type Ca^{2+} channels 20

1.2.4. Pharmacological properties of T-type Ca^{2+} channels 27

1.2.5. Modulation of T-type Ca^{2+} channels 30

1.3. PDZ ligands and domains: partnering regulatory enzymes to their targets 36

1.3.1. Structure and function 36

1.3.2.PDZ domains of nNOS 38

1.4. Functional relevance of nitric oxide and nitric oxide synthases 39

1.4.1. Molecular structure and composition 39

1.4.2. Synthesis of nitric oxide 41

1.4.3. Mechanisms of modulation by nitric oxide 44

1.4.4. Degradation of nitric oxide 45

1.4.5. Pharmacological properties of neuronal nitric oxide synthase 46

1.4.6. Expression of nNOS and roles of nNOS derived NO 47

1.5. Nitric oxide and nNOS in the ventilatory response 50

1.5.1. Neuronal pathways involved in respiration 50

1.5.2. Role of NOS in respiration 53

1.5.3. Properties and role of nNOS expressing microganglia in the glossopharyngeal nerve (GPN) 55

1.6. $Ca_v3.2$ channels and nociception 56

1.6.1. Neuronal pathways involved in nociception 56

1.6.2. Role of $Ca_v3.2$ channels in nociception 57

1.6.3. Role of nNOS in nociception 58

1.7. Thesis hypothesis and objectives 60

1.7.1. Hypothesis 60

1.7.2. Objectives 61

Chapter 2 62

2. $Ca_v3.2$ and nNOS interact physically and functionally to form a putative negative feedback regulatory loop 62

2.1. Introduction 62

2.2. Materials and methods 65

2.2.1. Generation of fusion peptides 65

2.2.2. Generation and transformation of chemically competent DH5α cells 69

2.2.3. Mutation of the $Ca_v3.2$ PDZ-3 binding ligand 70

2.2.4. nNOS and PSD-95 clones 71

2.2.5. Cell culture and transfection 74

2.2.6. Generation of stable cell lines 76

2.2.7. GST pull down 78

2.2.8. Co-immunoprecipitation 79

2.2.9. Western blot analysis 80

2.2.10. Nitric oxide detection assay 82

2.2.11. Whole cell patch clamp analysis 83

2.3. Results 86

2.3.1. $Ca_v3.2$ and nNOS interact via the PDZ-3 binding ligand located at the carboxyl terminus of $Ca_v3.2$ 86

2.3.2. The PDZ-3 domain of the PDZ-2 beta finger binding ligand of nNOS can facilitate the formation of larger protein complexes 91

2.3.3. The physical interaction between $Ca_v3.2$ and nNOS in required for $Ca_v3.2$ activity to stimulate the production of nitric oxide by nNOS 93

2.3.4. nNOS activity inhibits $Ca_v3.2$ channels in a heterologous expression system 98

2.4. Discussion 109

2.4.1. $Ca_v3.2$ and nNOS physically and functionally interact in a heterologous system 109

2.4.2. nNOS can facilitate the formation of larger protein complexes 113

2.4.3. Inhibition of $Ca_v3.2$ does not involve the activation of soluble guanylyl cylase 114

2.4.4. Potential implication of a $Ca_v3.2$/nNOS complex *in vivo* 115

Chapter 3 117

3. Disruption of the $Ca_v3.2$ and nNOS interaction *in vivo* alters the respiratory response in Sprague Dawley rats 117

3.1. Introduction 117

3.2. Materials and methods 120

3.2.1. Animal care 120

3.2.2. GPN dissection 120

3.2.3. Quantitative real-time-PCR 122

3.2.4. Immunohistochemistry 122

3.2.5. Design of the TAT fusion peptides 124

3.2.6. Respirometry 125

3.2.7. Analysis of respirometry data 129

3.3. Results 132

3.3.1. $Ca_v3.2$ is present in nNOS expressing microganglia within the GPN of Sprague Dawley rats 132

3.3.2. Disruption of the $Ca_v3.2$/nNOS interaction *in vivo* results in an augmented steady state response to hypoxic challenges 136

3.3.3. The hyperoxic response may be attenuated in animals where the $Ca_v3.2$/nNOS interaction is disrupted 146

3.4. Discussion 149

3.4.1. Disruption of the $Ca_v3.2$/nNOS complex has a significant effect on the respiratory rate in response to available oxygen 149

3.4.2. Implications of the observed increase in tidal volume and total ventilation following the administration of a mutant PDZ-3 TAT fusion peptide 154

3.4.3. Potential relevance to respiration 155

Chapter 4 156

4. Discussion 156

4.1. Overall significance of the thesis 156

4.1.1. Identification of a physical and functional interaction between $Ca_v3.2$ and nNOS 157

4.1.2. Potential relevance for nociception 158

4.1.3. Relevance to the respiratory system 159

4.2. The $Ca_v3.2$ T-type calcium channel and neuronal nitric oxide synthase physically and functionally interact forming a putative negative feedback regulatory loop 159

4.2.1. Working hypothesis 159

4.2.2. Limitations and weaknesses 160

4.3. Intraperitoneal injection of a TAT fusion peptide to disrupt the $Ca_v3.2$ and nNOS interaction *in vivo* produces an augmented respiratory response to changes in available oxygen in rats 162

4.3.1. Working hypothesis 162

4.3.2. Limitations and weaknesses 163

4.4. Conclusions 164

4.4.1. General conclusion 164

4.4.2. Relevance to modulation of neuronal networks co-expressing $Ca_v3.2$ and nNOS 165

4.4.3. Relevance to the respiratory system 166

4.4.4. Future directions 167

Bibliography 170

Appendix 1: Selective Inhibition of Cav3.3 T-type Calcium Channels by Gαq/11-coupled Muscarinic Acetylcholine Receptors 204

Appendix 2: $Ca_V2.1$ P/Q-type calcium channel alternative splicing affects the functional impact of familial hemiplegic migraine mutations 217

Appendix 3: Amyotrophic lateral sclerosis-immunoglobulins selectively interact with neuromuscular junctions expressing P/Q-type calcium channels 229

List of Tables:

Table 1.1: Evolution of the voltage-gated Ca^{2+} channel nomenclature. 7

Table 1.2: Summary of the biophysical characteristics of the low threshold Ca_v3 channels 19

Table 1.3: Summary of $Ca_v3.1$ and $Ca_v3.2$ knockout mice phenotypes 26

Table 2.1: Primers used to generate the clones utilized in this thesis 68

Table 2.2: Agents utilized to maintain selection pressure for the transfected constructs 76

Table 3.1: Summary of the respirometry responses from TAT-control, TAT-DEPV and TAT-DEPE injected animals 140

List of Figures:

Figure 1.1: Phylogeny of the voltage-gated Ca^{2+} channel family 8

Figure 1.2: Structural features of voltage-gated Ca^{2+} ion channels 11

Figure 1.3: Summary of the known modulators of Ca_v3 channel activity 35

Figure 1.4: Domain structure of nitric oxide synthases 41

Figure 1.5: Reaction schematic and electron flow diagram of the conversion of arginine to citrulline and nitric oxide 43

Figure 2.1: Alignment of voltage-gated Ca^{2+} channels demonstrating a PDZ-3 motif unique to $Ca_v3.2$ 65

Figure 2.2: $Ca_v3.2$ and nNOS can physically interact via the carboxyl PDZ-3 binding ligand of $Ca_v3.2$ 88

Figure 2.3: The physical interaction of $Ca_v3.2$ and nNOS can be competitively disrupted using a peptide containing the PDZ-3 binding ligand 90

Figure 2.4: The $Ca_v3.2$/nNOS complex can further interact with PSD-95 to form a larger complex 92

Figure 2.5: The PDZ-3 binding interaction between $Ca_v3.2$ and nNOS is required for $Ca_v3.2$ activity to stimulate nNOS to produce nitric oxide 96

Figure 2.6: nNOS activity inhibits $Ca_v3.2$ 101

Figure 2.7: A physical interaction between $Ca_v3.2$ and nNOS is required for the basal inhibition of $Ca_v3.2$ activity by nNOS 103

Figure 2.8: The inhibition of $Ca_v3.2$ by nNOS activity is independent of soluble guanylyl cyclase activation 105

Figure 2.9: Co-expression of PSD-95 with nNOS and $Ca_v3.2$ results in increased inhibition of $Ca_v3.2$ 107

Figure 2.10: The nNOS-mediated changes in peak current density are not the result of the direct action of L-NAME, TAT-DEPV or PSD-95 on $Ca_v3.2$ 109

Figure 2.11: Schematic summarizing the proposed physical and functional interaction between $Ca_v3.2$ and nNOS 112

Figure 3.1: Schematic summarizing the location and innervation of the carotid body 119

Figure 3.2: Experimental setup used to acquire the respirometry and metabolic data 127

Figure 3.3: Graphical representation of the respirometry protocol 128

Figure 3.4: qRT-PCR analysis illustrating the Ca^{2+} channel expression profile in the glossopharyngeal nerve (GPN) in Sprague Dawley rats 134

Figure 3.5: Immunohistological staining of $Ca_v3.2$, nNOS and ChAT in the microganglia of the glossopharyngeal nerve of Sprague Dawley rats 135

Figure 3.6: Disruption of the $Ca_v3.2$/nNOS interaction *in vivo* results in an elevated respiratory response to changes in oxygen concentration 142

Figure 3.7: Average tidal volume and total ventilation in TAT-DEPE injected Sprague Dawley rats differs significantly from $Ca_v3.2$/nNOS disrupted (TAT-DEPV) and TAT-control 144

Figure 3.8: Disruption of the $Ca_v3.2$/nNOS interaction alters the response in the hyperoxic response test 147

Figure 3.9: Schematic illustrating the hypothesized contribution of the $Ca_v3.2$/nNOS interaction to the NO mediated inhibition of the carotid body 153

List of Abbreviations:

7-NI: 7-Nitro indazole

AChR: acetylcholine receptor

ACR: air convection requirement

ADP: after depolarizing potential

AM: acetomethylester

AngII: angiotensin-II receptor II

ANOVA: analysis of variance

Arg: arginine

Ba^{2+}: barium

BH_4: tetrahydrobiopterin

BotC: Botzinger complex

Ca^{2+}: calcium

CaM: camodulin

CaMKII: camodulin dependent protein kinase kinase II

cAMP: cyclic monophosphate

CAPON: carboxy-terminal PDZ ligand of nNOS

ccm^{-1}: cubic centimeters per minute

cGK: cGMP dependent kinases

cGMP: cyclic guanosine monophosphate

CNS: central nervous system

CO_2: carbon dioxide

-COOH: carboxyl terminus

CRF-1: corticotropin-releasing factor receptor-1

CSN: carotid sinus nerve

CtBP; carboxyl-teminal binding protein

Cu^{2+}: copper (II) ion

cVRG: caudal ventral respiratory group

DAG: diacyl glycerol

DAR-4M: diaminorhodamine-4M AM

Dlg1: Drosophila disc large tumor suppressor

DMEM: Dulbecco's Modified Eagle Medium

DMSO: dimethyl sulfoxide

DNA: deoxyribonucleic acid

dNTP: deoxyribonucleotide triphosphate

DRG: dorsal root ganglion

DTNB: 5,5-dithio-bis-(2-nitrobenzoic acid)

DTT: dithiothreitol

EDTA: ethylenediaminetetraacetic acid

ET_A: endothelin type A receptor

eNOS: endothelial nitric oxide synthase

FAD: flavin adenine dinucleotide

FBS: fetal bovine serum

FMN: flavin adenine mononucleotide

GAERS: Genetic Absence Epilepsy Rat from Strasbourg

GDB: Human Gene Database

GFP: green fluorescent protein

GPN: glossopharyngeal nerve

GST: glutathione S-transferase

GTP: guanosine triphosphate

HEK: human embryonic kidney

HEPES: 4-(2-hydroxyethyl)-1-piperazineethanesulfonic acid

HUGO: Human Gene Organization

HVA: high voltage activated

Hz: hertz

IC_{50}: half maximal inhibitory concentration

iNOS: inducible nitric oxide synthase

IPTG: isopropyl β-D-1 thiogalactopyranoside

IUPHAR: International Union of Pharmacology

IV curve: current-voltage relationship

kHz: kilohertz

KLHL1: kelch-Like 1

LB: Lauria broth

L-NAME: methyl ester of N^{ω}-Nitro-L-arginine

L-NMA: N^{ω}-Methyl-L-arginine

L-NNA: N^{ω}-Nitro-L-arginine

LPA: lysophosphatidic acid

LTD: long term depression

LTP: long term potentiation

LTS: low threshold spike

LVA: low voltage activated

MΩ: megaOhm

mg: milligram

ml: millilitre

mM: millimolar

MOPS: 3-(N-morpholino)propanesulfonic acid

mOsm/kg: milliosmole per kilogram

mRNA: messenger ribonucleic acid

ms: millisecond

mV: millivolts

NADPH: nicotinamide adenine dinucleotide phosphate

ng: nanograms

nm: nanometer

nM: nanomolar

NHA: L-arginine to $N^{(\omega)}$-hydroxy-L-arginine

Ni^{2+}: nickel

$NiCl_2$: nickel chloride

NKR1: neurokini 1 receptor

nM: nanomolar

NMDAR: N-methyl-D-aspartic acid receptor

nNOS: neuronal nitric oxide synthase

NO: nitric oxide

NO^{2-}: nitrites

NO^{3-}: nitrates

NOS: nitric oxide synthase

nRT: thalamic reticular nucleus

NST: nucleus of the solitary tract

O_2: oxygen

ODQ: 1*H*-[1,2,4]oxadiazolo-[4,3-α]quinoxalin-1-one

$OONO^-$: peroxynitrites

pA: picoamperes

PBS: phosphate buffered saline

pCO2: partial pressure of carbon dioxide

PCR: polymerase chain reaction

PDE: phosphodiesaterase

PDZ: post synaptic density protein (PSD-95), Drosophila disc large tumor suppressor (Dlg1), and the zonula occludens-1 protein (Zo-1)

pF: picofarad

pFRG: parafacial respiratory group

qRT-PCR: quantitative real-time polymerase chain reaction

PIP2: phosphatidylinositol 4,5-bisphosphate

PKA: protein kinase A

PLCβ: phospholipase C β

pO2: partial pressure of oxygen

pre-BotC: pre-Botzinger complex

pS: picosiemens

PSD-95: post synaptic density protein – 95kDa

ROCK: Rho-associated protein kinase

RTN: retrotrapeziod nuleus

rVRG: rostral ventral respiratory group

sGC: soluble guanylyl cyclase

Sr^{2+}: strontium

TAT: human immunodeficiency Virus 1 transactivator of transcription

TRPV1: transient receptor potential vanilloid-1

µg: microgram

µl: microlitre

µM: micromolar

VGCC: voltage-gated calcium channel

V: volts

V_{50act}: half maximal activation voltage

$V_{50inact}$: half maximal inactivation voltage

Vol: volume

x *g*: relative centrifugal force

Zn^{2+}: zinc

Zo-1: zonula occludens-1 protein

Acknowledgements:

I would like to thank my supervisor, Terry Snutch, for the patience, guidance and encouragement he gave me during my PhD studies. A special thanks to Esperanza Garcia and her patience and advice; in addition to teaching me the theory and techniques of electrophysiology she taught me that a tool and technique is infinitely more useful when you understand why it works in addition to how it works. I thank John Tyson who provided much needed advice and encouragement when my immunoprecipitations were less than stellar. Many thanks to my supervisory committee: Steven Vincent, Yu Tian Wang, and William Milsom for their direction and advice.

I would like to extend additional acknowledgement to Steven Vincent for proposing that I explore the potential $Ca_v3.2$/nNOS interaction for my PhD and to William Milsom for providing a crash course in respirometry, knowledgeable advice, and for allowing me access to his laboratory and equipment. I would also like to thank Stella Lee from William Milsom's lab for her guidance in getting the respirometry equipment to behave and for being so accommodating when we were scheduling the equipment usage.

To all past and present members of the Snutch Lab, thank you for making the lab a great place to learn and work; the atmosphere was always welcoming and supportive.

My appreciation goes to the Michael Smith Foundation for Health Research, the BC Epilepsy Society and the UBC graduate fellowship program for providing me with trainee funding during my graduate studies.

A heartfelt thank you goes to my parents and grandparents for your support and for teaching me the value of hard work and persistence. Finally, I would like to express my endless gratitude to my wonderful wife Raagini for her support throughout all stages of my PhD studies.

Dedication:

To my wife Raagini,

my son Dylon,

my parents Ralph and Elaine,

and my grandparents Joe and Clara, and Frank and Katherine.

Chapter 1.

1. Introduction

1.1. Calcium channel overview

1.1.1. Brief history of calcium channels – Discovery of calcium currents

Evaluating the field of voltage-gated calcium (Ca^{2+}) channels (VGCCs) in 2012, one can confidently make the statement that VGCCs play numerous crucial roles in neuronal activity. A search for "calcium channels" using the online PubMed (US National Library of Medicine/National Institutes of Health) search engine reveals a plethora of over 60,000 peer reviewed articles and additional queries for the specific subtypes of VGCCs uncover even more articles indicating the considerable interest these ion channels have garnered in the research community. Sixty years ago this was not the case. In the early 1950s PubMed and online searches were elements in the realm of science fiction at best and the idea that a Ca^{2+} -specific voltage dependent ion channels even existed was only beginning to take shape.

The study of voltage dependent Ca^{2+} currents was slow to gain momentum, at the time many researchers in the field were focused on the sodium and potassium currents underlying the action potential (Hodgkin and Huxley, 1945; Hodgkin and Katz, 1949; Nastuk and Hodgkin, 1950; Draper and Weidmann, 1951; Huxley and Stampfli, 1951). However, amid a field of exciting discoveries including new findings on excitatory and inhibitory neuronal communication (Fatt and Katz, 1951, 1953a) and the quantal basis of neurotransmitter release (Del Castillo and Katz, 1954) arose guarded conclusions regarding the possible presence of Ca^{2+} currents in crustacean muscle fibers (Fatt and Katz, 1953b). These guarded conclusions did not immediately pique interest in Ca^{2+} channels and four years lapsed before additional evidence was put forward by Hodgkin and Keynes suggesting a potential role for Ca^{2+} in neuronal processes such as vesicle release and excitation-

contraction coupling (Hodgkin and Keynes, 1957). A year later, in 1958, Fatt and Ginsborg published a paper demonstrating that the movement of divalent ions (including Ca^{2+}) across the membrane could support action potentials (Fatt and Ginsborg, 1958) providing additional evidence to support their 1953 conclusions regarding the presence of a Ca^{2+} current in crustacean muscle fibers. Still, interest in the role Ca^{2+} currents in neuronal activity was slow to evolve. It was another five years before Fleckenstein discovered that verapamil, and later nifedipine (a dihydropyridine) inhibited excitation-contraction coupling by disrupting Ca^{2+} currents, highlighting the significance of Ca^{2+} in this process (reviewed in (Fleckenstein, 1983)). A few years afterwards, Reuter and coworkers used the voltage clamp technique to identify a voltage-dependent Ca^{2+} current in the purkinje fibers of sheep and calf hearts which further strengthened the link between Ca^{2+} currents and excitation-contraction coupling (Reuter, 1967). In the same year, Katz and Miledi put forward the Calcium Hypothesis of synaptic communication which stated "that inward movement of a positively charged Ca compound, or the Ca^{2+} ion itself, constitutes one of the essential links in the 'electro-secretory' coupling process of the axon terminal " (Katz and Miledi, 1967). Further elaboration and evidence of the Calcium Hypothesis was published in 1970 (Katz and Miledi, 1970). The evidence demonstrating the critical role Ca^{2+} currents play in synaptic activity was building and Ca^{2+} currents could no longer be ignored. A full review of the history of Ca^{2+} channels can be found in a superbly written albeit not entirely unbiased book chapter by Tsein and Barret (Tsien and Barrett, 2005).

1.1.2. Brief history of Ca^{2+} channels – Classes and nomenclature

The initial perception was that all Ca^{2+} currents were derived from a single channel type; a notion that had support up until the early 1980s (Brown et al., 1982) despite early

evidence from Hagiwara and coworkers which identified two distinct types of Ca^{2+} current (what are now known as high voltage activated (HVA) and low voltage activated (LVA)) (Hagiwara et al., 1975). However, by the mid-1980s due to the contributions from a number of groups there was general consensus that, based primarily on their threshold of activation, there were at least two distinct types of Ca^{2+} channels (Llinás and Yarom, 1981; Carbone and Lux, 1984a, 1984b; Armstrong and Matteson, 1985; Bean, 1985; Fedulova et al., 1985; Matteson and Armstrong, 1986). Upon further analysis, Nowycky and Fox identified a third type of Ca^{2+} channel and put forward criteria for defining the three types of channels (Nowycky et al., 1985). The new criteria identified the L-type channel as a high voltage-activated channel with a large unitary conductance and a long lasting Ba^{2+} current whereas the T-type channel has a low threshold of activation, a tiny unitary conductance and a transient current whole cell waveform with Ba^{2+} as the charge carrier. N-type currents were neither exactly L-type nor T-type, although like L-type channels the N-type were high voltage-activated and similar to T-type channels they required a significantly hyperpolarizing potential to be available for opening. Additionally, the N-type currents were found to be insensitive to the L-type dihydropyridine agonist Bay K8644 (Nowycky et al., 1985).

Acceptance of the new classification was not universal (Swandulla and Armstrong, 1988). Fortunately, a peptide toxin (ω-conotoxin GVIA) identified and isolated by Olivera and Yoshikami from venomous cone snails (Yoshikami et al., 1989; Olivera et al., 1991) proved to be a specific inhibitor of N-type channels (McCleskey et al., 1987; Plummer et al., 1989; Boland et al., 1994). This antagonist in conjunction with the L-type dihydropyridine antagonists identified by Flekenstein allowed for the isolation of the L-type and N-type HVA currents and was crucial in the further identification of various Ca^{2+} currents in peripheral neurons (Plummer et al., 1989).

A fourth Ca^{2+} channel class was identified in cerebellar Purkinje neurons. The non-inactivating, dihydropyridine insensitive currents were designated P-type because of their localization (Llinás et al., 1989, 1992) and were found to be uniquely sensitive to peptide toxins isolated from funnel web spider venom (ω-Aga-IVA and ω-Aga-IVB)(Mintz et al., 1992). This fourth class of Ca^{2+} channel soon after became known as the P/Q-type when it was discovered that the Q-type currents identified based upon their distinct inactivation kinetics and relative insensitivity to ω-Aga-IVA (Randall and Tsien, 1995) were highly similar in both distribution and biophysical properties to P-type currents (Stea et al., 1994). This notion was subsequently confirmed by Bourinet and coworkers who determined that the P- and Q-type currents result from alternative splicing of the same Ca_v gene (Bourinet, 1999).

While performing a pharmacological dissection of the Ca^{2+} currents found in cerebellar granule neurons, Randall and Tsien identified a fifth class of native Ca^{2+} channels resistant to the pharmacological compounds known to specifically block the other HVA channels and was given the designation R-type. The identification of R-type Ca^{2+} channel was met with some criticism as the currents recorded could potentially be explained by a number of mechanisms including incomplete pharmacological blockade or splice variation of one of the previously identified classes. Once again, peptide toxins provided confirmatory insights in the form of SNX-482, an apparent R-type specific antagonist isolated from tarantula (*Hysterocrates gigas*) venom (Newcomb et al., 1998). It should be noted here that Snutch and colleagues had previously identified and cloned a novel fifth type of Ca^{2+} channel that exhibited biophysical and pharmacological properties distinct from both HVA and LVA subtypes (Soong et al., 1993) and that Randall and Tsien's R-type current was largely confirmatory of this new Ca^{2+} conductance first described by molecular cloning.

Concurrent with the biophysical and pharmacological identification of the different classes of native Ca^{2+} currents, efforts were being made to identify and clone the underlying genes responsible for native Ca^{2+} currents. The first Ca^{2+} channel clones to be identified were from the dihydropyridine-sensitive L-type channel isolated from skeletal muscle (Tanabe et al., 1987) and subsequently the homologous L-type channels from cardiac and smooth muscles (Mikami et al., 1989; Biel et al., 1990; Koch et al., 1990). The primary structures of the L-type channels from the cardiac/smooth muscle tissue were more related to each other than to the L-type channel from skeletal muscle suggesting that they were encoded by different genes and further presented the possibility that multiple genetic isoforms for each pharmacological class may exist. This notion was subsequently confirmed in that two Ca^{2+} channel isoforms identified in the brain were found to be closely related to the cardiac/smooth muscle L-types (called α_{1C} and α_{1D}) while other brain cDNAs encoded quite distinct Ca^{2+} channel types (called α_{1A} and α_{1B}, and shown to encode P/Q-type and N-type channels, respectively) (Snutch et al., 1990; Starr et al., 1991; Dubel et al., 1992; Stea et al., 1994). Additionally, splice variants of the neuronal Ca^{2+} channel isoforms were shown to be expressed both in the brain and other tissues (Snutch et al., 1991). Taken together, the considerable structural and functional diversity of Ca^{2+} channels was becoming apparent.

By 1994, with the wealth Ca^{2+} channel cloned isoforms identified, it was becoming increasingly difficult to identify which exact combination of channel and auxiliary subunits was being used by the various researchers in the field; a very real problem considering that co-expression of auxiliary subunits can significantly affect channel biophysical properties. As such, the field adopted the letter naming scheme initiated by Snutch and co-workers to define the main pore forming α_1 subunits and numbers to refer to the β, $\alpha_2\delta$, and γ auxiliary subunit variants (Snutch et al., 1990, 1991; Starr et al., 1991; Birnbaumer et al., 1994). The

standardization of nomenclature was taken a step further in 1997 to include the gene names under a format approved by the Human Genome Organization/ Human Gene Database (HUGO/GDB) nomenclature committee (Lory et al., 1997). Finally, the current nomenclature was proposed in 2000 and approved by the International Union of Pharmacology (IUPHAR) committee in 2003; it is based on the amino acid sequence similarity to represent the phylogenic relationship of the channels (Ertel et al., 2000; Catterall et al., 2003). Table 1.1 provides a summary of the evolution of the Ca^{2+} channel nomenclature and Figure 1.1 illustrates how the most recent nomenclature better suits phylogenic alignment of VGCCs.

Table 1.1: Evolution of the voltage-gated Ca^{2+} channel nomenclature.

Group	Class	Historical Snutch nomenclature [1]	HUGO/GDB gene nomenclature [2]	IUPHAR nomenclature [3]	First described:
HVA	L-type	α_{1S}	CACNA1S	$Ca_v1.1$	4
		α_{1C}	CACNA1C	$Ca_v1.2$	5
		α_{1D}	CACNA1D	$Ca_v1.3$	6
		α_{1F}	CACNA1F	$Ca_v1.4$	7
	P/Q-Type	α_{1A}	CACNA1A	$Ca_v2.1$	8
	N-type	α_{1B}	CACNA1B	$Ca_v2.2$	9
	R-type	α_{1E}	CACNA1E	$Ca_v2.3$	10
LVA	T-type	α_{1G}	CACNA1G	$Ca_v3.1$	11
		α_{1H}	CACNA1H	$Ca_v3.2$	12
		α_{1I}	CACNA1I	$Ca_v3.3$	13

Table 1.1: Evolution of the voltage-gated Ca^{2+} channel nomenclature.

Summary of the evolution of the nomenclature used to identify the main pore forming unit of voltage-gated Ca^{2+} channels. HVA: high voltage-activated, LVA: low voltage-activated. [1](Birnbaumer et al., 1994). [2] (Lory et al., 1997). [3] (Ertel et al., 2000; Catterall et al., 2003). [4] (Tanabe et al., 1987). [5] (Mikami et al., 1989; Biel et al., 1990; Koch et al., 1990; Starr et al., 1991). [6] (Hui et al., 1991; Williams et al., 1992b). [7] (Strom et al., 1998; Naylor et al., 2000; McRory et al., 2001). [8] (Mori et al., 1991; Starr et al., 1991). [9] (Dubel et al., 1992; Williams et al., 1992a; Fujita et al., 1993). [10] (Niidome et al., 1992; Soong et al., 1993). [11] (Perez-Reyes et al., 1998; Zhuang et al., 2000). 12 (Cribbs et al., 1998; Williams et al., 1999). [13] (Lee et al., 1999a).

Figure 1.1: Phylogeny of the voltage-gated Ca^{2+} channel family

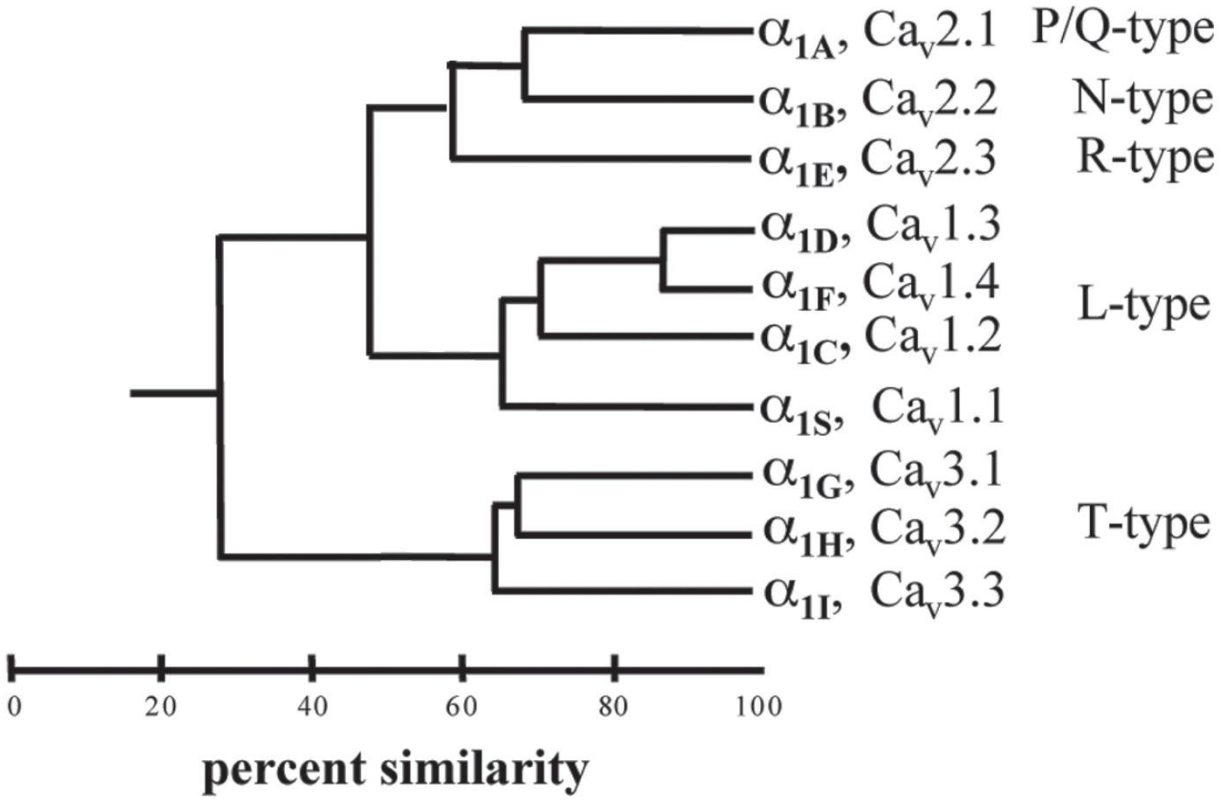

Figure 1.1: Phylogeny of the voltage-gated Ca^{2+} channel family

Phylogenic tree displaying the percent identity between the members of the voltage-gated Ca^{2+} channel family. Predicted amino acid sequences of each channel were compared pairwise and the percentage similarity plotted. The historical 1994 nomenclature followed by the IUPHAR nomenclature is used to identify each channel illustrating how the standardized IUPHAR nomenclature better reflects the phylogenic relationship of the channels. GenBank Accession Numbers of the VGCCs used: rat α1A, M64373; rat α1B, M92905; rat α1C, M67515; rat α1D, AF370009; rat α1E, L15453; human α1F, AJ224874; rat α1G, AF290212; rat α1H, AF290213; rat α1I, AF290214; rabbit α1S, M23919.

Adapted from Snutch *et al*. (Snutch et al., 2005)

1.1.3. Molecular structure and composition

Functional HVA VGCCs are multi-protein structures comprised of a main pore forming unit (α_1), together with several auxiliary subunits (β, $\alpha_2\delta$, and γ) (Takahashi et al., 1987; Campbell et al., 1988; Catterall et al., 1988; Ruth et al., 1989; Jay et al., 1990). The main pore forming unit is structurally similar to that of sodium channels (Tanabe et al., 1987), comprised of four homologous domains each with six hydrophobic transmembrane segments (S1-S6) (Campbell et al., 1988). The fourth segment (S4) of each domain acts as a voltage sensor due to the regularly repeating pattern of positively charged residues within this segment ((Lam et al., 2005; Kurejová et al., 2007) and reviewed in (Catterall, 2005, 2011; Snutch et al., 2005; Yu et al., 2005)). Between segments S5 and S6 in each domain a pore forming loop allows for the transport of ions through the channel and contains a conserved locus which confers Ca^{2+} ion specificity. The key residues within this conserved locus are four glutamates in HVA channels (EEEE locus) and a combination of glutamate and aspartic acid residues (EEDD locus) in LVA channels ((Kim et al., 1993; Talavera et al., 2001; Cens et al., 2007) and reviewed in (Sather, 2005)). The α_1 unit generally confers most of the biophysical and pharmacological properties of each Ca^{2+} channel subtype although various properties such as trafficking, voltage dependence, kinetics and second-messenger-dependent modulation have all been shown to be significantly altered by the auxiliary subunits (Hofmann et al., 1994; Stea et al., 1994; Hosey et al., 1996; Letts et al., 1998; Arikkath and Campbell, 2003; Cens et al., 2005; Herlitze and Mark, 2005; Snutch et al., 2005).

The S1-S6 segments and pore forming loops are well conserved across the VGCC family with approximately 80% amino acid similarity. However, when considering the entire channel the sequence similarity drops to about 70% within subfamilies and to less than 40%

between subfamilies (Catterall, 2000; Ertel et al., 2000). This dissimilarity arises primarily from the amino termini, cytosolic loops and carboxyl termini of the channels and is a major source of diversity within the VGCC family as they contain the β subunit binding site as well as many regulatory domains (Dolphin et al., 1999; Ivanina et al., 2000; Soong et al., 2002; Wolfe et al., 2002; Welsby et al., 2003; Chaudhuri et al., 2004; Dubel et al., 2004; DePuy et al., 2006).

The Ca_v3 (T-type) VGCCs are the most divergent of the VGCCs with only 40% similarity with the other classes and they do not retain such features such as the β subunit binding site in the cytosolic domain I-II linker and the E-F hand at the carboxyl terminus. As such, unlike the HVA channels, the auxiliary subunits are unlikely to play an important role in the regulation and function of the LVA channels (Dolphin et al., 1999; Dubel et al., 2004). An illustration of the typical topology of the pore forming unit of VGCCs can be seen in Figure 1.2.

Figure 1.2: Structural features of voltage-gated Ca^{2+} ion channels

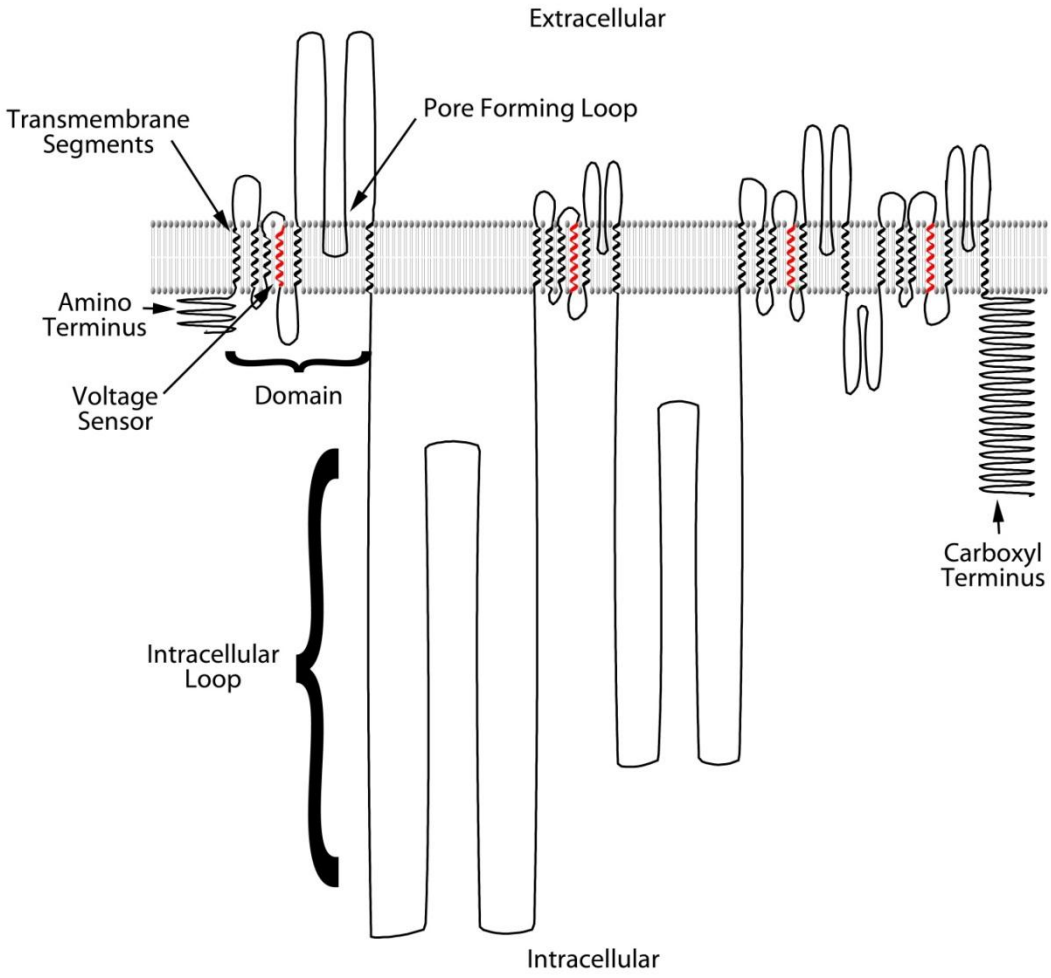

Figure 1.2: Structural features of voltage-gated Ca^{2+} ion channels

The main pore-forming unit of voltage-gated Ca^{2+} channels consists of four domains with six transmembrane segments each. Within each domain the fourth transmembrane segment (coloured red) contains positively charged residues which act a voltage sensor and respond to membrane depolarizations to confer a structural change in the channel which opens the pore. Between the fifth and sixth transmembrane segments of each domain there is a re-entrant extracellular loop that forms the pore of the channel and confers selectivity for Ca^{2+} ions. The domains are connected by intracellular loops, the amino acid sequence of which is highly variable between the channel types.

1.2. Ca_v3 calcium channels

1.2.1. Ca_v3 calcium channel expression

Ca_v3 channels (T-type) are expressed in various neuronal cell types of the central and peripheral nervous system as well in non-neuronal tissues throughout the body (reviewed in (Perez-Reyes, 2003)). Studies utilizing Northern blot analysis, immunohistochemistry, and reverse transcript PCR in conjunction with electrophysiological characterizations were effective in mapping the distribution of $Ca_v3.1$ (Perez-Reyes et al., 1998; Craig et al., 1999; Monteil et al., 2000a; McRory et al., 2001), $Ca_v3.2$ (Cribbs et al., 1998; McRory et al., 2001; Lee et al., 2002), and $Ca_v3.3$ (Lee et al., 1999a; Monteil et al., 2000b; McRory et al., 2001). Talley *et al*. were the first to characterize the distribution of the three Ca_v3 subtypes within the CNS using *in situ* hybridization (Talley et al., 1999). The mRNA expression profiles of the Ca_v3 subtypes display a significant amount of overlap which is most apparent in the hippocampus and the olfactory bulb where all three subtypes are expressed in moderate to high levels. In most regions however, expression is dominated by one (and sometimes two) subtype(s).

$Ca_v3.1$ is the most extensively expressed subtype with at least some degree of *in situ* mRNA staining observed in nearly every region of the CNS, whereas $Ca_v3.2$ and $Ca_v3.3$ expression within the CNS are relatively more isolated. $Ca_v3.1$ is the predominant subtype in many regions such as the bed nucleus of stria terminalis and claustrum of the basal forebrain, in most areas of the amygdala, the cerebral cortex, the thalamus (with the exception of the reticular nucleus) and hypothalamus, the medulla and spinal cord, the posterior granule cell and Purkinje cell layers of the cerebellum, and the inferior olive (Talley et al., 1999).

The expression of $Ca_v3.2$ is highest in the olfactory bulb and the hippocampus and it is the predominant subtype in the olfactory tubercle, the indusium griseum of the basal

forebrain, the granule cell layer of the dentate gyrus. Of note, the expression $Ca_v3.2$ mRNA is limited in the neocortex to layer 5 and to the reticular thalamic nucleus (nRT) of the thalamus suggesting that specific features of the $Ca_v3.2$ channel are important in these neurons. In the PNS, Cav3.2 expression is particularly significant in the dorsal root ganglia (Talley et al., 1999).

Similar to $Ca_v3.2$, the highest levels of $Ca_v3.3$ expression are found in the olfactory system and the hippocampus. The glomerular layer of the olfactory system is the only area identified in which $Ca_v3.3$ mRNA expression dominates over the other T-subtypes. In most cases $Ca_v3.3$ expression is similar to, or less than, the other Ca_v3 channels in other regions of the CNS and PNS (Talley et al., 1999).

Only a few of regions analyzed lacked or had limited expression of any of the Ca_v3 subtypes. For example, the globus pallidus of the basal forebrain, the substantia nigra and the reticular fields of the spinal cord appeared devoid of Ca_v3 expression using *in situ* hybridization (Talley et al., 1999). It is important to note that while the T-type channel mRNA expression patterns overlapped in many areas, *in situ* hybridization does not provide information as to whether the T-type channels themselves are expressed in similar or distinct subcellular regions of neurons or if they are isolated to distinct populations of cells within each region. In this regard, efforts have also been made to determine the subcellular localization of the T-type channel proteins. Immunohistochemical staining has shown that Ca_v3 expression can vary from primarily somatic expression (dentate gyrus granule cells and neurons of the midline thalamic nuclei) to include expression in the proximal dendrites (Layer 1-4 of the cortex and thalamic neurons) and extend as far as the distal dendrites (Purkinje cells, deep cerebellar neurons and pyramidal cells of cortical Layer 5 and the hippocampal formation) (Craig et al., 1999; McKay, 2006). Expression of the $Ca_v3.1$ and

$Ca_v3.2$ isoforms was found to be limited to the soma and the proximal dendrites in most instances with $Ca_v3.1$ expression in the deep cerebellar neurons extending to the distal dendrites being the exception. Conversely, expression of the $Ca_v3.3$ isoform extended to the distal dendrites in several of the neuronal cell types analyzed (Craig et al., 1999; McKay, 2006).

A detailed review of Ca_v3 expression in non-neuronal tissues such as the heart, kidney, smooth muscle tissue, skeletal muscle, germ cells, and endocrine tissues was written by Perez-Reyes in 2003 (Perez-Reyes, 2003). Examples of non-neuronal Ca_v3 expression include $Ca_v3.1$ and $Ca_v3.2$ in germ cells (Jagannathan et al., 2002; Son et al., 2002; Darszon et al., 2006), $Ca_v3.1$ in the renal tubules of the kidney (Andreasen et al., 2000), and in healthy mature cardiac tissue (Cribbs et al., 2001), $Ca_v3.2$ in the smooth muscle tissue in the kidney (Williams et al., 1999; Hansen et al., 2001), in embryonic and newborn skeletal muscle (Berthier et al., 2002), in the adrenal glands (Mlinar et al., 1993; Schrier et al., 2001; Levitsky and López-Barneo, 2009), and in the pituitary and pineal gland (Talley et al., 1999). It is interesting to note that $Ca_v3.3$ expression outside of the CNS is notably lacking (Perez-Reyes, 2003).

Developmental regulation of Ca_v3 expression has been demonstrated in several tissues. Overall expression of $Ca_v3.1$ in the rat brain is up-regulated during the early postnatal period from low levels at birth to higher levels comparable to that of adult mice by post natal day 11 whereas $Ca_v3.3$ expression is initially high and decreased substantially by post natal day 15 (Yunker, 2003). The splice variants of the Ca_v3 isoforms have also been shown to be developmentally regulated in rat brain (Emerick et al., 2006) and heart tissue (David et al., 2010). During embryogenesis there is a spatio-temporal regulation of $Ca_v3.2$ throughout many tissues, for example postnatal up-regulation of $Ca_v3.2$ in the testis (Son et al., 2002).

The developmental regulation is not limited to up regulation. Chromaffin cells display a developmental loss of $Ca_v3.2$ expression during maturity (Levitsky and López-Barneo, 2009), and the expression of both $Ca_v3.1$ and $Ca_v3.2$ in embryonic and newborn skeletal muscle decreases to undetectable by postnatal day 22 (Berthier et al., 2002). As a final example of the dynamic regulation of Ca_v3 channels during development, a switch in Ca_v3 expression occurs in cardiac tissue wherein $Ca_v3.2$ expression is down-regulated and $Ca_v3.1$ is up-regulated so that in the adult heart the predominant T-type channel isoform is $Ca_v3.1$ (Niwa et al., 2004; Cribbs, 2010).

In addition to developmental regulation, Ca_v3 expression is significantly altered in several pathological conditions/models. In rodents, an increase in $Ca_v3.2$ current density has been linked to diabetic neuropathic pain (Jagodic et al., 2007) and following status epilepticus (seizure activity lasting greater than thirty minutes or more than two seizures between which the subject does not regain consciousness (Heafield, 2000)), a transcriptional up-regulation of $Ca_v3.2$ has been suggested to contribute to the chronic epileptic condition (Su, 2002; Vitko et al., 2007; Becker et al., 2008). In cardiac tissue re-expression of the $Ca_v3.2$ channel has been shown to accompany the induction of hypertrophy (Nuss and Houser, 1993; Martínez et al., 1999; Huang et al., 2000; Chiang et al., 2009; Cribbs, 2010; David et al., 2010). Further, $Ca_v3.1$ expression is down-regulated and $Ca_v3.2$ up- regulated following hypoxia in acutely dissociated ventricular myocytes (Pluteanu and Cribbs, 2009) while in chronic hypoxia both $Ca_v3.1$ and $Ca_v3.2$ expression are up-regulated in adrenal chromaffin cells (Carabelli et al., 2007b; Levitsky and López-Barneo, 2009; Souvannakitti et al., 2010). Also in rat chromaffin cells, exposure to cAMP or β-adrenergic stimulation results in an up-regulation of $Ca_v3.2$ T-type channels which has been shown to be mediated by a PKA independent pathway involving the cAMP receptor Epac, a cAMP-guanine nucleotide

exchange factor (Novara et al., 2004). This is not an exhaustive list of examples of Ca_v3 dynamic regulation; although it does illustrate that each of the Ca_v3 isoforms likely plays key roles in many tissues during development and in various pathological conditions.

1.2.2. Biophysical properties of Ca_v3 channels

Initial attempts to characterize T-type channels were complicated by seemingly conflicting results and at first it was proposed that the discrepancies observed were due to differences in the recording solutions (Huguenard, 1996). However, with the identification of the three distinct Ca_v3 molecular subtypes ($Ca_v3.1$, $Ca_v3.2$ and $Ca_v3.3$) and subsequent determination of their expression profiles, it became apparent that many of the apparent discrepancies could be attributed to the differential expression of the Ca_v3 channels across cell types and tissues. With the availability of Ca_v3 cDNA clones the T-type channels were studied in isolation in heterologous systems enabling investigators to determine their biophysical, pharmacological and modulatory properties.

The LVA (T-type) class of VGCCs originally derived its name from three key features: a relatively negative threshold of activation, a small single channel conductance, and a rapidly inactivating waveform compared to HVA VGCCs. The activation threshold of Ca_v3 channels is generally between -75 and -60 mV with half maximal activation ($V_{50\ act}$) approximately -45 and -40 mV (McDonald et al., 1994; Huguenard, 1996; Perez-Reyes et al., 1998; Klöckner et al., 1999; Perez-Reyes, 2003; Talavera and Nilius, 2006). Half maximal inactivation ($V_{50\ inact}$) of the Ca_v3 channels is also quite negative, occurring between -80 and -60 mV (Huguenard, 1996; Klöckner et al., 1999; Talavera and Nilius, 2006). The overlap in activation and inactivation profiles results in a narrow range of potentials in which a small percentage of Ca_v3 channels can be open at the resting potential of many cell types. Known

as the "window current" (Coulter et al., 1989; Perez-Reyes, 2003; Cain and Snutch, 2010), it has been proposed to contribute to both intracellular Ca^{2+} homeostasis and to the shaping of neuronal firing patterns (Carbone and Lux, 1984a; Coulter et al., 1989; Williams et al., 1997; Hughes et al., 1999; Crunelli et al., 2005; Contreras, 2006; Dreyfus et al., 2010).

Ca_v3 channels are permeable to multiple divalent ions including Ca^{2+}, Ba^{2+} and Sr^{2+}. Utilizing heterologous expression systems is has been determined that $Ca_v3.1$ channels are slightly more permeable to Ca^{2+} over Ba^{2+} while $Ca_v3.2$ channels are slightly more permeable to Ba^{2+} over Ca^{2+} and $Ca_v3.3$ channels being equally permeable to Ca^{2+} and Ba^{2+} (McRory et al., 2001; Kaku, 2003). The single channel conductance of Ca_v3 channels is dependent on the external concentration of divalent cation with reports of 5-9 pS using extracellular recording solutions containing 10 to 110 mM Ca^{2+} or Ba^{2+} and a projected conductance of 1 pS in 2 mM Ca^{2+} (reviewed in (Huguenard, 1996)).

The "transient" characteristic of native Ca_v3 currents is attributable to their relatively fast inactivation kinetics. Comparison of the cloned Ca_v3 isoforms has revealed that $Ca_v3.1$ and $Ca_v3.2$ channels exhibit comparable inactivation kinetics to those generally observed for native T-type; a relatively low tau of inactivation and that is strongly voltage-dependent. $Ca_v3.3$ channels however, inactivate at a significantly lower rate resulting in more prolonged currents during depolarization. A similar distinction is observed concerning activation kinetics with $Ca_v3.1$ and $Ca_v3.2$ activation being faster than $Ca_v3.3$ channels. (Huguenard, 1996; Perez-Reyes et al., 1998; Klöckner et al., 1999; Kozlov et al., 1999; Lee et al., 1999a; Williams et al., 1999; McRory et al., 2001; Perez-Reyes, 2003). Consistent with native T-type currents, the cloned Ca_v3 channels exhibit a voltage-dependence of activation with activation kinetics increasing with further depolarization which generates a characteristic

crisscrossing pattern of the whole cell current traces (Huguenard, 1996; Randall and Tsien, 1997; Perez-Reyes, 2003) .

Following a depolarizing stimulus, Ca_v3 channels deactivate (close) comparatively slower than HVA channels resulting in a significant influx of Ca^{2+} as the driving force rapidly increases upon membrane potential repolarization. $Ca_v3.3$ channels deactivate the quickest followed by $Ca_v3.2$ and finally with $Ca_v3.1$ exhibiting the slowest deactivation kinetics (McCobb and Beam, 1991; Klöckner et al., 1999; Kozlov et al., 1999; Serrano et al., 1999; Monteil et al., 2000b). Additionally, there are differences in the rate of recovery from inactivation between the Ca_v3 channel isoforms with $Ca_v3.1$ recovering the fastest and $Ca_v3.2$ the slowest (Klöckner et al., 1999). A summary of the biophysical properties of the cloned Ca_v3 channels is presented in Table 1.2.

Table 1.2: Summary of the biophysical characteristics of the low threshold Ca_v3 channels

	$Ca_v3.1$	$Ca_v3.2$	$Ca_v3.3$	Reference
Threshold of activation	~ -60mV	~ -60mV	~ -60mV	(Klöckner et al., 1999)
Half peak activation (V_{50act})	-45.5 mV	-45.8 mV	-43.8 mV	(Klöckner et al., 1999)
Peak activation	-29.2 mV	-29.4 mV	-27.6 mV	(Klöckner et al., 1999)
Tau of activation (depolarization potential = -45mV)	6 ms	8 ms	30 ms	(Klöckner et al., 1999)
Voltage dependent activation	Yes	Yes	Yes	(Klöckner et al., 1999)
Tau of deactivation (repolarization potential = -120 mV)	1.7 ms	2.7 ms	1.0 ms	(Klöckner et al., 1999)
Voltage-dependent deactivation	Yes	Yes	Yes	(Klöckner et al., 1999)
Half Inactivation ($V_{50inact}$)	-72.8 mV	-72.0 mV	-72.5 mV	(Klöckner et al., 1999)
Tau of inactivation (depolarization potential = -45 mV)	30 ms	47 ms	137 ms	(Klöckner et al., 1999)
Potential difference for e-fold change in Tau of inactivation	18.7 mV	13.5 mV	13.9 mV	(Klöckner et al., 1999)
Tau of inactivation (positive depolarization potentials)	11 ms	16 ms	69 ms	(Klöckner et al., 1999)
Voltage-dependent inactivation	at negative potentials	at negative potentials	at negative potentials	(Klöckner et al., 1999)
Recovery from short term inactivation	117 ms	395 ms	359 ms	(Klöckner et al., 1999)
Recovery from long term inactivation	1806 ms	2587 ms	611ms	(Klöckner et al., 1999)
Conductance (barium)	7.5 pS	9 pS	11 pS	Reviewed in (Perez-Reyes, 2003)

Table 1.2: Summary of the biophysical characteristics of the low threshold Ca_v3 channels

Biophysical characteristics of the Ca_v3 channels cloned from rat ($Ca_v3.1$ and $Ca_v3.3$) and human ($Ca_v3.2$) and stably expressed in human embryonic kidney cells. The recordings were made using 1.25 mM Ca^{2+} as the charge carrier (Klöckner et al., 1999).

1.2.3. Physiological roles of T-type Ca^{2+} channels

T-type Ca^{2+} channels make important contributions to many neuronal and non-neuronal cell types. The low thresholds of activation and inactivation, window current, and the prolonged deactivation permit T-type channels to participate in burst firing, rhythmic oscillatory activity, and regulate intracellular Ca^{2+} levels and second-messenger-dependent pathways. Together, these unique properties have been shown to play significant roles in signal amplification (Williams et al., 1997; Hughes et al., 1999), sensory coding (Krahe and Gabbiani, 2004), rhythmic pace making (Park et al., 2010), hormone secretion (reviewed in (Perez-Reyes, 2003)), neurotransmitter release (Pan et al., 2001; Carbone et al., 2006a; Jacus et al., 2012), and the generation and maintenance of neuronal firing patterns which underlie physiologically important states such as sleep (review in (Steriade, 2005)).

The low threshold of activation of T-type channels permits depolarizing potentials that are insufficient to elicit an action potential to produce low threshold Ca^{2+} spikes (LTSs) which are critical for the low threshold burst-firing observed in many neuronal cell types. If the density of Ca_v3 channels is high enough, the LTS can depolarize the membrane sufficiently to surpass the action potential threshold required to trigger an action potential. LTSs may also be generated following hyperpolarization (e.g. following an action potential) as the Ca_v3 channels are reactivated during the restoration of the resting membrane potential. Depending upon the intensity and duration of the LTS, multiple action potentials can crest the LTS in a "burst" of activity. A LTS following an action potential burst is known as an after depolarization potential (ADP) which is capable of stimulating additional action potentials if the intensity and duration of the ADP is sufficient (Deschenes et al., 1982; Llinás and Jahnsen, 1982; Jahnsen and Llinás, 1984; Crunelli et al., 1989; White et al., 1989; Huguenard and Prince, 1992; Aptel et al., 2007; Cain and Snutch, 2010; Dreyfus et al., 2010).

T-type channels can participate in several distinct neuronal firing patterns depending on the resting membrane potential. For example, overlap of the steady-state activation and inactivation properties of the Ca_v3 channels (window current) contributes to a bi-stability in neuronal firing patterns (Williams et al., 1997; Hughes et al., 1999). If membrane potentials are sufficiently hyperpolarized to remove inactivation the T-type channels can drive a repetitive low threshold burst-firing pattern. As membrane potentials approach the window current a bi-phasic firing pattern can become apparent resulting in a slow (<1 Hz) oscillatory firing pattern (Coulter et al., 1989; Williams et al., 1997; Hughes et al., 1999; Crunelli et al., 2005; Cain and Snutch, 2010). At more depolarized resting potentials T-type channels are almost completely inactivated and appear to contribute little to neuronal activity in tonic firing states. Overall, amongst other contributions, this bi-stability plays an important role in establishing and maintaining the distinct neuronal firing patterns observed during sleep and wakefulness (reviewed in (Steriade, 2005)).

The low activation threshold and prolonged deactivation time course of T-type channels contributes to the intracellular Ca^{2+} increase that occurs in response to sub-threshold stimuli. In this regard, a T-type channel-mediated intracellular Ca^{2+} increase has been shown to be critically involved in hormonal secretion and more recently neurotransmitter release. T-type channels have been linked with stimulus-secretion coupling in the release of aldosterone and cortisol from cells in the adrenal glomerulosa (Cohen et al., 1988), in insulin secretion from β-cells of the pancreas (reviewed in (Perez-Reyes, 2003)), and in the cyclic release of gonadotropin releasing hormone (Zhang et al., 2009). Additionally, T-type currents have been identified and are believed to be involved in the hormone release in lactotropes, corticotropes, gonadotropes, and thyrotropes of the pituitary gland (reviewed in (Perez-Reyes, 2003)).

Recently, $Ca_v3.2$ channels have been found to be necessary for the release of catecholamines from chromaffin cells of the adrenal medulla in response to acute hypoxia. In the early post-natal period chromaffin cells possess oxygen sensing capabilities, which play a vital role in the transition to extrauterine life. This oxygen sensitivity is lost in early development along with an accompanying decrease in $Ca_v3.2$ expression in chromaffin cells. Under chronic hypoxia however, $Ca_v3.2$ channels are re-expressed and chromaffin cells regain oxygen sensitivity (Carbone et al., 2006b; Carabelli et al., 2007a, 2007b; Levitsky and López-Barneo, 2009). Acute sympathetic stress has also been found to recruit $Ca_v3.2$ channels resulting in a fast, low-threshold-dependent release of catecholamines as part of the fight or flight response (Novara et al., 2004; Giancippoli et al., 2006; Currie, 2010; Hill et al., 2011).

T-type channels have also been found to play roles in neurotransmitter release in several neuronal cell types such as retinal bi-polar cells (Pan et al., 2001), dendro-dendritic reciprocal synapses between granule cells and mitral/tufted cells of the olfactory bulb (reviewed in (Carbone et al., 2006a)), and in populations of nociceptive neurons in the superficial laminae of the dorsal horn (Bao et al., 1998; Jacus et al., 2012). The low threshold of activation of T-type channels allows for fast, low threshold exocytosis permitting retinal bipolar cells to respond to graded depolarizations (Pan et al., 2001). In the inhibitory synapses found between the granule and mitral cells of the olfactory bulb, T-type channel-mediated neurotransmitter release provides a means for low threshold inhibition which has been proposed to play a role in the gating of olfactory information to cortex (reviewed in (Carbone et al., 2006a)). Finally, more recently $Ca_v3.2$ channels have been identified as regulating the frequency of spontaneous micro excitatory postsynaptic currents in nociceptive

neuron within the dorsal horn and demonstrating a role for $Ca_v3.2$ in the regulation of the excitability associated with peripheral pain sensitization (Jacus et al., 2012).

T-type channels also play roles in pathological conditions such as cancer, epilepsy and cardiac hypertrophy. Recent studies suggest that T-type channels are important in the cell proliferation associated with some cancer cell lines (Li et al., 2009; Santoni et al., 2012; Zhang et al., 2012) . While the precise pathway(s) remain unclear, it has been suggested that T-type channels contribute to proliferation through the regulation of intracellular Ca^{2+} levels. In these studies the inhibition of T-type channel activity significantly reduces cell proliferation and migration in select cancer cell lines presenting the possibility that specific T-type channel isoforms may be potential therapeutic targets in for certain cancers (reviewed in (Santoni et al., 2012)).

T-type channels are abundantly expressed in the thalamus and participate in oscillatory neuronal activity within a reciprocally connected circuit comprised of thalamocortical, thalamic reticular and cerebral cortical neurons. Under normal physiological conditions this oscillatory activity contributes to naturally occurring processes such as sleep, while in the pathological conditions associated with certain types of epilepsy abnormal oscillatory activity within the thalamocortical circuit contributes to seizure activity (reviewed in (Zamponi et al., 2009; Santoni et al., 2012)). Several lines of evidence demonstrate that specific Ca_v3 channel subtypes are involved in various forms of epilepsy. In temporal lobe epilepsy an increase in $Ca_v3.1$ expression has been observed in thalamic cells and an accompanying increased low threshold activity is believed to contribute to the abnormal thalamocortical activity. Support for this can be found in $Ca_v3.1$ gene knock-out mice which are resistant to chemically induced spike and wave discharges which underlie seizure activity (Kim et al., 2001). Furthermore, naturally occurring mutations which alter the physiological

properties or expression of $Ca_v3.2$ channels have been associated with childhood absence epilepsy (Crunelli and Leresche, 2002; Chen et al., 2003b; Peloquin et al., 2006; Vitko et al., 2007). Additional evidence for a role of $Ca_v3.2$ channels in absence epilepsy has come from the Genetic Absence Epilepsy Rat from Strasbourg (GAERS) and the WAG/Rijj models of absence epilepsy wherein increased expression of $Ca_v3.2$ has been identified in the thalamic reticular nucleus. In the GAERS model, a mutation in the $Ca_v3.2$ gene has been identified that associates with the epileptic phenotype and that contributes to a gain-of-function in T-type channel activity in GAERS compared to control animals (Powell et al., 2009). Further convincing evidence for the involvement of T-type channels to epileptic phenotypes comes from a recent study demonstrating that selective Ca_v3 blockers significantly reduce the number and duration of seizures in the GAERS model (Tringham et al., 2012).

In cardiac tissue there is a developmental switch in Ca_v3 expression from predominantly $Ca_v3.2$ in neonate and early post-natal rats to almost exclusive $Ca_v3.1$ expression in the adult rat. Under normal physiological conditions the $Ca_v3.1$ subtype appears to be involved in the regulation of the pace making current in the sinoatrial node and excitation-contraction coupling (Mangoni et al., 2006; Vassort et al., 2006) while $Ca_v3.2$ is involved in the NO mediated vasodilation of the circulatory system (Chen et al., 2003a). In the pathological condition following hypertrophy induction or following myocardial infarction a remodeling of Ca_v3 expression occurs with $Ca_v3.2$ being re-expressed in cardiac tissue (reviewed in (Vassort et al., 2006)). Although the exact consequences of this remodeling of Ca_v3 expression remains unclear, it is interesting to note that the ratio of the $Ca_v3.2$ exon 25(+) vs. $Ca_v3.2$ exon 25(-) splice variants expressed after remodeling is significantly different that found in the neonatal heart. As shown by David and coworkers, the 25(+) splice variant confers a distinct voltage-dependent facilitation characteristic to

$Ca_v3.2$ channels thus the change in relative expression between splice variants may affect excitability and/or intracellular Ca^{2+}–mediated signaling (David et al., 2010).

In discussion of the physiological roles of T-type channels it is important to mention the phenotypes of $Ca_v3.1$ (Kim et al., 2001) and $Ca_v3.2$ (Chen et al., 2003a) knock-out mice strains. In the absence of subtype-specific antagonists the knock-out mice have been an invaluable tool in assessing the physiological consequences of complete T-type channel loss-of-function. Outwardly, the global loss of either $Ca_v3.1$ or $Ca_v3.2$ expression is not lethal and the knock-out mice generally appear phenotypically normal with the only reported noticeable difference being a decreased body size for the $Ca_v3.2$ knock-out mice. Further investigation however, has revealed differences in the cardiac and circulatory systems, nociceptive responses to peripheral and visceral pain, learning and memory, and in the threshold of seizure induction. Table 1.3 provides a summary of the phenotypes observed in the $Ca_v3.1$ and $Ca_v3.2$ knock-out mice. As of this writing there has been no report of the phenotypes associated with $Ca_v3.3$ gene knock-out.

Table 1.3: Summary of $Ca_v3.1$ and $Ca_v3.2$ knockout mice phenotypes

$Ca_v3.2$ Knock-out [1]	**$Ca_v3.1$ Knock-out** [2]
General phenotype	
- viable and fertile [1]	- viable and fertile [2]
- small body size [1]	-normal growth [2]
- General behaviour (motor associated and emotion-related functions) normal as determined by: [3]	- Not reported
- open box test	
- horizontal and vertical activities	
- rotarod	
- light/dark transition	
Cardiac/Circulatory system	
- heart rate normal [1]	-decreased heart rate [5]
- ECG waveforms normal [1]	- bradycardia [5]
- no cardiac arrhythmias [1]	- atrioventricular dysfunction [5]
Ventricles	- no histological defects in organs such as heart, intestine, kidney, pancreas, liver [2]
- 10 week - cardiac fibrosis [1]	
- 1 year - increases cardiac fibrosis, necrosis, lymphocyte infiltration [1]	
Vessels	
- constricted and irregular [1]	
Coronary arteries	
- NO mediated dilation is defective [1]	
Nociception	
- decreased LVA current in DRGs [1]	
- HVA currents unaffected [1]	
- decreased nociceptive response to: [3]	- normal nociceptive response to [6]
- mechanical stimuli (tail clip)	- mechanical stimuli (tail clip)
- thermal stimuli (hot plate)	- thermal stimuli (hot plate)
- chemical stimuli (capsaicin)	
- noxious chemical stimuli (both phases)	

Table 1.3: Summary of $Ca_v3.1$ and $Ca_v3.2$ knockout mice phenotypes - continued

$Ca_v3.2$ Knock-out [1]	$Ca_v3.1$ Knock-out [2]
Neuropathic pain	
- normal response [3]	- decreased spontaneous pain [7]
	- decreased mechanical hyperalgesia [7]
	- decreased thermal hyperalgesia [7]
Learning and Memory	
- late phase LTP lost in hippocampal slices [4]	- not reported
- normal memory formation [4]	- not reported
- decreased retrieval in context cued trace fear learning [4]	- not reported
- decreased retrieval in context cued passive avoidance task [4]	- not reported
Epilepsy	
- not reported	- brain morphology normal [2]
- not reported	- burst rebound action potentials lacking in thalamocortical neurons [2]
- not reported	- resistance to pharmacological initiation of spike and wave discharges (absence epilepsy) [2]
	~ γ-Baclofen
	~ γ -Butyrolactone
	~normal response to Bicuculline
- not reported	-normal susceptibility to tonic-clonic seizures (determined pharmacologically) [2]

Table 1.3: Summary of $Ca_v3.1$ and $Ca_v3.2$ knockout mice phenotypes

Summary of the phenotypes observed for $Ca_v3.1$ and $Ca_v3.2$ knock-out mice strains compared to wild type littermate controls. References: [1.] (Chen et al., 2003a), [2.] (Kim et al., 2001), [3.] (Choi et al., 2007), [4.] (Chen et al., 2012), [5.] (Mangoni et al., 2006), [6.] (Kim et al., 2003), [7.] (Na et al., 2008).

1.2.4. Pharmacological properties of T-type Ca^{2+} channels

One of the most significant hurdles in studying the LVA VGGCs *in vivo* has been the lack of T-type channel-specific antagonists to differentiate LVA currents from HVA currents and also Ca_v3 isoforms from each other. While the availability of Ca_v3 cDNAs has enabled

the characterization of their biophysical properties, there are limitations as to how far this information can translate to *in vivo* preparations. Specific antagonists would be particularly useful in determining the contribution of T-type channel isoforms to neuronal firing patterns which are comprised of multiple ionic conductances. Additionally, the involvement of specific Ca_v3 channel subtypes in pathological conditions such as pain (Bourinet et al., 2005), cardiac hypertrophy (Chiang et al., 2009) and epilepsy (Khosravani and Zamponi, 2006) makes them potential therapeutic targets. Towards these objectives efforts are ongoing to develop high affinity Ca_v3 specific antagonists (Shipe et al., 2008; Yang et al., 2008; Smith et al., 2010; Woo et al., 2011).

Nickel (Ni^{2+}) was one of the first T-type channel antagonists to be identified (reviewed in (Yunker, 2003)). While Ni^{2+} generally inhibits T-type currents, the affinity of this divalent cation was found to be highly variable across preparations (Kaneda et al., 1990; Satoh et al., 1991). Analysis of the Ni^{2+} sensitivity of cloned Ca_v3 channels subsequently revealed the differential inhibition of the three subtypes with $Ca_v3.2$ being the most sensitive (~ IC_{50} =12μM) and with $Ca_v3.1$ and $Ca_v3.3$ being less sensitive to Ni^{2+} blockade (~ IC_{50}s 250 μM and 216 μM, respectively; (Lee et al., 1999b). The differential sensitivity to Ni^{2+} has allowed for the selective block of $Ca_v3.2$ channels and provided a useful pharmacological tool although other considerations remain such as the partial blockade of the other T-type isoforms (Zamponi et al., 1996; Lee et al., 1999b). The structural determinant for the high Ni^{2+} sensitivity of $Ca_v3.2$ has been identified as a histidine residue at position 191 (H191) located on the putative extracellular loop linking segments S3-S4 linker of domain I (Kang et al., 2006). Interestingly, this same residue also confers $Ca_v3.2$ sensitive to zinc and copper (Kang et al., 2006; Traboulsie et al., 2006; Sun et al., 2007) which poses a problem if recording solutions or the tissue specimen are not free of these trace elements. A potential

solution to this issue is the use of divalent cation chelators (Nelson et al., 2007b). . A final note regarding divalent cation blockade is that while T-type channels are sensitive to Ni^{2+}, Zn^{2+} and Cu^{2+} they are resistant to cadmium (Cd^{2+}) at certain concentrations. Taking advantage of differences in the ion selectivity of the pore forming loop of HVA and LVA channels, Cd^{2+} may be used at low concentrations (20-100 μM) to block HVA currents while preserving Ca_v3 currents.

Another well-known T-type channel antagonist is mibefradil, an effective therapeutic antihypertensive that was subsequently withdrawn from the market due to potentially fatal side reactions (reviewed in (Welker et al., 1998)). Although mibefradil has proven useful as a relatively selective T-type channel antagonist at low concentrations (<1 μM (Martin et al., 2000), at higher greater concentrations it also inhibits HVA channels which has resulted in this agent generally being classified as a non-specific antagonist (Randall and Tsien, 1997; Viana et al., 1997). The non-specific inhibition of T-type channels by various pharmacological agents has been reviewed extensively (Perez-Reyes, 2003; Yunker, 2003) and continues to be addressed as additional compounds are identified (Joksovic et al., 2005; Freeze et al., 2006; Kraus et al., 2007). The general non-specific inhibition of the T-type channels is a common theme across an impressive list of pharmacological agents and highlights the real need for the development of Cav3-specific agents in order to better dissect their relative contributions to various pathological conditions. While peptide toxins have proven invaluable in the study of HVA channels there has not been a similar description of these agents towards T-type channels. For example, kurtoxin isolated from scorpions (*Parabuthus transvaalicus*) was originally found to block $Ca_v3.1$ and $Ca_v3.2$ channels although unfortunately later shown to also block sodium channels as well as L-type, N-type and R-type Ca^{2+} channels (Chuang et al., 1998; Sidach and Mintz, 2002). More recently, two

peptide toxins, ProTx-I and ProTx-II have been isolated from tarantula venom (*Thrixopelma pruriens*). ProTX-I differentially blocks $Ca_v3.1$ over $Ca_v3.2$ with IC_{50}s of 0.2 μM and 32 μM respectively and ProTX-II blocks $Ca_v3.3$ channels with an IC_{50} of 0.8 μM (Edgerton et al., 2010; Ohkubo et al., 2010). As such, these peptide toxins hold some promise as they can either be used in conjunction to completely block Ca_v3 currents or be used separately to isolate $Ca_v3.2$ or $Ca_v3.1$ currents in experimental preparations.

TTA-P2, a small synthetic piperidine-based molecule (Shipe et al., 2008; Yang et al., 2008) has been reported to selectively block T-type currents of the thalamocortical and reticular thalamic neurons with a high degree of potency (IC_{50} = 22 nM) while leaving HVA Ca^{2+} and sodium currents intact (Dreyfus et al., 2010). Development of this series of molecules is ongoing (Smith et al., 2010; Woo et al., 2011) although as TTA-P2 induces sleep upon administration to animals it remains to be seen if this agent/class of molecule will prove generally useful. Recently two new compounds, Z941 and Z944, have been demonstrated to block T-type channels with IC_{50}s in the nanomolar range. These novel small molecule blockers are highly selective for the T-type channels while leaving sodium and potassium currents relatively unscathed. Furthermore administration of the Z941 and Z944 has been found to reduce both the duration and frequency of seizures in the GAERS absence epilepsy model (Tringham et al., 2012).

1.2.5. Modulation of T-type Ca^{2+} channels

There is an accumulating amount of evidence regarding the physiological modulation of Ca_v3 channel isoforms. Some mechanisms appear conserved across all three Ca_v3 isoforms, such as current enhancement by protein kinase C (PKC) and protein kinase A (PKA), while other mechanisms such as the potentiation of $Ca_v3.2$ by Ca^{2+}/calmodulin-

dependent kinase II (CaMKII) appear selective for particular Ca_v3 subtypes (reviewed in (Iftinca, 2011)). As this thesis focuses on $Ca_v3.2$ channels the emphasis of this section will be on the $Ca_v3.2$ subtype.

The cytoplasmic loop linking domains II and III is an important regulatory domain for all Ca_v3 channels (reviewed in (Iftinca and Zamponi, 2009; Iftinca, 2011)). In $Ca_v3.2$ the modulatory sites for CaMKII, G protein β2 and γ subunits (Gβ2γ), PKA and ROCK have all been localized to the domain II-III linker (Welsby et al., 2003; Kim et al., 2006; Iftinca et al., 2007). Lu and coworkers demonstrated that T-type currents in adrenal glomerulosa cells could be enhanced by CaMKII activity (Lu et al., 1994) and subsequently this enhancement was demonstrated to be specific to $Ca_v3.2$ channels (Wolfe et al., 2002). Of note, the underlying mechanism occurs through direct phosphorylation of a serine residue at position 1198 in the domain II-III linker (Yao et al., 2006) which results in a shift in activation to more hyperpolarized potentials (Lu et al., 1994; Wolfe et al., 2002). In adrenal glomerulosa cells, stimulation of the angiotensin-II receptor II (AngII) has been shown to activate CaMKII to phosphorylate serine 1198 of $Ca_v3.2$ suggesting a possible role for this regulation in the progression of cardiac disease (Fern et al., 1995; Yao et al., 2006).

PKC was shown to enhance $Ca_v3.2$ (Park et al., 2003) and later $Ca_v3.1$ and $Ca_v3.3$ (Park et al., 2006) currents without affecting the surface expression of the channels in *Xenopus* oocytes. A crucial site for PKC modulation of $Ca_v3.1$ channels was localized to the domain II-III linker suggesting that possibility the interaction site may be similarly localized for $Ca_v3.2$ channels (Park et al., 2006; Rangel et al., 2010). Recently, Rangel and coworkers have described a signaling pathway involving neurokinin 1 receptors (NKR1) whereby stimulation of NKR1 activates $G\alpha_{q/11}$ which in turn activates phospholipase C β (PLCβ)

converting phosphatidylinositol 4,5-bisphosphate (PIP2) to diacylglycerol (DAG) to activate PKC and ultimately enhance $Ca_v3.2$ currents (Rangel et al., 2010).

The domain II-III linker was also found to be involved with the augmentation of $Ca_v3.2$ currents by PKA in *Xenopus* oocytes (Kim et al., 2006). Interestingly, the modulation of $Ca_v3.2$ currents by PKA and PKC was only reproducible in mammalian cells at physiological temperatures (Chemin et al., 2007) which emphasizes an important point to consider when investigating modulatory interactions outside of normal physiological parameters. In mouse neonatal ventricular myocytes PKA augmentation of $Ca_v3.2$ currents was found to be regulated by caveolin-3 with siRNA silencing of caveolin-3 occluding the effect of PKA activation (Markandeya et al., 2011). On the other hand, PKA has also been found to be essential in mediating an inhibitory effect of Gβ2γ (Hu et al., 2009). It is possible that PKA plays a dual role it modulation of $Ca_v3.2$ channels and that its effect depends upon the specific interactions available within the cell with some interactions resulting in augmentation and others in inhibition.

In 1997 it was discovered that T-type currents in the adrenal glomerulosa could be inhibited by activation of the dopamine D1 G-protein-coupled receptor and to occur specifically via Gβγ (Drolet et al., 1997). Later, Wolfe and coworkers used heterologous expression and chimeric Ca_v3 constructs to determine that G-protein Gβ2γ subunits selectively inhibit $Ca_v3.2$ currents through a direct interaction with the domain II-III linker (Welsby et al., 2003). It was further determined that the inhibition was due to a decrease in the open probability of $Ca_v3.2$ channels and not to changes in channel expression or waveform kinetics (DePuy et al., 2006). Utilizing human adrenocortical carcinoma cell line Hu and coworkers found that the inhibition of $Ca_v3.2$ currents via the activation of dopamine

receptors was more complicated than originally envisioned; requiring the activation of D1 and D2 dopamine receptors and the presence of activated PKA (Hu et al., 2009).

In HEK293T cells, stimulation of an exogenously expressed corticotropin-releasing factor receptor-1 (CRF-1) inhibited $Ca_v3.2$ currents through a cholera-toxin sensitive, Gα pathway which was dependent on Gβγ (Tao et al., 2008). In the MN9D cell line CRF-1 inhibition of Ca_v3 currents was shown to occur through a PKC-dependent signaling pathway (Kim et al., 2007). The difference in findings between groups may be attributable to the different cell types utilized in each study. Considering that in other studies, PKC was found to generally enhance Ca_v3 currents, the results from Kim *et al*. suggest that PKC modulation of $Ca_v3.2$ may involve additional cellular mechanisms that are as yet unidentified (Iftinca, 2011).

Lysophosphatidic acid (LPA) was found to differentially modulate the three Ca_v3 channels with inhibition of $Ca_v3.1$ and $Ca_v3.3$ and enhancement of $Ca_v3.2$ currents occurring through the phosphorylation of conserved ROCK phosphorylation sites in the domain II-III linker. Enhancement of $Ca_v3.2$ currents by LPA/ROCK was shown to be the result of a hyperpolarizing shift in voltage-dependent activation and inactivation whereas these parameters were unaffected in the $Ca_v3.1$ and $Ca_v3.3$ channels (Iftinca et al., 2007).

Recently, it has been shown that the presence of Kelch-Like 1 (KLHL1), a neuronal actin binding protein, both increases the deactivation time of $Ca_v3.2$ and causes in increase in the number of $Ca_v3.2$ channels in the membrane (Aromolaran et al., 2009, 2010). It would be interesting to know whether the effect is constitutive or further regulated through KLHL1 expression levels or through unidentified pathways yet to be described.

Among the Ca_v3 channels, $Ca_v3.2$ is unique in that it is exquisitely sensitive to redox modulation. Redox sensitivity of $Ca_v3.2$ has been demonstrated in both acutely dissociated

dorsal root ganglia (DRG) neurons and in nRT neurons in thalamic slices. $Ca_v3.2$ currents are attenuated in the presence of oxidizing agents such as 5,5-dithio-bis-(2-nitrobenzoic acid) (DTNB) and enhanced by reducing compounds such as dithiothretiol (DTT) and the endogenous amino acid L-cysteine (Todorovic et al., 2001b; Joksovic et al., 2006). Nitric oxide (NO), an important chemical messenger present throughout the body, also inhibits $Ca_v3.2$ currents (Joksovic et al., 2007).

The same residue which bequeaths Ni^{2+} sensitivity to $Ca_v3.2$, histidine at position 191 (H191), has also been identified as essential for the redox sensitivity of $Ca_v3.2$ currents. Nelson and coworkers have provided evidence that reducing compounds enhance $Ca_v3.2$ currents through the chelation of metal ions (Zn^{2+}) from the histidine residue thereby relieving a tonic inhibition of the $Ca_v3.2$ channel (Nelson et al., 2007b). In the presence of certain metals (Zn^{2+} for example) ascorbate can oxidize histidine residues through metal catalyzed oxidization (Samuni et al., 1983; Stadtman, 1991; Schöneich, 2000). After observing that ascorbate inhibited $Ca_v3.2$ it was concluded that inhibition was attributable to the oxidation of H191 (Nelson et al., 2007a). Selective inhibition of $Ca_v3.2$ currents by nitrous oxide was also found to be the result of metal catalyzed oxidization of H191 (Todorovic et al., 2001a; Joksovic et al., 2007; Bartels et al., 2009; Orestes et al., 2011) . A summary of the known modulators of Ca_v3 activity is presented in Figure 1.3.

Figure 1.3: Summary of the known modulators of Ca_v3 channel activity

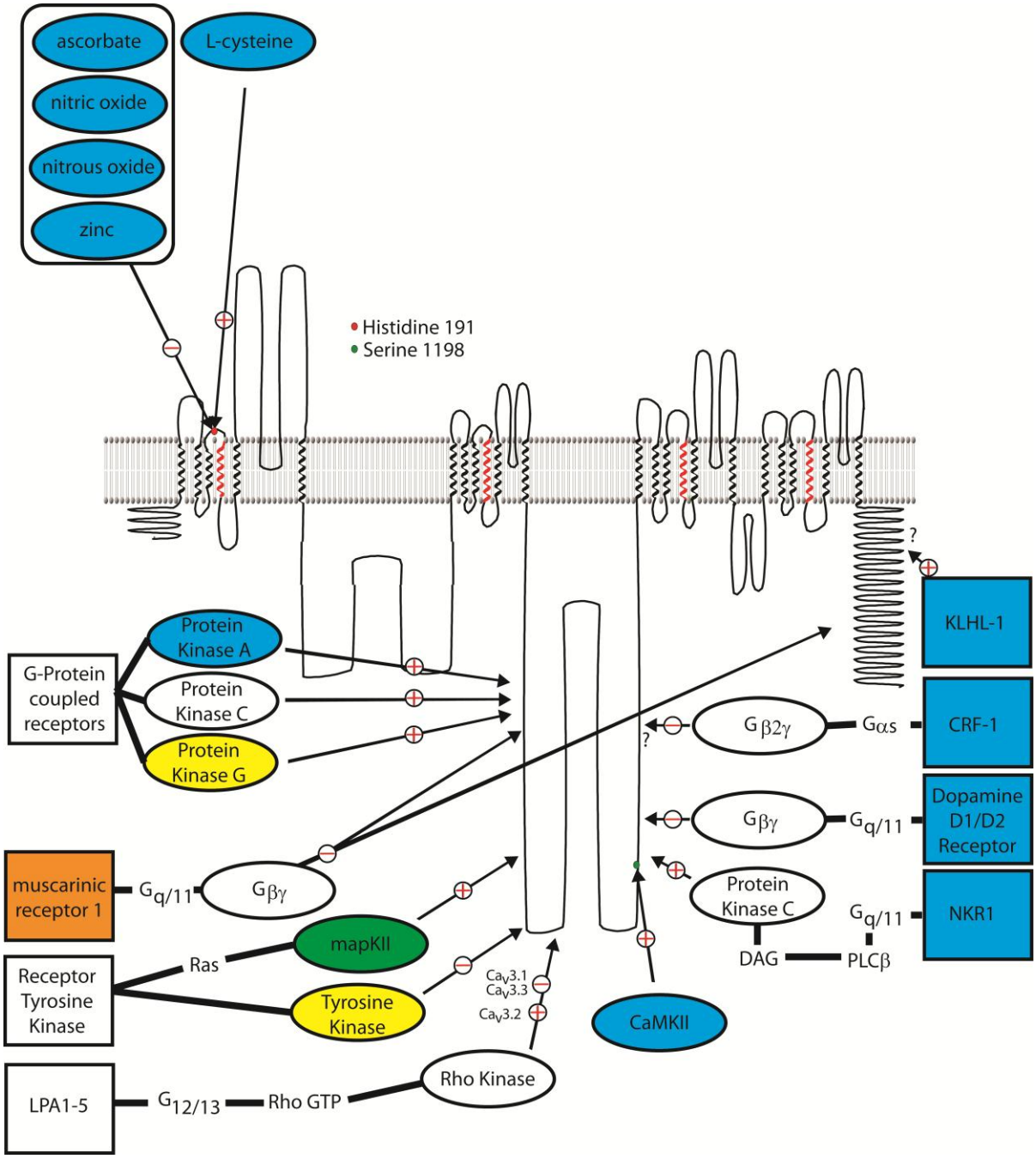

Figure 1.3: Summary of the known modulators of Ca_v3 channel activity

The square boxes represent various receptors known to initiate modulation of Ca_v3 channels. Ovals represent the reagents or effector molecules that modulate the channels. A question mark indicates the mode of action and/or site of action is undetermined. Blue indicates $Ca_v3.2$ specific modulation, green is $Ca_v3.1$ specific, orange is $Ca_v3.2$ specific and white is non-specific. Abbreviations: LPA1-5 = Lysophosphatidic acid receptors 1 to 5, MaPKII = mitogen associated protein kinase II, CaMKII = calmodulin-dependent protein kinase II, NKR1 = neurokinin 1 receptor, CRF-1 = corticotropin releasing hormone receptor 1and KLHL-1 = kelch-like 1.

1.3. PDZ ligands and domains: partnering regulatory enzymes to their targets

1.3.1. Structure and function

The carboxyl terminus of $Ca_v3.2$ possesses a motif that corresponds with the consensus sequence of class 3 PDZ binding ligands which could potentially facilitate interactions with proteins containing PDZ-3 binding domains. PDZ domains were first identified as modular repeats of ~90 amino acids in several proteins including post synaptic density protein (PSD-95), *Drosophila* disc large tumor suppressor (Dlg1) and the zonula occludens-1 protein (Zo-1); hence the PDZ acronym. As one of the most common protein interaction domains identified in sequenced genomes, PDZ domains are known to play significant roles in facilitating interactions between both membrane bound and cytosolic proteins to form macro and micro domains of signaling complexes (reviewed in (Sheng and Sala, 2001; Hung and Sheng, 2002)). Numerous proteins have been identified that possess one or more PDZ domains, of particular note are scaffolding proteins such as PSD-95 and glutamate receptor interacting proteins (GRIPs) which allows them to multimerize and form protein scaffolds (Srivastava et al., 1998; Dong et al., 1999), cluster membrane bound channels (Hsueh et al., 1997; Hsueh and Sheng, 1999), participate in the trafficking of

receptors to the membrane (Lu and Ziff, 2005) and bring together signaling complexes (Christopherson et al., 1999). More detail on the functional diversity of PDZ domains can be found in excellent reviews on this topic (Sheng and Sala, 2001; Hung and Sheng, 2002).

Structurally, PDZ domains are comprised of five to six β strands and two α helices. This structure forms a binding groove with a terminal hydrophobic pocket which contains a carboxylate-binding loop and signature Glycine-Leucine-Glycine-Phenylalanine (GLGF) motif. The first reports of PDZ specific interactions were between the carboxyl terminus of *Shaker*-type potassium channels, the NR2 subunit of N-methyl-D-aspartic acid receptors (NMDAR) and the PDZ domains of PDS-95 ((Kim et al., 1995; Kornau et al., 1995; Niethammer et al., 1996) and reviewed in (Sheng and Sala, 2001)). Carboxyl terminal binding has since been found to be typical of PDZ interactions although internal PDZ binding structures have also been reported; a specific example of which is the β-hairpin structure found near the amino-terminus of neuronal nitric oxide synthase (nNOS) (Hillier et al., 1999; Tochio et al., 1999; Trejo, 2005).

There is considerable variation in amino acids sequence amongst PDZ domains resulting in domains with different specificities and binding affinities (Gee et al., 2000). Three classes of PDZ domains have been identified based on specificity to the last four amino acids of the carboxyl tail of the binding peptide. The residues at position 0 (last carboxyl amino acid) and, proceeding towards the amino terminus, position -2 are the most crucial for PDZ binding (reviewed in (Sheng and Sala, 2001)). A hydrophobic residue is invariably found at position 0 which, when bound, is aligned to fit within the hydrophobic pocket of the PDZ domain (Cohen et al., 1996; Songyang et al., 1997; Niethammer et al., 1998). Specificity for the residue at position -2 defines the PDZ domain class. Class I PDZ domains are characterized by serine or threonine residues at position -2 and which may be

phosphorylated to regulate binding affinity as in the case of the interaction between the α-amino-3-hydroxy-5-methyl-4-isoxazolepropionic acid (AMPA) receptor GluR2 and the PKC interacting protein (PICK1) ((Lu and Ziff, 2005) and reviewed in (Sheng and Sala, 2001)). A hydrophobic residue at position -2 is characteristic of class II domains (Songyang et al., 1997) and negatively charged residue defines class III domains. The residues at position -1 and -3 generally do not define specificity, however they have been found to interact within the PDZ domain and certain PDZ interactions prefer some residues over others (Doyle et al., 1996; Songyang et al., 1997; Sheng and Sala, 2001).

1.3.2. PDZ domains of nNOS

Residues 11 to 133 of nNOS contains both PDZ ligand and PDZ domains immediately adjacent each other (Tochio et al., 1999). An internal class II PDZ (PDZ-2) binding ligand with a β-finger structure (residues 100 to 133) (Hillier et al., 1999; Tochio et al., 1999) mediates interactions with proteins such as PDS-95, PSD-93, and syntrophin (Brenman et al., 1996a, 1996b) whereas a class III PDZ (PDZ-3) binding domain (residues 11 to 100) (Stricker et al., 1997; Tochio et al., 1999)permits PDZ interactions with proteins such as CAPON (carboxyl-terminal PDZ ligand of nNOS) and carboxyl-terminal binding protein (CtBP) (Jaffrey et al., 1998; Riefler and Firestein, 2001).

Key residues within the PDZ domain are required to stabilize the β-finger binding ligand of nNOS which suggests that the formation internal β-finger ligands depends on the proximity to PDZ domains for stabilization (Hillier et al., 1999; Tochio et al., 2000). Consequently, it has been proposed that the head-to-tail arrangement of PDZ domain/ligand organization may not be uncommon as alignment of several known PDZ sequences has revealed sequences similar to nNOS (Hillier et al., 1999). Contrastingly, an internal PDZ

ligand that is not adjacent to a PDZ domain was identified within the endothelin type A receptor (ET_A) protein demonstrating that the head-to-tail arrangement of PDZ domain/ligand is not essential for the formation of an internal β-finger PDZ binding ligand (reviewed in (Trejo, 2005)).

The presence of both a PDZ ligand and a domain within the amino terminus of nNOS could potentially facilitate the formation of larger complexes utilizing both structures; however evidence indicates that binding of CAPON to the PDZ domain of nNOS disrupts the interaction with PSD-95 which is mediated by the β-finger PDZ binding ligand of nNOS (Jaffrey et al., 1998).

The PDZ-2 mediated interaction between nNOS and PSD-95 allows nNOS to be functionally coupled to NMDA receptors. This functional interaction has been shown to mediate glutamate neurotoxicity by linking nitric oxide (NO) production with NMDA receptor activity (Dawson et al., 1991; Sattler et al., 1999). Disruption of the nNOS/PSD-95 interaction also disturbs the functional interaction between nNOS and NMDA receptors which has been demonstrated to reduce NMDA receptor-dependent excitotoxicity (Aarts et al., 2002).

1.4. Functional relevance of nitric oxide and nitric oxide synthases

1.4.1. Molecular structure and composition

A physiological role for NO was first identified in the early 1980s when an endogenous factor released from the endothelium was found to play an important role in blood vessel relaxation. Throughout the 1980s efforts to identify this endothelium-derived relaxation factor culminated in the identification of NO as the active substance (Ignarro, 1989). During this period additional roles for NO were unveiled, including a role in the

macrophage response to both infection and tumor cells (Nathan and Hibbs, 1991; Moilanen and Vapaatalo, 1995), in the stimulation of soluble guanylyl cyclase (sGC) to produce cyclic guanosine monophosphate (cGMP) (Böhme et al., 1984), in the modulation of NMDA receptor activity in brain tissue (Manzoni et al., 1992).Purification of nNOS, one of the enzymes responsible for NO synthesis, in 1990 and subsequent cloning in 1991 allowed for further characterization and understanding of the physiological function of the highly reactive and unstable NO molecule (reviewed in (Bredt, 1995)). The eventual cloning of neuronal (nNOS) (Bredt et al., 1991; Nakane et al., 1993; Ogura et al., 1993), endothelial (eNOS) (Janssens et al., 1992; Lamas et al., 1992; Sessa et al., 1992) and inducible (iNOS) forms (Lyons et al., 1992; Lowenstein et al., 1993; Xie et al., 1993) revealed a structurally similar but physiologically diverse family of enzymes.

Structurally, NOS can be divided into two functional regions, an amino terminal oxygenase domain and a carboxyl terminal reductase domain which bears significant similarity to cytochrome P450 reductase. The oxygenase domain forms binding sites for the substrate arginine as well as for cofactors haem and tetrahydrobiopterin (BH_4). The cytochrome P450 reductase-like carboxyl terminus possesses binding sites for cofactors reduced nicotinamide adenine dinucleotide phosphate (NADPH), flavin adenine dinucleotide (FAD), and flavin adenine mononucleotide (FMN). Between the two functional regions lies a calmodulin (CaM) binding site. The molecular weight of NOS in monomeric form ranges from ~130 kDa for eNOS and iNOS to 160 kDa for nNOS. Functional NOS enzyme consists of a NOS protein dimer with attached cofactors: haem, BH_4, NADPH, FAD, FMN, and CaM. nNOS is the only isoform which possesses PDZ ligand and binding domains (reviewed in (Bredt, 1995; Mayer, 1995; Andrew and Mayer, 1999; Alderton et al., 2001; Li and Poulos, 2005). Figure 1.4 illustrates the domain structure of the NOS isoforms.

Figure 1.4: Domain structure of nitric oxide synthases

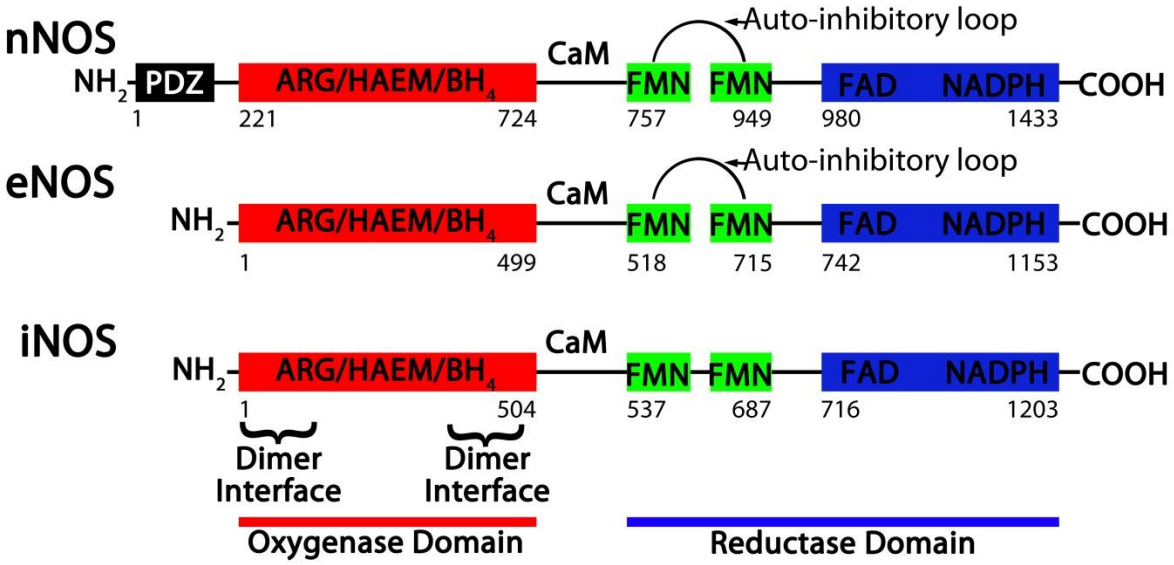

Figure 1.4: Domain structure of nitric oxide synthases

The structure of the three nitric oxide synthases is very similar with the oxygenase domain (red boxes) containing the arginine, haem and BH_4 binding sites situated towards the amino half of the enzyme and the reductase domain (green and blue boxes) containing the FMN, FAD and NADPH binding sites positioned towards the carboxyl portion of the enzyme. The calmodulin binding domain (CaM) is positioned between the oxygenase domain and the reductase domain. The amino acid number of the start and stop of each domain is indicated to illustrate that the distribution of the domains is similar for all three isoforms. Notable structural differences between the structures are the presence of a PDZ-3 domain and the PDZ-2 internal binding ligand at the amino terminus of nNOS (black box), and the lack of an auto-inhibitory loop within the FMN region of the iNOS enzyme. Figure adapted from Alderton *et al.* (Alderton et al., 2001)

1.4.2. Synthesis of nitric oxide

Activation of the neuronal and endothelial isoform of NOS requires CaM binding. Increases in intracellular Ca^{2+} activate CaM which in turn activates nNOS/eNOS thus these isoforms are considered Ca^{2+}/CaM-dependent. Further, NO production is only stimulated by

an intracellular increase in Ca^{2+} thereby allowing constitutive expression and they are often referred to as constitutive NOS isoforms. Conversely, iNOS binds CaM with an affinity range such that iNOS remains active even in the presence of Ca^{2+} chelators and instead NO production via iNOS is regulated by transcriptional and translational mechanisms.

Binding of CaM to its recognition site induces changes in structural conformation. These conformational changes result in a displacement of auto-inhibitory control element within NOS to permit the flow of electrons from the flavin cofactors to the haem domain. Evidence indicates that the conformational shift also propagates to the carboxyl tail of NOS which is believed to remove a conformational constraint on the FMN subdomain allowing for more efficient activity (reviewed in (Li and Poulos, 2005)).

The conversion of arginine is a two-step reaction: 1) conversion of L-arginine to N^{ω}-hydroxy-L-arginine (NHA) and 2) conversion of NHA to the final products: NO and citrulline (Figure 1.5). Three electrons are required to drive this conversion with the flow of electrons being donated by NADPH. The electrons are passed to FAD and then to FMN within the reductase domain. The haem cofactor within the oxygenase domain, where arginine binds, is then reduced by electrons received from FMN in the reductase domain. An oxygen molecule binds to the reduced haem which then receives an electron from the BH_4 cofactor. Two protons are used to cleave the haem-bound oxygen to generate a reactive haem-oxygen species which transfers the oxygen to one of the chemically equivalent guanidino-nitrogens of arginine to produce NHA. Once the electron complement of BH_4 is restored, courtesy of an electron from the flavin cofactors, the process is repeated to convert NHA into NO and L-citrulline. Each NADPH can provide two electrons meaning that for each mole of L-citrulline and NO produced 1.5 moles of NADPH are consumed (Mayer, 1995; Alderton et al., 2001; Hurshman et al., 2003; Li and Poulos, 2005). In the absence of

arginine the reaction is incapable of producing NO; instead, two highly reactive oxygen species, superoxide anions and hydrogen peroxide, are produced which can interact with NO to form peroxynitrite (reviewed in (Mayer, 1995)).

Figure 1.5: Reaction schematic and electron flow diagram of the conversion of arginine to citrulline and nitric oxide

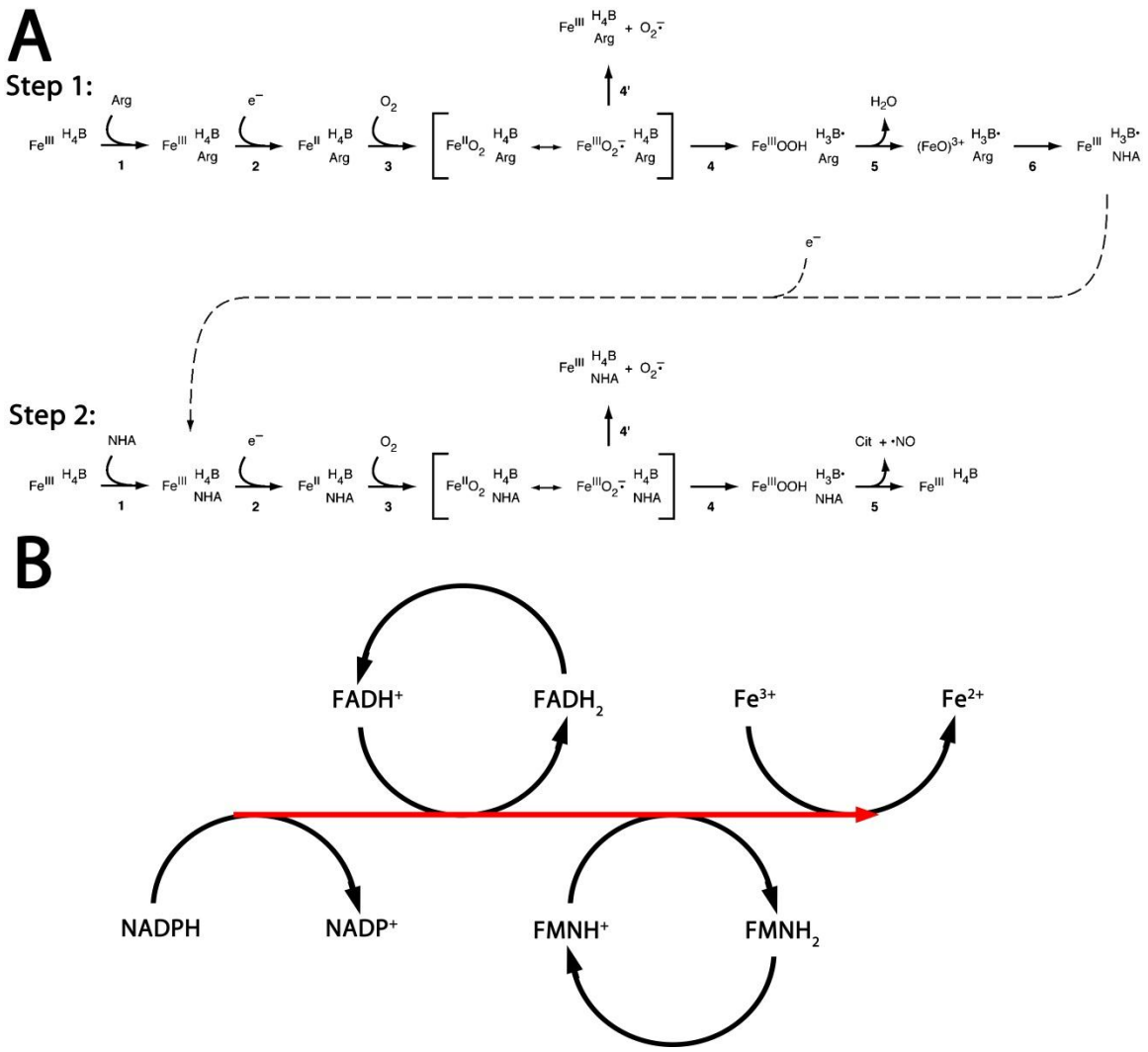

Figure 1.5: Reaction schematic and electron flow diagram of the conversion of arginine to citrulline and nitric oxide

A schematic illustrating the two-step process involved in the production of nitric oxide from arginine (A). Step 1 illustrates the hydroxylation of arginine (Arg) to produce the intermediate N^{ω}-hydroxy-L-arginine (NHA) and Step 2 illustrates the oxidization of N^{ω}-hydroxy-L-arginine to produce NO and citrulline. Three electrons are required for the production of NO, one for the hydroxylation of arginine, one to reduce H_3B to H_4B prior to the initiation of step two and a third for the oxidization of N^{ω}-hydroxy-L-arginine. Each NADPH can supply two electrons therefore three NADPH are required for the synthesis of two nitric oxide molecules. The electron transfer flow is illustrated in panel B. Electrons from NAPDH are received by FAD, passed to FMN and then to haem in the course of nitric oxide synthesis. The schematic in panel A was originally published by Hurshman *et al.* (Hurshman et al., 2003) and the electron flow diagram is adapted from Alderton *et al*. (Alderton et al., 2001)

1.4.3. Mechanisms of modulation by nitric oxide

NO and its reaction products can influence cellular physiology through several different mechanisms. The best characterized nNOS/NO pathway involves the activation of sGC which converts guanosine triphosphate to cyclic guanosine monophosphate (cGMP). Downstream targets of cGMP include two types of phosphodiesterase (PDE) isoforms (PDE2 and PDE3) (Bender and Beavo, 2006; Zaccolo and Movsesian, 2007), cyclic nucleotide-gated ion channels ((Kaupp and Seifert, 2002), and cGMP dependent protein kinases (cGK). cGKs have been found to affect a diverse range of downstream targets (Hofmann et al., 2009); consequently, NO has the potential to influence a wide array of cellular processes through the activation of sGC (Wang and Robinson, 1997; Domek-Łopacińska and Strosznajder, 2005; Guix et al., 2005; Bender and Beavo, 2006; Kleppisch and Feil, 2009). A

description of the extensive array of processes affected by cGMP is outside the scope of this thesis however, the topic has been reviewed extensively in the citations listed above.

Under physiological conditions NO undergoes various reactions, the products of which include nitrites (NO_2^-), nitrates (NO_3^-) and peroxynitrites ($OONO^-$). Peroxynitrites can react with tyrosine residues to produce 3-nitrotyrosine (Beckman, 1996; Galiñanes and Matata, 2002). Protein nitrotyrosination can alter the protein function through conformational changes (Cassina et al., 2000; Amici et al., 2003) and through inhibition of phosphorylation events (Newman et al., 2002). Nitroxyl anions (NO^-), a byproduct of breakdown of NO (Murphy and Sies, 1991) and the arginine intermediate NHA (Fukuto et al., 1992) can react with thiol group of cysteine residues to produce S-nitrothiols. The main targets for protein S-nitrosylation appears to be enzymes and kinases (Broillet, 1999) however the modulation of proteins such as NF-κβ (Marshall and Stamler, 2001) and NMDA receptors (Choi et al., 2000; Jaffrey et al., 2001) by S-nitrosylation has also been demonstrated.

1.4.4. Degradation of nitric oxide

NO diffuses freely from the source of production and readily crosses the lipid cell membrane. Given the reactive nature of NO and its reaction products it is logical that a method of deactivation must exist to constrain the sphere of influence of NO and its conversion products to prevent cytotoxicity. The sphere of influence of NO refers to how far NO diffuses before it is degraded to the concentration where it is no longer physiologically active. Degradation of NO occurs through several pathways including simple diffusion away from the site (Lancaster, 1994; Wood and Garthwaite, 1994) and reaction with oxyhaemoglobin in nearby blood vessels (Lancaster, 1994; Liu et al., 1998), with superoxide (O_2^-) (Kissner et al., 1997) and lipid peroxyl radicals (O'Donnell et al., 1997).

The half-life of NO was previously reported to be 3-5 seconds (Palmer et al., 1987; Ignarro, 1989), however these studies assumed physiological NO concentrations on the micro molar scale. More recent studies indicate that nanomolar concentrations of NO are more probable (Garthwaite, 2005). Using a rat brain tissue Hall and Garthwaite developed a model to investigate NO degradation and found that at nanomolar concentrations the half-life of NO may be as low as 10 ms (Hall and Garthwaite, 2006). With such a brief half-life the sphere of influence of NO is likely tightly regulated and implies that the intended targets must be localized near the source of NO production for optimal efficiency.

1.4.5. Pharmacological properties of neuronal nitric oxide synthase

A number of compounds have been shown to disrupt the NOS activity, however due to similarities with cytochrome P450 many of these agents are not considered NOS specific (reviewed in (Mayer, 1995). As such, the search for pharmaceutical agents capable of selectively antagonizing the specific isoforms of NOS at therapeutically relevant dosages is ongoing (reviewed in (Granik and Grigor'ev, 2002)). Here, I discuss three NOS specific inhibitors which have proven invaluable in research and which many of the newer compounds are derived from. The first compound used for NOS inhibition was N^{ω}-Methyl-L-arginine (L-NMA). This arginine derivative is a competitive inhibitor for the binding site of L-arginine and inhibits all NOS isoforms. L-NMA inhibits NO synthesis but it does not block the reduction of oxygen in first phase of the conversion process which results in the production of superoxide and hydrogen peroxide. Additionally, L-NMA itself can be slowly metabolized by NOS to produce NO. Other L-arginine derived inhibitors are N^{ω}-Nitro-L-arginine (L-NNA) and its methyl ester, (L-NAME). The main difference between L-NNA and L-NAME is that L-NAME remains inactive until it is hydrolyzed by esterases within the

cell. Inhibition of NOS by L-NNA or L-NAME occurs through competition with the L-arginine binding site and it is presumed that occupation of the site results in a conformational change in NOS. The effects of L-NNA and L-NAME are reversible with the addition of excess L-arginine. With these inhibitors the formation of hydrogen peroxide and superoxide is also blocked and further, neither L-NNA nor L-NAME can be metabolized by NOS. The constitutive isoforms are preferentially inhibited by L-NNA and L-NAME. The third class of compound, 7-Nitro indazole (7-NI), blocks NO synthesis by competing with both L-arginine and HB_4 binding through a distinct functional domain preventing arginine binding and oxygenase activity. A drawback to 7-NI is its insolubility in water requiring aprotic solvents such as dimethylformamide or dimethyl sulfoxide which could adversely affect cellular and tissue preparations (reviewed in (Mayer, 1995; Granik and Grigor'ev, 2002)).

1.4.6. Expression of nNOS and roles of nNOS derived NO

nNOS is the predominant NOS isoform and its expression in the brain has been studied extensively (Kowall et al., 1985; Mizukawa et al., 1988; Kinjo et al., 1989; Mizukawa, 1989; Leigh, 1990; Davis, 1991; Meyer et al., 1991; Vincent, 1992; Vincent and Kimura, 1992; DeFelipe, 1993; Meyer and González-Hernández, 1993; Sugaya and McKinney, 1994). Fortunately, the extensive body of information regarding nNOS has been consolidated in comprehensive reviews by (Vincent, 1994, 1995b).

nNOS is expressed in varying degrees throughout the brain in a variety of neuronal cell types which will be summarized here. In the telencephalon of the rat brain NOS expressing neurons are scattered through layers II through VI of the cortex, and in the striatum and the amygdala. The basket cells and interneurons of the dentate gyrus express nNOS, as do magnocellular neurons of the diagonal band of Broca and the medial septum.

nNOS is found in the interneurons of the hippocampus however and its presence in pyramidal cells is controversial. Additionally, many neurons within the olfactory bulb contain nNOS with the granular layer displaying a high percentage of expressing cells. In the diencephalon populations of magnocellular neurosecretory neurons within the hypothalamus are nNOS positive and nNOS is present in gonadotrophs and folliculo-stellate cells of the anterior pituitary. In the retina nNOS can be found in rod cells (cone cells in humans), interneurons and the ganglion cell layer. In the midbrain NOS is found in neurons within the inferior colliculus, intercollicular commissure, posterior commissure and superior colliculus. There are also nNOS expressing neurons in the dorsolateral periaqueductal grey, laterodorsal and pedunculopontine tegmental nuclei. In the medulla, many neurons in the nucleus of the solitary tract and the ventrolateral medulla and scattered neurons in the reticular formation express nNOS. The cerebellum exhibits high nNOS expression in the granule cells as well as basket cells in the molecular layer. Finally, in the spinal cord nNOS is expressed in a subset of neurons of laminae I through IV and in ganglia of the dorsal root.

Although across species nNOS expression has been generally found to be highly similar, differences have been noted; for example, in humans only a small percentage of neurons in the subcortical white matter have been found to be NOS positive whereas in the rat nNOS is found in most of the these neurons (Mizukawa et al., 1988; Springall et al., 1992; Vincent and Kimura, 1992; DeFelipe, 1993; Vincent, 1995a). nNOS expression has been demonstrated outside of the central nervous system as well. A splice variant of nNOS, nNOSμ, has been identified in the skeletal muscle (Silvagno et al., 1996), smooth muscle (Boulanger et al., 1998; Schwarz et al., 1999), cardiac muscle (Xu et al., 1999) and the corpora cavernosa of the penis and the lower urinary tract (Magee et al., 1996).

Given the wide range of nNOS expression in the brain it would be impractical to review here all of the physiological roles of nNOS-derived NO in each area. Here, I will touch upon two areas of research which have received considerable attention in the research community because of the potential therapeutic applications.

Long term potentiation (LTP) and long term depression (LTD) have long been the proposed mechanisms underlying the synaptic plasticity required for learning and memory. NO has been reported to be important in the induction of LTP in the cerebellum (Jacoby et al., 2001; Qiu and Knöpfel, 2007), hippocampus (Phillips et al., 2008; Taqatqeh et al., 2009) and neocortex (Hardingham and Fox, 2006). Additionally, NO has been identified to play a role in the induction of LTD in the cerebellum (Shin and Linden, 2005; Ogasawara et al., 2007). Many *in vivo* studies using NOS inhibitors have shown that NO plays an important role in learning and memory ((Böhme et al., 1993; Hölscher et al., 1996; Richards et al., 2003; Koylu et al., 2005) and reviewed in (Susswein et al., 2004)). It has become apparent, however, that the contributions of NO to learning and memory varies with the type of learning (classical conditioning vs. habitual learning for example) and the stage of memory formation (short vs. long term memory) (reviewed in (Susswein et al., 2004)). This variation is perhaps not surprising given that nNOS is expressed in many of the neuronal populations involved in learning and memory and since NO can have differential effects among distinct populations of neurons depending on the available neuronal mechanism. For example, in one population of neurons NO may have a direct effect on synaptic plasticity through the nitrosylation of NMDA receptors to suppress LTP whereas in another population synaptic plasticity may be affected through the activation of cGMP and its downstream effectors (reviewed in (Susswein et al., 2004)). Understanding the mechanisms that are involved in

learning and memory is crucial in developing effective strategies to facilitate the learning process and to increase memory formation and retention.

Neuronal cell death following a stroke can have debilitating and often deadly consequences depending on the size and location of the infarct. In ischemia there is an initial increase followed by a decline in NO levels and after reperfusion NO levels are elevated compared to pre-ischemic conditions suggesting that NO may contribute to neuronal damage following an ischemic event (Malinski et al., 1993). A NMDA receptor/NO signaling cascade has been identified as a major contributor towards neurotoxicity suggesting that NMDA and nNOS play a role in excitotoxicity and the damaging effects of ischemia (Dawson et al., 1993). In support of this is evidence from nNOS knockout mice; in these animals neuronal tissue displays resistance to ischemic insult (Dawson et al., 1996; Ferriero et al., 1996; Huang et al., 2000). Additionally, disrupting the PSD-95 mediated interaction between NMDA receptors and nNOS using membrane permeable TAT-peptides reduce the ischemic damage (Aarts et al., 2002). Taken together, evidence suggests that nNOS and/or the NMDA/nNOS interaction may be potential targets for the development of pharmaceuticals to minimize damage due to stroke.

1.5. Nitric oxide and nNOS in the ventilatory response

1.5.1. Neuronal pathways involved in respiration

Respiration is the exchange of O_2 and CO_2 through rhythmic alternating cycles of inspiration and expiration. A sophisticated network of neuronal circuits sustains this involuntary process while maintaining the flexibility to adapt to changes in metabolic demand and ambient conditions as well as conscious control and interruptions such as sneezing, coughing, vomiting and vocalization. Despite the substantial amount of research

that has been devoted to the respiratory system, our understanding of the neuronal networks that comprise this system is far from complete. Indeed, over the years numerous models have been proposed and either subsequently rejected or significantly refined as new evidence is put forward.

Current models propose a series of intricately connected circuits that are spatially distributed within the pons and the caudal region of the medulla. Together these circuits generate rhythmic patterns creating a breathing pattern that consists of 3 phases: inspiration, post-inspiration and expiration (Ramirez and Richter, 1996). A detailed review of the emerging views regarding the neuronal circuits of the respiratory network was published by Smith and coworkers (Smith et al., 2009). Here, I will introduce these circuits and summarize their contributions to respiration.

The components required for the initiation, maintenance and termination of inspiration are all present in the pre-Botzinger complex (pre-BotC) making it a critical component of the respiratory system. Within this circuit there is a heterogeneous mix of neurons with different electrophysiological profiles and which form an auto rhythmic circuit which projects excitatory connections to the premotor inspiratory neurons to initiate and maintain inspiration. Also present in the pre-BotC are inhibitory neurons which are activated by the increase in inspiratory drive and facilitate both the termination of the inspiratory phase and coordinate the onset of the expiration. Activity within the pre-BotC circuit is under a number of modulatory influences including tonic excitatory inputs and rhythmic inhibitory signals which regulate and shape the stimulation pattern of the premotor inspiratory neurons.

Activity within the rostral ventral respiratory group (rVRG) is driven largely through inputs from the pre-BotC. This circuit does not possess rhythmogenic capability; instead activation of this circuit produces an ascending ramp of stimulation that shapes the

inspiratory motor output pattern. A number of respiratory drive signals converge on the rVRG to shape the characteristic ramping pattern, fine tuning the inspiratory pattern to satisfy the demands placed on the system. The expiratory counterpart to the rVRG is considered to be the caudal ventral respiratory group (cVRG). While the rVRG is inhibited during expiration, the cVRG receives excitatory input from several sources including the Botzinger complex to modulate the pattern of excitatory drive to pre-motor neurons.

The Botzinger complex (BotC) provides oscillating inhibitory input to most of the other circuits of the respiratory network including the pre-BotC and the rVRG to facilitate the transition from inspiration and engage expiration in the post-inspiration and expiration phases. This auto rhythmic inhibitory circuit is the main source of expiratory activity within the respiratory network. Similar to the circuits discussed previously, activity within the BotC is modulated through inputs from other circuits which helps maintain the alternating inspiration/expiration pattern of respiration.

Almost all of the respiratory circuits receive excitatory drive signals which have been postulated to maintain the rhythmogenic oscillations of the various circuits. A major source of this excitatory drive is the retrotrapeziod nucleus/parafacial respiratory group (RTN/pFRG). The RTN has chemosensing capability, responding to CO_2 levels and providing the excitatory drive necessary to meet metabolic demand. Additionally, the RTN integrates excitatory drive input from other chemoreceptors such as the carotid and arterial bodies and forwards the necessary response to the core respiratory networks enabling the entire network to adapt to the metabolic state of the system. Other sources of respiratory drive come from the PONS, raphe nucleus and the NST which project to one or more circuits within the respiratory network and provide information regarding the metabolic state of the body.

The RTN and pFRG are mentioned as a single group because there is spatial overlap between the two circuits. The contribution of the pFRG circuit is currently debated. Evidence has been put forward that oscillatory activity of pFRG provides a significant drive for the rhythmic activity of the pre-BotC. There is also experimental evidence suggesting that the pFRG facilitates inspiration/expiration phase transitions. Future investigations should provide the insight necessary to better determine the contributions of this circuit to the respiratory network.

While much has been done over the past century to understand the seemingly simple activity of respiration we are only now identifying the neuronal populations and interactions involved in this process that is absolutely essential for life.

1.5.2. Role of NOS in respiration

NO plays a significant role in the ventilatory response during hypoxia. Systemic inhibition of NOS significantly attenuates the ventilatory response to hypoxia suggesting that NO promotes neuronal activity either directly by increasing excitability of the neurons involved, or indirectly through the inhibition of the incoming inhibitory connections (Haxhiu et al., 1995; Gozal et al., 1996b; Antoniou and Murariu, 1999). NOS expressing neurons are found in several modulatory structures/circuits involved in respiration such as the NTS, the carotid body, the petrosal ganglion and microganglia within the glossopharyngeal nerve (Vincent and Kimura, 1992; Wang et al., 1993; Grimes et al., 1994; Haxhiu et al., 1995). Inhibition of NOS within the NTS using microinjection results in a decrease of neuronal activity and an attenuated hypoxic response which coincides with the results from the systemic NOS inhibition studies (Ma et al., 1995; Ogawa et al., 1995) and suggests a stimulatory role for NO in respiration. Additional support for a stimulatory role for NO

during hypoxia comes from eNOS knock-out mice which, in general, display a blunted hypoxic response (Kline et al., 2000). Conversely, in the carotid body, localized administration of NOS inhibitors which preferentially inhibit nNOS results in an increase of activity in neurons of the carotid sinus nerve and an augmented hypoxic response *in vivo* (Wang et al., 1994; Gozal et al., 1996a; Valdés et al., 2003) implying that NO can play either an inhibitory or excitatory role depending on the source of NO and the respiratory circuits affected. Furthermore, the ventilatory response to hypoxia in nNOS knock-out mice is augmented and these animals also display attenuation of short term facilitation and long term potentiation of ventilation demonstrating that nNOS derived NO plays a significant role in regulating the respiratory response (Kline et al., 1998, 2002). Clearly, the contribution of NO to respiration is significant however; our understanding of the contribution of the eNOS and nNOS isoforms within the various structures involved in respiration remains limited.

The systemic inhibition of NOS resulting in inhibition of both eNOS and nNOS provides valuable information regarding the global contribution of NO but little concerning the contribution of either isoform or of the role of NO within the various structures involved in respiration. Knock-out mice provide an excellent resource for determining the contribution of NO derived from either isoform but again, the effects are systemic and there is a lack of studies investigating the specific respiratory structures involved utilizing these animals. Investigations utilizing the microinjection of relatively specific NOS isoform inhibitors have been performed but due to the lack of truly specific NOS inhibitors, inhibition of the other NOS informs remains a possibility in these investigations. An additional complication arises when we consider that NOS inhibitors can differently alter ventilatory behaviour in different strains of animals and which can make comparison between research groups problematic

(Subramanian et al., 2002). Finally, little is known about the cellular mechanisms within these structures that mediate the production of NO in the respiratory pathway.

1.5.3. Properties and role of nNOS expressing microganglia in the glossopharyngeal nerve (GPN)

Two populations of nNOS positive microganglia have been identified within the GPN, one proximal to the bifurcation to the carotid sinus nerve (CSN) and another located distally along the GPN, which are a major source of efferent fibers to the carotid body (Wang et al., 1993, 1995a, 1995b; Prabhakar, 1999; Campanucci et al., 2003; Campanucci and Nurse, 2005). The carotid bodies are peripheral chemoreceptors that sense pH, pCO_2 and pO_2 levels in the blood and provide afferent communication via the CSN and the GPN to confer information regarding the state of the body and modulate respiratory activity (reviewed in (Gonzalez et al., 1994)). It has been demonstrated that the microganglia of the GPN are involved in the NO mediated efferent inhibition of the carotid body and that the inhibition of nNOS results in increase of activity in Type I glomerus cells of the carotid body and ultimately in an increase in phrenic nerve activity (Wang et al., 1994; Gozal et al., 1996a; Valdés et al., 2003; Campanucci et al., 2006). These findings are congruent with those of Kline and coworkers who observed increased CNS activity and an augmented hypoxic response in nNOS knock-out mice compared to wild type controls (Kline et al., 1998) suggesting that the exaggerated hypoxic response in these mice may be due to the lack of efferent inhibition of the carotid body. Campanucci and Nurse have made significant contributions to our understanding of the NO mediated efferent inhibition of the carotid body. They identified a novel O_2 sensing mechanism (Campanucci et al., 2003), demonstrated the expression of purinergic P2X receptors (Campanucci et al., 2006) and

characterized the whole cell ionic currents of the GPN microganglia (Campanucci and Nurse, 2005). From these observations a model was put forward outlining the mechanism of NO-mediated efferent inhibition of the carotid body (Campanucci and Nurse, 2007).

In the model, the efferent inhibition of the carotid body is peripheral in origin. Under hypoxic conditions the O_2 sensing mechanism of the microganglia causes a depolarization resulting in an increase in excitability and consequently increased activity. This increased activity results in the activation of the multiple VGCCs types, including a nickel sensitive T-type Ca^{2+} channel, which has been proposed to increase intracellular Ca^{2+} levels sufficient to stimulate nNOS. Upon activation, nNOS produces NO which diffuses across the plasma membrane to the Type I glomerus cells of the carotid body where inhibition of the L-type (Ca_v1) VGCCs has been proposed to result in the reduction of carotid body activity (Summers et al., 1999). It is further proposed that activation of ionotropic purinergic P2X receptors in the microganglia by ATP released from the carotid body while under hypoxia may also contribute to the intracellular Ca^{2+} levels and facilitate nNOS stimulation.

1.6. $Ca_v3.2$ channels and nociception

1.6.1. Neuronal pathways involved in nociception

Mechanical, thermal and chemical noxious stimuli are detected by Aδ and C nociceptive fibers in the peripheral nervous system. Receptors within these fibers transduce the noxious stimuli into a sensory potential and, if the potential is great enough, an action potential is triggered within the dorsal root ganglion (DRG). The action potential travels along the axon to the dorsal horn of the spinal cord where it synapses onto nociceptive-specific neurons within the superficial laminae. The nociceptive neurons within the spinal cord can be part of either the ascending tract or interneurons that are involved with reflex

pathways. Signals propagating along the ascending tract into the brain activate the thalamocortical system. The lateral thalamocortical system, which is composed of relay nuclei in the lateral thalamus and areas SI and SII of the post central gyrus, interprets the incoming information to determine intensity, duration and localization of the pain and conveys this information to the consciousness as acute pain. The affective aspects of pain are subsequently mediated by the medial thalamocortical system and efferent signals from the periaqueductal grey and nucleus raphe magnus descend the dorsolateral funiculus of the spinal cord and synapse onto interneurons within the dorsal horn to suppress the nociceptive signal (reviewed in (Kandel et al., 2000; Schaible and Richter, 2004; Hildebrand and Snutch, 2006)).

1.6.2. Role of $Ca_v3.2$ channels in nociception

T-type Ca^{2+} currents have been identified in small (20-27 μm) and medium (33-38 μm) sized DRG neurons suggesting a potential nociceptive role (Carbone and Lux, 1984a; Nowycky et al., 1985; Scroggs and Fox, 1992). The systemic administration of mibefradil has been demonstrated to have an analgesic effect on mechanical and thermal stimuli (Todorovic et al., 2002; Dogrul et al., 2003; Kim et al., 2003) providing pharmacological evidence for a nociceptive role for T-type channels. However, given the questionable specificity of mibefradil (Viana et al., 1997; Jimenez et al., 2000), these results are not conclusive proof.

In one study in rats, Todorovic and colleagues described the redox modulation of $Ca_v3.2$ currents in small (21-27 μm), capsaicin-sensitive DRGs; in this study the oxidizing agent DTNB inhibited and reducing agents DTT and L-cysteine enhanced $Ca_v3.2$ currents. They further showed that microinjection of DTNB into the paw produced analgesic responses

to mechanic and thermal stimuli and that reducing agents produced hyperalgesic responses suggesting that $Ca_v3.2$ channels play a role in peripheral nociception (Todorovic et al., 2001b).

Subsequently, a novel population of small (26-31 μm) DRGs with substantial T-type currents and virtually no HVA Ca^{2+} currents that responded to capsaicin and stained positive for the nociceptive marker IB_4 was described (Nelson et al., 2005). Utilizing these "T-rich" DRGs, Nelson and coworkers provided evidence that the main nociceptive role of $Ca_v3.2$ channels may be a contribution to regulating the excitability of DRGs. In these experiments the application of the endogenous reducing agent L-cysteine enhanced an ADP generated by $Ca_v3.2$ currents and which increased the likelihood of triggering action potential firing during the ADP.

The most conclusive evidence yet of a nociceptive role for $Ca_v3.2$ channels was presented by Bourinet and colleagues who showed that the selective antisense-mediated knock-down of $Ca_v3.2$ channel RNA and protein in the L5 and L6 dorsal spinous processes both had an analgesic effect in healthy rats and relieved the hyperalgesia associated with mechanical and thermal stimuli in a chronic constriction injury model of neuropathic pain (Bourinet et al., 2005).

1.6.3. Role of nNOS in nociception

A significant body of pharmacological evidence demonstrates that NOS is involved in the mechanical and thermal hyperalgesia observed in neuropathic models of pain. Reduction of mechanical and thermal hyperalgesia has been observed with systemic (Hao and Xu, 1996; Yoon et al., 1998; Dableh and Henry, 2011) and intrathecal (Meller et al., 1992; Roche et al., 1996; Guan et al., 2007; Chacur et al., 2010) administration of NOS inhibitors. A comparison

of nNOS and eNOS knock-out mice reveals that a reduction in neuropathic hyperalgesia is present only in the nNOS knock-out mice (a 50% reduction in thermal hyperalgesia and a total reversal of mechanical hyperalgesia) (Boettger et al., 2007; Guan et al., 2007). More recently, it has been shown that nNOS is up-regulated in small and medium sized DRGs following nerve injury and is likely a contributing factor towards hyperalgesia (Chacur et al., 2010; Kim et al., 2011). Support for nNOS up-regulation underlying peripheral hyperalgesia was also provided using antisense knock-down of the various nNOS isoforms. Examining the formalin induced pain model Kolesnikov and coworkers showed that intrathecal administration of siRNA targeting the α and β variants of nNOS inhibited hyperalgesia during the tonic phase of the formalin response. Interestingly, only the siRNA targeting the α variant inhibited hyperalgesia when delivered supraspinally or peripherally (Kolesnikov et al., 2009). One of the most significant structural differences between the two nNOS isoforms is the lack of the PDZ-3 binding domain and internal PDZ-2 ligand in the β isoform which suggests localization and/or trafficking of nNOS may be important for the contribution of nNOS to nociception in the supraspinal and peripheral regions.

The mechanism and effects of nNOS up-regulation are poorly understood although it has been suggested that an NMDA receptor/nNOS interaction is involved (Kim et al., 2011) since MK-801, a NMDA antagonist, delays the onset of neuropathic pain (Jang et al., 2004). Support for a role of a NMDA receptor/nNOS interaction in the development of hyperalgesia has been found in the mechanism behind morphine tolerance. A NMDA/NO/PKC pathway in involved in the development of morphine tolerance and systemic administration of L-NNA prevents and reverses morphine tolerance indicating that NOS plays an important role in this process (Kolesnikov et al., 1993). This evidence suggests that the interaction between

NMDA and nNOS may facilitate neuronal excitability resulting in increased sensitivity to mechanical and thermal stimuli.

1.7. Thesis hypothesis and objectives

1.7.1. Hypotheses

I originally noted that the carboxyl terminus of the $Ca_v3.2$ channel possesses a putative PDZ binding ligand which is conserved across human, rat and mouse. Further, the amino acid sequence of the PDZ binding ligand corresponds with the consensus sequence for the PDZ-3 biding domain of nNOS suggesting the possibility that the two proteins may physically interact *in vivo*. As nNOS is a Ca^{2+}-dependent enzyme which produces NO, and given that NO has been shown to inhibit $Ca_v3.2$ currents, I hypothesized that a functional interaction may also occur. While the external application of redox agents has been show to modulate $Ca_v3.2$ activity, an *in vivo* mechanism for redox modulation of $Ca_v3.2$ channels has not been previously identified. The expression profiles of $Ca_v3.2$ and nNOS overlap in several regions of the central and peripheral nervous systems including two structures involved with the ventilatory response, the NTS and microganglia within the GPN, presenting a potential role for a putative $Ca_v3.2$/nNOS interaction in the ventilatory response. In this thesis I specifically hypothesized:

1) that $Ca_v3.2$ and nNOS physically interact via the carboxyl PDZ-3 ligand of $Ca_v3.2$ channels
2) that the $Ca_v3.2$ and nNOS interaction results in the production of NO allowing for a functional feedback regulation wherein $Ca_v3.2$ activity stimulates nNOS to produce NO which in turn feeds back to inhibit $Ca_v3.2$ channels

3) that systemic disruption of the putative $Ca_v3.2$/nNOS interaction *in vivo* will have a measurable effect on the ventilatory response to hypoxia

1.7.2. Objectives

In order to address these hypotheses the following scientific objectives were generated:

1) Determine whether $Ca_v3.2$ and nNOS can physically interact via the carboxyl PDZ-3 binding ligand of $Ca_v3.2$ through co-immunoprecipitation and western blot analysis
2) Determine whether $Ca_v3.2$ activity is sufficient to stimulate nNOS to produce NO in a heterologous expression system
3) Determine whether $Ca_v3.2$ activity is inhibited when co-expressed with functional nNOS in a heterologous expression system
4) Investigate a potential role for the putative $Ca_v3.2$/nNOS interaction *in vivo* by disrupting the PDZ-3 mediated interaction and measuring parameters of the ventilatory response of rats under hypoxic conditions.

Chapter 2.

2. $Ca_v3.2$ and nNOS interact physically and functionally to form a putative negative feedback regulatory pathway

2.1. Introduction

T-type VGCCs play important roles in regulating neuronal activity. In addition to contributing to neuronal excitability, the shaping of action potentials and mediating intracellular Ca^{2+} influx, the unique biophysical properties of T-type channels supports a range of firing patterns from rhythmic low threshold burst-firing to slow oscillations (reviewed in (Perez-Reyes, 2003; Cain and Snutch, 2010)). This versatility allows T-type channels to play important roles in functions as diverse as aldosterone and cortisol secretion, boosting of nociceptive signals, and mediating thalamocortical rhythms (reviewed in (Park et al., 2003; Steriade, 2005; Jevtovic-Todorovic and Todorovic, 2006)).

A number of cellular mechanisms such as G-protein coupled receptors (Wolfe et al., 2003; Hildebrand et al., 2007), secondary messengers PKC and PKA (Park et al., 2003; Kim et al., 2006; Chemin et al., 2007), tyrosine kinase (Arnoult et al., 1997), Rho-associated protein kinase (Iftinca et al., 2007) and reducing/oxidizing agents (Todorovic et al., 2001b; Nelson et al., 2007a, 2007b) have been shown to modulate Ca_v3 activity and affect the excitability and firing patterns of neurons in which they are expressed (Nelson et al., 2005, 2007a, 2007b; Joksovic et al., 2006, 2007; Iftinca et al., 2007; Hildebrand et al., 2009) indicating that Ca_v3 modulation may be an important *in vivo* mechanism for regulating neuronal activity.

Of the T-type channels, $Ca_v3.2$ is uniquely sensitive to redox modulation. Todorovic *et al*. have demonstrated that reducing agents such as DTT and L-cysteine enhance $Ca_v3.2$ activity by removing the tonic Zn^{2+} inhibition at the histidine residue at position 191 whereas

oxidizing agents such as DNTB, ascorbate and NO inhibit $Ca_v3.2$ activity through metal catalyzed oxidization (Nelson et al., 2007a, 2007b). Furthermore, enhancement of $Ca_v3.2$ activity with the application of reducing agents increases the likelihood of stimulating a second action potential in acute preparations of nociceptive DRGs and increases burst firing in nRT neurons of thalamic slices while the inhibition of $Ca_v3.2$ by oxidizing agents reduces the amplitude and duration of the after depolarizing potential in DRGs and inhibits burst firing in nRT neurons (Nelson et al., 2005, 2007a, 2007b; Joksovic et al., 2006, 2007). Phenotypically, Todorovic *et al*. show that in the neuropathic pain model, administration of reducing agents intrathecally or by localized microinjection exacerbates the nociceptive response to noxious stimuli whereas the hyperalgesic response is minimized with the administration of oxidizing agents (Todorovic et al., 2001b, 2004; Nelson et al., 2007b).

The effect of the endogenous compounds L-cysteine, ascorbate and NO on $Ca_v3.2$ activity and consequently DRG and nRT neurons suggests that redox modulation of $Ca_v3.2$ may occur *in vivo* to regulate neuronal activity. In particular, the inhibitory effects of NO are intriguing as nNOS has been found to be expressed in nociceptive DRGs and up-regulated in the neuropathic pain model (Steel et al., 1994; Choi et al., 1996; Luo et al., 1999).. nNOS is a Ca^{2+} -dependent enzyme which catalyzes the synthesis of NO and L-citrulline from L-arginine; co-expression of the $Ca_v3.2$ channel and nNOS within the same neuron would provide a convenient source of NO for the regulation of $Ca_v3.2$ activity.

We have identified a putative PDZ-3 binding ligand at the carboxyl terminus of the $Ca_v3.2$ channel (Figure 2.1A). Alignment of the carboxyl amino acids of the channels within the Ca^{2+} family demonstrates that the putative PDZ-3 binding motif is unique to $Ca_v3.2$ and that it is conserved across human, rat and mouse species (Figure 2.1B). The sequence of the PDZ-3 motif corresponds with the consensus sequence known to interact with the PDZ-3

domain of nNOS suggesting that a physical interaction between the two proteins is possible (Schepens et al., 1997; Stricker et al., 1997). Furthermore, a physical interaction between $Ca_v3.2$ and nNOS may facilitate a functional interaction by anchoring nNOS within effective range of the localized Ca^{2+} influx generated during activation of $Ca_v3.2$(Augustine et al., 2003).

I hypothesize that $Ca_v3.2$ and nNOS physically interact via the carboxyl PDZ-3 ligand of $Ca_v3.2$ allowing for the functional feedback regulation wherein $Ca_v3.2$ activity stimulates nNOS to produce nitric oxide which in turn further inhibits $Ca_v3.2$ channels. In this section I put forward evidence that $Ca_v3.2$ and nNOS can physically and functionally interact via the carboxyl PDZ-3 motif of $Ca_v3.2$ forming a novel feedback loop. Utilizing a heterologous expression system I demonstrate that a physical interaction between $Ca_v3.2$/nNOS is feasible and that this interaction facilitates a functional interaction whereby $Ca_v3.2$ mediated Ca^{2+} entry stimulates nNOS activity which in turn inhibits $Ca_v3.2$ activity. This putative negative feedback loop could potentially play an important role in regulating neuronal activity in DRGs involved in nociception under normal and pathological conditions and in nRT neurons during development.

Figure 2.1: Alignment of voltage-gated Ca^{2+} channels demonstrating a PDZ-3 motif unique to $Ca_v3.2$

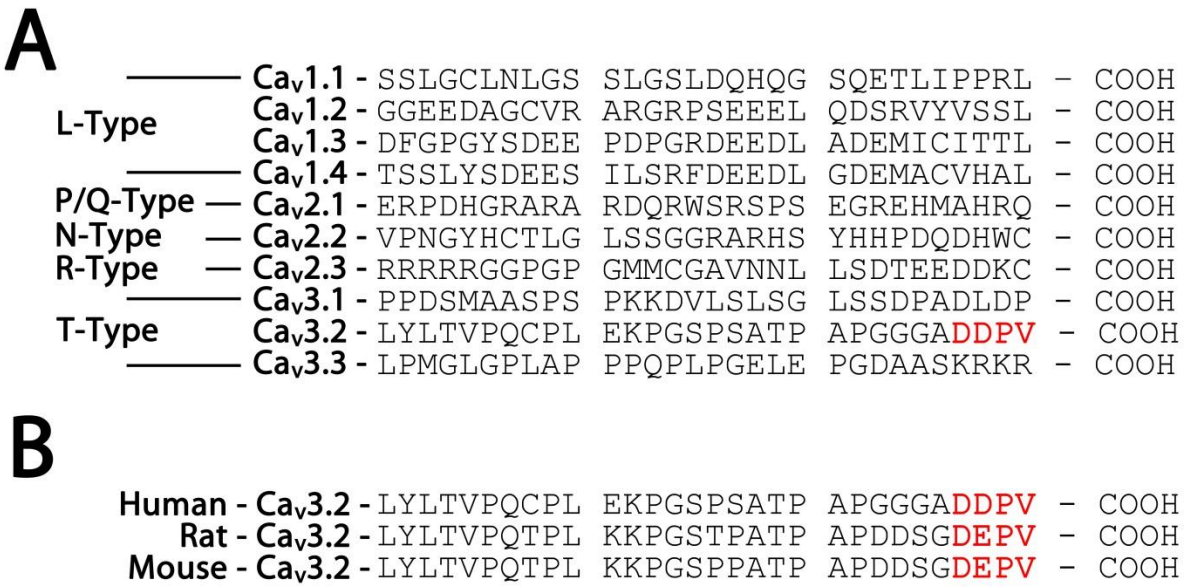

Figure 2.1: Alignment of voltage-gated Ca^{2+} channels demonstrating a PDZ-3 motif unique to $Ca_v3.2$

Alignment of the last 30 residues from the amino acid sequences of human voltage-gated Ca^{2+} channels (A). The $Ca_v3.2$ is the only VGCC with a carboxyl sequence that corresponds with the PDZ-3 binding motif consensus sequence x-D/E-x-V/I/L-COOH (Schepens et al., 1997; Stricker et al., 1997). Alignment of the carboxyl human, rat and mouse $Ca_v3.2$ amino acid sequences shows that the consensus sequence for the PDZ-3 binding ligand is conserved across species (B).

2.2. Materials and methods

2.2.1. Generation of fusion peptides

Plasmids encoding the glutathione S-transferase (GST) fusion protein constructs were generated by inserting the carboxyl terminal coding sequence of $Ca_v3.2$ or $Ca_v3.1$ in frame and downstream of the GST coding sequence. Polymerase chain reactions (PCRs) consisting of Taq DNA polymerase, HotStarTaq Master Mix with Q solution (Qiagen, Toronto, ON,

Canada), 200μM dNTPs (Invitrogen, Grand Island, NY, USA), and 0.4μM forward and reverse oligos (refer to Table 2.1 for oligo sequences) were performed to amplify the coding sequence of the carboxyl 100 amino acids of pcDNA3.1 zeo (+) plasmid clones of human $Ca_v3.2$ (NCBI accession number: NM_001005407) and human $Ca_v3.1$ (NCBI accession number: NM_018896). For the $Ca_v3.2$ GST fusion proteins, oligonucleotides (oligos) were designed to introduce BamHI and XhoI restriction endonuclease recognition sites at the 5' and 3' ends, respectively. $Ca_v3.1$ oligos introduced an EcoRI restriction endonuclease site at the 5' end and an XhoI restriction endonuclease site at the 3' end. Further, a GST/$Ca_v3.2$ fusion peptide lacking a PDZ-3 binding ligand was generated using a downstream oligo designed to introduce a stop codon at the start of the DDPV-COOH motif of $Ca_v3.2$. A PTC-200 gradient thermocycler (MJ Research/ BioRad, Mississauga, ON, Canada) was utilized to perform a 25 cycle profile of 98°C for 30 seconds for denaturation, 50 to 65 ^{o}C for 1 minute for annealing, and 65 ^{o}C to 78 ^{o}C for 1 minute for extension. Once amplified, the $Ca_v3.2$ fragments were digested with BamHI (New England Biolabs, Ipswich, MA, USA) and XhoI (New England Biolabs, Ipswich, MA, USA) restriction endonucleases and the $Ca_v3.1$ fragment with EcoRI (New England Biolabs, Ipswich, MA, USA) and XhoI restriction endonucleases before ligation using T4 ligase (New England Biolabs, Ipswich, MA, USA) into a pGEX4T1 vector (GE Healthcare, Baie d'Urfe, QC, Canada) which was digested using the same endonulceases. The ligated fragments were transformed into chemically competent DH5α cells (Invitrogen, Grand Island, NY, USA) using the heat shock protocol detailed in Section "2.2.2. Generation of transformation and chemically competent DH5α cells" and plated on lysogeny broth (LB) agar plates (1% (w/v) tryptone, 1% (w/v) NaCl, 0.5% (w/v) yeast extract, 1.5 w/v agar) (Bertani, 1951, 2004) with 50 μg/ml ampicillin to select for transformed cells. After incubating the LB agar plates with ampicillin overnight at 37°C

individual colonies were cultured overnight at 37°C in 5ml of LB with 50 μg/ml ampicillin, and the DNA was extracted using a commercial DNA miniprep kit (Invitrogen, Grand Island, NY, USA). The GST fusion protein clones were sequenced (NAPS, UBC) to ensure the sequence was correct and encoded the desired fusion protein. BL21DE (Invitrogen, Grand Island, NY, USA) cells were utilized to express the GST fusion proteins. The cells were transformed using the described heat shock protocol and then plated on LB agar plates with 50 μg/ml ampicillin to select for transformed cells. After incubating the LB ampicillin plates overnight at 37°C an individual colony was cultured at 37°C in 50ml of LB for use as a started culture. After 18 hours in a shaking incubator the optical density (A600) of the starter culture was measured using a spectrophotometer and used to seed 500ml of LB at an optical density of 0.2. The 500ml culture was monitored and when the optical density reached 0.6 induction of the GST fusion protein expression was initiated with the addition of 300μM isopropyl β-D-1 thiogalactopyranoside (IPTG) and incubating for 3 hours at 37°C with shaking. The induced cells were pelleted by centrifugation at 7000 x *g* for 10 minutes, re-suspended in GST lysis buffer (25 mM Tris, 2 mM EDTA, pH 7.6 with HCl) and lysed with 1mg/ml lysozyme (GE Healthcare, Baie d'Urfe, QC, Canada) for 20 minutes at room temperature. A ten minute sonication in a sonicating water bath was used to assist the lysing of the cells and the lysate was centrifuged for 20 minutes at 18,000 x *g* at 4 °C to remove the cell debris before the lysate was transferred to new 1.5ml tubes and frozen at -20°C until required for subsequent experiments.

Cell-penetrating TAT-fusion peptides were designed and ordered from Gensrcipt (Piscataway, NJ, USA). The peptides contained the protein transduction domain of the Human Immunodeficiency Virus 1 transactivator of transcription (TAT) protein (YGRKKRRQRRR) fused with the last 9 amino acids of the rat $Ca_v3.2$ sequence

(PDDSGDEPV) which possess a carboxyl terminal PDZ-3 binding ligand. A second TAT-fusion peptide with a mutation in the Cav3.2 PDV-3 binding ligand (PDDSGDEPE) was also designed ordered. The peptides were used at a concentration of 50 nM.

Table 2.1: Primers used to generate the clones utilized in this thesis

Purpose	Target	Primer orientation	Primer sequence 5' to 3'	Amino acid substitution details	Restriction Sites
GST - fusion protein	Cav3.2	Forward	*CGGATCTGGTTCCGC GT*GGATCCTCCTGC CGGGCTGAGCACCT GACC	No amino acid substitution	Introduces BamHI Restriction endonuclease site
GST - fusion protein	Cav3.2	Reverse	*TCAGTCACGATGCGG CCG*CTCGAGCTACA CGGGGTCATCTGCA CCAC	No amino acid substitution	Introduces XhoI Restriction endonuclease site
GST - fusion protein	Cav3.2	Reverse	*CAGTCACGATGCGGC CG*CTCGAGCTATGC ACCACCCCCTGGGG CAGGGGT	Introduces stop codon to remove last 4 amino acids (deletes **DDPV** sequence)	Introduces XhoI Restriction endonuclease site
GST - fusion protein	Cav3.1	Forward	GCCTGGACGAATTC TCCCAACCCCACCTG GGCACAGACCCCTC T	No amino acid substitution	Introduces EcoRI Restriction endonuclease site
GST - fusion protein	Cav3.1	Reverse	AAGTGGGGCTCGAG TCAGGGGTCCAGGT CTGCTGGGTCAGAG G	No amino acid substitution	Introduces XhoI Restriction endonuclease site
Full length mutant	Cav3.2	Duplex oligo	*CTGCC*CCAGGGGGT GGTGCAGATGCCCC CGCGTAGCTCGGTC TAGA*GTGC*	DEPV to DAPA mutation	Native $Ca_v3.2$ PflMI and pcDNA3.1 vector XhoI Restriction endonuclease sites utilized
Removal of GST from nNOS clone	nNOS	Duplex oligo	CTTAGTAAGCGGCC GCTTACTAAG	Introduce native stop codon at carboxyl terminus of nNOS	nNOS NotI Restriction endonuclease site utilized
Tagging of PSD-95 with DsRED2	DsRED 2	Forward	GGAATTCGGATGGC CTCCTCCGAGAACGT CATCA	No amino acid substitution	Introduces EcoRI Restriction endonuclease site
Tagging of PSD-95 with DsRED2	DsRED 2	Reverse	GGAATTCTAGAGTC GCGGCCGCTACAGG AACA	No amino acid substitution	Introduces EcoRI Restriction endonuclease site

Table 2.1: Primers used to generate the clones utilized in this thesis

To generate the plasmid constructs used in the study various oligos were designed that introduced restriction endonuclease recognition sites (bold blue bases) to facilitate the in frame cloning of the PCR fragments. For a few of the constructs the oligos were also used to introduce base pair mutations into the coding sequence (bold red bases) to alter the amino acid sequence. The bases in normal black type are those that match and bind to the target, those in black italics are a random assortment of bases required for to optimize the digestion of the PCR fragments with the restriction enzymes.

2.2.2. Generation and transformation of chemically competent DH5α cells

DH5α cells (Invitrogen, Grand Island, NY, USA) were maintained as glycerol stocks at -150°C. To prepare chemically competent cells a scraping of the DH5α glycerol stock was used to seed a 5ml starter culture of SOC++ media (2% w/v tryptone, 0.5% w/v yeast extract, 0.05% w/v NaCl, 250 mM KCl, 2 M $MgCl_2$, 1 M glucose, pH 7.4 with NaOH) which was incubated overnight at 37 ^{o}C with shaking. The next day 1ml of the started culture was used to seed a 75 ml of SOC++ media culture which was incubated at 19°C with shaking until the optical density (A600) was 0.6 at which time the cell were pelleted with a 10 minute 3,000 x *g* centrifugation at 4°C. One wash using 80ml of ice cold TB buffer (10 mM PIPES, 15 mM $CaCl_2$*$2H_2O$, 250 mM KCl, 55 mM $MnCl_2$*$4H_2O$, pH 6.7 with KOH) was completed and the cells were re-suspended in 20 ml of TB buffer. 1.5 ml dimethyl sulfoxide (DMSO) (Sigma-Alrich, St.Louis, MO, USA) was added to the re-suspended cells to assist in cryoprotection and 200 µl aliquots were flash frozen in liquid nitrogen followed by long term storage at -80 ^{o}C.

Transformation of the chemically competent DH5α cells was accomplished using a heat shock protocol. The plasmid DNA (the entire ligation mixture OR 500ng of purified

plasmid) was gently mixed with a 200μl aliquot of DH5α cells which were allowed to thaw on ice. After a 10 minute incubation on ice the cells were placed in a 42°C water bath for 60 seconds and then immediately transferred to an ice bath for 5 minutes. The heat shock treated cells were transferred to 1ml of pre-warmed (37°C) LB and incubated at 37°C with shaking for 1 hour and then plated on LB agar plates with the appropriate selection agents.

2.2.3. Mutation of the $Ca_v3.2$ PDZ-3 binding ligand

Key amino acids of the carboxyl PDZ-3 motif of $Ca_v3.2$ were mutated to determine whether full length $Ca_v3.2$ and nNOS interact via the PDZ-3 domain of nNOS. Using the 3' terminus as a template, a 50-mer duplex oligo was designed to introduce two single base pair mutations near the stop codon of $Ca_v3.2$. The mutations encode for two amino acid substitutions; one at the -2 position where the second Aspartic acid of the –DDPV-COOH motif is changed to Alanine, and the other at position 0 where the hydrophobic valine residue is substituted with Alanine. The 5' end of the duplex oligo spanned a native PflMI restriction endonuclease site and the 3' region was designed to include an XbaI restriction endonuclease recognition site downstream of the $Ca_v3.2$ stop codon. Restriction endonulceases PflMI (New England Biolabs, Ipswich, MA, USA) and XbaI (New England Biolabs, Ipswich, MA, USA) were used to digest the full length Cav3.2 clone in pcDNA3.1 zeo (+).The duplex oligo and the digested fragments were separated by size on a 0.8% low melting point agarose (Sigma-Alrich, St.Louis, MO, USA) gel in TAE buffer (40 mM Tris, 5.71% glacial acetic acid, 1mM EDTA, pH 8.0) at a constant voltage of 100 V and a commercial gel extraction kit (Qiagen, Toronto, ON, Canada) was used to recover individual fragments from the gel. A single fragment of ~50 base pairs was recovered from the duplex oligo digest. There are two PflMI restriction endonulcease recognition sites within the $Ca_v3.2$ clone, therefore two fragments of

4306 and 7665 base pairs in size were recovered from the digest; the third fragment of 123 base pairs was discarded. The larger 7665 base pair fragment was dephosphorylated by adding 2 μl each of alkaline phosphatase and buffer (Roche, Laval, QC, Canada) to 20 μl of the fragment sample and incubating at 37°C for 1 hour. Ligation of the plasmid clone was completed in two steps. The 4306 base pair fragment from the $Ca_v3.2$ digest was first ligated to the digested duplex oligo using T4 DNA ligase at 16 ^{o}C. After 40 minutes the dephosphorylated 7665 base pair fragment was added to the ligation mixture and all 3 fragments were ligated overnight at 16 ^{o}C. The ligated fragments were transformed into chemically competent DH5α cells using the described heat shock protocol and plated on LB agar plates with 50 μg/ml ampicillin to select for transformed cells. After incubating the LB ampicillin plates overnight at 37°C an individual colonies were cultured overnight at 37 ^{o}C in 5 ml of LB with 50 μg/ml ampicillin and the DNA was extracted using a DNA miniprep kit (Invitrogen, Grand Island, NY, USA). A test restriction endonulcease digest using the BstXI restriction endonulcease (New England Biolabs, Ipswich, MA, USA) was performed to confirm the proper insertion of the duplex oligo fragment. After confirming that the oilgo fragment was ligated successfully, a sample of the transformed bacterial stock was cultured overnight at 37°C in 200 ml of LB with 50 μg/ml ampicillin and the DNA was extracted using a commercial midiprep kit (Invitrogen, Grand Island, NY, USA). The clones were sequenced (NAPS, UBC) to ensure the single base pair mutations were present in the clone and to ensure sequence errors were not introduced during the cloning process.

2.2.4. nNOS and PSD-95 clones

The original full length neuronal nitric oxide synthase (nNOS) (NCBI accession number: NM_052799) was cloned into a pCIS vector by D.S.Bredt (Johns Hopkins

University School of Medicine) (Bredt et al., 1991). A green fluorescent protein (GFP) tagged version of the full length nNOS clone in the pCIS vector was generously provided by Dr. S.R. Vincent (University of British Columbia). This GFP tagged nNOS clone was utilized in the electrophysiology experiments so that transfected cells could be readily identified. A second nNOS construct was generated to remove the GFP tag to eliminate the possibility of background fluorescence from the GFP in the nitric oxide detection assay; this construct was used for all experiments other than electrophysiology. To remove the GFP tag the pCIS nNOS-GPF clone was digested with XbaI for to linearize the clone a immediately 5' of where the stop codon is positioned in the wild type nNOS sequence. Mung Bean Nuclease (New England Biolabs, Ipswich, MA, USA) was used to digest the XbaI 5' overhang to create a blunt ended linear fragment. A second digestion using the NotI restriction endonulcease (New England Biolabs, Ipswich, MA, USA), which recognizes a restriction site 3' of the GFP sequence of the nNOS/GFP plasmid was performed to excise the GFP coding sequencing from the linearized plasmid. The digested fragments were separated by size on a low melting point gel and the large fragment containing the nNOS coding sequence and vector backbone was recovered using a commercial gel extraction kit (Qiagen, Toronto, ON, Canada).

To reconstitute the native nNOS sequence a phosphorylated palindromic oligonucleotide was generated (Integrated DNA Technologies: San Diego, California) which contained the final five nucleotides of the native nNOS coding sequence and a NotI restriction endonuclease recognition site 3' of the native nNOS stop codon. Digestion of the palindromic oligonucleotide with NotI generated two identical fragments containing a blunt 5' end possessing the last five nucleotides of the native nNOS sequence and a NotI 5' overhang at the 3' end. The digested oligo fragments were ligated with the nNOS vector

fragment using T4 DNA ligase (New England Biolabs, Ipswich, MA, USA) for 2 hours at room temperature and then transformed into chemically competent DH5α chemically competent cells using the described heat shock protocol and plated on LB agar plates with 50 μg/ml ampicillin to select for transformed cells. After incubating the LB agar plates overnight at 37 ^{o}C individual colonies were cultured overnight at 37 ^{o}C in 5 ml of LB with 50 μg/ml ampicillin for selection, and the DNA was extracted using a DNA miniprep kit. A test digest was performed using the KpnI restriction endonuclease (New England Biolabs, Ipswich, MA, USA) to determine proper excision of the GFP tag and the re-ligated clone was sequenced to ensure the restored sequence corresponded to the native nNOS sequence.

The Post Synaptic Density Protein 95kD (PSD-95) (NCBI accession number: NM_019621) clone was originally generated by Dr. D. S. Bredt (University of California) (Topinka and Bredt, 1998) and a green fluorescent protein (GFP) tagged version of this full length PSD-95 clone in a GW1 vector was received from Dr. Y.T.Wang (University of British Columbia). Since the nNOS clone already contained a GFP tag, the GFP tag of the PSD-95 clone was substituted with a DsRED tag from the pDsRED2 vector. This DsRED tagged PSD-95 clone was used for all experiments requiring expression of PSD-95. PCR primers were designed to amplify the coding sequence of the DsRED tag from the pDsRED2 vector (CloneTech: Mountain View, CA, USA) and to introduce EcoRI restriction endonuclease recognition sites at the 5' and 3' ends of the PCR fragment. EcoRI (New England Biolabs, Ipswich, MA, USA) restriction endonulcease was used to digest both the PCR fragment and the PSD-95 clone to excise the GFP tag. The digests were separated by size on a low melting point agarose gel and the vector backbone as well as the PCR fragment was recovered using a commercial gel extraction kit. The vector backbone was dephosphorylated and the PCR fragment was ligated into the backbone using T4 DNA ligase.

The ligated fragments were transformed into chemically competent DH5α cells using the described heat shock protocol and plated on LB agar plates with 50 μg/ml ampicillin to select for transformed cells. After incubating the LB agar plates with ampicillin overnight at 37 ^{o}C individual colonies were cultured overnight at 37 ^{o}C in 5 ml of LB with 50 μg/ml ampicillin, and the DNA was extracted using a commercial DNA miniprep kit. A restriction endonuclease test digest using SbfI (New England Biolabs, Ipswich, MA, USA) and BamHI was performed to confirm the insertion of the PCR fragment in the proper orientation. The newly generated DsRed2 tagged PSD-95 clone was sequenced to ensure that DNA sequence errors were not introduced during the cloning process.

2.2.5. Cell culture and transfection

Human embryonic kidney (HEK293) cells were grown in Dulbecco's Modified Eagle Medium (Invitrogen, Grand Island, NY, USA) supplemented with 10% fetal bovine serum (FBS) (Invitrogen, Grand Island, NY, USA) which was heat inactivated at 55°C for 30 minutes, 50 U/ml penicillin/50 μg/ml streptomycin (Invitrogen, Grand Island, NY, USA) and 1% non-essential amino acids (Invitrogen, Grand Island, NY, USA). A humidified chamber was utilized to incubate the cells at 37°C in 5% CO_2 balanced with room air. The reagents used to maintain selection pressure for the various cell lines stably expressing $Ca_v3.2$ are listed in Table 2.2. Selection pressure was maintained during cell growth and the selection reagents were refreshed with each media change.

A Ca^{2+} phosphate transfection procedure was utilized to transiently transfect HEK293cells. The day before transfection the cells were dissociated using 0.25% trypsin-EDTA (Invitrogen, Grand Island, NY, USA) and diluted in growing media without selection reagents so that the confluency of the re-seeded T-25 flasks (Fisher Scientific, Ottawa, ON,

Canada) was between 20-25%. On the day of transfection the cells were typically between 35-45% confluent. For each T-25 to be transfected, 150 µl Ca^{2+} chloride (250 mM) and 150 µl 2x HEPES Buffered Saline (HeBS) (274 mM NaCl, 40 mM HEPES, 12 mM D-glucose, 10 mM KCl, 1.4 mM $Na_2HPO_4*7H_2O$, pH 7.04) were dispensed into separate 5 ml tubes. 1.8 µg of the pCIS nNOS clone and/or 2 µg of the GW1 PSD-95 clone were gently pipetted into the Ca^{2+} chloride solution and empty pBlueScript SK (-) vector was added to bring the total amount of DNA up to 6 µg. The mixture was then added drop-wise to the 2xHEBS solution to initiate the formation of phosphate precipitate. Precipitates were allowed to form for 20 minutes at room temperature during which time the media in the flasks was aspirated and replaced with fresh media without selection reagents. The transfection mixture was added drop wise to the cell media and allowed to incubate in a humidified chamber at 37^oC with 5% CO_2 balanced with room air for 12 hours before the media was replaced with fresh growing media. Transfections which were to be used for immunoprecipitation experiments were incubated an additional 30-36 hours before lysis. Transfections intended for electrophysiology experiments were dissociated 24 hours after transfection using 0.25% Trypsin/EDTA, diluted using fresh growing media and seeded into 35mm petri dishes at 10% confluency. The nitric oxide assay required the transfections to be dissociated and diluted in phenol free DMEM (Invitrogen, Grand Island, NY, USA) and seeded into 12 well cell culture plates (Costar: 3336) at 30% confluency. For experiments utilizing the HEK293-TREX cell line stably expressing Kir2.3 and $Ca_v3.2$ under an inducible promoter (a gift from Neuromed Pharmaceuticals: Vancouver, BC, Canada), was induced with 1.5 µg/ml doxycycline to initiate $Ca_v3.2$ expression at this time. The newly seeded 35 mm dishes and the 12 well culture plates were incubated for an additional 24 hours before use.

Table 2.2: Agents utilized to maintain selection pressure for the transfected constructs

Cell Type	Type of Expression	Construct	Selection Agent(s)	Mutation Details
HEK293H	-Stable	Cav3.2 (Human)	50 μg/ml Zeocin	
HEK293H	-Stable	Cav3.2 (Human) with PDZ-3 mutation	50 μg/ml Zeocin	DDPV to DAPA
HEK tsa201	-Stable -Stable	Cav3.2 (Human) Kir 2.1 (Human)	25 μg/ml Zeocin 300 μg/ml Geneticin	
HEK tsa201	-Stable -Stable	Cav3.2 (Human) with PDZ-3 mutation Kir 2.1 (Human)	25 μg/ml Zeocin 300 μg/ml Geneticin	DDPV to DAPA
HEK293-TREX	-Inducible (1.5μg/ml Doxycyclin) -Stable	Cav3.2 (Human) Kir 2.3(Human)	150 μg/ml Hygromycin 600 μg/ml Geneticin 10 μg/ml Blasticidin	

Table 2.2: Agents utilized to maintain selection pressure for the transfected constructs

Several cell lines stably expressing $Ca_v3.2$ were used in this study. To maintain the stable expression of transfected constructs the various cell lines were cultured in the presence of selection agents. The concentration of the selection agents used for each cell line is listed in table. Doxycycline was used to induce the expression of the $Ca_v3.2$ construct in the HEK-TRex cell line.

2.2.6. Generation of stable cell lines

The wild type $Ca_v3.2$ clone and the $Ca_v3.2$ clone with the mutant PDZ-3 ligand were transfected into HEK293 cells and into tsa201 cells, a HEK293 derivative, already stably expressing the inward rectifying potassium channel Kir2.1 (a gift from Neuromed Pharmaceuticals: Vancouver, Canada) to generate cell lines which stably express either the wild type or mutant $Ca_v3.2$ channel. The cells were maintained and transfected using the protocol described in Section "2.2.5. Cell Culture and Transfection". Total DNA used for the

transfection was 1.8 μg of either the wild type or PDZ-3 mutant $Ca_v3.2$ clone and 4.2 μg of an empty pBlueScript SK (-) vector. The pcDNA3.1 zeo (+) plasmid contains a zeocin resistance gene therefore transfected HEK293 cultures were treated with 50 μg/ml zeocin (Invitrogen, Grand Island, NY, USA) to select for cells transfected with the pcDNA3.1 zeo (+) $Ca_v3.2$ clone. A Kir2.1 inward rectifier clone which confers geneticin resistance was previously transfected and was stably expressed in tsa201 cells, therefore 25 μg/ml zeocin and 300 μg/ml geneticin (Invitrogen, Grand Island, NY, USA) were used to select for cells expressing both the $Ca_v3.2$ clone and the Kir2.1 clone. A media change was performed 12 hours after transfection and did not include selection reagents; however, subsequent media changes contained the selection agents and were performed every 24 hours. After 1 week the cells were dissociated with 0.25% Trypsin-EDTA and diluted in fresh selection media so that the re-seeded confluency in the fresh T-25 flask was 20%. The selection media was replaced daily until the number of cells perishing daily due to lack of the antibiotic resistance was substantially reduced, at which time the cells were dissociated and re-seeded into 24-well cell culture plates (BD Biosciences, Mississauga, ON, Canada) at 5% confluency. Two additional selection media changes were performed 24 hours apart and then the frequency of the media changes was reduced to once every 72 hours. In the following weeks, colonies developed from individual cells (1-2 per well) which were gently removed with a 1000 μl pipette tip, mechanically dissociated in fresh selection media and re-seeded into 24 well culture plates. Every 72 hours the selection media in the 24 well plates was replaced and as the cultures in various wells reached confluency they were dissociated and transferred to 12 well culture plates (BD Biosciences, Mississauga,ON, Canada), then 6 well culture plates (Fisher Scientific, Ottawa, ON, Canada) and finally T-25 flasks. Each new cell line was tested for $Ca_v3.2$ expression using Western blot analysis and whole cell patch clamp electrophysiology.

Acceptable cell lines were expanded and cryogenically frozen in freezing media containing 7.5% heat inactivated FBS, 12.5% DMSO and 0.5% non-essential amino acids in DMEM.

2.2.7. GST pull down

Glutathione sepharose 4B beads (GE Healthcare, Baie d'Urfe, QC, Canada) were used to precipitate the wild type $Ca_v3.2$, wild type $Ca_v3.1$ and $Ca_v3.2$ with the deleted PDZ-3 ligand GST fusion proteins. The beads were washed once with 10 volumes of phosphate buffered saline solution (PBS) (136 mM NaCl, 2.6 mM KCl, 1 mM $Na_2HPO_4*7H_2O$, 1.8 mM KH_2PO_4, pH 7.4), twice with 10 volumes of GST lysis buffer and re-suspended in GST lysis buffer immediately before use. 200 µl of GST fusion protein extract was incubated with a 40µl bed volume of washed beads for 30 minutes with gentle agitation at room temperature. A two minute centrifugation step 500 x *g* was applied to sediment the sepharose beads so that the lysate could be aspirated and the beads retained. The bead bound GTS fusion proteins were then used to probe 50 µl of lysate extracted from human embryonic kidney cells (HEK293) (ATCC, Manassas, VA, USA) which were transiently transfected with the nNOS clone and the total sample volume was brought to 250 µl with GST lysis buffer. After one hour incubation the sepharose beads were washed once with 10 volumes of PBS and twice with higher stringency washes of 10 volumes of PBS with an additional 100 mM NaCl added. Two washes of 80ul glutathione elution buffer (10 mM reduced glutathione (Sigma-Alrich, St.Louis, MO, USA) and 50mM Tris, pH 8.0 with HCl) were used to release the GST fusion and associated proteins from the beads. The eluate was denatured with the addition of an equal volume of Laemmli buffer (0.5 M Tris, 10% SDS, 20% glycerol, 2% b-mercaptoethanol, 0.004% bromophenol blue) and 10 minute incubation at 80^oC.

2.2.8. Co-immunoprecipitation

To ensure that the ratio of $Ca_v3.2$, nNOS and PSD-95 proteins were consistent between samples cell lysate from HEK293 cells expressing $Ca_v3.2$, nNOS and PSD-95 was prepared individually and the lysates were mixed immediately prior to incubation with the $Ca_v3.2$ specific polyclonal antibody used to precipitate $Ca_v3.2$. $Ca_v3.2$ lysate was harvested from HEK293 cells stably expressing either wild type $Ca_v3.2$ clone or the $Ca_v3.2$ clone with the mutant PDZ-3 ligand. nNOS and PSD-95 lysate was harvested from HEK293 cells that were transiently transfected with the respective plasmid clones using the methodology described in section "2.2.5. Cell Culture and Transfection". To harvest the lysate the cells were grown to confluency in a T-25 flask, washed twice with 1ml of PBS and scraped using a sterile cell scraper into 300 µl of lysis buffer (50 mM Tris, 150 mM NaCl, 50 mM EDTA, pH 7.5) with 0.5% NP-40 and Complete EDTA-free protease inhibitor (Roche, Laval, QC, Canada) added. The lysis solution was repeatedly passed through a 26 gauge syringe followed by a 29 gauge insulin syringe to mechanically disrupt the cell membrane and then centrifuged at 18,000 x *g* for 30 minutes at 4°C to pellet to cell debris so the supernatant could be transferred to a fresh 1.5 ml tube. The nNOS lysate was pre-cleared at 4°C for 30 minutes on a rotating mixer with 50 µl/ml Protein G PLUS Agarose (Santa Cruz Biotechnology: Santa Cruz, CA, USA) which was washed 3 times with 10 volumes of lysis buffer and re-suspended in lysis buffer with 0.5% NP-40 added. Following the pre-clear, the nNOS lysate was centrifuged at 1,000 x *g* for 5 minutes at 4°C and the supernatant was retained. A Qubit Protein Assay Kit (Invitrogen, Grand Island, NY, USA) was utilized to determine the concentration of the lysates. Only fresh lysate was used to in the immunoprecipitation samples and, unless otherwise indicated, the amount of each lysate used was 200µg of Cav3.2 lysate, 150µg of nNOS lysate and 100µg of PSD-95. In addition to the

cell lysate, the immunoprecipitation samples consisted of, 0.4 μg of Cav3.2 specific polyclonal antibody (Santa Cruz Biotechnology: Santa Cruz, CA, USA: Cat-SC-16261), 30 μl of washed protein G PLUS agarose, and were brought up to a final volume of 200 μl using lysis buffer without NP-40. After incubating the samples overnight at 4°C on a rotating mixer the samples were washed once with 1.5 ml lysis buffer with 0.5% NP-40, twice with 1.5ml of lysis buffer without NP-40 and re-suspended in 35 μl of 2x Laemmli buffer. The re-suspended samples were denatured at 80°C for 10 minutes and stored at -20°C.

2.2.9. Western blot analysis

NuPAGE® 4–12% Bis-Tris 20 well Gels (Invitrogen, Grand Island, NY, USA) and a Novex NuPAGE® SDS-PAGE Gel System were used to separate the proteins in the samples by molecular weight. MOPS running buffer (50 mM MOPS, 50 mM Tris, 0.1% SDS, 1 mM EDTA, pH 7.7) was used to provide denaturing and reducing conditions during separation. 15 μl of sample was loaded in each well and a constant voltage of 120 V was applied for 80 minutes to separate the proteins. Protein transfer to a membrane consisted of tightly sandwiching the gel containing the proteins between the Hybond ECL Nitrocellulose membrane (GE Healthcare, Baie d'Urfe, QC, Canada) and filter paper, submersing in western blot transfer buffer (25 mM Tris, 200 mM Glycine, 20% methanol (vol/vol) and 0.001% SDS) and applying a constant 100 V potential across the surface of the gel for 1 hour so that the proteins migrate towards the positively charged pole of the apparatus and bind to the nitrocellulose membrane.

A thirty minute incubation on a shaker with 2% skim milk in PBS was used to block the membrane and prevent non-specific antibody binding. Incubation with primary antibodies was performed at room temperature with shaking for 2 hours followed by three 15 minute

washes with 25 ml 2% skim milk in PBS. Antibodies specific to $Ca_v3.2$ (Santa Cruz Biotechnology: Santa Cruz, CA, USA: Cat- SC-16261), nNOS (Santa Cruz Biotechnology: Santa Cruz, CA, USA: Cat-SC5302) or PSD-95 (Fisher Scientific, Ottawa, ON, Canada: Cat-MA1-046) were diluted in 2% skim milk in PBS at 1:2,000, 1:5,000 and 1:2,000 respectively. Peroxidase conjugated secondary antibodies, donkey anti-goat (Santa Cruz Biotechnology, Santa Cruz, CA,USA:Cat-SC-2020) for use against the $Ca_v3.2$ primary antibody and goat anti-mouse (Fisher Scientific, Ottawa, ON, Canada: PI31444) for use against the nNOS and PSD-95 primary antibodies were diluted 1:10,000 in 2% skim milk and incubated with the membrane for 1 hour. Three 15 minute washes of 25ml PBS were used to remove excess blocking agent and excess antibodies from the membrane. The SuperSignal West Pico Chemiluminescent Substrate (Fisher Scientific, Ottawa, ON, Canada) and Amersham Hyperfilm ECL film(GE Healthcare, Baie d'Urfe, QC, Canada) were utilized to visualize the protein bands. Equal volumes of the peroxide solution and the luminol solution of the chemiluminescent substrate were mixed as needed and 3ml of the mixture was incubated on the membrane for 5 minutes. Excess chemiluminescent substrate was poured off and the membrane was gently pulled across the lip of the incubation tray to remove the remaining substrate before the membrane was wrapped in plastic film. A dark room was utilized to expose the membranes to the film. Typically, three exposures were made with durations of 5 seconds, 30 seconds and 2 minutes. Additional exposures of longer or shorter duration were made if necessary. A Kodak X-Omat M35 processor was used to develop the film.

2.2.10. Nitric oxide detection assay

A flourometric assay was developed using Diaminorhodamine-4M AM (DAR-4M AM) (Millipore, Billerica, MA, USA) to detect nitric oxide production within HEK293 cells transiently transfected with nNOS. Cells were transfected and prepared for the assay using the methodologies described in Section "2.2.5. Cell Culture and Transfection". On the day of the experiment the cells were loaded with DAR-4M by replacing the media with loading buffer (18.4 mM HEPES, 118 mM NaCl, 11.7 mM D-glucose, 1.2 mM K_2HPO_4, 0.5 mM $MgSO_4*7H_2O$, 4 mM KCl, 10 μM DAR-4M AM, 295 mOsm/kg (adjusted with mannitol), pH 7.2) (adapted from (Kim et al., 2004; Belardetti et al., 2009)) and incubated for 25 minutes at 37^oC and 5% CO2/room air atmosphere. The acetomethylester (AM) component allows the dye to pass through the cell membrane where cellular esterases cleave the AM component leaving the non-permeable DAR-4M fluorophore confined within the cell. The loading buffer was aspirated and excess dye was removed with a single wash using 600ul wash buffer (140 mM choline chloride, 16mM HEPES, 10 mM D-glucose, 1mM $MgCl_2*6H_2O$,1mM KCl, 295 mOsm/kg, pH 7.4 (adjusted with N-Methyl-D-glucamine)) (adapted from (Belardetti et al., 2009)). A 20 minute incubation at 37^oC and 5% CO2/room air atmosphere in 600ul of assay buffer (140 mM choline chloride, 16 mM HEPES, 10 mM D-glucose, 1 mM $MgCl_2*6H_2O$,1 mM KCl, 2 mM $CaCl_2$, 25 μM N-[Tris(hydroxymethyl)methyl]glycine (tricine), 295 mOsm/kg, pH 7.4 (adjusted with N-Methyl-D-glucamine)) (adapted from (Belardetti et al., 2009)) prepared the cells for the depolarization step. Calcium entry was facilitated by either introducing ionomycin, a Ca^{2+} ionophore, at a concentration of 7 μM or by activating the $Ca_v3.2$ channels through chemical depolarization which involved rapidly increasing the KCl concentration of the assay buffer by 65 mM (66 mM final concentration). Ionomycin treated cells were incubated for 1 hour

and the chemically depolarized cells were incubated for 20 minutes at 37°C and 5% CO2/room air atmosphere before the relative fluorescence was measured using a GeminiXS fluorometer using the SoftMAX Pro software version 4 (Molecular Devices, Sunnyvale, CA, USA). The fluorometer was set to excite the sample at 530 nm and read the emission at 580 nm with a cutoff value of 570 nm and with the photomultiplier set to automatic. A total of 69 data points were per well were analyzed to obtain average relative fluorescence for each well. Each data set was normalized to the average relative fluorescence of the wells of the same set which were stimulated but treated with an inhibitor. For example: the data from the nNOS transfected cells stimulated with KCl was normalized to nNOS transfected cell stimulated with KCl stimulated but inhibited with L-NAME (Sigma-Alrich, St.Louis, MO, USA).

nNOS activity was inhibited with the application of L-NAME at a concentration of 300 μM which was added to both the loading buffer and the assay buffer of the appropriate wells. The Cav3.2 channels were inhibited with 25 μM $NiCl_2$ which was added to the appropriate wells when the assay buffer was applied. All data were exported in text format using the SoftMAX pro software and imported into MicroSoft Excel 2010 to calculate the average signal for each well and to perform the normalization calculations. Statistical analysis, ANOVA followed by Tukey's Multiple Comparison test, was performed using the GraphPad Prism software version 5.

2.2.11. Whole cell patch clamp analysis

Whole cell electrophysiological recordings of the exogenous Ca currents due were obtained from HEK293 cells stably expressing either the wild type $Ca_v3.2$ or $Ca_v3.2$ with the mutant PDZ-3 ligand. GFP tagged nNOS and DsRED tagged PSD-95 were individually or co-transfected into the stable cell lines using the Ca^{2+} phosphate protocol outlined in Section

"2.2.5. Cell Culture and Transfection" and electrophysiological recordings were obtained using the whole cell patch clamp technique 48 hours after transfection. The cells were bathed in external recording solution consisting of 92 mM cesium chloride, 40 mM tetraethylammonium chloride, 10 mM HEPES, 1 mM $MgCl_2$, 2 mM $CaCl_2$, 10 mM D-glucose, 150 μM L-arginine, 25 μM tricine, 300 mOsm/kg, pH 7.4 and electrically grounded with a 3M KCl agar bridge. Borosilicate glass patch pipettes (Sutter Instrument Company, Novato, CA, USA: Cat-BF150-86-10) with 3-5 MΩ resistance were made using a horizontal puller (Sutter Instrument Company, Novato, CA,USA), fire polished with a mircoforge (Narishige, East Meadow, NY, USA) and filled with internal solution (130mM cesium methanesulphonate, 10 mM HEPES, 2 mM $MgCl_2*6H_2O$, 0.1 mM EDTA, 5 mM Mg-ATP, 0.3 mM Na-GTP, 10 μM L-arginine, 100 nM flavin adenine dinucleotide disodium salt hydrate, 100 nM (6R)-5,6,7,8-Tetrahydrobiopterin dihydrochloride, 295 mOsm/kg, pH 7.4). An Axopatch 200A amplifier and CV203BU head stage were utilized to record the whole cell currents (Molecular Devices, Sunnyvale, CA, USA). The recordings were filtered at 2 kHz using the low pass Bessel filter on the amplifier, digitized with a Digitdata 1322A (Molecular Devices, Sunnyvale, CA, USA), sampled at 10 kHz and stored using a personal computer running the pClamp version 9 software package (Molecular Devices, Sunnyvale, CA, USA).

Currents were measured during 80ms depolarizing pulses from a holding membrane potential of -110 mV to membrane potentials ranging from -80 to 50 mV in 10 mV steps with 5mV steps between -50 and -10 mV and plotted as a function of the depolarizing potential. To avoid accumulation of inactivation there was a three second pause at a holding potential of -110mV between test pulses. Current-voltage curves were fitted using a modified Boltzmann equation: $I=(G_{max}*(V_m-E_r))/(1+\exp((V_m-V_{50})/k))$, where G_{max} is the maximum

slope conductance, V_m is the depolarizing potential, E_r is the reversal potential, V_{50} is the half-activation potential and k is the slope of the activation curve (goodness of fit had R^2 values ≥ 0.993).

The conductance was calculated from the current-voltage curves and plotted as a function of membrane potential to generate activation curves. The data was fit with the Boltzmann equation: $G/G_{max}=A1+(A2-A1)/(1+\exp((V_m-V_{50})k)))$, where A2 is the maximum normalized conductance, A1 is the minimum normalized conductance, V_m is the test potential, V_{50} is the half-activation potential and k is the slope of the activation curve (goodness of fit had R^2 values ≥ 0.993).

Current density due to Ca^{2+} ion flow was determined for each cell using the whole cell recordings used to generate the current voltage relationship and the membrane capacitance compensation values from the amplifier (Iwasaki et al., 2008). The recordings were analyzed to determine the absolute value for the peak current (pA) due to Ca^{2+} ion flow. The peak current values were then divided by the capacitance of the cell (pF), which correlates with cell size, to determine the current density due to Ca^{2+} ion flow (pA/pF) for each cell. Normalization of the current density data consisted of dividing the current density for each cell by the average current density of similarly transfected cells treated with L-NAME. For example: [cell current density ($Ca_v3.2$+nNOS)] / [average current density ($Ca_v3.2$+nNOS+L-NAME)]

Inactivation curves were generated by calculating the maximum normalized current from currents measured during a 60 ms membrane depolarization to a membrane potential of -40mV from a series of holding potentials ranging from -120 to -20 mV in 10 mV steps and plotting as a function of membrane potential. The holding potentials were held for 10 seconds to allow inactivation of the channel to reach a steady state. The data was fit using the

Boltzmann equation: $I/I_{max}=A1+(A2-A1)/(1+\exp((V_m-V_{50})k)))$, where A2 is the maximum normalized conductance, A1 is the minimum normalized conductance, V_m is the test potential, V_{50} is the half-activation potential and k is the slope of the activation curve (goodness of fit had R^2 values ≥ 0.993). Axon instruments' pClamp version 9 software was utilized to extract the data from the recorded currents, Excel 2010 (Microsoft) was used to perform the normalization calculations and Origin software version 8 (OriginLabs, Northampton, MA, USA) was used to graph the data and perform statistical analysis.

2.3. Results

2.3.1. Cav3.2 and nNOS interact via the PDZ-3 binding ligand located at the carboxyl terminus of $Ca_v3.2$

Protein precipitations utilizing tagged fusion proteins are particularly useful in determining whether a particular domain of one protein interacts with another protein. Precipitations utilizing tagged proteins are generally more robust than immunoprecipitation as concerns regarding antibody affinity and specificity under the precipitation conditions are mitigated. Therefore, to initiate the investigation of whether the putative PDZ-3 binding ligand of $Ca_V3.2$ is capable of interacting with nNOS, GST fusion proteins which contain the carboxyl 100 amino acids of the human $Ca_v3.2$ isoform were generated and used to probe lysate from HEK293H cells transiently transfected with nNOS.

Western blot analysis (Figure 2.2A) shows that the full-length nNOS co-precipitates with the $Ca_v3.2$ carboxyl-GST fusion protein but not with a GST fusion protein possessing the 100 carboxyl residues of $Ca_v3.1$ channel which lacks the putative carboxyl PDZ-3 motif. Further, deletion of the carboxyl residues that constitute the PDZ-3 binding motif of $Ca_v3.2$ (-DDPV) resulted in complete loss of nNOS binding demonstrating that the putative binding

motif is required for nNOS binding. Non-transfected HEK293H cell lysate (H labeled lanes) was also probed and run alongside the nNOS transfected lysate (N labeled lanes) as negative controls to show that the antibody used in the Western blot analysis was specific for nNOS. Coomassie staining (Figure 2.2A) shows that the amount of GST fusion protein that precipitated was relatively equal across all samples.

The full-length $Ca_v3.2$ protein is a sizable 255 kDa which may introduce steric effects which could potentially shield the PDZ-3 binding motif of $Ca_v3.2$ and inhibit an interaction with nNOS. To address this, full length $Ca_v3.2$ was immunoprecipitated from lysate of cells stably expressing $Ca_v3.2$ with a $Ca_v3.2$ specific antibody in the presence of lysate from cells transiently expressing nNOS. Western blot analysis (Figure 2.2B) shows that nNOS co-immunoprecipitates with full length $Ca_v3.2$ but not when the key amino acids of the $Ca_v3.2$ PDZ-3 binding motif at positions 0 and -2 (relative to the carboxyl terminus) are substituted with residues not found in the PDZ-3 consensus sequence (Schepens et al., 1997; Stricker et al., 1997). An antibody that does not recognize the $Ca_v3.2$ protein was used in immunoprecipitations and run in parallel to demonstrate that the results were not due to the non-specific precipitation of $Ca_v3.2$ and nNOS.

The $Ca_v3.2$/nNOS interaction could be competitively inhibited with synthetic peptides possessing a PDZ-3 binding motif. Figures 2.3A and 2.3B that when a peptide containing a PDZ-3 binding ligand (-DEPV) is introduced the co-immunoprecipitation of nNOS is substantially reduced compared to immunoprecipitations in the presence of a peptide with a mutated PDZ-3 binding ligand (-DEPE).

Figure 2.2: $Ca_v3.2$ and nNOS can physically interact via the carboxyl PDZ-3 binding ligand of $Ca_v3.2$

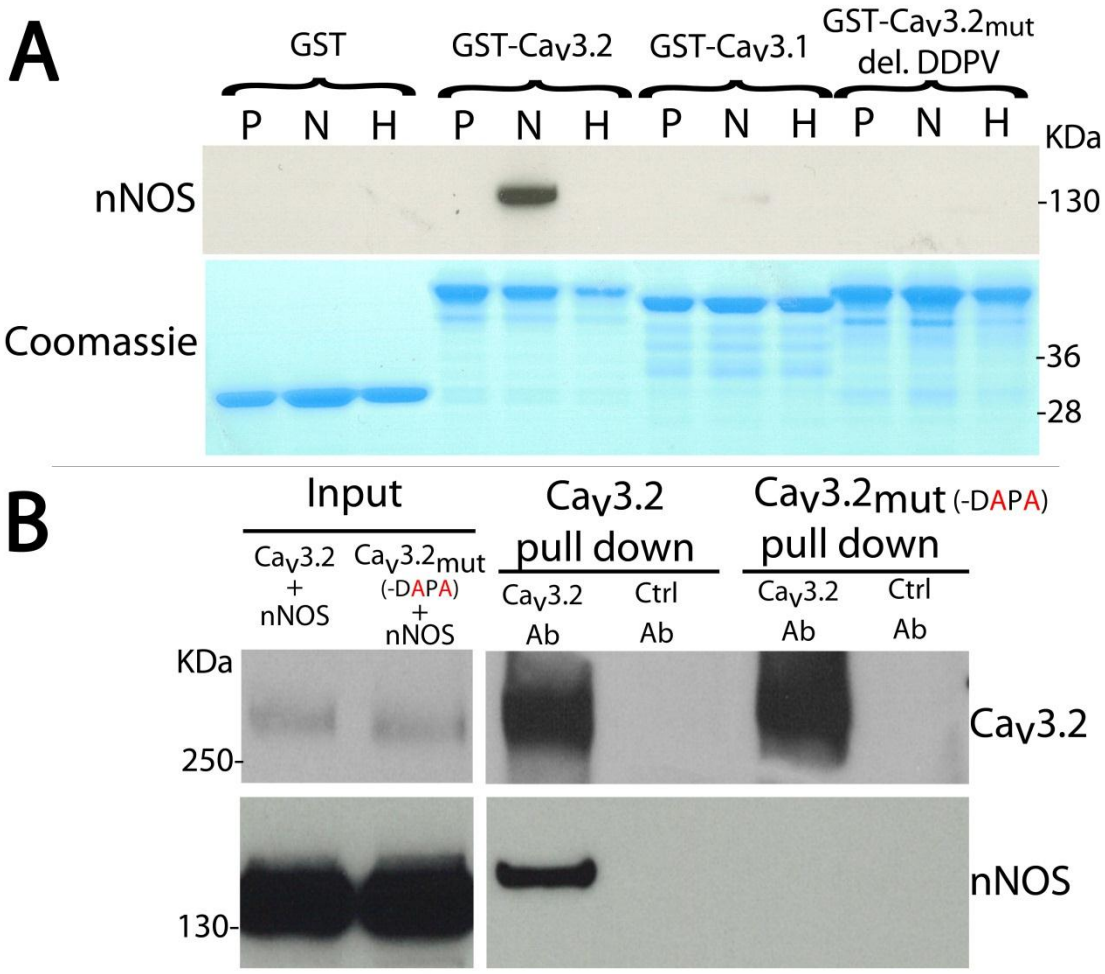

Figure 2.2: $Ca_v3.2$ and nNOS can physically interact via the carboxyl PDZ-3 binding ligand of $Ca_v3.2$

(A) GST fusion proteins generated from the carboxyl 100 amino acids of human $Ca_v3.2$ and human $Ca_v3.1$ were incubated with full length nNOS from lysate of nNOS transfected ("N" labeled lanes) and non-transfected ("H" labeled lanes) HEK293H cells and a nNOS specific monoclonal antibody was used to probe the membrane in the Western analysis (top panel). nNOS co-precipitated with the GST-$Ca_v3.2$ fusion protein but not with the GST or GST-$Ca_v3.1$ fusion protein controls which lack the PDZ-3 binding ligand (-DDPV-COOH). Additionally, nNOS did not co-precipitate when the last four amino acids (-DDPV-COOH), which comprise the PDZ-3 binding ligand, were removed from the carboxyl terminus of the GST-$Ca_v3.2$ fusion protein (GST-$Ca_v3.2_{mut}$ del. DDPV). Coomassie staining (bottom panel) shows that the amount of GST fusion peptide recovered in the precipitations was comparable to amount recovered with the control precipitations where no HEK293 lysate was added ("P" labeled lanes). (B) Co-immunoprecipitation of full length $Ca_v3.2$ and nNOS. nNOS co-immunoprecipitated with full length human $Ca_v3.2$ using a polyclonal $Ca_v3.2$ specific antibody but did not co-immunoprecipitate when the key residues of the PDZ-3 binding ligand of $Ca_v3.2$ were mutated from -DDPV-COOH to –DAPA-COOH ($Cav3.2_{mut\ (-DAPA-COOH}$). An anti-mGluR1 antibody was used as a control against non-specific precipitation.

Figure 2.3: The physical interaction of $Ca_v3.2$ and nNOS can be competitively disrupted using a peptide containing the PDZ-3 binding ligand.

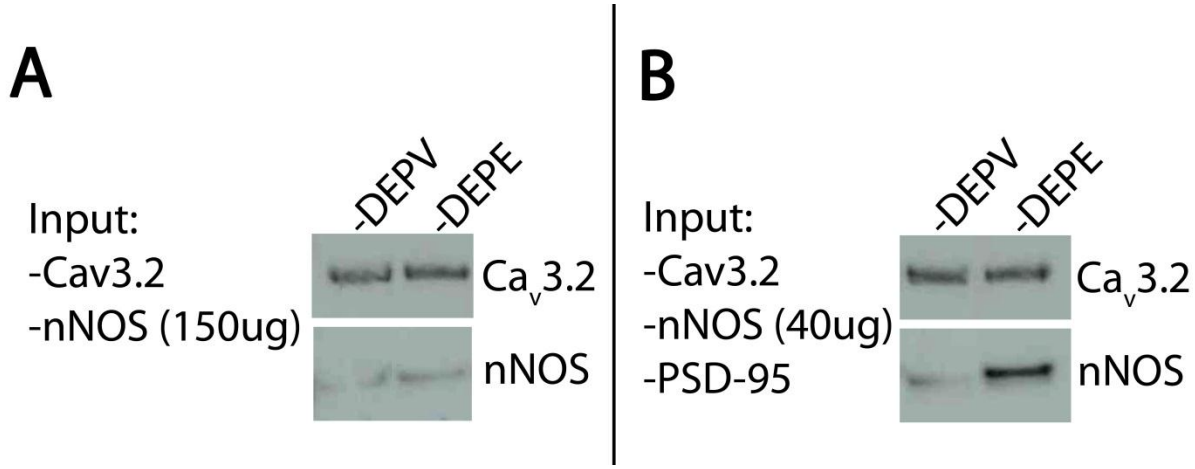

Figure 2.3: The physical interaction of $Ca_v3.2$ and nNOS can be competitively disrupted using a peptide containing the PDZ-3 binding ligand.

A TAT fusion peptide consisting of the transactivator of transcription (TAT) coding sequence (GRKKRRQRRRPQ) and the PDZ-3 binding ligand of the rat $Ca_v3.2$ channel (-DEPV-COOH) was designed to compete for the PDZ-3 domain of nNOS and disrupt the $Ca_v3.2$/nNOS interaction. As a control, a second peptide was designed with an amino acid substitution at key residue of the PDZ-3 binding ligand (-DEPE-COOH). The $Ca_v3.2$/nNOS (A) and $Ca_v3.2$/nNOS/PSD-95 (B) samples were prepared using lysate from separate HEK293 cultures individually transfected with $Ca_v3.2$, nNOS or PSD-95. A $Ca_v3.2$ specific antibody was utilized to precipitate $Ca_v3.2$ and the associated proteins in the presence of the TAT-DEPV or the TAT-DEPE peptides. $Ca_v3.2$ specific and nNOS specific antibodies were used to detect the precipitated proteins in Western analysis. It can be seen that co-incubation of TAT-DEPV reduces the amount of nNOS co-immunoprecipitation in both samples whereas the TAT-DEPE peptide does not. In the presence of PDS-95 (B) a noticeable increase in the amount of nNOS that co-precipitated with $Ca_v3.2$ was observed. The band intensity was 4.95 times more intense (when normalized to $Ca_v3.2$ staining) in the presence of PSD-95 even though the nNOS concentration in the $Ca_v3.2$/nNOS/PSD-95 lysate mix was less than half the concentration used in the $Ca_v3.2$/nNOS lysate mix.

2.3.2. The PDZ-3 domain and the PDZ-2 beta finger binding ligand of nNOS can facilitate the formation of larger protein complexes

In addition to possessing a PDZ-3 binding domain, nNOS also possesses an internal PDZ-2 binding ligand in a head-to-tail arrangement (Hillier et al., 1999; Tochio et al., 2000). This head-to-tail arrangement stabilizes the internal PDZ-2 binding ligand so that it can interact with proteins possessing PDZ-2 domains such as PSD-95 and syntrophin (Brenman et al., 1996a, 1996b). The presence of both a PDZ-3 domain and an internal PDZ-2 binding ligand presented the possibility that nNOS can facilitate the formation of larger protein complexes. To test this possibility, co-immunoprecipitation experiments were performed in the presence of PSD-95. Figure 2.4A shows that when nNOS is present PSD-95 is able to co-immunoprecipitate with $Ca_v3.2$ indicating that nNOS can interact with both $Ca_v3.2$ and PSD-95 simultaneously. The co-immunoprecipitation of PSD-95 in the presence of a competing peptide containing a PDZ-3 binding ligand is markedly reduced compared to a peptide with a mutation in the PDZ-3 motif providing further evidence that the interaction between $Ca_v3.2$ and PSD-95 is facilitated by nNOS (Figure 2.3B).

Interestingly, it was observed that the apparent efficiency of the nNOS co-immunoprecipitation increased substantially when PSD-95 was introduced. To explore this, $Ca_v3.2$, nNOS and PSD-95 lysate was harvested separately and specific amounts of each lysate were mixed such that the amount of $Ca_v3.2$ and nNOS was kept constant while the amount of PSD-95 varied. Western blot analysis of the immunoprecipitations shows that as the concentration of PSD-95 in the mixture increased, the amount of nNOS that co-immunoprecipitated with $Ca_v3.2$ also increased (Figure 2.4B). To address the possibility that the additional cell lysate containing the PSD-95 protein may have contributed to the increased nNOS immunoprecipitation, possibly through the stabilization of the proteins

and/or the interaction site, $Ca_v3.2$ and nNOS were immunoprecipitated with either an equal concentration of non-transfected HEK cell lysate or 2% glycerol in order to help stabilize the interaction (Vagenende et al., 2009). As observed in Figure 2.4C, neither untransfected HEK cell lysate nor 2% glycerol increased the amount of nNOS co-immunoprecipitation, and in fact the treatments appeared to have had a negative effect.

Figure 2.4: The $Ca_v3.2$/nNOS complex can interact with PSD-95 to form a larger complex.

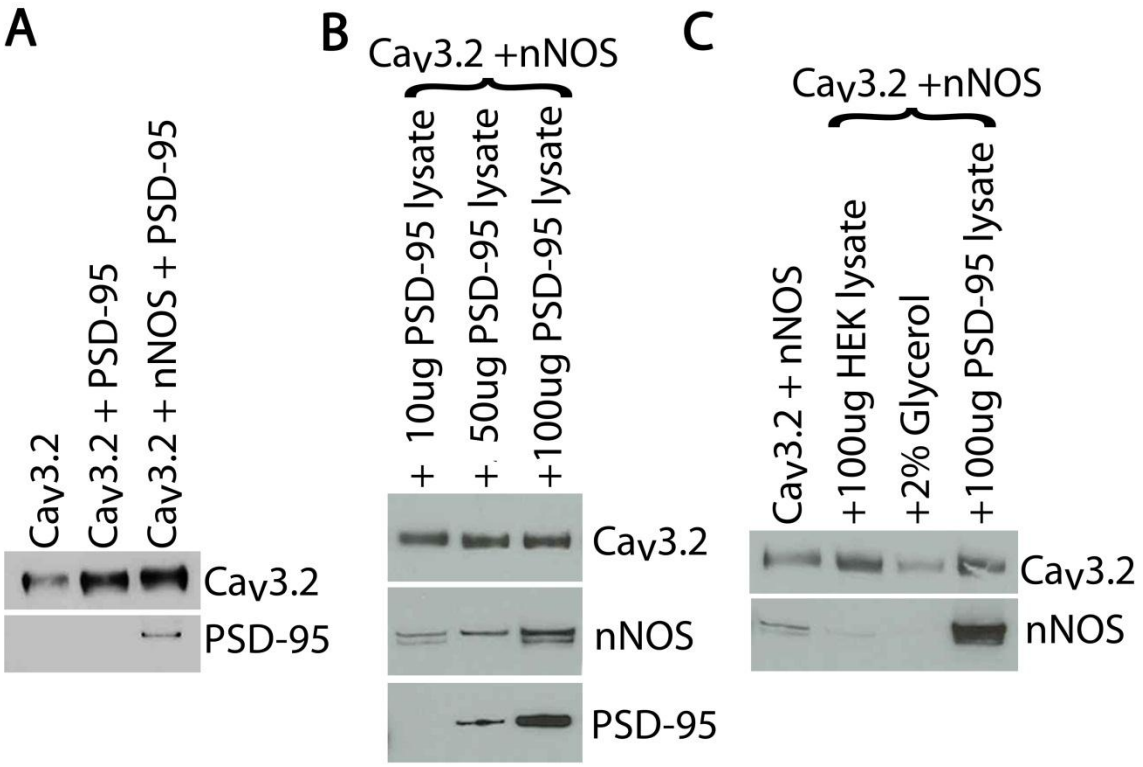

Figure 2.4: The $Ca_v3.2$/nNOS complex can interact with PSD-95 to form a larger complex.

Adjacent to the PDZ-3 binding domain of nNOS is a PDZ-2 beta-finger binding ligand which is known to interact with proteins that possess a PDZ-2 binding domain such as PSD-95 and Syntrophin. (A) Western blot analysis of the $Ca_v3.2$ immunoprecipitation from HEK cell lysate containing $Ca_v3.2$, nNOS and PSD-95 shows that PSD-95 co-precipitates with $Ca_v3.2$ only when nNOS is present in the lysate mixture. To ensure a consistent ratio of $Ca_v3.2$, nNOS and PSD-95 protein in the lysate samples the $Ca_v3.2$, nNOS and PSD-95 plasmids were transfected individually into separate HEK293H cell cultures and cell lysate from each culture was mixed immediately prior to incubation with the $Ca_v3.2$ specific polyclonal antibody. (B) The amount of nNOS that co-immunoprecipitates with $Ca_v3.2$ increases as the concentration of PSD-95 in the lysate mixture is increased. The $Ca_v3.2$ and nNOS concentrations remained the same for all samples and the concentration of PSD-95 was increased by adding additional PSD-95 transfected HEK lysate. All samples were brought to equal volumes using the same buffer used to prepare the lysates. To determine if the increase in nNOS co-precipitation was due to a stabilization of the $Ca_v3.2$/nNOS interaction due to the overall increase in HEK protein levels the immunoprecipitations were repeated using non-transfected HEK lysate and with 2% glycerol. (C) The addition non-transfected HEK293H cell lysate or 2% glycerol failed to increase nNOS co-precipitation and actually reduced the amount of nNOS precipitated with $Ca_v3.2$.

2.3.3. A physical interaction between Cav3.2 and nNOS is required for Cav3.2 activity to stimulate the production of nitric oxide by nNOS

A NO sensitive fluorometric assay was developed in order to determine if $Ca_v3.2$ channel activity can result in the stimulation of nNOS to produce NO. nNOS is considered to be Ca sensitive in that binding with activated calmodulin is required to stimulate the enzymatic activity. HEK cells have been reported to express calmodulin however in

heterologous expression systems the endogenous levels of Ca^{2+} may be a limiting factor (Persechini and Stemmer, 2002; Dai et al., 2010; Tian et al., 2011). To determine if there is sufficient calmodulin present in HEK cells to activate nNOS the ionophore ionomycin was used to facilitate Ca^{2+} influx. Figure 2.5A illustrates that NO can be detected nNOS transfected cells following the application of ionomycin. nNOS transfected cells display a significant increase ($p<0.001$) in fluorometric signal compared to cells treated with the nNOS inhibitor L-NAME and to non-ionomycin treated cells. No increase in fluorometric signal was observed in sham transfected cells treated with ionomycin. For each group the data were normalized to the L-NAME treated cells. These results indicate that endogenous levels of calmodulin are sufficient for the activation of nNOS.

tsa201 HEK cells stably expressing both $Ca_v3.2$ and an inwardly rectifying potassium channel (Kir2.1) were utilized in this assay to investigate whether $Ca_v3.2$ activity can activate nNOS (Figure 2.5B). Expression of Kir2.1 allowed for the manipulation of the resting membrane potential into a more hyperpolarized state and removing $Ca_v3.2$ channel inactivation. The cells could then be depolarized chemically by a rapid increase in the external KCl concentration. In the nNOS co-transfected cells chemical depolarization to a calculated membrane potential of ~-30 mV produced a significant increase ($p<0.001$) in the fluorometric signal compared to the L-NAME inhibited and non-stimulated cells. Contrastingly, KCl-induced depolarization had no effect on non-transfected control cells. For each group the data was normalized to the L-NAME treated cells.

To demonstrate that the increase in NO sensitive fluorometric signal was due to the activation of $Ca_v3.2$ channels, a cell line stably expressing $Ca_v3.2$ under an inducible promoter as well as constitutive Kir2.3 expression (an inward rectifying potassium channel) was examined. The cells were transfected with nNOS and stimulated under $Ca_v3.2$ induced

and non-induced conditions. Chemical depolarization produced a significant increase ($p<0.001$) in NO fluorometric signal in the induced cells compared to non-induced cells (Figure 2.5C). Block of $Ca_v3.2$ channels with 25 μM Ni^{2+} application (a concentration known to inhibit $Ca_v3.2$) (Lee et al., 1999b) prevented the ability of KCl depolarization to induce NO production. In these experiments the data were normalized to the non-induced/Ni^{2+} treated cells.

A cell line stably expressing Kir2.1 and $Ca_v3.2$ with point mutations introduced into the PDZ-3 binding ligand was further generated to determine whether the $Ca_v3.2$/nNOS physical interaction is required for the stimulation of nNOS (and NO production) following $Ca_v3.2$ activation. When selecting an appropriate stable cell line the $Ca_v3.2$ current density was measured and matched to a cell line stably expressing Kir2.1 and wild type $Ca_v3.2$ to ensure that Ca^{2+} influx was relatively similar in both groups. Both cell lines were transiently transfected with nNOS and chemically depolarized with KCl. The wild type $Ca_v3.2$ cell line produced a significantly greater ($p<0.05$) fluorometric signal in the KCl-stimulated nNOS transfected cells compared to both non-stimulated cells and to stimulated cells treated with L-NAME (Figure 2.5D). Of note, no significant difference was observed in the NO fluorometric signal between the stimulated, non-stimulated and L-NAME treated stimulated groups of the cells expressing the $Ca_v3.2$ channel with point mutations in the PDZ-3 binding ligand (-DAPA). For each group the data were normalized to the L-NAME treated cells.

Figure 2.5: The PDZ-3 binding interaction between $Ca_v3.2$ and nNOS is required for $Ca_v3.2$ activity to stimulate nNOS to produce nitric oxide.

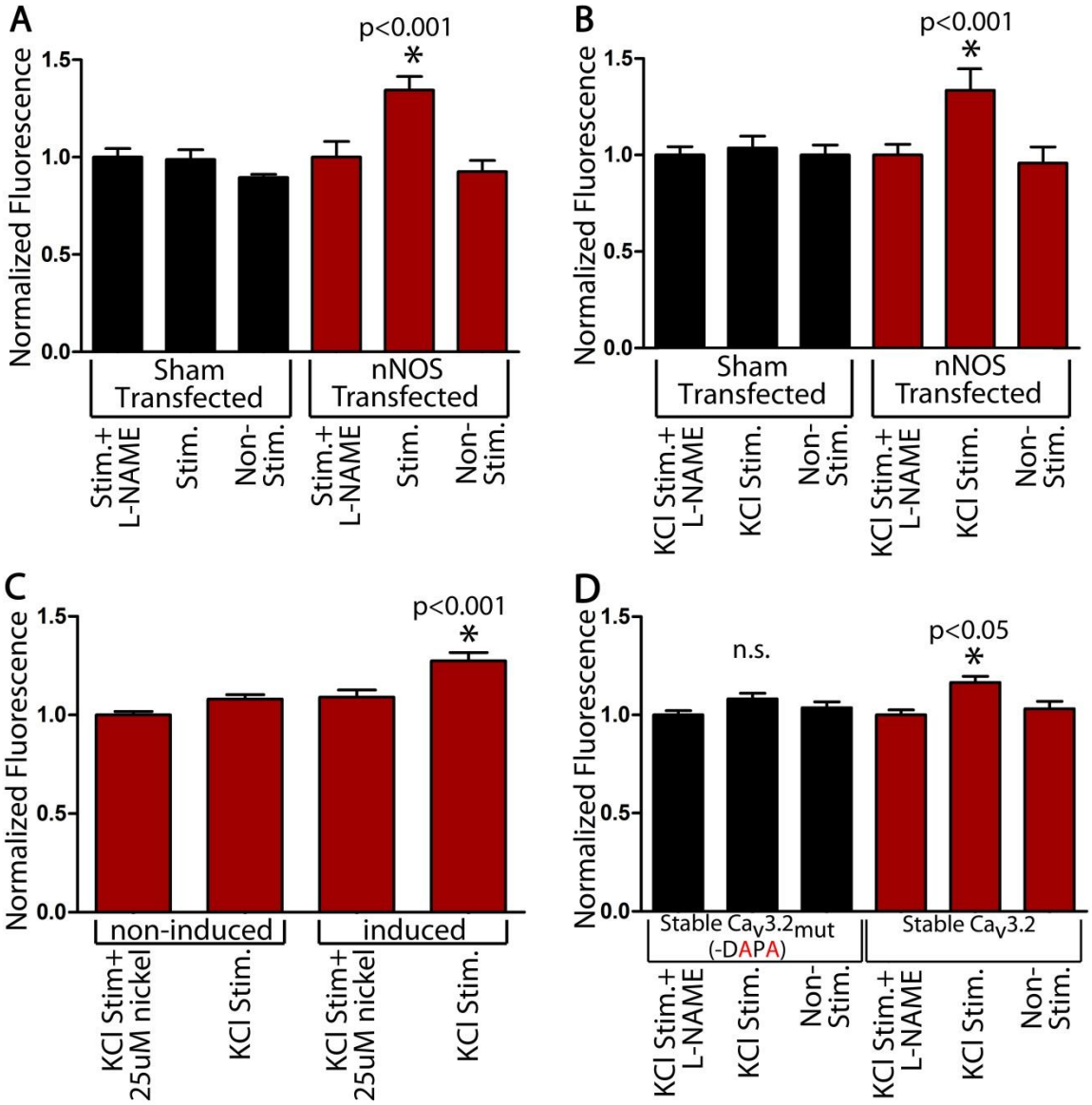

Figure 2.5: The PDZ-3 binding interaction between $Ca_v3.2$ and nNOS is required for $Ca_v3.2$ activity to stimulate nNOS to produce nitric oxide.

A NO-sensitive fluorometric assay was developed to detect NO production following stimulation of $Ca_v3.2$ channels. (A) Demonstration of the NO detection capabilities of the assay. The ionophore ionomycin was used to allow Ca^{2+} to permeate the membrane of HEK293H cells transfected with nNOS or empty vector (sham) and preloaded with the NO-sensitive fluorophor DAR-4M AM. Ionomycin treatment produced a significant increase in the fluorescent signal in cells transfected with nNOS and this increase in signal was inhibited when the cells were pre-incubated with the nNOS inhibitor L-NAME ($p<0.001$ [ANOVA followed by Tukey's multiple comparison test], n=4). No significant difference in the fluorometric signal was observed in the sham transfected cells. (B) HEK293H cells stably expressing a potassium inward rectifier (Kir2.3) and $Ca_v3.2$ under an inducible promoter were transfected with nNOS or an empty vector and chemically depolarized with a rapid increase in the external KCl concentration from 1 mM to 66 mM. $Ca_v3.2$ expression was induced in both nNOS transfected and sham transfected cells and chemical depolarization produced a significant increase in fluorometric signal in the nNOS transfected cells ($p<0.001$ [ANOVA followed by Tukey's multiple comparison test], n=8). The increase in signal was not observed in non-transfected cells and was inhibited in the transfected cells by pre-incubation with 300 μM L-NAME. (C) To demonstrate that the increase in the NO fluorescent signal is due to the activation of $Ca_v3.2$, induced cells were compared to non-induced cells using nNOS transfected stable Kir2.3/inducible $Ca_v3.2$ cells. Depolarization with KCl produced a significant increase in fluorescent signal in the $Ca_v3.2$ induced cells and this signal was inhibited with the application of Ni^{2+} at a concentration known to inhibit $Ca_v3.2$ (25 μM) ($p<0.001$) [ANOVA followed by Tukey's multiple comparison test], n=27). D: A physical interaction between $Ca_v3.2$ and nNOS is required for activation of nNOS by $Ca_v3.2$. Cells stably expressing Kir2.1 and either $Ca_v3.2$ with wild type carboxyl PDZ-3 binding ligand (-DDPV-COOH) or $Ca_v3.2$ with mutant carboxyl PDZ-3 binding ligand (-DAPA-COOH) were transfected with nNOS and then chemically depolarized. An increase in

NO fluorescent signal was observed when the $Ca_v3.2$ PDZ-3 binding ligand was intact ($p<0.05$ [ANOVA followed by Tukey's multiple comparison test], n=12) whereas no increase in signal was observed when the PDZ-3 binding interaction was interrupted ($p>0.05$ [ANOVA followed by Tukey's multiple comparison test], n=12). In panels A, B and D each experimental data group was normalized to the L-NAME inhibited data set within the group. In panel C the data was normalized to the non-induced, KCl-stimulated group. Error bars represent standard error. The n's indicate the number of cultures tested for each condition in the experiment.

2.3.4. nNOS activity inhibits Cav3.2 channels in a heterologous expression system

The redox modulation of $Ca_v3.2$ channels by NO results in a reduction in the maximum amplitude of macroscopic currents (Joksovic et al., 2007). The maximum macroscopic current that can be recorded from a cell depends on several factors including the physical size of the cell and the channel expression level. The physical size of the cell can be accounted for by determining the current density which is a measure of the whole cell current divided by the capacitance of the cell membrane which is reflective of the size of the cell (Haedo and Golowasch, 2006; Khorkova and Golowasch, 2007; Iwasaki et al., 2008; Golowasch et al., 2009). Cell lines stably expressing $Ca_v3.2$ were utilized to minimize the effects of varying expression levels on the current density measurements. With the aforementioned considerations, a reduction in the macroscopic $Ca_v3.2$ current due to nNOS activity would be expected to present as a reduction in T-type current density.

It was noted that the maximal T-type current density of cells stably expressing $Ca_v3.2$ and transiently expressing nNOS was approximately 25% lower (statistical significance $p<0.01$) than similar cells treated with the nNOS inhibitor L-NAME suggesting that nNOS activity might basally inhibit $Ca_v3.2$ channels (Figure 2.6A). The application of L-NAME

had no significant effect on T-type current density in non-nNOS transfected cells further supporting the notion that the effect results from the inhibition of nNOS activity and not as a result of a non-specific enhancement of $Ca_v3.2$ currents/expression by the NOS inhibitor. No significant differences in the current/voltage relationship (IV curve), steady state inactivation and steady state activation of $Ca_v3.2$ currents were observed between non-transfected and nNOS transfected cells (Figure 2.6B) or between L-NAME inhibited and non-inhibited cells (Figure 2.6C). Additionally, no obvious differences were observed in $Ca_v3.2$ current kinetics under the various experimental conditions (Figure 2.10B).

nNOS co-expression has no significant effect on T-type current density when expressed in cells stably expressing $Ca_v3.2$ containing point mutations in its PDZ-3 binding ligand site (Figure 2.7A). This result suggests that the $Ca_v3.2$/nNOS physical interaction is required for the nNOS/NO-mediated inhibition of $Ca_v3.2$. To support these findings, the current density was measured in cells expressing $Ca_v3.2$ and nNOS and treated with membrane permeable TAT fusion peptides containing either an intact PDZ-3 binding ligand and or a non-functional mutant PDZ-3 ligand (Figure 2.7B). Competitively disrupting the $Ca_v3.2$/nNOS interaction with a TAT fusion peptide possessing an intact PDZ-3 ligand relieved the reduction in T-type current density to the same extent as that for L-NAME treatment ($p<0.05$). Contrastingly, in cells treated with the TAT fusion peptide containing the mutant PDZ-3 ligand T-type current density remained suppressed, similar to that observed for L-NAME treatment. The TAT fusion peptide itself did not directly affect $Ca_v3.2$ currents as application of the peptide had no effect on the current density (see Figure 2.10A). Figure 2.7C shows that the mutation of the PDZ-3 binding ligand of $Ca_v3.2$ did not alter the current voltage relations of the channel compared to wild type.

A well characterized target of NO is sGC, an enzyme which synthesizes cGMP from GTP (reviewed in (Krumenacker et al., 2004; Potter, 2011)). cGMP-dependent protein kinases (PKG) have been demonstrated to affect T-type currents in newt olfactory receptor cells (Kawai and Miyachi, 2001) and although direct modulation of $Ca_v3.2$ by PKG has not been reported, there is a possibility that downstream effectors may influence the channel. To exclude sGC activity and subsequent activation of secondary messenger pathways as the mechanism of $Ca_v3.2$ inhibition in this study, the well documented sGC inhibitor [1*H*-[1,2,4]oxadiazolo-[4,3-α]quinoxalin-1-one] (ODQ) was utilized at a concentration of 20 μM (Zhao et al., 2000). Figure 2.8A illustrates that the application of ODQ or the solvent (DMSO) both failed to relieve the reduction in T-type current density indicating that the inhibition of $Ca_v3.2$ currents does not involve the activation of sGC or its downstream effectors. ODQ did have a significant effect on channel activation at membrane potentials of -50 mV and -45 mV, however, the differences at these potentials has minimal contribution to the current density measurements since the current density was calculated from the peak of the IV (~-30 mV) (Figure 2.8B).

As the presence of PSD-95 was found to increase the efficiency of the co-immunoprecipitation of nNOS, it was of interest to also examine the effect of nNOS and PSD-95 co-expression on T-type current density in $Ca_v3.2$ stably expressing cells. Of note, co-expression of PSD-95 resulted in a further reduction of the T-type current density compared to the cells transfected with nNOS alone (Figure 2.9A; $p<0.005$ [Student's t-test]). In cells co-expressing nNOS and PSD-95 the current density was reduced to ~50% of the L-NAME treated control cells and current density could be restored by treatment with either L-NAME or the competitively disrupting TAT-DEPV fusion peptide ($p<0.001$). Co-expression of PSD-95 did not have a significant effect on either the $Ca_v3.2$ current-voltage relation

(Figure 2.9B) or on current kinetics (Figure 2.10B). Additionally, PSD-95 did not have a significant effect on T-type current density of $Ca_v3.2$ stably expressing cells in which nNOS was also not co-expressed (Figure 2.10A) indicating that nNOS is required for the increased inhibition of basal $Ca_v3.2$ macroscopic currents.

Figure 2.6: nNOS activity inhibits $Ca_v3.2$

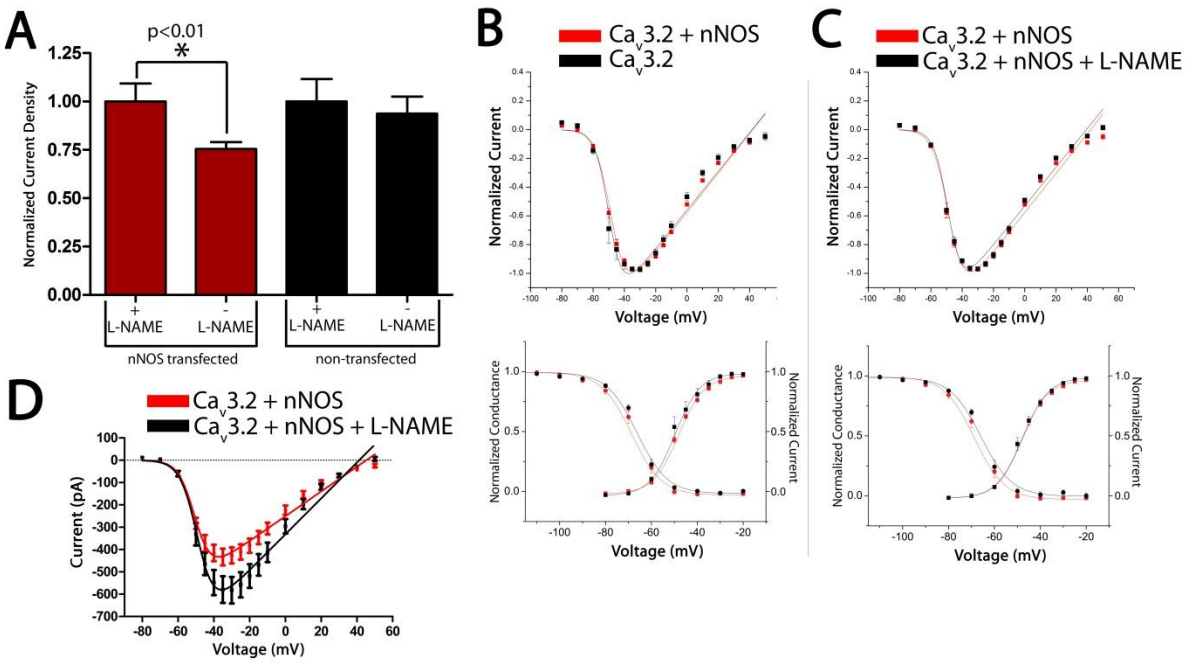

Figure 2.6: nNOS activity inhibits $Ca_v3.2$

The T-type current density due to Ca^{2+} influx was calculated for HEK293H cells stably expressing $Ca_v3.2$ with and without transient transfection of nNOS. (A) To determine current density [pA/pF] the peak recorded Ca^{2+} current [pA] was divided by the capacitance of the cell [pF] which correlates with cell size. The data for each experimental group was normalized to the L-NAME inhibited data. In nNOS transfected cells, the current density due to Ca^{2+} influx was significantly lower ($p<0.01$) than when the cells were pre-incubated with the nNOS inhibitor L-NAME. This difference was not observed in the non-transfected cells. (B) Normalized current/voltage (IV) curves and the steady state activation/inactivation curves comparing HEK293H cells stably expressing $Ca_v3.2$ and transfected with nNOS to the non-transfected cells. No significant difference was observed between the two groups. (C) Normalized current/voltage (IV) curves and the steady state activation/inactivation curves comparing HEK293H cells stably expressing $Ca_v3.2$ and transfected with nNOS under nNOS inhibited (L-NAME treated) and uninhibited conditions. The application of L-NAME did not significantly affect the IV or steady-state inactivation profiles. (D) IV curve comparing HEK293H cells stably expressing $Ca_v3.2$ and transfected with nNOS under nNOS inhibited (L-NAME treated) and uninhibited conditions. The error bars represent standard error. (cell numbers: nNOS transfected + L-NAME=18, nNOS transfected no L-NAME=32, non-transfected + L-NAME= 6, non-transfected no L-NAME=6)

Figure 2.7: A physical interaction between $Ca_v3.2$ and nNOS is required for the basal inhibition of $Ca_v3.2$ activity by nNOS

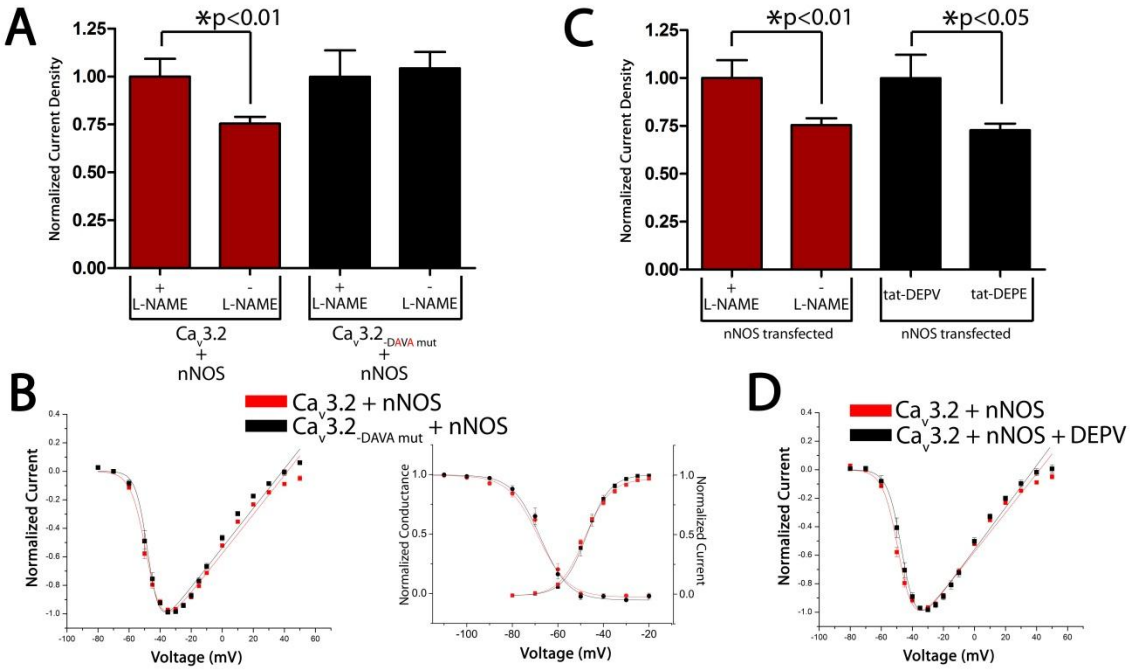

Figure 2.7: A physical interaction between $Ca_v3.2$ and nNOS is required for the basal inhibition of $Ca_v3.2$ activity by nNOS

(A) A HEK293H cell line was generated that stably expresses a mutant form of $Ca_v3.2$ where key $Ca_v3.2$ carboxyl terminal amino acids of the PDZ-3 binding ligand are mutated (-DDPV to -DAPA). The $Ca_v3.2$ mutant expressing cell line was transfected with nNOS and the current density due to Ca^{2+} influx was calculated. To determine current density [pA/pF] the peak recorded Ca^{2+} current [pA] was divided by the capacitance of the cell [pF]. No significant difference of peak current density was observed between the nNOS transfected $Ca_v3.2$ mutant expressing cell line under L-NAME inhibited and uninhibited conditions. ($p>0.05$ [Student's t-test], n=[$Ca_v3.2$+nNOS+LNAME=18, $Ca_v3.2$+nNOS no L-NAME=32, $Ca_v3.2_{mut}$+nNOS+L-NAME=7, $Ca_v3.2_{mut}$+nNOS no L-NAME=8]) (B) Normalized current/voltage (IV) curves and the steady state activation/inactivation curves comparing HEK293H cells stably expressing $Ca_v3.2$ and transfected with nNOS to HEK293H cells stably expressing the $Ca_v3.2$ PDZ-3 mutation (DAPA-COOH) and transfected with nNOS. No significant difference was observed between the two groups. (C) A HEK293H cell line stably expressing $Ca_v3.2$ and transiently expressing nNOS was pre-incubated with TAT-fusion peptides designed to competitively disrupt the $Ca_v3.2$/nNOS interaction (tat-DEPV). A second peptide similar to the first but with a mutation in a key residue of the PDZ-3 binding ligand (tat-DEPE) was used as a vehicle control. The current density of the TAT-DEPV peptide treated cells was significantly greater than the cells treated with the non-disrupting tat-DEPE control peptide ($p<0.05$ [Student's t-test]). The relief in the inhibition of current density was similar to that observed with the application of the nNOS inhibitor L-NAME. ($p<0.05$ [Student's t-test], n=[L-NAME=18, no L-NAME=32, tat-DEPV=9, tat-DEPE=9]) (D) Normalized current/voltage (IV) curves from nNOS transfected HEK293H cells stably expressing $Ca_v3.2$ with nNOS under normal and tat-DEPV treated conditions. In the current-voltage profile the application of the TAT-DEPV peptide did have one point at -50 mV where the normalized current was significantly less than the non-treated cells ($p<0.05$ [Student's t-test]) however, for all other voltages there was no significant difference and since the current density was calculated using the peak current at -30 mV the difference at -50 mV does not

affect the current density results. The data in the L-NAME experimental group was normalized to the L-NAME inhibited data set and the data in the TAT peptide data set was normalized to the TAT-DEPV data set so that the degree of $Ca_v3.2$ inhibition could be visualized. The error bars represent standard error.

Figure 2.8: The inhibition of $Ca_v3.2$ by nNOS activity is independent of soluble guanylyl cyclase activation

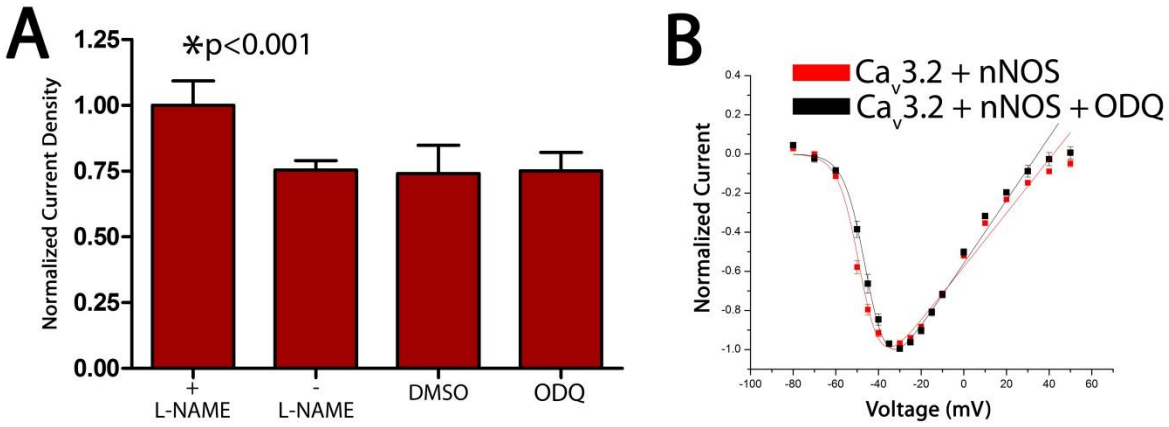

Figure 2.8: The inhibition of $Ca_v3.2$ by nNOS activity is independent of soluble guanylyl cyclase activation

A potential downstream target of NO is soluble guanylyl cyclase (sGC) which, when activated, catalyzes the conversion of guanosine triphosphate (GTP) to cyclic guanosine monophosphate (cGMP). (A) HEK293H cells stably expressing $Ca_v3.2$ and transfected with nNOS were treated with either the sGC inhibitor ODQ [1H-[1,2,4]Oxadiazolo[4,3-a]quinoxalin-1-one] (20μM) or dimethyl sulfoxide (DMSO) as the vehicle control. ODQ and DMSO were ineffective at relieving the nNOS-mediated inhibition of $Ca_v3.2$ currents as current density remained significantly lower than that for L-NAME treated cells ($p<0.001$ [ANOVA followed by Tukey's Multiple Comparison test], n=[L-NAME=18, no L-NAME=32, DMOS=8, ODQ=10). The data for all data sets was normalized to the L-NAME inhibited data set. (B) Normalized current-voltage profiles from HEK293H cells stably expressing $Ca_v3.2$ and transfected with nNOS show that overall ODQ had little effect on the IV relationship. At -50 mV and -45 mV there the normalized current was significantly less in the ODQ treated cells ($p<0.05$ [Student's t-test]) however, there was no significant difference at the current use to calculate T-type current density (-30 mV). To determine current density (pA/pF) the peak recorded Ca^{2+} current (pA) was divided by the cell capacitance (pF). The error bars represent standard error.

Figure 2.9: Co-expression of PSD-95 with nNOS and $Ca_v3.2$ results in increased inhibition of $Ca_v3.2$

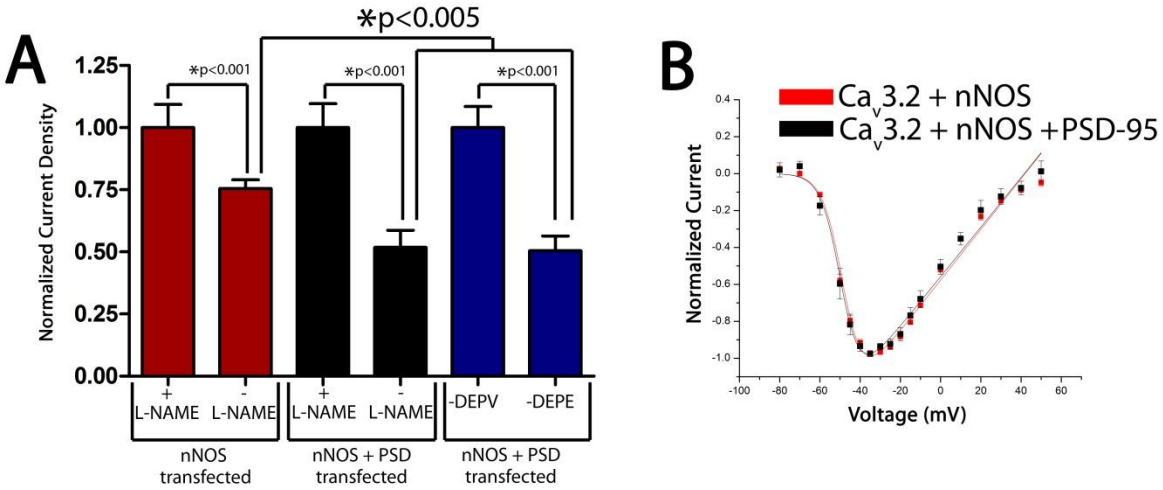

Figure 2.9: Co-expression of PSD-95 with nNOS and $Ca_v3.2$ results in increased inhibition of $Ca_v3.2$

(A) HEK293H cells stably expressing $Ca_v3.2$ were co-transfected with nNOS and PSD-95 and the T-type current density calculated. To determine current density [pA/pF] the peak Ca^{2+} current [pA] was divided by the cell capacitance [pF]. In the presence of PSD-95 and nNOS (n=7) the current density was significantly lower than nNOS only transfected cells (n=32) ($p<0.005$ [Student's t-test]). Incubation of the PSD-95/nNOS transfected cells with L-NAME (n=7) relieved the inhibition similar to that observed in the nNOS only transfected cells. ($p<0.001$ [ANOVA followed by Tukey's multiple comparison test]) Additionally, pre-incubation with the TAT-DEPV peptide (n=9) was effective in relieving the Cav3.2 inhibition ($p<0.001$ [ANOVA followed by Tukey's multiple comparison test]) whereas the current density of TAT-DEPE treated cells (n=9) remained significantly lower than the non-treated nNOS only cells ($p<0.005$ [Student's t-test]). The data in each experimental group was normalized to the L-NAME inhibited data set except for the data in the TAT-peptide data set which was normalized to the TAT-DEPV data set so that the degree of $Ca_v3.2$ inhibition could be compared to the L-NAME experimental group. (B) Normalized current-voltage (IV) profiles from HEK293H cells stably expressing $Ca_v3.2$ and transfected with nNOS and PSD-95 compared to nNOS transfection alone shows that PSD-95 did not significantly alter the IV relation. The error bars represent standard error.

Figure 2.10: The nNOS-mediated changes in peak current density are not the result of the direct action of L-NAME, TAT-DEPV or PSD-95 on $Ca_v3.2$

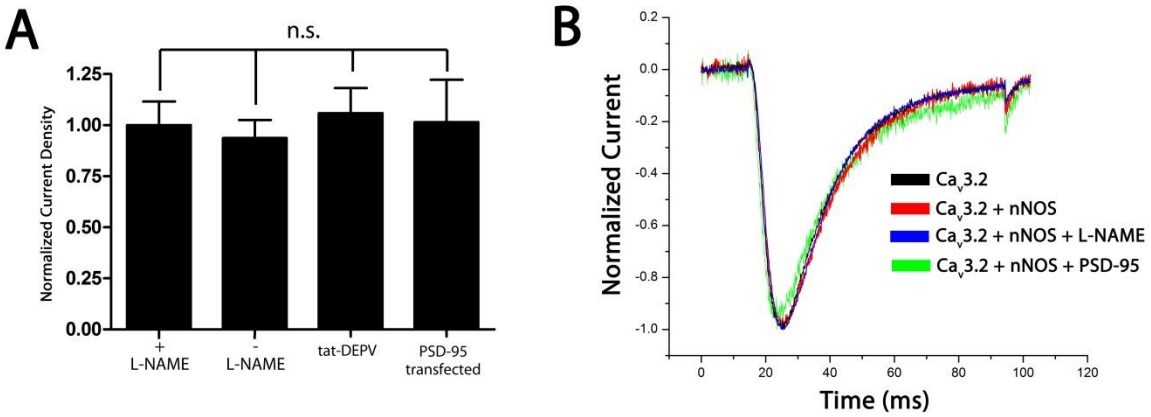

(A) To ensure that the various experimental conditions examined (L-NAME, TAT-DEPV and PSD-95) did not alter$Ca_v3.2$ channel activity directly, the T-type current density experiments were performed on non-transfected HEK293H cells stably expressing $Ca_v3.2$. Pre-incubating cells with L-NAME or TAT-DEPV peptide had no significant effect on the current density of the cells and neither did the transfection of PSD-95. All data sets were normalized to the L-NAME treated data set for comparison to the previous figures. The error bars represent standard error. (B) Representative traces of macroscopic $Ca_v3.2$ currents evoked at -30 mV. The traces are normalized and overlaid to demonstrate that the kinetics of the channel was not noticeably affected by the various treatments. ($p>0.05$ [Student's t-tests], n=[L-NAME=18, no l-NAME=32, tat-DEPV=9,PSD-95=5])

2.4. Discussion

2.4.1. $Ca_v3.2$ and nNOS physically and functionally interact in a heterologous system

This study presents the first evidence that the $Ca_v3.2$ T-type channel and nNOS can physically and functionally interact in a heterologous system. The results from the GST-fusion/immunoprecipitation experiments demonstrate that $Ca_v3.2$ channels and nNOS can physically interact. In support, deletion or mutation of the PDZ-3 binding motif located at the

carboxyl terminal of the $Ca_v3.2$ channel prevents the co-precipitation of nNOS. Together, these results indicate that the interaction occurs through the PDZ-3 binding ligand at the carboxyl terminus of $Ca_v3.2$. Intracellular Ca^{2+} concentrations are highly regulated, generally ranging from 10-100 nM under basal conditions. This tight regulation of intracellular concentration imposes limitations on Ca^{2+} signaling with the speed and magnitude of the signal being inversely proportional to the distance between the Ca^{2+} source and its target (reviewed in (Bootman and Berridge, 1995; Berridge et al., 1998; Augustine et al., 2003; Clapham, 2007)). A physical interaction between $Ca_v3.2$ and nNOS which anchors the Ca^{2+}-dependent nNOS near a Ca^{2+} source could have numerous important implications *in vivo*.

Functionally, the results from the NO-sensitive fluorometric assay show that depolarization of cells co-expressing $Ca_v3.2$ and nNOS stimulates the production of NO. Utilizing cells expressing $Ca_v3.2$ under an inducible promoter we further showed that chemical depolarization produced an increase in NO levels only when $Ca_v3.2$ channel expression had been induced and that the application of Ni^{2+} to block $Ca_v3.2$, precluded the production of NO. This result demonstrates that $Ca_v3.2$ activity is sufficient to stimulate NO production from co-expressed nNOS. Furthermore, and relevant to a negative feedback type of regulation, the NO produced by nNOS is sufficient to inhibit $Ca_v3.2$ activity as revealed by analysis of the T-type current density in cells co-expressing $Ca_v3.2$ and nNOS. The PDZ-3 mediated interaction between $Ca_v3.2$ and nNOS is required for a functional interaction to occur; disrupting the $Ca_v3.2$/nNOS interaction through point mutations in the $Ca_v3.2$ PDZ-3 binding ligand prevented an increase in fluorometric signal in the NO assay following depolarization. This result suggests that nNOS must be properly anchored to $Ca_v3.2$ for Ca^{2+} entering through the channel to effectively activate the enzyme. Consequently, nNOS expression has no effect on the T-type current density in $Ca_v3.2$ expressing cells when the

interaction is disrupted either through point mutation of the PDZ-3 binding ligand or after application of a peptide that competes for the PDZ-3 binding domain of nNOS.

Taken together the evidence demonstrates that a physical interaction between the $Ca_v3.2$ T-type channel and nNOS can occur in a heterologous system. Furthermore, a functional interaction wherein $Ca_v3.2$ activity stimulates nNOS to produce NO and which, in turn, feeds back inhibit $Ca_v3.2$ activity has also been shown to occur. A schematic summarizing the $Ca_v3.2$/nNOS interaction is presented Figure 2.11. This putative negative feedback circuit may potentially play an important role in regulating neuronal activity through the rapid modulation of $Ca_v3.2$ activity.

Figure 2.11: Schematic summarizing the proposed physical and functional interaction between $Ca_v3.2$ and nNOS

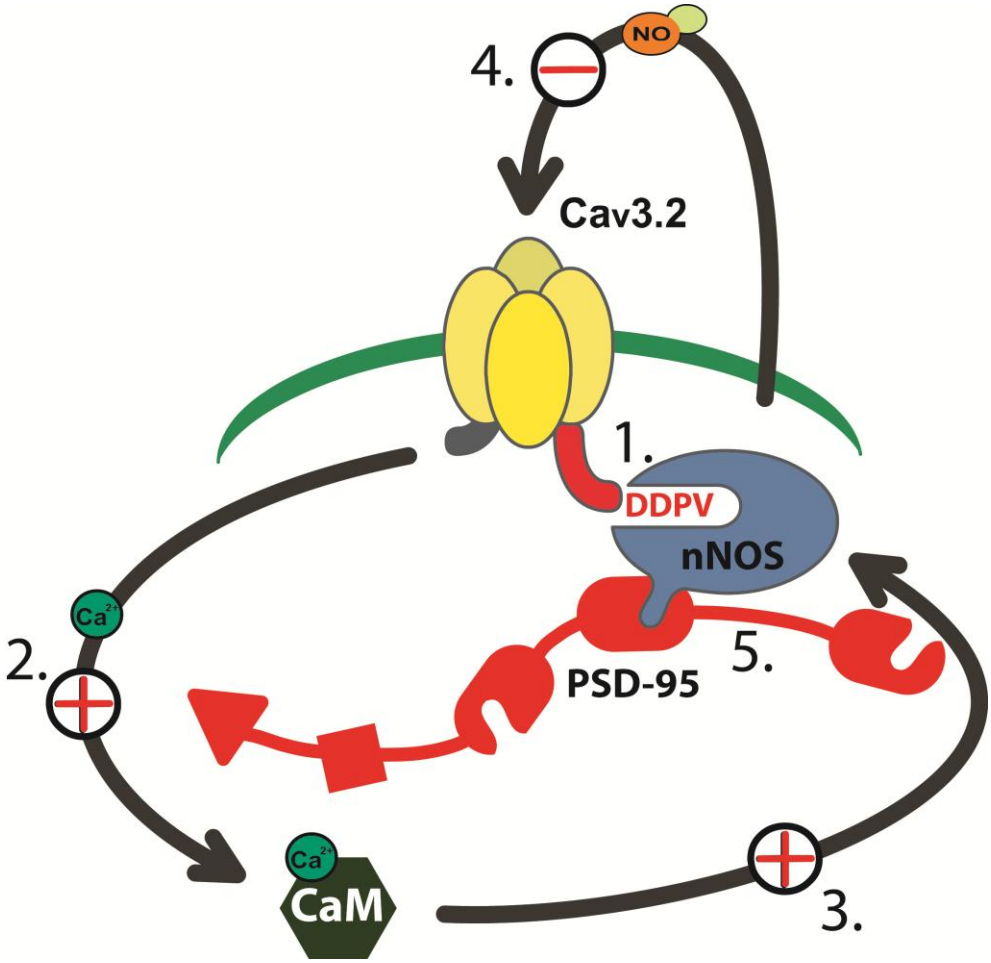

$Ca_v3.2$ and nNOS interact via a PDZ-3 binding ligand located at the carboxyl terminus of the $Ca_v3.2$ channel (1). Calcium influx from $Ca_v3.2$ activity is proposed to increase the local intracellular Ca^{2+} concentration and activate calmodulin (2) which binds to, and activates, nNOS. Once active, nNOS converts L-arginine to nitric oxide (NO) (3) which inhibits further $Ca_v3.2$ activity (4) through metal catalyzed oxidization of the H191 residue. nNOS possesses both a PDZ-3 domain and an internal PDZ-2 β-finger which can both be utilized to potentially facilitate the formation of larger complexes via interactions with PDZ-2 containing scaffold proteins such as PSD-95 (5).

2.4.2. nNOS can facilitate the formation of larger protein complexes

The results of this study suggest that the PDZ-3 domain and the PDZ-2 internal binding ligand of nNOS can be occupied simultaneously. The presence of PSD-95 facilitates the co-immunoprecipitation of nNOS which is in contrast to the work of Jaffery *et al*. who showed that a PDZ-2 mediated interaction between nNOS and PSD-95 is disrupted by the binding of CAPON to the PDZ-3 domain of nNOS (Jaffrey et al., 1998). It is possible that the binding of CAPON to nNOS introduces a specific allosteric inhibition or conformational change in the PDZ-2 internal binding ligand which disrupts the interaction between PSD-95 and nNOS. Support for our immunoprecipitation data can be found in the current density experiments wherein PSD-95 and nNOS were co-expressed in $Ca_v3.2$ expressing cells. We observed an additional inhibition of $Ca_v3.2$ activity in the presence of PSD-95 and nNOS which was evident by a significant reduction in T-type current density compared to effects of nNOS alone. It is possible that the binding of nNOS induces a conformational change in nNOS which increases the affinity of the $Ca_v3.2$/nNOS interaction and might explain the immunoprecipitation results. An increase in the affinity of the $Ca_v3.2$/nNOS interaction may also explain the increased $Ca_v3.2$ inhibition as a greater percentage of $Ca_v3.2$ channels could bind nNOS resulting in more $Ca_v3.2$ channels being inhibited by NO and resulting in reduced macroscopic currents. An alternative explanation may come from the multimerization of PSD-95 (Hsueh et al., 1997; Hsueh and Sheng, 1999; Keith and El-Husseini, 2008). In theory, a multimerized PSD-95 complex would be able to recruit several nNOS proteins which could potentially co-immunoprecipitate as a large unit. Additionally, the recruitment of multiple nNOS proteins to $Ca_v3.2$ could potentially increase the local NO concentration following Ca^{2+} influx; e.g., an increased NO level may increase the likelihood of metal

catalyzed oxidation of $Ca_v3.2$ resulting in a higher fraction of $Ca_v3.2$ channels being inhibited.

The internal PDZ-2 ligand of nNOS may facilitate the anchoring of $Ca_v3.2$ to scaffolding proteins such as PSD-95. The PDZ-2 domain is found in many scaffolding proteins (for review see (Hung and Sheng, 2002; Lee and Zheng, 2010)) as well other proteins such as α-syntrophin (Brenman et al., 1996a). A PDZ-2 mediated interaction may play a role *in vivo to* anchor the $Ca_v3.2$/nNOS complex to regions of the cell where it would be functionally relevant.

2.4.3. Inhibition of Cav3.2 does not involve the activation of soluble guanylyl cyclase

Soluble guanylyl cyclase is a well-documented target of NO. When activated, sGC catalyzes the conversion of GTP to cGMP, an important secondary messenger which has a number of downstream effectors including PKG, phosphodiesterases (PDE) and cyclic nucleotide-gated channels (Krumenacker et al., 2004; Domek-Łopacińska and Strosznajder, 2005; Kleppisch and Feil, 2009). In our current density analysis experiments utilizing ODQ we found that the inhibition of $Ca_v3.2$ currents through nNOS activity does not involve the activation of sGC. More likely, the mechanism of inhibition of $Ca_v3.2$ is through the metal catalyzed oxidization of the H191 residue of the $Ca_v3.2$ channel (Joksovic et al., 2007; Nelson et al., 2007a). Even though sGC appears not to be involved in the NO-mediated inhibition of $Ca_v3.2$, it is possible that the NO produced via the $Ca_v3.2$/nNOS complex may still activate this secondary messenger pathway. The consequences of activating sGC are difficult to predict as this depends upon the downstream effectors and targets expressed within a given cell type; however, it has been shown that the catalytic activity of nNOS can

be inhibited by PKG (Dinerman et al., 1994) which could function as a regulatory component in interaction between $Ca_v3.2$ and nNOS. Activation of the sGC/cGMP pathway has also been demonstrated to modulate several members of the VGCC family. L-type Ca^{2+} channels have been shown to be inhibited in Bovine chromaffin cells, rat insulinoma cells, and glomus cells of the rat carotid body (Grassi et al., 1999; Summers et al., 1999; Carabelli et al., 2002), N-type Ca^{2+} channels have been found to be inhibited in DRGs innervating the bladder of rats and in human neuroblastoma cells (Yoshimura et al., 2001; D'Ascenzo et al., 2002), whereas P/Q-type Ca^{2+} channels were demonstrated to be inhibited in rat insulinoma cells (Grassi et al., 1999) and augmented in the mouse medial nucleus of the trapezoid body (Tozer et al., 2012).

2.4.4. Potential implications of a Cav3.2/nNOS complex *in vivo*

Redox modulation of $Ca_v3.2$ channels has been shown to affect the excitability of nociceptive DRG neurons and to alter the response threshold to noxious stimuli in the rat neuropathic pain model. Of note, nNOS has also been found to be expressed in nociceptive DRGs suggesting that a $Ca_v3.2$/nNOS complex might contribute to the transmission and/or regulation of nociceptive signaling. Conceivably, activation of the $Ca_v3.2$/nNOS complex would allow for a rapid NO-driven response to excitatory input until the NO-mediated feedback inhibition of $Ca_v3.2$ reduced channel activity and either attenuated or dampened the signal. In this model, an initial nociceptive stimulus would invoke a rapid maximal response by activation of $Ca_v3.2$ channels, affecting both DRG excitability directly via Ca^{2+} influx and secondarily through nNOS activation to produce NO to then regulate various target effectors relevant to pain signaling.

Gain of function point mutations in the $Ca_v3.2$ channel have been associated with childhood epilepsy and other forms of idiopathic generalized epilepsy (Chen et al., 2003b; Heron et al., 2004; Khosravani and Zamponi, 2006; Peloquin et al., 2006; Vitko et al., 2007; Zamponi et al., 2009). Recently, a gain-of-function mutation in the $Ca_v3.2$ gene has been shown to segregate with the seizure phenotype in the Genetic Absence Epilepsy Rats of Strasbourg (GAERS). Further, the mutation affects the firing of nRT neurons in such a way that favours synchronous firing within the thalamocortical circuit (Powell et al., 2009). nNOS has been found to be developmentally expressed in the nRT of the ferret (McCauley et al., 2002) and it is possible that the transient expression of nNOS during development serves to add an inhibitory influence to the developing circuitry.

$Ca_v3.2$ and nNOS are co-expressed in a number of populations of neurons in the brain thus there are many potential areas of functional interaction. One notable region where both proteins are expressed is the olfactory bulb which is of interest since there is considerable plasticity involved in both learning new odours and in becoming desensitized to them over prolonged exposure (Kaba and Huang, 2005; Gao and Strowbridge, 2009). It is possible that a $Ca_v3.2$ and nNOS interaction may contribute to the synaptic plasticity of neurons in the olfactory bulb, although further investigation is required to fully understand any contribution of a potential $Ca_v3.2$/nNOS complex *in vivo*. The future consideration of the consequences of $Ca_v3.2$ inhibition on neuronal activity towards NO-regulated downstream effectors of cGMP would also be important to examine. In this regard, it may be necessary to first determine the contribution, if any, of sGC and to then study the effects of silencing both $Ca_v3.2$ and nNOS expression in relevant signaling pathways.

Chapter 3.

3. Disruption the $Ca_v3.2$ and nNOS interaction *in vivo* alters the respiratory response in Sprague Dawley rats

3.1. Introduction

Respiratory drive plays a crucial role in the initiation of inspiration in the respiratory cycle. A major source of respiratory drive comes from the carotid body in the peripheral respiratory network. Located at the bifurcation of the carotid artery, this major chemoreceptor is composed of two cell types: sustentacular type II glomus cells and chemosensory type I glomus cells that respond to changes in O_2 and CO_2 levels in the blood and sends modulatory signals via the carotid sinus nerve to the central respiratory network contributing to the regulation of overall respiratory activity (Figure 3.1A and B)The importance of this peripheral chemosensor has long been acknowledged and substantial progress has been made in the understanding of the transduction pathways and neurotransmitters involved in the processing of the afferent signals from the carotid body. Less is understood however, of the efferent modulation of the carotid body. Even though efferent innervation of this major peripheral chemoreceptor has long been identified, the complexities of this process have only recently begun to unfold (reviewed in (Campanucci and Nurse, 2007)).

Campanucci and coworkers have put forward a model for the NO-mediated efferent inhibition of carotid bodies by the microganglia of the GPN. In this model two mechanisms were proposed for the stimulation of nNOS activity: 1) that under hypoxic conditions the intrinsic O_2 sensing capability conferred by a halothane inhibitable K^+ channel related to the 2-pore domain inwardly rectifying TWIK potassium channels results in neuronal depolarization and increased neuronal excitability which in turn results in the activation of

the various VGCCs in the microganglia and consequently the stimulation of nNOS activity, and 2) that ATP released from type I glomus cells of the carotid body during hypoxia stimulates ionotropic purinergic P2X receptors of the microganglia to permit Ca^{2+} influx necessary to stimulate nNOS activity (Campanucci and Nurse, 2007).

Our data together with evidence put forward by others suggests that for optimal activation of nNOS, it should be localized near the source of Ca^{2+} responsible for stimulating NO production (Aarts et al., 2002). Whole cell Ca^{2+} currents in the microganglia of the GPN have been described including a Ni^{2+} sensitive T-type current which may represent $Ca_v3.2$ activity. These findings, in conjunction with our own regarding the $Ca_v3.2$ and nNOS interaction, present the possibility that $Ca_v3.2$ and nNOS may physically and functionally interact within the GPN microganglia and contribute the NO mediated inhibition of the carotid body.

I hypothesized that an interaction between $Ca_v3.2$/nNOS contributes to the NO mediated inhibition of the carotid body and that disruption of this interaction would result in an increase in the hypoxic response similar that observed both after the localized administration of NOS inhibitors (Gozal et al., 1996a) and in nNOS knockout mice (Kline et al., 1998). In the current study we investigate the effect of intraperitoneal administration of membrane permeable peptides designed to disrupt the $Ca_v3.2$/nNOS interaction on the hypoxic and hyperoxic response of Sprague Dawley rats.

Figure 3.1: Schematic summarizing the location and innervation of the carotid body

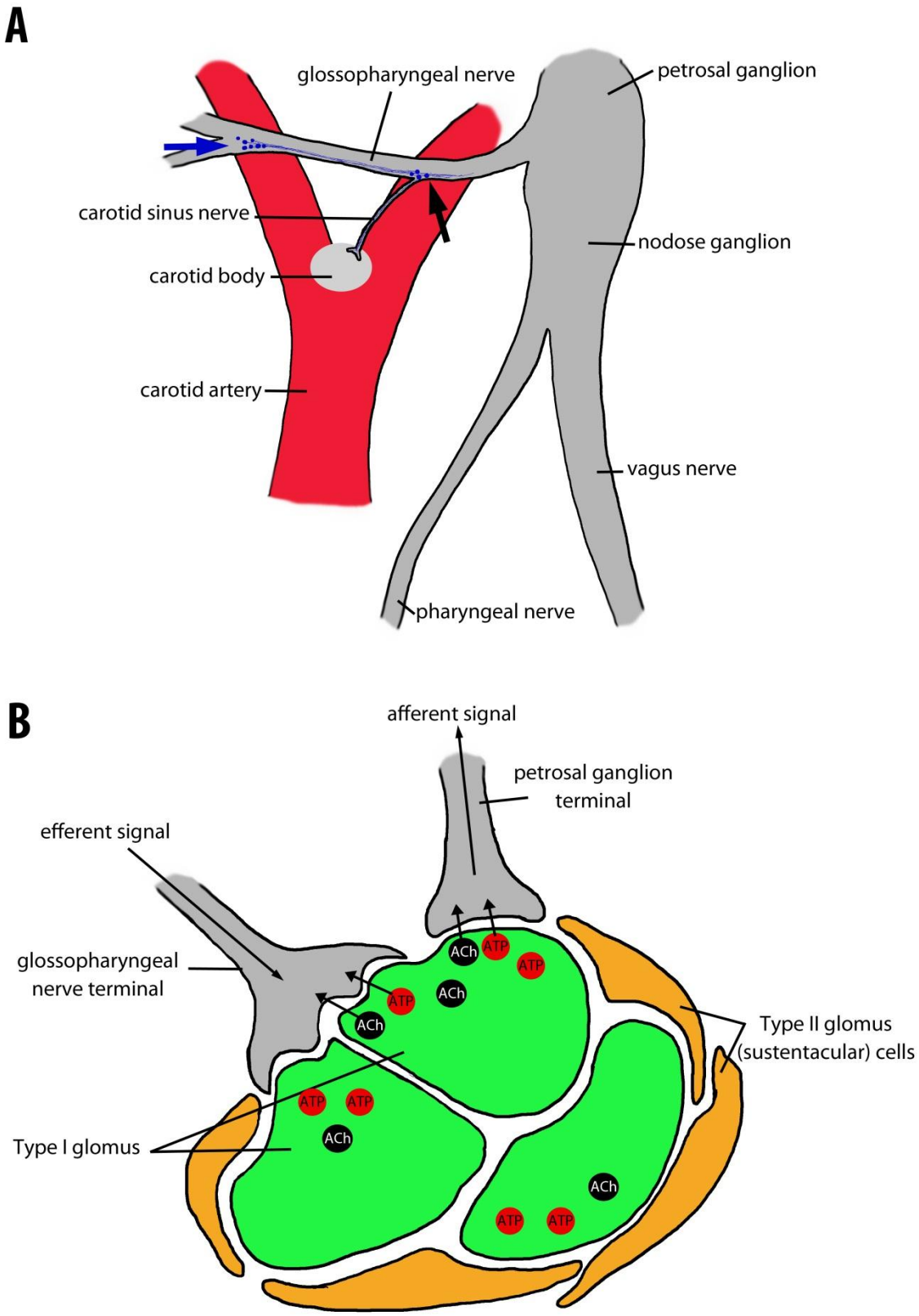

Figure 3.1: Schematic summarizing the location and innervation of the carotid body

(A)The carotid body is located in the bifurcation of the carotid artery and is innervated by the carotid sinus nerve which branches from the glossopharyngeal nerve. The nNOS expressing proximal (black arrow) and distal (blue arrow) microganglia both innervate the carotid body (Wang et al., 1993; Campanucci et al., 2003) and are connected through reciprocal projections. (B) Two types of cells make up the carotid body, the sustentacular type II glomus and the chemosensory type I glomus cells. Type I glomus cells receive efferent inhibition from microganglia in the GPN and send modulatory signals via the carotid sinus nerve to the CNS in response to changes in O_2 and CO_2 levels in the blood.

3.2. Materials and methods

3.2.1. Animal care

All experimental procedures involving animals and their care were performed in accordance with recommendations of the Canadian Council on Animal Care and the regulations and policies of the University of British Columbia Animal Care Facility and the University Animal Care Committee (Animal care certificate number: A10-0286). The 18 to 25 day old male Sprague Dawley rats utilized in this study were obtained from the University of British Columbia Animal Care Center, Vancouver, BC, Canada.

3.2.2. GPN dissection

The glossopharyngeal nerves (GPN) of 18 to 25 day old Sprague Dawley rats were isolated for quantitative real-time-PCR and immunohistochemical analysis. Isoflurane (Sigma-Alrich, St.Louis, MO, USA) was used to anaesthetize the animals and was delivered with an isoflurane vapourizer (VetEquip, Pleasanton, CA, USA) connected to a

polycarbonate chamber. Once sufficiently sedated (indicated by a failure to respond to the Toe-Pinch reflex test), the animal was painlessly sacrificed by decapitation using a guillotine. The head and neck were mounted ventral side up in a Sylgard filled petri dish and an incision was made in the skin to expose the trachea and hyoid bone which were carefully removed along with the surrounding muscle tissue to reveal the carotid arteries and vagus nerves. Muscle and fatty tissue were also removed to expose the tympanic bulla and the posterior lacerated foramen. To isolate the GPN the connective tissue along the carotid artery and vagus nerve was carefully removed as the structures were gently lifted and pulled anteriorly. Once the carotid bifurcation and nodose ganglion were free of the connective tissue they were lifted away from the posterior lacerated foramen by gently pulling posteriorly on the severed ends of the carotid artery and vagus nerve. Microscissors were used to cut blood vessels and nerves as distal from the carotid bifurcation and the nodose ganglion as possible and a scalpel was used to sever the nerves where they exited the posterior lacerated foramen. Once isolated, the carotid bifurcation, nodose ganglion and proximal tissues were placed in a dissecting dish filled with L-15 media (Invitrogen, Grand Island, NY, USA) where any remaining connective tissue was removed to expose the GPN. In dissections destined for quantitative real-time-PCR the GPN was cut from the petrosal ganglion and immediately frozen in liquid nitrogen for later processing. For immunohistochemical analysis, the GPN was left connected to the nervous tissue immediately adjacent which included the petrosal ganglion, the nodose ganglion and the proximal regions of the vagus, pharyngeal and superior laryngeal nerves.

3.2.3. Quantitative real-time-PCR

Quantitative real-time-PCR analysis was performed on a pooled sample of 26 GPNs dissected from 13 animals. The tissue was flash frozen in liquid nitrogen at the time of dissection and stored at -80 ^{o}C until needed for cDNA synthesis. RNA extraction was performed using the MagMAX-96 total RNA isolation kit (Invitrogen, Grand Island, NY, USA). The tissue was thawed and homogenized in 200 µl of TRI-reagent using a Dounce homogenizer. 20 µl of 1-bromo-3-chloro-propane was added to the homogenate and the mixture was allowed to incubate for 5 minutes at room temperature before being centrifuged at 12,000 x *g* for 10 minutes at 4 ^{o}C. After centrifugation, 100 µl of the aqueous phase was transferred to a 1.5 ml tube with 50 µl of isopropanol and mixed for one minute before being bound to 10µl of RNA binding beads for 3 minutes. The beads were washed twice with 150µl of wash solution and allowed to air dry before the RNA was eluted with 50 µl of elution buffer. cDNA synthesis was performed using a High-Capacity reverse transcriptase kit from Applied Biosystems/Invitrogen (Invitrogen, Grand Island, NY, USA).

The relative cDNA levels of each VGCC present in the GPN were determined using an Applied Biosystems 7500 Real-Time PCR System. Primers and Taman probes designed to amplify and quantitate the respective cDNA targets were purchased from Applied Biosystems/Invitrogen (Invitrogen, Grand Island, NY, USA). Analysis of the cDNA expression levels using each primer/probe set was run in triplicate and the expression levels were normalized to the housekeeping gene β-actin.

3.2.4. Immunohistochemistry

$Ca_v3.2$ (Santa Cruz Biotechnology: Santa Cruz, CA, USA: Cat-SC-16261), and nNOS (Santa Cruz Biotechnology: Santa Cruz, CA, USA: Cat-SC-5302), specific antibodies were

used to probe the GPN for immunohistochemical analysis. The GPN was dissected with the petrosal ganglion, nodose ganglion and proximal sections of the vagus, pharyngeal, and superior laryngeal nerves intact to provide a frame of reference for the mounted material. Additionally the nuclei were stained with DAPI and the preparation was probed with a choline acetyltransferase (ChAT) specific polyclonal antibody (Abcam, Toronto, ON, Canada: Cat-AB34419) as previous work has shown that the nNOS positive neurons of the GPN are cholinergic; expressing ChAT and vesicular acetylcholine transporter (Wang et al., 1993; Campanucci et al., 2003). Immediately after dissection the tissue was submersed in a 4% paraformaldehyde/PBS solution. After 4 hour incubation the nerves were washed for 5 minutes in 1ml PBS, flash frozen in liquid nitrogen for 3 seconds and thawed in PBS. The nerves were permeabilized and pre-blocked for 1 hour with a PBS solution containing 0.5% Triton X-100, 1% normal donkey serum and 0.25% BSA before application of the primary antibodies. Primary antibodies were diluted 1:400 in PBS with 1% normal donkey serum and 0.25% BSA and incubated with the nerves for 48 hours at 4° C on a rotator. After three 5 minute washes with 1 ml PBS, Alexa Fluor (Invitrogen, Grand Island, NY, USA) or DyLight Fluor (Fisher Scientific, Ottawa, ON, Canada) conjugated secondary antibodies were diluted 1:400 and 4',6-diamidino-2-phenylindole (DAPI) was diluted 1:300 in PBS with 1% normal donkey serum and 0.25% BSA and incubated with the tissue for four hours at room temperature. A final three washes with PBS were performed and the nerves were whole mounted on slides with Vectashield mounting media (Fisher Scientific, Ottawa, ON, Canada) and sealed with nail polish. An Olympus Fluoview 10i confocal microscope was utilized to acquire images from the preparations. A 60x oil immersion objective with a numerical aperture of 1.35 was used to acquire the images. Within the software image quality was set to

8x with 1024x1024 pixels and an aperture setting of 2.5x. Typically the laser intensity was kept at 25% or lower and the sensitivity maintained at approximately 45%.

3.2.5. Design of the TAT fusion peptides

The protein transduction domain of the Human Immunodeficiency Virus 1 TAT protein (Green and Loewenstein, 1988) is able to mediate the transport of heterologous proteins across the cell membrane (Fawell et al., 1994). TAT fusion proteins have been shown to be able to transduce functional proteins into a variety of tissues including neuronal tissue (Schwarze et al., 1999; Cao et al., 2002). Additionally TAT fusion peptides have been used *in vivo* to competitively disrupt protein interactions such as the interaction between the NMDA receptor and PSD-95 (Aarts et al., 2002). The TAT fusion peptides were ordered from Genscript (Piscataway, NJ, USA) and contained the protein transduction domain of the human immunodeficiency Virus 1 transactivator of transcription (TAT) protein (YGRKKRRQRRR) fused with the last 9 amino acids of the rat $Ca_v3.2$ sequence (PDDSG**DEPV)** which possess a carboxyl terminal PDZ-3 binding ligand. A TAT-fusion peptide with a mutation in the Cav3.2 PDV-3 binding ligand (PDDSG**DEPE**) and a peptide with just the TAT sequence were also ordered. The peptides were injected at a concentration of 9 mg/kg (~3.6μmoles/kg for the TAT fusion peptides and 5.6 μmoles/kg for the TAT control) as it was the highest level of TAT peptide injection that we could find in the literature that did not appear to have adverse effects (Cao et al., 2002).

3.2.6. Respirometry

The experimental setup is illustrated in Figure 3.2. A Cameron Instruments gas-mixing flow meter (Cameron Instruments, Brownsville, TX) was used to mix pure gases and

deliver 100%, 21% and 12% oxygen (O_2) with the balance comprised of nitrogen. The air mixtures were bubbled through water to humidify the mixture and sampled continuously to monitor the O_2 concentration with a galvanic O_2 sensor. The single mixed airline was split to provide air to two identical 500 ml plethysmograph chambers; an experimental chamber where the animal was placed and a reference chamber. A differential pressure transducer (DP103) (Valydine, Northridge, CA,USA) with a #06 diaphragm and a CD16 carrier demodulator (Valydine, Northridge, CA,USA) was used to measure the pressure differential between the two chambers generated by the ventilation of the animal (Malan, 1973; Jacky, 1978). A Gould DC amplifier was used to amplify the signal from the pressure transducer and to provide low pass filtering at 5 Hz. The post-chamber gases were analyzed for carbon dioxide (CO_2) using a non-dispersing infrared sensor and a second O_2 sensor was plumbed so that same sensor could be utilized to obtain post-chamber oxygen values and pre-chamber values to be used to calculate oxygen consumption. The air flow measurements were obtained using a Fleisch Pneumotachograph connected to a differential pressure transducer with a #14 diaphragm and a CD16 carrier demodulator (Valydine, Northridge, CA, USA). A Gould integrator was utilized to provide signal gain. All data were digitized with a DATAQ model DI-205 digitizer and acquired with Windaq software version Pro+ DI-720 at a sample rate of 166.66 Hz per channel using a personal computer running Microsoft Windows XP.

The animals were kept in the transport container undisturbed for 30 minutes after delivery to allow for acclimatization to the laboratory before proceeding with the experiments. An intraperitoneal injection of one of the TAT-fusion peptides (TAT-DEPV, TAT-DEPE or TAT-0) was administered at a dose of 9 mg/kg immediately prior to placing the animal within the plethysmograph chamber. A minimum of 15 minutes was provided for acclimatization to the chamber with a gas mixture of 100% O_2 with a flow rate of 400

ml/min; if the respiratory parameters did not stabilize within the 15 minute period additional time was allowed. Before each respiratory response test the chamber was purged at 2000 ml/min for 7 minutes with the O_2 percentage required for the subsequent test. For example: in the 100% O_2 test, the chamber was purged for 7 minutes with 100% O_2 and then the respiratory response of the animal was measured at 100% O_2 with 400 ml/min flow for 7 minutes. The testing procedure consisted of measuring the respiratory responses at 100%, 21% and 12% O_2. This was followed by a hyperoxic transition test (Dejour's test) which consisted of a 10 minute purge of 100% O_2, followed by a conditioning phase of 12% O_2 at 2000 ml/min for 10 minutes and a test phase of 100% O_2 at 2000 ml/min for 5 minutes. A second round of tests was performed after a 10 minute purge at 100% O_2. A graphical representation of the protocol can be seen in Figure 3.3. After completion of the test procedures the animals were anaesthetized and painlessly sacrificed by decapitation per recommendations of the Canadian Council on Animal Care and the regulations and policies of the University of British Columbia Animal Care Facility and the University Animal Care Committee (Animal care certificate number: A10-0286)

Figure 3.2: Experimental set-up used to acquire the respirometry and metabolic data

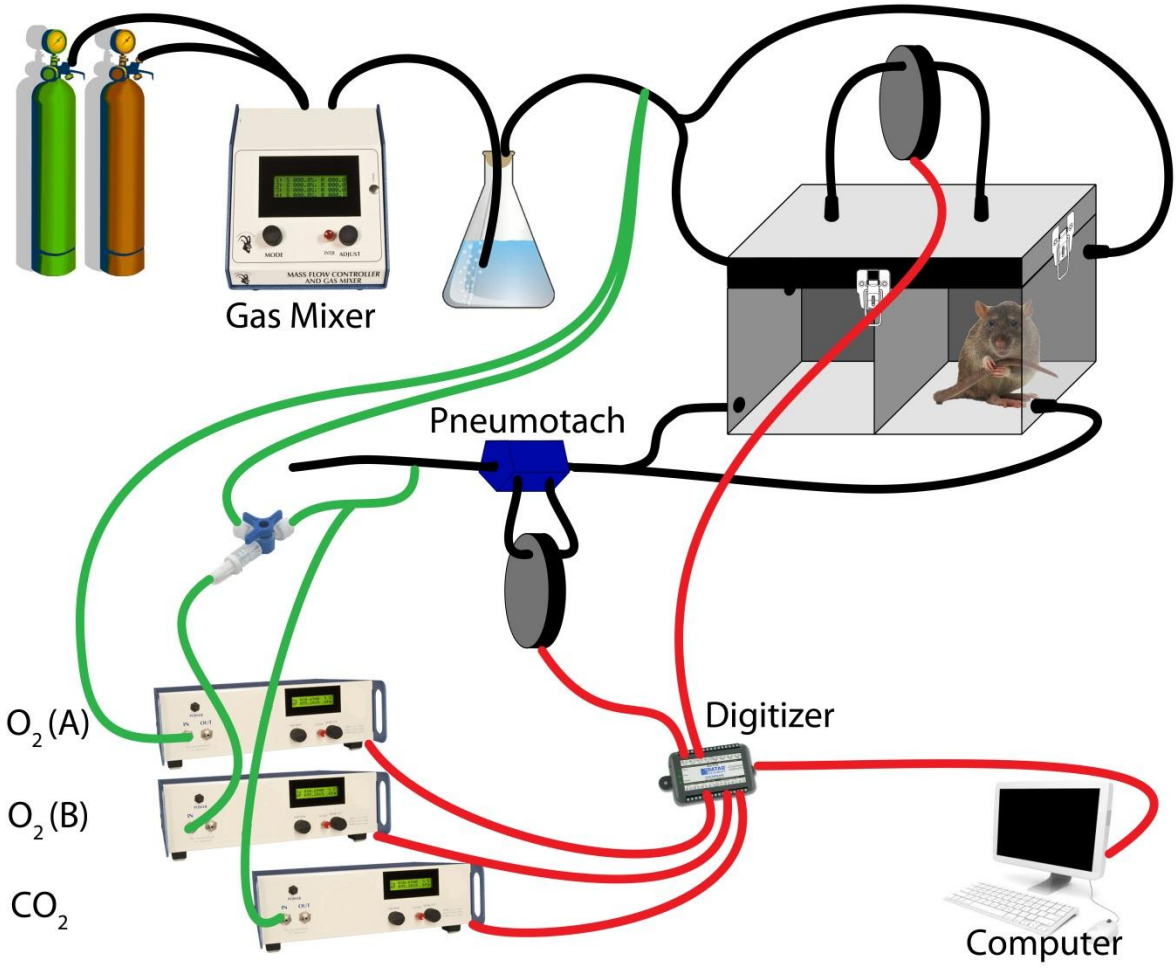

Figure 3.2: Experimental set-up used to acquire the respirometry and metabolic data

Pure oxygen and nitrogen were mixed using a gas mixer to produce 100%, 21% or 12% O_2 with balance nitrogen. The mixed gas was humidified by bubbling through water in an Erlenmeyer flask and the flow was split to feed both sides of the plethysmograph chamber. The respiratory rate and tidal volume were calculated from the pressure difference in the air between the animal half and the reference half of the chamber. A pneumotach connected to a differential pressure transducer was used to monitor the flow rate of the gas. To ensure the appropriate O_2 concentrations were being mixed an oxygen sensor sampled the gas mixture before the chamber. A second oxygen sensor was utilized to take readings pre-chamber and post-chamber to determine O_2 consumption. CO_2 production was measured post-chamber using a CO_2 sensor. All the data was digitized, recorded and stored on a computer for analysis.

Figure 3.3: Graphical representation of the respirometry protocol

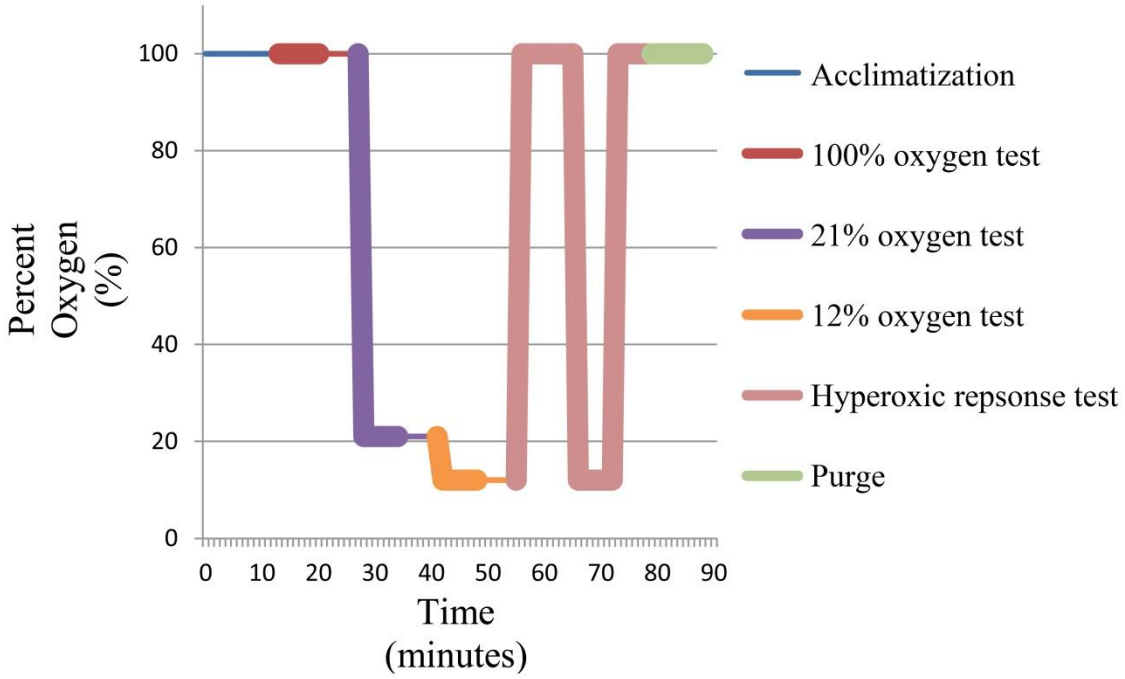

Figure 3.3: Graphical representation of the respirometry protocol

The respirometry protocol represented as percent oxygen over time. Thick lines represent a flow rate of 2000 ml/min and thin lines represent 400 ml/min flow rate.

3.2.7. Analysis of respirometry data

For each respiratory response test a 15 second window of data from as late in the testing period as possible was obtained from the acquired data using the Windaq software and saved in CSV format. Microsoft Excel was used to open the CSV file and transfer the data into Origin software version 8. Care was taken to ensure that the animal was settled but not sleeping during the period taken for analysis. The ventilation pattern during sleep could be determined visually and compared to notes taken during the experiment to determine if the animal was sleeping. Indicators that the animal was unsettled were sniffing (sharp repetitive spikes in the ventilation data) and fluctuations in the CO_2 recordings indicative of animal movement such as pacing or scratching. The respiratory rate (inspirations/min) was calculated by counting the number of inspirations on the graph, multiplying by 60 (seconds/min) and dividing by the number of seconds between the peak of the first inspiration and the last inspiration. Tidal volume was calculated using the following formula (Jacky, 1980):

$$\mathbf{V_t = \{(P_m \times V_{cal} \times T_b(P_b - P_{cH2O})) / (P_{cal} \times [T_b(P_b - P_{ch2o}) - T_c(P_b - P_{aH2O})])\} / \{[1-T_i/T_{tot}(1 - G_a/G_n)]\}}$$

V_t= Tidal volume corrected for partial pressure of water at the given barometric pressure

V_{cal}= Volume used to calibrate the equipment

P_m= Observed pressure reading

P_b= Barometric pressure (mm Hg)

P_{cal}= Pressure reading observed from input of calibrated volume

P_{cH2O}= Water vapour pressure in chamber based on ambient temperature from table (Dejours, 1988)

P_{aH2O}= Water vapour pressure based on alveolar temperature of animal (Dejours, 1988)

T_b= Absolute temperature of alveoli (310.5K) (Jacky, 1980)

T_c= Absolute temperature of the chamber

T_i= Duration of inspiration

T_{tot}= Total breath duration

G_a= Constant defined as = $[T_b * (P_b - P_{cH2O})] / [T_b * (P_b - P_{cH2O}) - T_c * (P_b - P_{aH2O})]$

G_n= Constant defined as = $[T_b * (P_b - P_{nH2O})] / [T_b * (P_b - P_{nH2O}) - T_n * (P_b - P_{aH2O})]$

P_{nH2O}= Water vapour pressure based on nasal temperature from table (Dejours, 1988)

T_n=Absolute temperature at the nose (301.8K) (Jacky, 1980)

During acquisition the baseline tended to drift from center depending on movements from the animal, therefore the inspiration time and total breath duration had to be calculated manually. To facilitate data collection I compiled a short script for Origin 8 that allows the manual selection of data points and the automatic recording of the x and y coordinates to a temporary spreadsheet. The script has been submitted to the file exchange on the Originlab website (http://www.originlab.com/fileexchange/details.aspx?fid=137) and to date it has been downloaded 585 times. The full script is as follows:

```
del r1;
del r2;
del datatemp;
```

```
create datatemp -c 150;
define EndToolBox
{
create tempor -wn 2 Xaxis Yaxis;
range [tempor]Sheet1 r1=Col(Xaxis), r2=Col(Yaxis);
r2 = datatemp;
r1 = datatemp_A;
};
getpts -n datatemp 60;
```

Using this script the peak values and the baseline for each inspiration were identified and recorded. The time points of initiation and cessation of inspiration as well as the conclusion of expiration were recorded and used to determine the inspiration duration and the total breath duration.

The data for the hyperoxic response test was transferred to Origin 8 software in the same manner as the respiratory response data. The data collection script mentioned above was used to locate the peak of every inspiratory event within a 2 minute window starting from the switch from 12% O_2 to 100% O_2. The data was filtered for sniffs and animal movement such and scratching using the two criteria. Periods of sniffing and scratching were compared to quiescent periods to determine the criteria to filter sniff and scratching events. The nominal respiratory rate of rats is approximately 90 breaths per minute and the maximum respiratory rate approximately 170 breaths per minute (Gozal et al., 1996b; Subramanian et al., 2002). We observed that the peak to peak interval during sniff and scratch event was considerably less than regular breathing and setting a maximum of 200 breaths per minute was sufficient to filter sniffs and scratching events lasting longer than 600

ms. For sniff and scratch events lasting less than 600 ms it was determined that sniffs and scratches could be identified by a disproportionate decrease in the peak to peak interval compared to the preceding three peaks; a factor of 1.6x was sufficient to exclude the majority of sniffs and scratches lasting less than 600ms from the data. Once collected and filtered a rolling average of four events was calculated and normalized to the respiratory rate at the 10 second mark. The ten second mark was chosen as the normalization point as it was at this point that O_2 concentration started to increase; the delay in the increase was due to the dead space volume present in the tubing and the chamber of the experimental setup. For each experimental group the timelines were synchronized, divided in to 0.75 second intervals and the average respiratory rate for each animal within every interval calculated. Finally, the respiratory rates of each 0.75 s interval for all the animals in the experimental group were averaged together and plotted.

3.3. Results

3.3.1. $Ca_v3.2$ is expressed in nNOS expressing microganglia within the GPN of Sprague Dawley rats

Campanucci and colleagues originally characterized whole cell currents in acute preparations of microganglia in the GPN of rats (Campanucci and Nurse, 2007). Pharmacological dissection of the VGCC currents revealed that all VGCC classes are represented in these neurons including those for T-type channels. Since antagonists capable of differentiating the three Ca_v3 channels are not available, the specific T-type isoforms expressed within the microganglia of the GPN were not identified. However, in finding that Ni^{2+} at 100 μM resulted in current blockade suggests that the T-type currents are most likely due to the Ni^{2+}-sensitive $Ca_v3.2$ channel (rather than the $Ca_v3.1$ and $Ca_v3.3$ channels which

have Ni^{2+} IC_{50}s of ~250 μM and ~215 μM, respectively). Figure 3.4 shows that based on quantitative real-time PCR, mRNAs for the $Ca_v2.1$ (P/Q-type) and $Ca_v2.2$ (N-type) channels are the most abundant occurring at significantly higher levels ($p<0.05$) than those for the other VGCCs. $Ca_v1.2$, $Ca_v1.3$ (L-types), $Ca_v2.3$ (R-type) and $Ca_v3.2$ (T-type) mRNAs were also detected; however the levels were low compared to those of $Ca_v2.1$ and $Ca_v2.2$. Together, all of the VGCCs giving rise to the currents detected by Campanucci and colleagues (Campanucci and Nurse, 2007) are represented in the quantitative Real-Time PCR analysis. In comparing $Ca_v3.1$, $Ca_v3.2$ and $Ca_v3.3$ T-type mRNA expression, Figure 3.4B shows that the level of mRNA for $Ca_v3.2$ is significantly greater ($p<0.05$) than either that for $Ca_v3.1$ or $Ca_v3.3$ and which corresponds with well with the pharmacological data (Campanucci and Nurse, 2007).

Further evidence for the presence of the $Ca_v3.2$ T-type channel in the microganglia of the GPN is revealed using immunohistochemical staining. Whole nerve preparations of the GPN were probed with $Ca_v3.2$, nNOS and ChAT specific antibodies. A low magnification image of a whole nerve mount is displayed in Figure 3.5A. The petrosal ganglion, GPN and carotid sinus nerve are labeled and the locations of the high magnification confocal images are indicated with arrows (1. = Proximal, 2. = Distal). Figure 3.5B shows high magnification confocal images of neurons within the microganglia of the proximal (1.) and distal (2.) regions of the GPN. In these representative images it can be seen that $Ca_v3.2$ staining can be found in the neurons that comprise the microganglia of the GPN and the merged images show that a subset of these neurons also express nNOS. A ChAT-specific antibody was used as a marker for cholinergic neurons as previous work indicated that the nNOS positive microganglia also stained positive for the vesicular acetylcholine transporter and ChAT (Wang et al., 1993; Campanucci et al., 2003). All neurons within the regions of interest

stained positive for ChAT indicating that they are the microganglia identified by Camanucci and colleagues. The co-expression of $Ca_v3.2$ and nNOS in these microganglia presents the possibility that a $Ca_v3.2$/nNOS functional interaction exists within these cells.

Figure 3.4: qRT-PCR analysis illustrating the Ca^{2+} channel expression profile in the glossopharyngeal nerve (GPN) in Sprague Dawley rats

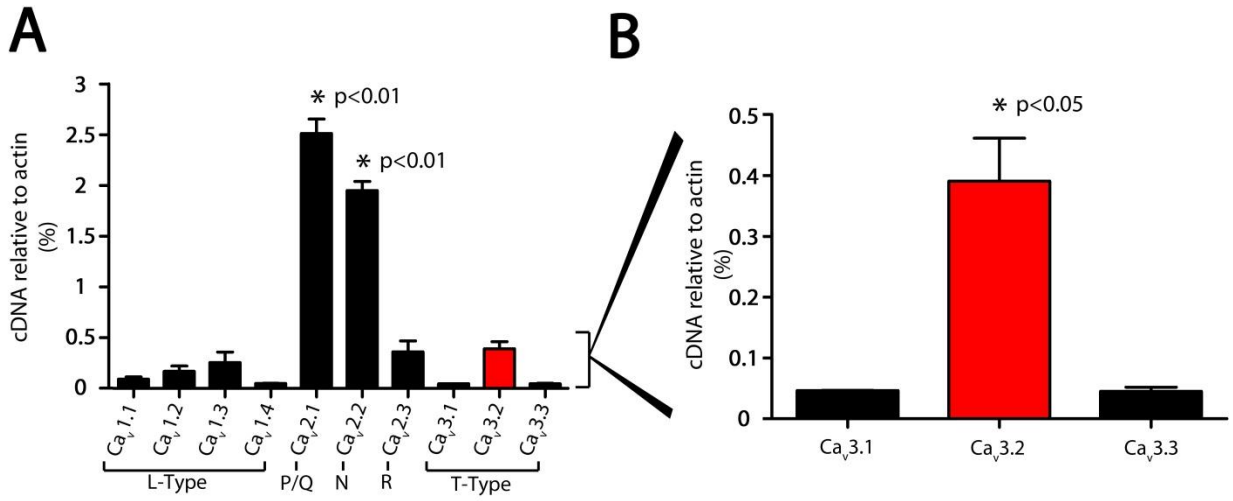

A 3.5 mm to 4 mm segment encompassing the proximal and distal microganglia of the GPN was harvested from 16 Sprague Dawley rats (P18 to P25). qRT-PCR oligos specific for each Ca^{2+} channel were used to amplify cDNA generated from RNA extracted from the pooled GPNs. The values were normalized to actin B expression. (A) Full Ca^{2+} channel expression profiles for the GPN of Sprague Dawley rats shows the L-, P/Q-, N-, R- and T-type isoforms expressed in rat GPN. Expression levels for the $Ca_v2.1$ and $Ca_v2.2$ are both significantly higher than the other VGCCs ($p<0.01$ [ANOVA followed by Tukey's multiple comparison test]) (B) Scaled up view of the T-type channel transcript profile illustrating that $Ca_v3.2$ is the predominant T-type channel isoform present in the glossopharyngeal nerve with approximately 8x greater abundance compared to the other T-types ($p<0.05$ [ANOVA followed by Tukey's multiple comparison test]). The error bars represent standard error.

Figure 3.5: Immunohistological staining of $Ca_v3.2$, nNOS and ChAT in the microganglia of the glossopharyngeal nerve of Sprague Dawley rats

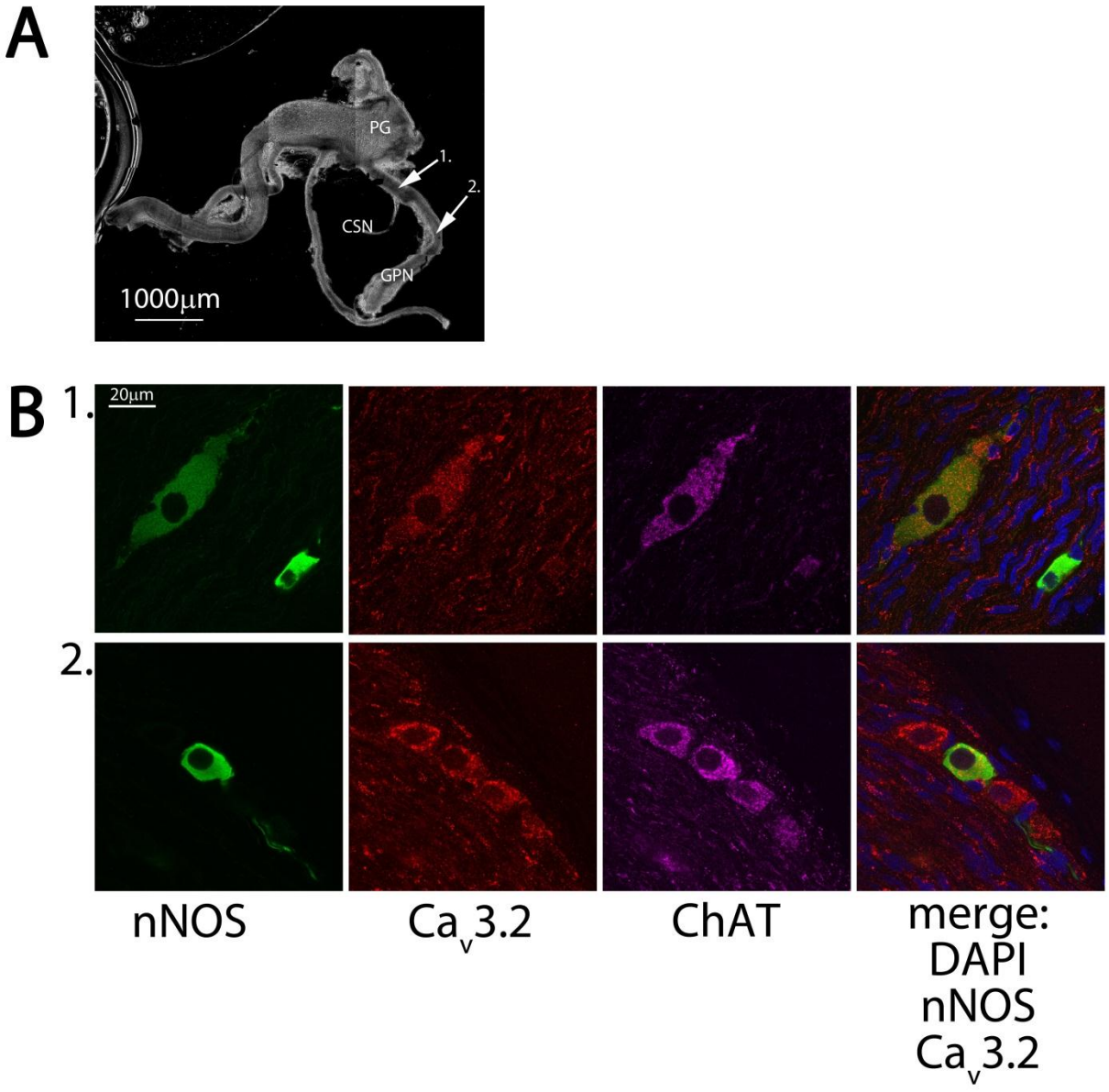

Figure 3.5: Immunohistological staining of $Ca_v3.2$, nNOS and ChAT in the microganglia of the glossopharyngeal nerve of Sprague Dawley rats

The glossopharyngeal nerve of Sprague Dawley rats was isolated, probed with $Ca_v3.2$, nNOS, ChAT specific antibodies and DAPI and whole mounted on a slide for confocal analysis. (A) 10x phase contrast scan of the mounted nerve with the petrosal ganglion (PG), glossopharyngeal nerve (GPN) and carotid sinus nerve (CSN) labeled. Images were acquired of the microganglia located proximal (1.) and distal (2.) to the bifurcation to the CSN. (B) representative 60x confocal images of neurons within the proximal (1.) and distal (2.) microganglia of the GPN showing nNOS (green), $Ca_v3.2$ (red) and ChAT (purple) expression. The choline acetyltransferase was used as a marker for the microganglia (purple) (Wang et al., 1993; Campanucci et al., 2003). Many of the microganglia express both $Ca_v3.2$ and nNOS although some express one and not the other (e.g., those illustrated in set 2 in panel B).

3.3.2. Disruption of the $Ca_v3.2$/nNOS interaction *in vivo* results in an augmented steady state response to hypoxic challenges

Systemic administration of a TAT-fusion peptide designed to bind to the PDZ-3 domain of nNOS and competitively disrupt the $Ca_v3.2$/nNOS interaction resulted in an augmented steady state response to hypoxic challenges. Figures 3.4, 3.5 and Table 3.1 illustrate the effect of intrathecal injection of the PDZ-3 binding peptide TAT-DEPV or the mutant non-binding peptide TAT-DEPE versus control experiments consisting of administration of a peptide containing only the TAT sequence.

No significant difference in the respiratory rate under hyperoxic (100% O_2) or normoxic (21% O_2) conditions was observed between any of the experimental groups (Figure 3.6A and Table 3.1). Under hypoxic (12% O_2) conditions the respiratory rate of all groups was significantly higher ($p<0.05$) compared to the hyperoxic and normoxic conditions. The

increase in the respiratory rate in the TAT-DEPV treated animals was modestly, but not significantly, higher than that in the TAT peptide control animals and the non-disrupting peptide treated animals (Figures 3.4B, 3.4C and 3.4D). No significant change in the respiratory rate was observed between the hyperoxic and normoxic conditions in any group (Figure 3.6B), which is expected as neither condition is anticipated to increase respiratory drive. In contrast, there was a considerable increase in the respiratory rate of the TAT-DEPV treated animals compared to the controls when comparing the normoxic to hypoxic steady state respiratory rate (Figure 3.6C). This increase was also significantly greater ($p<0.05$) than that seen in the non-disrupting TAT-DEPE treated group but not compared to the TAT-only control group. This result is comparable to that seen in nNOS inhibited (Gozal et al., 1996b) and nNOS knockout mice (Kline et al., 1998) wherein significant differences in respiratory response were observed in response to changes in the available oxygen when nNOS activity was absent. When comparing the two extremes, hyperoxia to hypoxia (Figure 3.6D), the response in the TAT-DEPV treated group was significantly greater than that in the TAT-only and the TAT-DEPE treated animals ($p<0.05$) and this is also in agreement with the data from the nNOS knockout mouse study of Kline *et al*. (1998).

Hypoxia produced a significant increase in tidal volume in the TAT and TAT-DEPV treated animals but not in the TAT-DEPE treated group (Figure 3.7A). Correspondingly, the total ventilation increased significantly ($p<0.05$) in the TAT peptide and TAT-DEPV groups in 12% O_2 compared to 100% O_2 and 21% O_2 but not in the TAT-DEPE treated animals (Figure 3.7B).

Given the slightly greater increases observed in the respiratory rate (Figure 3.6A) and tidal volume (Figure 3.7A) of the TAT-DEPV treated animals under hypoxic conditions (summarized in Table 3.1) it was anticipated that the total ventilation under hypoxia

(Respiratory rate * Tidal Volume) would be significantly greater in the TAT-DEPV treated group compared to TAT treated control animals. As observed from Figures 3.5D, however, even though the total ventilation on 12% O_2 was higher in the TAT-DEPV treated group, it still was not significantly greater than the responses of the TAT and TAT-DEPE treated groups (Figure 3.7D and Table 3.1). In contrast to data from nNOS knockout mice which display a significantly higher tidal volume under normoxic conditions compared to wild type mice (Kline et al., 1998), in the current study no significant difference was observed in the tidal volume or total ventilation under normoxic conditions between the TAT-DEPV treated group and the TAT control group. Interestingly, the TAT-DEPE injected animals displayed a significantly greater ($p<0.05$) tidal volume in 100% O_2 and 21% O_2 compared to the TAT and TAT-DEPV animals (Figure 3.7C and Table 3.1) and this translated into a significantly greater total ventilation ($p<0.05$) (Figure 3.7D and Table 3.1). The increased tidal volume at 100% and 21% O_2 measured in the TAT-DEPE animals likely explains why no significant difference was observed in this group when the total ventilation under hyperoxic, normoxic and hypoxic conditions were compared.

Oxygen consumption and carbon dioxide release are directly related to metabolic rate. When considering the hyperoxic, normoxic, and hypoxic conditions we observed that expired CO_2 was greatest under hypoxic conditions and least under normoxic conditions with expired CO_2 levels under hyperoxic conditions falling in between; a pattern that was consistent across all three groups. However, the differences were not statistically significant between the TAT, TAT-DEPV, and TAT-DEPE groups (Table 3.1). These results contrast with the nNOS knockout mice of Kline's study which report a significant decrease in the expired CO_2 under hypoxic conditions compared to hyperoxic conditions. Oxygen consumption at 100% O_2 was slightly, but not significantly increased in the TAT-DEPV group which is comparable

to the Kline *et al.* study. Unfortunately, observed O_2 consumption at 21% and 12% O_2 concentrations was deemed inaccurate since the values were physiologically improbable, a finding discovered during analysis after the data had been collected. The most probable explanation for the erroneous O_2 values is a flaw in the chamber design which allowed the 100% O_2 purge air to become trapped which then escaped sporadically during the testing phase which artificially inflated the O_2 readings for the 21% and 12% O_2 tests. The air convection requirement (ACR) was calculated assuming a respiratory quotient of 1.0. For the TAT-DEPV and TAT groups the ACR was significantly greater ($p<0.05$) at 12% O_2 compared to 21% and 100% O_2. No significant difference was observed between the groups when comparing the ACR at 100%, 21% and 12% O_2.

Table 3.1: Summary of the respirometry responses from TAT-control, TAT-DEPV and TAT-DEPE injected animals

$\%O_2$ (balance N_2)	Injection	Respiratory Rate (breath/ min)	Tidal Volume (V_t) ($\mu l/g_{[BW]}$)	Total Ventilation (V'_E) ($\mu l/g_{[BW]}$/ min)	CO_2 production (ml/min/ $g_{[BW]}$)	O_2 Consumption (ml/min/ $g_{[BW]}$)	Air Convection Requirement (ventilation / metabolism) (ml/ml)
100%	tat injected (n=12)	113.3 +/- 3.43	7.83 +/- 0.35	882.7 +/- 39.13	0.0334 +/- 0.0023	0.0379 +/- 0.0033	28336 +/- 2612
	tat-DEPV injected (n=12)	111.3 +/- 4.55	8.08 +/- 0.55	909.2 +/- 85.39	0.0329 +/- 0.0013	0.0480 +/- 0.0072	29478 +/- 2354
	tat-DEPE injected (n=10)	117.0 +/- 3.46	9.79 +/- 0.61 [2]	1141 +/- 72.28 [4]	0.0351 +/- 0.0025	0.0342 +/- 0.0216	33937 +/- 3198
21%	tat injected (n=12)	115.4 +/- 4.36	7.35 +/- 0.37	853.2 +/- 62.69	0.0320 +/- 0.0016	N/A	27350 +/- 3184
	tat-DEPV injected (n=12)	116.3 +/- 4.56	7.27 +/- 0.50	855.6 +/- 81.47	0.0301 +/- 0.0018	N/A	29376 +/- 2338
	tat-DEPE injected (n=10)	121.1 +/- 3.23	8.96 +/- 0.67 [2]	1090 +/- 92.07 [4]	0.0331 +/- 0.0022	N/A	34527 +/- 3350
12%	tat injected (n=12)	137.3 +/- 4.65 *	8.61 +/- 0.36 [1]	1173 +/- 45.77 [3]	0.0309 +/- 0.0020	N/A	39724 +/- 2037[5]
	tat-DEPV injected (n=12)	147.8 +/- 4.01 *	9.06 +/- 0.59 [1]	1350 +/- 109.1 [3]	0.0297 +/- 0.0017	N/A	50052 +/- 4124[5]
	tat-DEPE injected (n=10)	137.4 +/- 3.71 *	9.53 +/- 0.55	1305 +/- 75.43	0.0324 +/- 0.0020	N/A	40447 +/- 2332[5]

Table 3.1: Summary of the respirometry responses from TAT-control, TAT-DEPV and TAT-DEPE injected animals

The average respiratory rate, tidal volume, O_2 consumption and CO_2 production were measured directly during the experiment. Total ventilation (respiratory rate * tidal volume) and the respiratory quotient (CO_2 produced/ O_2 consumed) were calculated from the measured variables. (*) The average respiratory rate on 12% O_2 was significantly higher than the rate at 100% or 21% O_2 for all three groups ($p<0.001$ [ANOVA followed by Tukey's multiple comparison test]). ([1]) Average tidal volume in the TAT-0 and TAT-DEPV treated animals was significantly greater at 12% O_2 however the TAT-DEPE treated animals were not ($p<0.05$ [Student's t-test]). ([2]) The tidal volume of the TAT-DEPE treated animals was significantly greater than the TAT-0 and TAT-DEPV treated animals at 100% and 21% O_2 ($p<0.05$ [Student's t-test]). ([3]) Total ventilation of the TAT-0 and TAT-DEPV injected animals was significantly greater at 12% compared to 21% and 100% O_2 ($p<0.05$ [Student's t-test]). ([4]) Total ventilation for the TAT-DEPE treated animals was significantly greater than the TAT-0 injected animals at 100% and 21% O_2 ($p<0.05$ [Student's t-test]). ([5]) The air convection requirement in the TAT-0 and TAT-DEPV treated animals was significantly greater at 12% O_2 however the TAT-DEPE treated animals were not ($p<0.05$ [[ANOVA followed by Tukey's multiple comparison test]) Across the O_2 concentrations and between the treatment groups there was no significant difference in CO_2 production and O_2 consumption. All data are represented +/- standard error.

Figure 3.6: Disruption of the $Ca_v3.2$/nNOS interaction *in vivo* results in an elevated respiratory response to changes in oxygen concentration

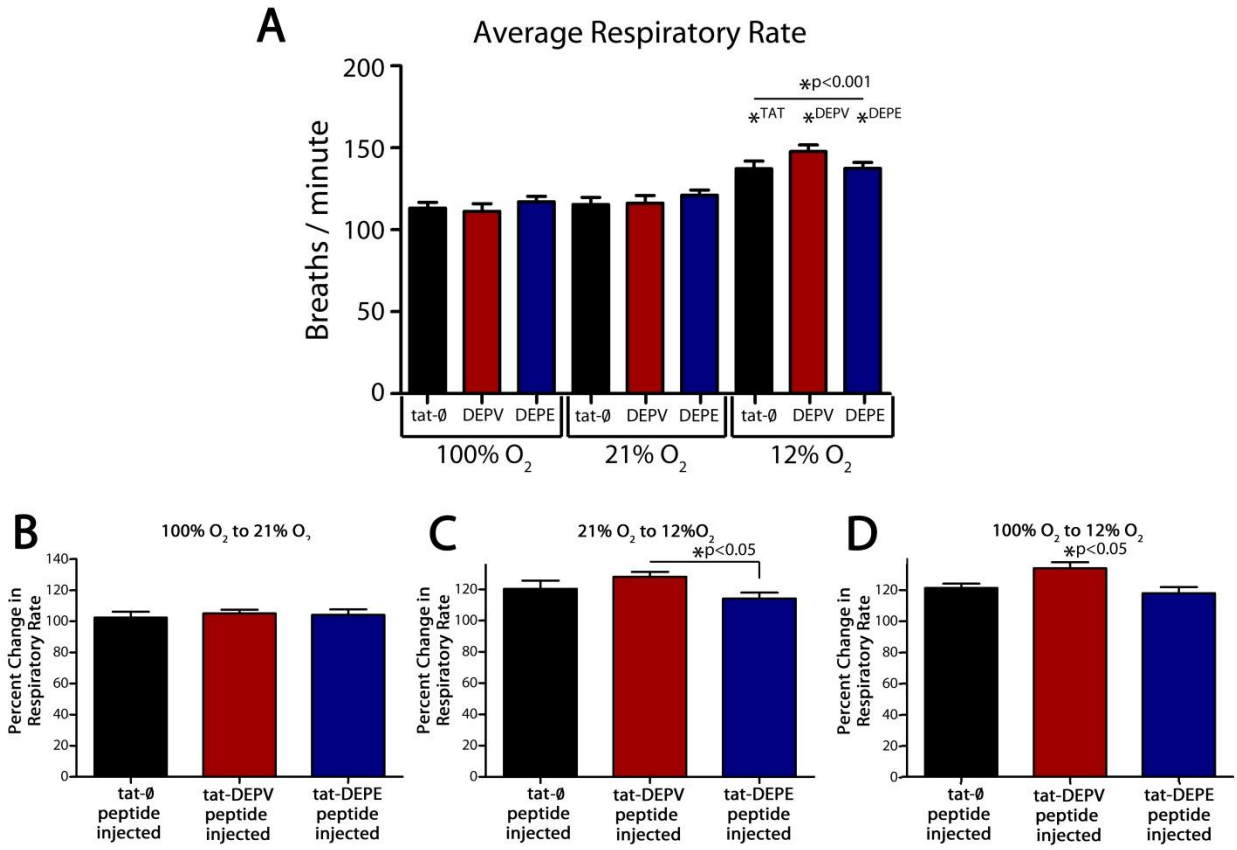

Figure 3.6: Disruption of the $Ca_v3.2$/nNOS interaction *in vivo* results in an elevated respiratory response to changes in oxygen concentration

Sprague Dawley rats (P18 to P25) received an intraperitoneal injection in the abdomen of the $Ca_v3.2$/nNOS disrupting TAT-DEPV peptide (n=12) or the non-disrupting TAT-0 (n=12) or TAT-DEPE peptides (n=10) and respirometry and metabolic data was collected at 100% O_2, 21% O_2 and 12% O_2 (balance nitrogen). The peptides were injected at dose of 9 mg/kg which equates to a blood concentration of approximately 720 μM (assuming a blood volume of approximately 5 ml) (A) All three treatment groups displayed a normal physiological response to hypoxia with a significantly higher respiratory rate at 12% O_2 compared to 21% and 100% O_2. The animals injected with the $Ca_v3.2$/nNOS disrupting TAT-DEPV peptide showed a slightly elevated respiratory rate over the TAT-0 and TAT-DEPE controls however the difference was not significant. (B, C and D) Graphs illustrating the percent change in respiratory rate at steady state comparing 100% to 21% O_2. There was no significant difference between the groups in the percent change in the respiratory rate comparing 100% O_2 to 21% O_2 (B). When comparing the respiratory rates at 21% O_2 and 12% O_2 (C) the TAT-DEPV treated animals displayed a significantly higher ($p<0.05$ [Student's t-test], n= TAT-DEPV=12, TAT-DEPE=10) response compared to the TAT-DEPE treated animals but no significant difference compared to the TAT-0 treated animals. (D) At 100% O_2 to 12% O_2 the difference in respiratory rates between the groups becomes more apparent and the TAT-DEPV injected animals display a significantly higher percentage change compared to the TAT-0 and TAT-DEPE controls ($p<0.05$ [ANOVA followed by Tukey's multiple comparison test] , n=[TAT=12, tat-DEPV=12, tat-DEPE=10). The error bars represent standard error and the asterisk indicate significance at the p value indicated.

Figure 3.7: Average tidal volume and total ventilation in TAT-DEPE injected Sprague Dawley rats differs significantly from $Ca_v3.2$/nNOS disrupted (TAT-DEPV) and TAT-control animals

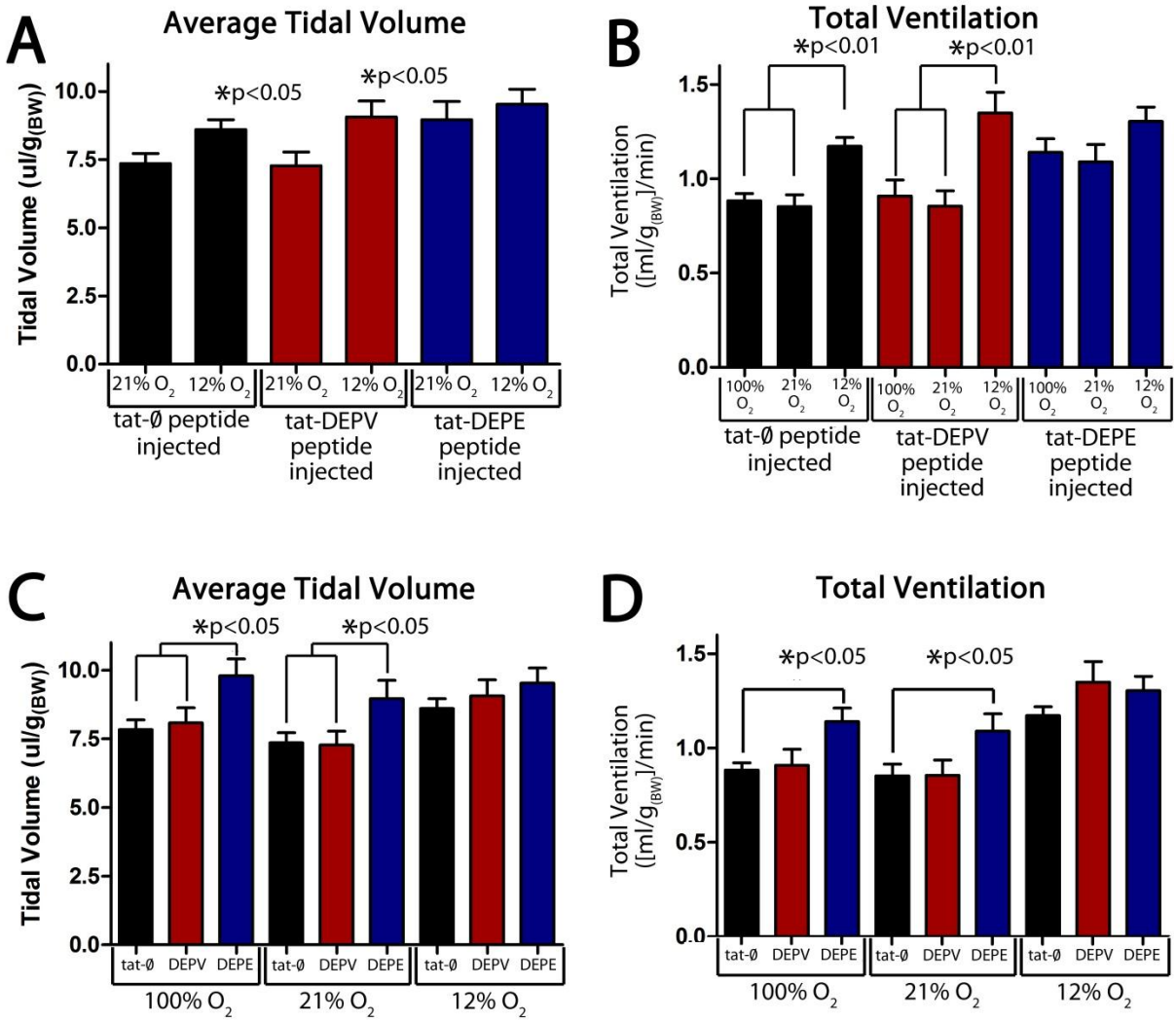

Figure 3.7: Average tidal volume and total ventilation in TAT-DEPE injected Sprague Dawley rats differs significantly from $Ca_v3.2$/nNOS disrupted (TAT-DEPV) and TAT-control animals.

Sprague Dawley rats (P18 to P25) received an intraperitoneal injection of either the $Ca_v3.2$/nNOS disrupting TAT-DEPV peptide (n-12) or the non-disrupting TAT-0 (n=12) or TAT-DEPE peptides (n=10) and respirometry and metabolic data were collected at 100% O_2, 21% O_2 and 12% O_2 (balance nitrogen). (A) Average tidal volume of TAT and TAT-DEPV animals was significantly higher ($p<0.05$ [Student's t-test]) at 12% O_2 compared to 21% O_2 whereas no significant difference was observed in TAT-DEPE injected animals. (B) Consequently, the total ventilation (respiratory rate * tidal volume) in the TAT-0 and TAT-DEPV treated animals was also significantly greater at 12% O_2 compared to 21% and 100% O_2 ($p<0.001$ [ANOVA followed by Tukey's multiple comparison test]). The TAT-DEPV treated animals also demonstrated higher total ventilation at 12% O_2 compared to 21% and 100% O_2 but the difference was not significant. (C) Comparing the average tidal volumes of the TAT-0, TAT-DEPV and TAT-DEPE treated animals shows that the total ventilation of the TAT-DEPE injected animals is significantly greater than the TAT-0 and TAT-DEPV injected animals at 100% and 21% O_2 ($p<0.05$ [Student's t-test]). The total ventilation (D) of the TAT-DEPE treated animals was also elevated at 100% O_2 and 21% O_2 compared to the TAT-0 and TAT-DEPV injected rats but only reached significance compared to the TAT-0 injected animals ($p<0.05$ [Student's t-test]. The error bars represent standard error and the asterisks indicate significance at the p value indicated.

3.3.3. The hyperoxic response may be attenuated in animals where the $Ca_v3.2$/nNOS interaction is disrupted

The goal of the hyperoxic transition test is to observe the respiratory response of the animal when the concentration of available oxygen is rapidly changed from normal or hypoxic conditions to a hyperoxic condition. If the exchange is sufficiently rapid the initial response is largely mediated by the peripheral chemoreceptors (Dejours, 1962). TAT peptide and TAT-DEPV injected animals were pre-conditioned under hypoxic conditions (12% O_2) before exposure to 100% O_2 at the maximum flow rate allowed by the experimental equipment (2000 ml/min). Due to the dead space in the air lines, approximately 10 seconds elapsed before the O_2 concentration began to rise (indicated by the green line in Figure 3.8 which represents the O_2 concentration over time). Initially, the respiratory rate of the TAT peptide group (black squares) and the TAT-DEPV group fell with the same trajectory, however at approximately the 40 second time point, the respiratory rate of the TAT-DEPV treated animals stabilized whereas respiratory rate of TAT injected animals continued to decline for an additional 10 seconds before rebounding and stabilizing at respiratory rate similar to the TAT-DEPV treated animals. During the short period that the two traces diverged 6 of the 12 TAT-DEPV data points were significantly higher ($p<0.05$) than the nearest TAT peptide data point. These results suggest that the TAT-DEPV treatment may be affecting the peripheral chemoreceptors resulting in a blunted hyperoxic response. The TAT-DEPE animals were also tested and it was anticipated that these animals would display a response similar to the TAT injected animals, however there was insufficient data after filtering for sniffs and scratches to accurately plot the respiratory response.

Figure 3.8: Disruption of the $Ca_v3.2$/nNOS interaction alters the response in the hyperoxic response test

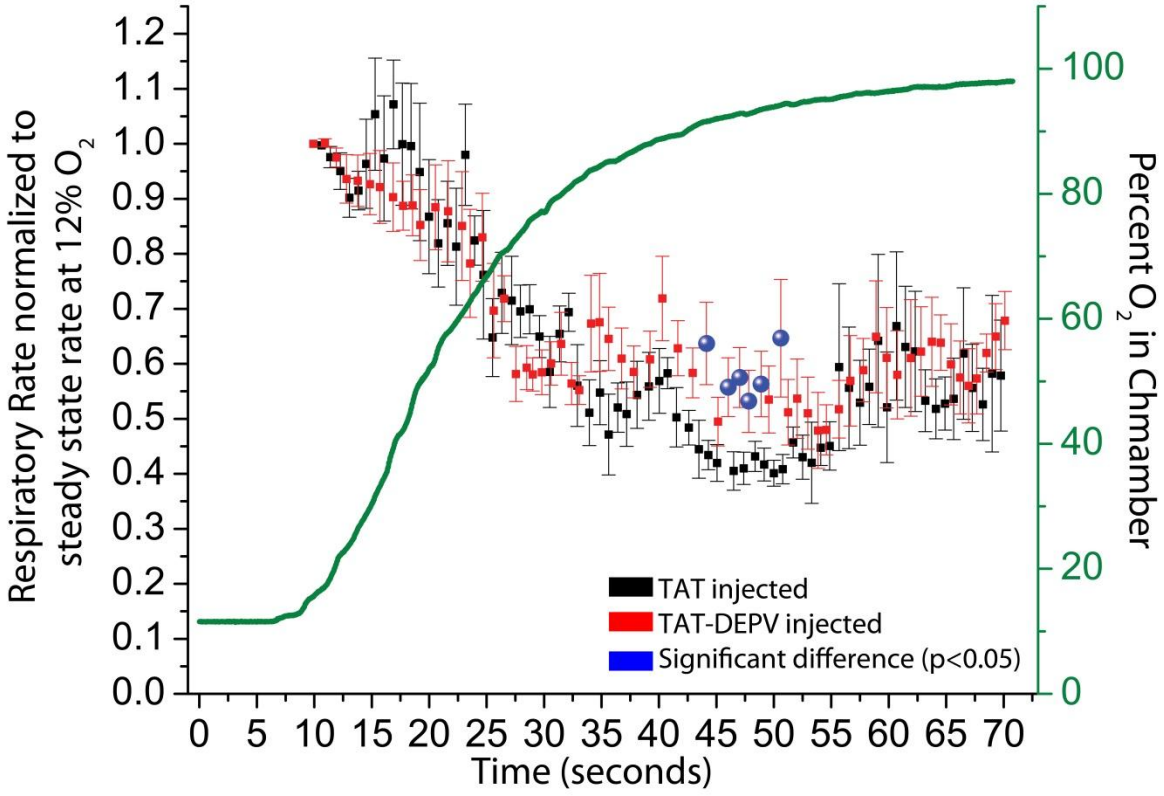

Figure 3.8: Disruption of the $Ca_v3.2$/nNOS interaction alters the response in the hyperoxic response test

The respiratory rate of Sprague Dawley rats (p18 to P25) during a rapid change in available oxygen was analyzed to determine the effect of disrupting the $Ca_v3.2$/nNOS interaction *in vivo*. The animals received an intraperitoneal injection of either TAT-DEPV (n=6) or TAT-0 (n=7) and 12% O_2 was administered at a flow rate of 2000 ccm^{-1} until the respiratory rate stabilized. 100% O2 was then administered at 2000 ccm^{-1} and the respirometry data was recorded. The green line represents the oxygen concentration in the chamber (right scale). There was approximately a 10 second delay from the initiation of the 100% O2 gas flow until the O_2 concentration within the chamber began to increase which is the point the analysis began. Sniffs and animal movement were excluded from the analysis using two criteria: 1) If the rate between two data points was 60% greater than the average of the previous four data points it was excluded. 2) If the rate between two data points was greater than the equivalent of 200 breaths per minute (20% faster than the maximum rate observed under all conditions in this study) it was excluded. A rolling average using a window of five successive data points was used to calculate the change in the respiratory rate over time for each animal. The rolling averages for each animal were normalized to the steady state respiratory rate of the animal at 12% O_2 and then aligned with a standard time course and each experimental group was averaged at 0.75 second intervals and plotted. The response of the two groups is similar until the oxygen concentration surpasses 80% at approximately the 40 second mark. At this time the respiratory rate of the TAT-DEPV treated animals stabilized whereas respiratory rate of TAT injected animals continued to decline for an additional 10 seconds before rebounding and stabilizing at rate similar to the TAT-DEPV treated animals. At the point where the two traces diverged the respiratory rate at 6 of the 12 TAT-DEPV data points was significantly greater ($p<0.05$ [Student's t-test]) than the nearest TAT-0 peptide data point. The TAT-DEPE animals were also tested however there was insufficient data after filtering for sniffs and scratches to accurately plot the respiratory response.

3.4. Discussion

3.4.1. Disruption of the $Ca_v3.2$/nNOS complex has a significant effect on the respiratory rate in response to available oxygen

The central and peripheral chemoreceptors play a crucial role in adjusting respiration in response to both changes in metabolic demand and environmental cues such as oxygen availability. In this study we provide preliminary evidence that $Ca_v3.2$/nNOS interactions may be involved with the modulation of respiratory activity, potentially through negative feedback modulation of carotid glomus cell chemosensitivity by the microganglia of the GPN. In animals treated with the TAT-DEPV peptide there was a greater percent increase in breathing frequency, tidal volume, total ventilation and air convection requirement when switching from 21% to 12% O_2 compared to the other two groups. While the increase in these parameters is congruent with the original hypothesis they are not statistically greater than the controls. The percent increase in the respiratory rate was significantly greater in the TAT-DEPV animals when going from 100% O_2 to 12% O_2 which also supports the original hypothesis. Considering that a definite trend towards an increased percent change in the aforementioned parameters, the most likely explanations as to why significance was observed in only one parameter and only under artificial extremes is the physiological range of the parameters. If the respiratory rate has a larger range than the tidal volume then the smaller changes observed in the tidal volume could potentially be lost in the variation between the animals. With some refinement of the experimental technique and additional repetitions it is possible that a significant increase may be seen in tidal volume, total ventilation, and air convection requirement as well. These results are comparable to those observed in previous studies examining the effects of NOS inhibitors or nNOS knockout animals (Gozal et al., 1996b; Kline et al., 1998; Subramanian et al., 2002) indicating that disruption of the

$Ca_v3.2$/nNOS interaction inhibits NO production and suggests a role in attenuating the hypoxic respiratory response; potentially through the NO mediated inhibition of carotid glomus cell chemosensitivity. The attenuated hyperoxic response in the TAT-DEPV treated animals supports this notion as this experimental challenge is designed to test the contribution of the peripheral receptors involved in the respiratory response (Dejours, 1962).

The quantitative real-time PCR results show that $Ca_v3.2$ is the predominant T-type Ca^{2+} channel expressed in the GPN supportive of the notion that the T-type currents recorded by Campanucci and coworkers in the microganglia of the GPN result from $Ca_v3.2$. We also find that $Ca_v3.2$ and nNOS can both be found in the neurons which comprise the microganglia of the GPN, suggesting that a $Ca_v3.2$/nNOS functional interaction is possible in these cells.

The microganglia of the GPN are an integral part of the peripheral chemoreceptor network which project efferent fibers to the carotid body, a major peripheral chemosensor. These efferent projections have been shown to provide NO mediated inhibition of the O_2 sensing type I glomus cells in the carotid body and it has been proposed that the microganglia of the GPN function as part of a peripheral negative feedback circuit to modulate the hypoxic reflex response. The microganglia possess some O_2 sensing capability and are depolarized to become more excitable under hypoxic conditions. In the current proposed model, this increase in excitability in conjunction with the reciprocal activation of purinergic receptors of the microganglia by type I cells of the carotid body provides a condition specific stimulus for NO production necessary for the inhibition of the hypoxic response of the carotid body (Campanucci and Nurse, 2007). A caveat in this model is that the source of Ca^{2+} for nNOS activation has not been demonstrated. The data presented in Chapter 2 of this thesis, together with the work of others, suggests that for optimal stimulation of nNOS the source of Ca^{2+}

should be local. A functional interaction between $Ca_v3.2$ and nNOS melds nicely with the proposed model linking nNOS with a source of Ca^{2+} influx. In a revised model incorporating the data from the present study, increased microganglia activity would activate the $Ca_v3.2$ channels that drives Ca^{2+} influx sufficient to activate nNOS and to produce NO which in turn inhibits the hypoxic response of the carotid body. A schematic of the revised hypothetical model is presented in Figure 3.9. This new model may account for the increased hypoxic response observed in the animals treated with the $Ca_v3.2$/nNOS disrupting TAT-DEPV peptide. Potentially, dissociating nNOS from the Ca^{2+} source ($Ca_v3.2$ channels) in the microganglia could severely inhibit NO synthesis and as a result the NO-mediated efferent inhibition of the carotid body would be compromised and the hypoxic reflex response would proceed unabated.

Our results demonstrating an attenuated hyperoxic response conflicts with the data obtained from nNOS knockout mice that display an exaggerated hyperoxic response (Kline et al., 1998). It is possible that since nNOS expression is eliminated globally in the knockout mice, the exaggerated response observed by Kline *et al.* is indicative of the total contribution nNOS activity on respiration which includes nNOS activated by other Ca^{2+} sources at other sites in the chemoreflex pathway. Only a few proteins have been shown to interact with the PDZ-3 domain of nNOS with $Ca_v3.2$ being the only protein identified to date that is capable of providing a source of Ca^{2+} for the activation of nNOS. Utilizing a TAT fusion peptide demonstrated to disrupt the $Ca_v3.2$/nNOS interaction in a heterologous system the results of the present study suggest that $Ca_v3.2$ activity may contribute to the activation of nNOS and the modulation of respiratory activity. The hypothesized revisions to the model proposed by Campanucci and co-workers would accommodate our data suggesting an attenuated hyperoxic response in the following way. It is possible that, in the control animals exposed to

hypoxic conditions, NO mediated inhibition moderates the reflex response from the carotid body and, with the sudden introduction of a hyperoxic environment, this inhibition may remain for a short period until the NO and any secondary messenger signals are degraded to relieve the inhibition of the carotid body. This would explain the more pronounced decrease and the subsequent rebound observed in the respiratory rate in the TAT control animals. In animals treated with the disrupting TAT-DEPV peptide, the NO-mediated inhibition of the carotid body is repressed and as a result there would be little delay in the response of the carotid body to the hyperoxic conditions and the respiratory rate would follow a trajectory that corresponds directly with the O_2 environment without the slight overshoot observed in the control animals. Considering the TAT-DEPV peptide was administered through intraperitoneal injection and therefore acting systemically, it is possible that the peptide is disrupting $Ca_v3.2$/nNOS or other PDZ-3 mediated interactions in other neuronal regions involved in respiration such as the NST. Further investigations are required to provide the evidence required to distinguish between the scenarios hypothesized above. One potential experiment would be to use a co-culture of acutely dissociated microganglia and type I glomus cells of the carotid body (Campanucci et al., 2006) to demonstrate the effect of disrupting the $Ca_v3.2$/nNOS interaction on the NO-mediated inhibition of type I glomus cells. Another potential experiment would be to obtain electrophysiological recordings of carotid sinus nerve activity during the hyperoxic response test under normal and $Ca_v3.2$/nNOS disrupted conditions. This approach would have the advantage of *in vivo* recording and offer the possibility of applying TAT peptides locally rather than systemically. This, however, would require sedating the animals which has been shown to affect respiratory responses. In addition to providing a potential source of NO for the inhibition of the carotid body response, the $Ca_v3.2$/nNOS interaction may also contribute to the regulation of microganglia activity

wherein the NO produced feeds back to inhibit $Ca_v3.2$ channels potentially reducing the excitability of the microganglia. Electrophysiological recordings of acutely dissociated microganglia to examine the contribution of a $Ca_v3.2$/nNOS interaction would address this possibility.

Figure 3.9: Schematic illustrating the hypothesized contribution of the $Ca_v3.2$/nNOS interaction to the NO-mediated inhibition of the carotid body

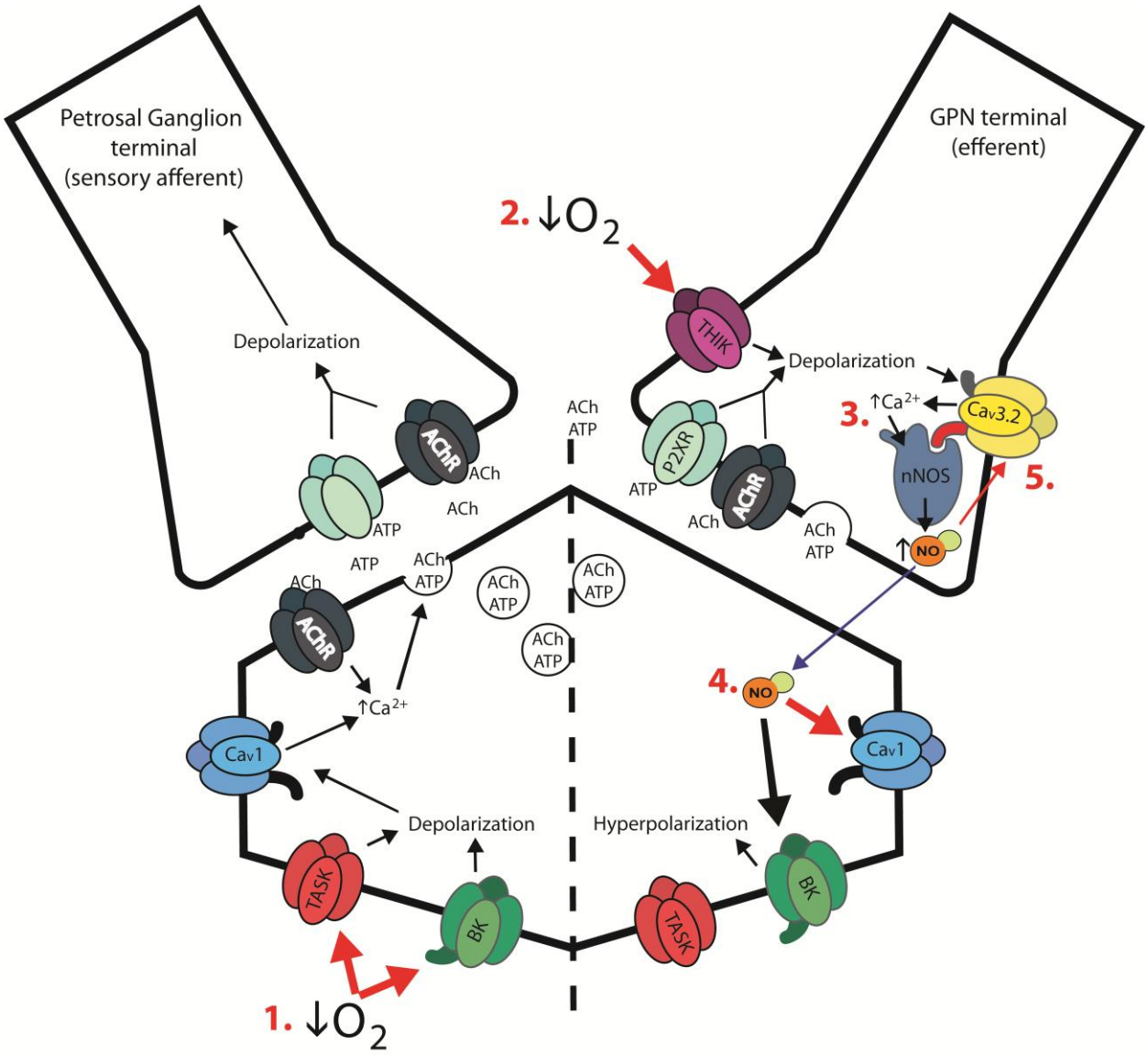

Figure 3.9: Schematic illustrating the hypothesized contribution of the $Ca_v3.2$/nNOS interaction to the NO-mediated inhibition of the carotid body

Hypoxia causes an inhibition of TASK-like and large conductance Ca^{2+}-activated (BK) potassium channels in type I cells (1) resulting in depolarization of the cell and leading to Ca^{2+} influx which results in the release of acetylcholine and ATP. The neurotransmitters bind to purinergic P2X receptors (P2XR) and nicotinic acetylcholine receptors (AChR) in the sensory nerve endings which relay the chemosensory signal to the central nervous system. Hypoxic conditions also activate TWIK-related halothane inhibitable K^+ channels (THIK) in the microganglia (2) which results in depolarization and increases neuronal excitability. Potentially, the increased excitability would lead to the activation of $Ca_v3.2$ channels in the membrane and the Ca^{2+} dependent activation of nNOS to produce nitric oxide (NO) (3). NO diffuses freely across the neuronal membranes to inhibit Ca_v1 channels in the type I glomus cells and increase BK channel activity (4) resulting in decreased depolarizing activity and hyperpolarization of the cell. In addition to the NO mediated inhibition of type I cells of the carotid body, NO could potentially feedback to inhibit further $Ca_v3.2$ (5) to limit the degree of inhibition imposed on the type I cell.

3.4.2. Implications of the observed increase in tidal volume and total ventilation following administration of a mutant PDZ-3 TAT fusion peptide

Interestingly, administration of the TAT peptide with a mutated PDZ-3 motif (DEPE) resulted in a significant increase in the tidal volume and consequently in the total ventilation under hyperoxic and normoxic conditions. In Chapter 2 of this thesis we showed that this peptide does not affect either the co-immunoprecipitation or the functional interaction of $Ca_v3.2$ and nNOS. We were unable to find any reference in the literature of the mutated motif interacting with other proteins, however, given that the peptides are administered systemically it is possible that the mutant peptide could disrupt protein-protein interactions

and/or act as an agonist/antagonist on as yet unidentified proteins involved in the respiratory network. Considering that the mutant TAT peptide had an effect on the tidal volume and not the respiratory frequency, it is unlikely to affect the central respiratory oscillator but probably affects one or more of the inhibitory and excitatory circuits that directly modulate the inspiratory motor neurons.

Identifying which protein(s) the mutant peptide interacts with and/or the potential interactions that it disrupts would be a first step in identifying the mode of action of this peptide on the respiratory system. Precipitation studies using the TAT-DEPE peptide as the bait followed by mass spectrometry analysis would be an interesting way to begin this investigation.

3.4.3. Potential relevance to respiration

The data obtained from the present experiments suggest that a functional interaction between $Ca_v3.2$ and nNOS contributes to the regulation of the respiratory response to oxygen, potentially through a NO mediated inhibition of type I glomus cells of the carotid body by the microganglia in the GPN. These results contribute to our understanding of the regulatory mechanisms that modulate the respiratory response under hyperoxic, normoxic and hypoxic conditions. The interactions that underlie the neuronal activity providing respiratory drive to the central respiratory circuits are complex and a greater understanding of these interactions is required to enable critical evaluation and treatment of respiratory pathologies such as sleep apnea (reviewed in (Bradley, 2002; Eckert et al., 2007)). This knowledge would also help us develop better strategies to acclimate the body to relatively extreme conditions such the decreased oxygen levels found at higher altitudes which has

been found to have a pronounced effect on the respiratory system and the body as a whole (reviewed in (Eckert et al., 2007)).

Chapter 4.

4. Discussion

4.1. Overall significance of the results

4.1.1. Identification of a physical and function interaction between $Ca_v3.2$ and nNOS

We presented data from immunoprecipitation, NO sensitive fluorometric assay and electrophysiology experiments demonstrating a novel physical and functional interaction between the $Ca_v3.2$ T-type Ca^{2+} channel and nNOS. This interaction closely localizes nNOS to a source of Ca^{2+} influx and further links NO production to neuronal activity. We show that the NO produced following the activation on nNOS is sufficient to inhibit $Ca_v3.2$ activity forming a putative negative feedback pathway which could contribute to the regulation of neuronal activity in cells where both proteins are expressed. Additionally, since NO is able to freely diffuse throughout the cell, the NO produced from the $Ca_v3.2$/nNOS interaction may also influence other cellular functions either through direct action or through second messenger pathways via the activation of soluble guanylyl cyclase. Furthermore we demonstrate that nNOS may facilitate the formation of larger complexes by utilizing both the PDZ-3 binding domain and the internal PDZ-2 binding ligand at the amino terminus of the protein. This capability could potentially associate the $Ca_v3.2$/nNOS complex with other neuronal proteins which respond to increases in local Ca^{2+} or NO concentrations such as large conductance Ca^{2+}-dependent potassium channels (BK channels) (Bolotina et al., 1994; George and Shibata, 1995). Such interactions would significantly increase the contribution of the $Ca_v3.2$/nNOS interaction to neuronal activity; potentially linking sub-threshold stimulation and low threshold spikes to NO production and the regulation of numerous

cellular events through Ca^{2+} influx, NO production or the activation of secondary messenger pathways.

4.1.2. Potential relevance for nociception

$Ca_v3.2$ channels and nNOS have both been demonstrated to play a significant role in nociception. Mice lacking the $Ca_v3.2$ channel display a significant reduction in the response to noxious stimuli (Choi et al., 2007) and redox modulation of $Ca_v3.2$ has been shown to modulate the nociceptive response (Todorovic et al., 2004). nNOS knockout mice have also been shown to display analgesia to noxious mechanical, thermal and chemical stimuli (Guan et al., 2007). The $Ca_v3.2$/nNOS interaction identified in this study could explain how such similar phenotypes could arise from silencing either protein. It is feasible that the $Ca_v3.2$/nNOS complex would permit the stimulation of DRGs to activate $Ca_v3.2$ to produce a localized increase in intracellular Ca^{2+} and stimulate nNOS to produce NO which would then proceed to influence other cellular processes involved in producing the nociceptive response. Given that the nNOS knockout mice display analgesia to noxious stimuli, a similar response would be anticipated following disruption of the $Ca_v3.2$/nNOS interaction with the TAT-DPEV fusion peptide. Additionally, the negative feedback of $Ca_v3.2$ by NO may serve to regulate the production of NO to limit the nociceptive response and possibly to avoid the potential cytotoxic buildup of NO within the cell.

The potential for nNOS to facilitate the formation of larger protein complexes may also contribute to the modulation of nociception. Recently, activation of transient receptor potential vanilloid-1 (TRPV1) channels in rat DRG neurons have been demonstrated to inhibit $Ca_v3.2$ channels which may be a potential mechanism underlying capsaicin-induced analgesia (Comunanza et al., 2011). Several members of the TRPV family have been shown to interact with proteins possessing PDZ domains (Islam, 2011) suggesting that nNOS could

potentially mediate a functional interaction between $Ca_v3.2$ and TRPV1 by facilitating the co-localization of the two channels.

4.1.3. Relevance to the respiratory system

The data presented in this study suggests that a functional interaction between $Ca_v3.2$ and nNOS contributes towards the regulation of the respiratory rate in response to available oxygen. The hyperoxic response data suggests that this contribution occurs in the peripheral nervous system. I propose the hypothesis that the $Ca_v3.2$/nNOS interaction associates nNOS with a source of Ca^{2+} influx in the microganglia of the GPN which directly links NO production with the intrinsic O_2 sensing capability of the microganglia to provide efferent inhibition of the carotid body. NO mediated inhibition of the respiratory response by the microganglia within the GPN has been suggested to occur independently of the central respiratory system which is interesting as it presents the possibility of enhancing the respiratory drive to stimulate increased respiration without negatively impacting the complex circuits which comprise the central respiratory network. This may have an impact on conditions where a decreased respiratory drive contributes to pathological conditions such as central sleep apnea.

4.2. The $Ca_v3.2$ T-Type calcium channel and neuronal nitric oxide synthase physically and functionally interact forming a putative negative feedback regulatory loop

4.2.1. Working hypothesis

The evidence presented in Chapter 2 demonstrates that $Ca_v3.2$ and nNOS can physically and functionally interact when co-expressed in a heterologous system. The physical interaction is mediated by the PDZ-3 binding ligand situated at the carboxyl

terminus of the $Ca_v3.2$ which interacts with the PDZ-3 domain of nNOS. This interaction facilitates the Ca^{2+} dependent activation of nNOS by $Ca_v3.2$ activity which results in the production of NO. The NO produced by nNOS in turn inhibits further $Ca_v3.2$ activity thereby completing the negative feedback circuit. In addition to inhibiting $Ca_v3.2$ the NO produced as a result of this circuit could potentially mediate other cellular events through the direct interaction with other proteins or through the activation of sGC to produce the secondary signaling molecule cGMP.

We also demonstrate that nNOS can facilitate the formation of larger complexes through the internal PDZ-2 binding ligand adjacent to the PDZ-3 domain. In this study PSD-95 was utilized to show that both PDZ structures of nNOS can be occupied simultaneously. PSD-95 is a scaffolding protein well known to associate nNOS with other proteins, such as NMDA receptors, to facilitate NO-mediated modulation of various targets. Additionally, sGC has been shown to bind to PSD-95 which could potentially link T-type channel activity with the production of cGMP. Furthermore, we show that in the presence of PSD-95 the inhibitory effects of nNOS on $Ca_v3.2$ are significantly increased suggesting that the utilization of the internal PDZ-2 ligand of nNOS may increase the affinity of the $Ca_v3.2$/nNOS interaction thereby supporting the possibility of this interaction occurring *in vivo*.

4.2.2. Limitations and weaknesses

The inhibition of $Ca_v3.2$ by NO has been demonstrated to occur through metal catalyzed oxidization of the histidine residue at position 191 of the channel. Inhibition of $Ca_v3.2$ channels in this study was assumed to occur through this process as well; however experiments to confirm that the H191 residue is involved in the inhibition were not

examined. A solution would be to generate a $Ca_v3.2$ mutant substituting the H191 for glutamine as was done by Kang *et al*., Bartels *et al*., and Orestes *et al*. and repeat the current density experiments utilizing this construct (Kang et al., 2006; Bartels et al., 2009; Orestes et al., 2011). A second potential weakness is that L-NAME introduces a slight structural conformation change in the nNOS protein which is believed to contribute to the inhibition of nNOS (Mayer, 1995). While unlikely, it is possible that the reduction in T-type current density observed is due to the physical interaction of nNOS and $Ca_v3.2$ and that application of L-NAME relieves the inhibition due to the shift in the structural conformation of nNOS. To test this possibility the current density experiments could be repeated in the presence of a NO scavenger such as CPTIO in order to remove NO as it is produced. In these experiments we would expect the application of the NO scavenger to restore the current density to levels similar to those observed with application of the NOS inhibitor. Alternatively, the current density experiments could be repeated in the presence of barium rather than Ca^{2+}. Barium should not activate nNOS therefore we would not expect to see a difference in current density with the application of L-NAME.

A potential limitation of this study is that while we have evidence to show that the $Ca_v3.2$/nNOS interaction is required for the activation of nNOS, we do not have evidence to determine whether the interaction is required for the NO produced from nNOS to inhibit $Ca_v3.2$. A possible solution would be to co-transfect constitutively active calmodulin with nNOS into the stable cell line expressing the $Ca_v3.2$ with the mutant PDZ-3 motif and perform current density analysis. If the interaction is not required for $Ca_v3.2$ inhibition by nNOS derived NO then we would expect a decrease in the current density with the constitutively active calmodulin. We recognize that these weaknesses and limitations exist and do not believe that they would significantly alter the conclusions presented here.

4.3. Intraperitoneal injection of TAT fusion peptide to disrupt the $Ca_v3.2$ and nNOS interaction *in vivo* produces an augmented respiratory response to changes in available oxygen in rats

4.3.1. Working hypothesis

We present evidence that a membrane permeable peptide designed to disrupt the $Ca_v3.2$/nNOS interaction has a significant effect on the respiratory response to hypoxia. The data from the hyperoxic response experiments suggests that the disrupting peptide is affecting the peripheral network of the respiratory system. We also show that $Ca_v3.2$ and nNOS are both expressed in the microganglia of the GPN which has been demonstrated to contribute to the efferent inhibition of the carotid body, a major chemoreceptor of the peripheral respiratory system. Our working hypothesis is that a physical/functional interaction between $Ca_v3.2$ and nNOS contributes to the NO-mediated efferent inhibition of the carotid body by the microganglia of the GPN. Building on the model put forward by Campanucci *et al*. we propose that the intrinsic O_2 sensing capability of the microganglia of the GPN increases the excitability of the microganglia which activates $Ca_v3.2$ channels and consequently stimulates NO to produce NO in response to hypoxic conditions. The NO produced then participates in the inhibition of the reflex hypoxic response generated by the carotid body thereby imposing a cap on the increase in the respiratory drive which contributes to the modulation of the respiratory rate. Disruption of the interaction between $Ca_v3.2$ and nNOS would prevent the generation of NO therefore inhibition of the response of the carotid body would not occur, effectively removing the cap from the increase of the respiratory drive and which may reflect the observed increase in respiratory rate under hypoxic conditions.

4.3.2. Limitations and weaknesses

The metabolic data in this respiratory response study is incomplete due to a likely design limitation in the chamber allowing minute quantities of pure oxygen to become trapped and slowly escape during normoxic and hypoxic challenges. This was discovered during the analysis of the data after the U.B.C. Animal Care license expired therefore additional data could not be collected. Since the amount of O_2 trapped was small and only resulted in a partial percentage change in O_2 concentration it was not likely that this limitation significantly affected the respiratory rate, tidal volume or the CO_2 measurements. Another potential limitation is the maximum possible air flow allowed by the equipment (2000 ml/min). Ideally, for the hyperoxic response test, it is desirable to exchange to O_2 concentration as rapidly as possible to invoke the maximum peripheral response with minimal input from the central respiratory circuits. The flow rate used in this study was acceptable but not ideal therefore we cannot state with certainty that the observed effects are purely peripheral in origin as modulatory efferent signals from the central respiratory circuits may be present.

Systemic administration of the peptide presents a few possible experimental limitations. The peptide is not limited to the GPN therefore the data may also include effects of the peptides in other regions of the body involved in the respiratory response and that express both $Ca_v3.2$ and nNOS and which might either mask or exaggerate the data. The proposed model is speculative based on the available data; further investigations into the effect of disrupting the $Ca_v3.2$/nNOS interaction within the GPN are required to substantiate the model. While the PDZ-3 domain has thus far been found to be unique to nNOS and few proteins have been identified as having compatible PDZ-3 binding ligands, there is the possibility that the peptides can disrupt interactions that have yet to be identified. Co-

precipitation using the peptides as the bait and utilizing high-pressure liquid chromatography to analyze proteins that co-precipitate may be one way to determine the specificity of the peptides. Additionally, it has been shown that the protein CAPON possesses a PDZ-3 binding ligand and can bind to nNOS which disrupts the PDZ-2 interaction between PSD-95 and nNOS. It is possible that the peptide designed to disrupt the $Ca_v3.2$/nNOS interaction may also disrupt PDZ-2 interactions with other proteins *in vivo*. Localized administration of the TAT-fusion peptides is one method which may minimize possible effects of non-specific disruption of protein interactions. Another potential option would be to use $Ca_v3.2$ knockout mice to generate knock-in mice with a mutant $Ca_v3.2$ channel lacking the PDZ-3 binding ligand. With these knock-in mice concerns regarding the non-specific effects of a systemically administered compound would be elevated.

Degradation of the injected peptides after injection is a possible limitation. We administered the peptides at a dose of 9 mg/kg as it was the highest level of TAT peptide injection that we could find in the literature that did not appear to have adverse effects. Lower doses have been utilized in the literature with the same degree of efficacy which minimized our concerns regarding the degradation of the peptide. Furthermore, animals underwent two rounds of testing with approximately one hour between the start of the first round and the start of the second, thus if significant degradation occurred in that period a difference between the observed responses should have been apparent.

4.4. Conclusions

4.4.1. General conclusion

Here we present evidence of a novel physical and functional interaction between $Ca_v3.2$ and nNOS. We show that $Ca_v3.2$ possesses a carboxyl PDZ-3 binding ligand that can

interact with the PDZ-3 domain of nNOS and that this integration facilitates the activation of nNOS by $Ca_v3.2$ mediated Ca^{2+} influx. We also demonstrate that NO produced by nNOS can in turn feedback to inhibit $Ca_v3.2$ activity. To our knowledge this is the first description of an interaction between these proteins and the first evidence of a self-inhibiting circuit involving the $Ca_v3.2$ channel. We further demonstrate the potential for $Ca_v3.2$ and nNOS to form larger complexes through the utilization of both the internal PDZ-2 binding ligand and the PDZ-3 domain of nNOS. Evidence for a role for the $Ca_v3.2$/nNOS interaction *in vivo* is also presented. We found that administration of membrane permeable peptides designed to disrupt the $Ca_v3.2$/nNOS interaction has an effect on the respiratory response to hypoxia suggesting a possible role for this complex in the modulation of respiratory drive.

4.4.2. Relevance to modulation of neuronal networks co-expressing $Ca_v3.2$ and nNOS

A functional interaction between $Ca_v3.2$ and nNOS may contribute to the regulation of neuronal activity in networks where both proteins are expressed. Tight control over neuronal activity ensures the efficient and proper function of the brain as a whole and disruption of the modulatory mechanisms can, under the right circumstances, lead to abhorrent activity such as seizures. The contribution of $Ca_v3.2$ activity to neuronal excitability and the generation of specific firing patterns such as burst firing have been well documented. A self-inhibiting circuit consisting of $Ca_v3.2$ and nNOS would potentially impose an upper limit to the contribution of $Ca_v3.2$ channel activity to neuronal activity in certain populations of cells. This restriction could assist in preventing the over stimulation of neuronal networks and affect the establishment of firing patterns that underlie certain pathological conditions such as epilepsy.

Additionally, the interaction between $Ca_v3.2$ and nNOS provides a link between neuronal depolarization and the production of NO which has been demonstrated to play a role in the modulation of neuronal activity and tuning of neuronal networks. In this scenario the contribution of $Ca_v3.2$ and nNOS could extend well beyond the modulation of cell excitability and the contribution of $Ca_v3.2$ to neuronal firing patterns to include the cell-to-cell signaling events and possibly have longer lasting effects such as short term facilitation and long term potentiation.

4.4.3. Relevance to the respiratory system

Our understanding of the complexity of the neuronal networks that comprise the respiratory system is steadily improving, however there is still much that remains a mystery. The evidence presented here showing that $Ca_v3.2$ and nNOS are potentially involved in the regulation of the hypoxic respiratory response contributes to the overall understanding of the respiratory system, particularly the modulation of respiratory drive.

Modulation of respiratory drive allows for rapid responses to changes in metabolic demand and the environment. In some pathological conditions the respiratory drive or the respiratory response to this drive is insufficient resulting in potentially life threating conditions. For example, a decreased respiratory drive is one of the key factors in the pathological condition of central sleep apnea (Bradley, 2002; Eckert et al., 2007). Additionally, significant alterations in cardiorespiratory responses have been observed in patients with obstructive sleep apnea syndrome. These respiratory adaptations are a result of chronic intermittent hypoxia exposure that has been shown to invoke adaptive changes in the peripheral chemosensory reflex (Kline et al., 2007). The peripheral chemosensory reflex has also been demonstrated to be critical for the acclimation of the respiratory response to the

decreased O_2 concentrations at high altitude (hypoxic ventilatory acclimation). Furthermore, at altitudes greater than 2,500 m, permanent residents are at risk of developing chronic mountain sickness, a condition associated with the reduced sensitivity of the peripheral chemoreceptors (reviewed in (Joseph and Pequignot, 2009)). As our understanding of the factors that underlie and modulate the respiratory drive improve we can likely develop better options for the clinical treatment and prevention of conditions such as central sleep apnea, chronic intermittent hypoxia exposure and chronic mountain sickness. Additionally, pharmaceuticals may be developed to speed high altitude acclimation that would improve the safety of those needing to ascend to high altitude rapidly such as alpine rescue teams.

4.4.4. Future directions

The results presented in this thesis demonstrate that a physical and functional interaction between $Ca_v3.2$ and nNOS can occur in a heterologous expression system. Further investigations are required, however, to elucidate the role(s) of this interaction in *vivo*. Data have been presented which indicate that an interaction between $Ca_v3.2$ and nNOS may play a role in the regulation of the respiratory response; presumably involving the efferent inhibition of the carotid body. To further investigate the contribution of $Ca_v3.2$ channels and nNOS to the efferent inhibition of the carotid body it would be necessary to identify whether the two proteins truly interact in microganglia of the GPN. Electrophysiological recordings of acutely dissociated cultures of the microganglia of the GPN to determine if disruption of the $Ca_v3.2$/nNOS interaction has an effect on the $Ca_v3.2$ currents would be one indicator of an interaction. Another possible indicator would be demonstration that the synthesis of NO is significantly reduced when the $Ca_v3.2$/nNOS interaction is disrupted. From there, it would be interesting to investigate the contribution of the $Ca_v3.2$ and nNOS to the efferent inhibition of

the carotid bodies utilizing a co-culture of acutely dissociated microganglia from the GPN and type I glomus cells from the carotid bodies. The results of the electrophysiological recordings obtained from cells of the co-culture could then be used to justify further *in vivo* experiments, particularly electrophysiological recordings of the carotid sinus nerve in TAT-DEPV treated animals. As mentioned in the previous chapter, in these experiments the peptide could be applied locally to the region of interest, alleviating the problems inherent with systemic administration of the peptide.

The NO assay data presented in Chapter 1 has been forwarded to Dr. E. Bourinet as part of collaboration between Dr.T. P. Snutch's laboratory and Dr. Bourinet's laboratory (Université de Montpellier, France) into the role of $Ca_v3.2$ and nNOS in nociception. $Ca_v3.2$ and nNOS have both been identified in the nociceptive DRGs and given that $Ca_v3.2$ knockout mice display an increased nociceptive threshold would expect the disrupting the $Ca_v3.2$/nNOS interaction would produce a hyperalgesic response. On the other hand, nNOS knockout mice also display an increased nociceptive threshold suggesting that the role of the $Ca_v3.2$/nNOS interaction may not be via the direct regulation of $Ca_v3.2$ but rather via facilitation of the production of NO by anchoring nNOS to a source of Ca^{2+} related to other activities of the cell. The NO produced as a result of $Ca_v3.2$ activity may play a role in the nociceptive response through the activation of second-messenger systems and/or the direct action on other cellular signaling pathways. Using cultures of acutely dissociated DRGs it should be possible to determine if $Ca_v3.2$ and nNOS interact within these neurons. This information could then be used to justify *in vivo* experiments examining the effect of peptides designed to disrupt the $Ca_v3.2$/nNOS interaction on nociceptive responses. Furthermore, it would be interesting to investigate the effects on the nociceptive response of inhibiting the downstream targets of NO such as soluble guanylyl cyclase.

Mutations in the $Ca_v3.2$ channel have been associated with the pathological condition of childhood absence epilepsy. Interestingly, this condition generally resolves itself as the patient reaches maturity suggesting that the $Ca_v3.2$ mutations are able to contribute to seizure activity for a limited period during development. It has been found that nNOS is developmentally expressed in the nRT of ferrets and the same developmental expression may occur in the animal models of childhood absence epilepsy. It is possible that a $Ca_v3.2$/nNOS interaction may play a role in the regulation of the neuronal networks during development and that the $Ca_v3.2$ mutations disrupt the balance of neuronal activity thereby contributing to seizure activity. Investigations into this possibility would involve identifying nNOS expression in the nRT of the absence epilepsy models followed by electrophysiological recordings from acute brain slices through the nRT at different stages of development to determine if disrupting the $Ca_v3.2$/nNOS interaction has a significant impact on the neurological activity in that region.

Here, only a few suggestions have been made for possible avenues of investigation into the role of $Ca_v3.2$ and nNOS *in vivo*. There are many other potential projects that could also be considered including the role of a $Ca_v3.2$ and nNOS interaction in learning and memory and also in the olfactory response. It is apparent that investigations concerning the roles of $Ca_v3.2$ channels in neuronal circuits should also include a possible interaction with nNOS. Conversely, when investigating the role of nNOS, $Ca_v3.2$ channels should likely be considered as a potential source Ca^{2+} for the stimulation of nNOS activity.

Bibliography:

Aarts, M., Liu, Y., Liu, L., Besshoh, S., Arundine, M., Gurd, J.W., Wang, Y.-T., Salter, M.W., and Tymianski, M. (2002). Treatment of ischemic brain damage by perturbing NMDA receptor- PSD-95 protein interactions. Science *298*, 846–850.

Alderton, W.K., Cooper, C.E., and Knowles, R.G. (2001). Nitric oxide synthases: structure, function and inhibition. Biochem. J. *357*, 593–615.

Amici, M., Lupidi, G., Angeletti, M., Fioretti, E., and Eleuteri, A.M. (2003). Peroxynitrite-induced oxidation and its effects on isolated proteasomal systems. Free Radic. Biol. Med. *34*, 987–996.

Andreasen, D., Jensen, B.L., Hansen, P.B., Kwon, T.H., Nielsen, S., and Skøtt, O. (2000). The alpha(1G)-subunit of a voltage-dependent Ca^{2+} channel is localized in rat distal nephron and collecting duct. Am. J. Physiol. Renal Physiol. *279*, F997–1005.

Andrew, P.J., and Mayer, B. (1999). Enzymatic function of nitric oxide synthases. Cardiovascular Research *43*, 521–531.

Antoniou, H., and Murariu, C. (1999). Role of nitric oxide in hypoxic hypometabolism in rats. J. Appl. Physiol *87*, 104–110.

Aptel, H., Hilaire, C., Pieraut, S., Boukhaddaoui, H., Mallié, S., Valmier, J., and Scamps, F. (2007). The $Ca_v3.2/\alpha1H$ T-type Ca^{2+} current is a molecular determinant of excitatory effects of GABA in adult sensory neurons. Molecular and Cellular Neuroscience *36*, 293–303.

Arikkath, J., and Campbell, K.P. (2003). Auxiliary subunits: essential components of the voltage-gated calcium channel complex. Curr. Opin. Neurobiol. *13*, 298–307.

Armstrong, C.M., and Matteson, D.R. (1985). Two distinct populations of calcium channels in a clonal line of pituitary cells. Science *227*, 65–67.

Arnoult, C., Lemos, J.R., and Florman, H.M. (1997). Voltage-dependent modulation of T-type calcium channels by protein tyrosine phosphorylation. EMBO J. *16*, 1593–1599.

Aromolaran, K.A., Benzow, K.A., Cribbs, L.L., Koob, M.D., and Piedras-Rentería, E.S. (2009). Kelch-like 1 protein upregulates T-type currents by an actin-F dependent increase in α(1H) channels via the recycling endosome. Channels (Austin) *3*, 402–412.

Aromolaran, K.A., Benzow, K.A., Cribbs, L.L., Koob, M.D., and Piedras-Rentería, E.S. (2010). T-type current modulation by the actin-binding protein Kelch-like 1. Am. J. Physiol., Cell Physiol. *298*, C1353–1362.

Augustine, G.J., Santamaria, F., and Tanaka, K. (2003). Local calcium signaling in neurons. Neuron *40*, 331–346.

Bao, J., Li, J.J., and Perl, E.R. (1998). Differences in Ca^{2+} channels governing generation of miniature and evoked excitatory synaptic currents in spinal laminae I and II. J. Neurosci. *18*, 8740–8750.

Bartels, P., Behnke, K., Michels, G., Groner, F., Schneider, T., Henry, M., Barrett, P.Q., Kang, H.-W., Lee, J.-H., Wiesen, M.H.J., et al. (2009). Structural and biophysical determinants of single Ca(V)3.1 and Ca(V)3.2 T-type calcium channel inhibition by N(2)O. Cell Calcium *46*, 293–302.

Bean, B.P. (1985). Two kinds of calcium channels in canine atrial cells. Differences in kinetics, selectivity, and pharmacology. J. Gen. Physiol. *86*, 1–30.

Becker, A.J., Pitsch, J., Sochivko, D., Opitz, T., Staniek, M., Chen, C.-C., Campbell, K.P., Schoch, S., Yaari, Y., and Beck, H. (2008). Transcriptional upregulation of $Ca_v3.2$ mediates epileptogenesis in the pilocarpine model of epilepsy. The Journal of Neuroscience *28*, 13341–13353.

Beckman, J.S. (1996). Oxidative damage and tyrosine nitration from peroxynitrite. Chem. Res. Toxicol. *9*, 836–844.

Belardetti, F., Tringham, E., Eduljee, C., Jiang, X., Dong, H., Hendricson, A., Shimizu, Y., Janke, D.L., Parker, D., Mezeyova, J., et al. (2009). A fluorescence-based high-throughput screening assay for the identification of T-type calcium channel blockers. Assay Drug Dev Technol *7*, 266–280.

Bender, A.T., and Beavo, J.A. (2006). Cyclic nucleotide phosphodiesterases: molecular regulation to clinical use. Pharmacol. Rev. *58*, 488–520.

Berridge, M.J., Bootman, M.D., and Lipp, P. (1998). Calcium - a life and death signal. Nature *395*, 645–648.

Bertani, G. (1951). Studies on lysogenesis. I. The mode of phage liberation by lysogenic Escherichia coli. J. Bacteriol. *62*, 293–300.

Bertani, G. (2004). Lysogeny at Mid-Twentieth Century: P1, P2, and Other Experimental Systems. J Bacteriol *186*, 595–600.

Berthier, C., Monteil, A., Lory, P., and Strube, C. (2002). Alpha(1H) mRNA in single skeletal muscle fibres accounts for T-type calcium current transient expression during fetal development in mice. J. Physiol. (Lond.) *539*, 681–691.

Biel, M., Ruth, P., Bosse, E., Hullin, R., Stühmer, W., Flockerzi, V., and Hofmann, F. (1990). Primary structure and functional expression of a high voltage activated calcium channel from rabbit lung. FEBS Lett. *269*, 409–412.

Birnbaumer, L., Campbell, K.P., Catterall, W.A., Harpold, M.M., Hofmann, F., Horne, W.A., Mori, Y., Schwartz, A., Snutch, T.P., Tanabe, T., et al. (1994). The naming of voltage-gated calcium channels. Neuron *13*, 505–506.

Boettger, M.K., Uceyler, N., Zelenka, M., Schmitt, A., Reif, A., Chen, Y., and Sommer, C. (2007). Differences in inflammatory pain in nNOS-, iNOS- and eNOS-deficient mice. Eur J Pain *11*, 810–818.

Böhme, E., Grossmann, G., Herz, J., Mülsch, A., Spies, C., and Schultz, G. (1984). Regulation of cyclic GMP formation by soluble guanylate cyclase: stimulation by NO-containing compounds. Adv Cyclic Nucleotide Protein Phosphorylation Res *17*, 259–266.

Böhme, G.A., Bon, C., Lemaire, M., Reibaud, M., Piot, O., Stutzmann, J.M., Doble, A., and Blanchard, J.C. (1993). Altered synaptic plasticity and memory formation in nitric oxide synthase inhibitor-treated rats. Proc. Natl. Acad. Sci. U.S.A. *90*, 9191–9194.

Boland, L.M., Morrill, J.A., and Bean, B.P. (1994). omega-Conotoxin block of N-type calcium channels in frog and rat sympathetic neurons. J. Neurosci. *14*, 5011–5027.

Bolotina, V.M., Najibi, S., Palacino, J.J., Pagano, P.J., and Cohen, R.A. (1994). Nitric oxide directly activates calcium-dependent potassium channels in vascular smooth muscle. Nature *368*, 850–853.

Bootman, M.D., and Berridge, M.J. (1995). The elemental principles of calcium signaling. Cell *83*, 675–678.

Boulanger, C.M., Heymes, C., Benessiano, J., Geske, R.S., Lévy, B.I., and Vanhoutte, P.M. (1998). Neuronal nitric oxide synthase is expressed in rat vascular smooth muscle cells: activation by angiotensin II in hypertension. Circ. Res. *83*, 1271–1278.

Bourinet, E. (1999). Splicing of 1A subunit gene generates phenotypic variants of P- and Q-type calcium channels. Nature Neuroscience *5*, 407–415.

Bourinet, E., Alloui, A., Monteil, A., Barrere, C., Couette, B., Poirot, O., Pages, A., McRory, J., Snutch, T.P., Eschalie, A., et al. (2005). Silencing of the $Ca_v3.2$ T-type calcium channel gene in sensory neurons demonstrates its major role in nociception. The EMBO Journal *24*, 315–324.

Bradley, T.D. (2002). Crossing the Threshold Implications for Central Sleep Apnea. Am. J. Respir. Crit. Care Med. *165*, 1203–1204.

Bredt, D.S. (1995). Molecular Characterization of the Nitric Oxide Synthase. In NItric Oxide in the Nervous System, (San Diego: Academic Press), pp. 1–19.

Bredt, D.S., Hwang, P.M., Glatt, C.E., Lowenstein, C., Reed, R.R., and Snyder, S.H. (1991). Cloned and expressed nitric oxide synthase structurally resembles cytochrome P-450 reductase. Nature *351*, 714–718.

Brenman, J.E., Chao, D.S., Gee, S.H., McGee, A.W., Craven, S.E., Santillano, D.R., Wu, Z., Huang, F., Xia, H., Peters, M.E., et al. (1996a). Interaction of Nitric Oxide Synthase with the Postsynaptic Density Protein PSD-95 and [alpha]1-Syntrophin Mediated by PDZ Domains. Cell *84*, 757–767.

Brenman, J.E., Christopherson, K.S., Craven, S.E., McGee, A.W., and Bredt, D.S. (1996b). Cloning and Characterization of Postsynaptic Density 93, a Nitric Oxide Synthase Interacting Protein. J. Neurosci. *16*, 7407–7415.

Broillet, M.C. (1999). S-nitrosylation of proteins. Cell. Mol. Life Sci. *55*, 1036–1042.

Brown, A.M., Camerer, H., Kunze, D.L., and Lux, H.D. (1982). Similarity of unitary Ca^{2+} currents in three different species. Nature *299*, 156–158.

Cain, S.M., and Snutch, T.P. (2010). Contributions of T-type calcium channel isoforms to neuronal firing. Channels (Austin) *4*, 475–482.

Campanucci, V.A., Fearon, I.M., and Nurse, C.A. (2003). A novel O2-sensing mechanism in rat glossopharyngeal neurones mediated by a halothane-inhibitable background K+ conductance. J. Physiol. (Lond.) *548*, 731–743.

Campanucci, V.A., and Nurse, C.A. (2005). Biophysical characterization of whole-cell currents in O2-sensitive neurons from the rat glossopharyngeal nerve. Neuroscience *132*, 437–451.

Campanucci, V.A., Zhang, M., Vollmer, C., and Nurse, C.A. (2006). Expression of multiple P2X receptors by glossopharyngeal neurons projecting to rat carotid body O2-chemoreceptors: role in nitric oxide-mediated efferent inhibition. J. Neurosci. *26*, 9482–9493.

Campanucci, V.C., and Nurse, C.A. (2007). Autonomic innervation of the carotid body: Role in efferent inhibition. Respiratory Physiology & Neurobiology *157*, 83–92.

Campbell, K.P., Leung, A.T., and Sharp, A.H. (1988). The biochemistry and molecular biology of the dihydropyridine-sensitive calcium channel. Trends Neurosci. *11*, 425–430.

Cao, G., Pei, W., Ge, H., Liang, Q., Luo, Y., Sharp, F.R., Lu, A., Ran, R., Graham, S.H., and Chen, J. (2002). In Vivo Delivery of a Bcl-xL Fusion Protein Containing the TAT Protein Transduction Domain Protects against Ischemic Brain Injury and Neuronal Apoptosis. J. Neurosci *22*, 5423–5431.

Carabelli, V., D'Ascenzo, M., Carbone, E., and Grassi, C. (2002). Nitric oxide inhibits neuroendocrine Ca(V)1 L-channel gating via cGMP-dependent protein kinase in cell-attached patches of bovine chromaffin cells. J. Physiol. (Lond.) *541*, 351–366.

Carabelli, V., Marcantoni, A., Comunanza, V., and Carbone, E. (2007a). Fast exocytosis mediated by T- and L-type channels in chromaffin cells: distinct voltage-dependence but similar Ca^{2+} -dependence. Eur. Biophys. J. *36*, 753–762.

Carabelli, V., Marcantoni, A., Comunanza, V., De Luca, A., Díaz, J., Borges, R., and Carbone, E. (2007b). Chronic hypoxia up-regulates alpha1H T-type channels and low-threshold catecholamine secretion in rat chromaffin cells. J. Physiol. (Lond.) *584*, 149–165.

Carbone, E., Giancippoli, A., Marcantoni, A., Guido, D., and Carabelli, V. (2006a). A new role for T-type channels in fast "low-threshold" exocytosis. Cell Calcium *40*, 147–154.

Carbone, E., and Lux, H.D. (1984a). A low voltage-activated calcium conductance in embryonic chick sensory neurons. Biophys. J. *46*, 413–418.

Carbone, E., and Lux, H.D. (1984b). A low voltage-activated, fully inactivating Ca channel in vertebrate sensory neurones. Nature *310*, 501–502.

Carbone, E., Marcantoni, A., Giancippoli, A., Guido, D., and Carabelli, V. (2006b). T-type channels-secretion coupling: evidence for a fast low-threshold exocytosis. Pflügers Archiv: European Journal of Physiology *453*, 373–383.

Cassina, A.M., Hodara, R., Souza, J.M., Thomson, L., Castro, L., Ischiropoulos, H., Freeman, B.A., and Radi, R. (2000). Cytochrome c nitration by peroxynitrite. J. Biol. Chem. *275*, 21409–21415.

Del Castillo, J., and Katz, B. (1954). Quantal components of the end-plate potential. J. Physiol. (Lond.) *124*, 560–573.

Catterall, W.A. (2000). Structure and regulation of voltage-gated Ca^{2+} channels. Annu. Rev. Cell Dev. Biol. *16*, 521–555.

Catterall, W.A. (2005). Biochemical Studies of Voltage-Gated Ca^{2+} Channels. Voltage-Gated calcium Channels 48–60.

Catterall, W.A. (2011). Voltage-gated calcium channels. Cold Spring Harb Perspect Biol *3*, a003947.

Catterall, W.A., Seagar, M.J., and Takahashi, M. (1988). Molecular properties of dihydropyridine-sensitive calcium channels in skeletal muscle. J. Biol. Chem. *263*, 3535–3538.

Catterall, W.A., Striessnig, J., Snutch, T.P.., and Perez-Reyes, E. (2003). International Union of Pharmacology. XL. Compendium of Voltage-Gated Ion Channels: Calcium Channels. Pharmacological Reviews *55*, 579 –581.

Cens, T., Restituito, S., Rousset, M., and Charnet, P. (2005). Role of beta subunits in voltage-gated calcium channel functions. Voltage-Gated calcium Channels *(New York: Kluwer Academic)*, 95–112.

Cens, T., Rousset, M., Kajava, A., and Charnet, P. (2007). Molecular determinant for specific Ca/Ba selectivity profiles of low and high threshold Ca^{2+} channels. J. Gen. Physiol. *130*, 415–425.

Chacur, M., Matos, R.J.B., Alves, A.S., Rodrigues, A.C., Gutierrez, V., Cury, Y., and Britto, L.R.G. (2010). Participation of neuronal nitric oxide synthase in experimental neuropathic pain induced by sciatic nerve transection. Braz. J. Med. Biol. Res. *43*, 367–376.

Chaudhuri, D., Chang, S.-Y., DeMaria, C.D., Alvania, R.S., Soong, T.W., and Yue, D.T. (2004). Alternative splicing as a molecular switch for Ca^{2+}/calmodulin-dependent facilitation of P/Q-Type Ca^{2+} channels. J. Neurosci. *24*, 6334–6342.

Chemin, J., Mezghrani, A., Bidaud, I., Dupasquier, S., Marger, F., Barrère, C., Nargeot, J., and Lory, P. (2007). Temperature-dependent modulation of Ca_v3 T-type calcium channels by protein kinases C and A in mammalian cells. J. Biol. Chem. *282*, 32710–32718.

Chen, C.-C., Lamping, K.G., Nuno, D.W., Barresi, R., Prouty, S.J., Lavoie, J.L., Cribbs, L.L., England, S.K., Sigmund, C.D., Weiss, R.M., et al. (2003a). Abnormal coronary function in mice deficient in alpha1H T-type Ca^{2+} channels. Science *302*, 1416–1418.

Chen, C.-C., Shen, J.-W., Chung, N.-C., Min, M.-Y., Cheng, S.-J., and Liu, I.Y. (2012). Retrieval of Context-Associated Memory is Dependent on the $Ca_v3.2$ T-Type Calcium Channel. PLoS One *7*,.

Chen, Y., Lu, J., Pan, H., Yuehua, Z., Husheng, W.H., Xu, K., Xiaoyan, L.X., Jiang, Y., Bao, X., Yao, Z., et al. (2003b). Association between genetic variation of CACNA1H and childhood absence epilepsy. Annals of Neurology *54*, 239–243.

Chiang, C.-S., Huang, C.-H., Chieng, H., Chang, Y.-T., Chang, D., Chen, J.-J., Chen, Y.-C., Chen, Y.-H., Shin, H.-S., Campbell, K.P., et al. (2009). The $Ca_v3.2$ T-type Ca^{2+} channel is required for pressure overload-induced cardiac hypertrophy in mice. Circ. Res. *104*, 522–530.

Choi, S., Na, H.S., Kim, J., Lee, J., Lee, S., Kim, D., Park, J., Chen, C.C., Campbell, K.P., and Shin, H.S. (2007). Attenuated pain responses in mice lacking $Ca_v3.2$ T-type channels. Genes, Brain and Behavior *6*, 425–431.

Choi, Y., Raja, S.N., Moore, L.C., and Tobin, J.R. (1996). Neuropathic pain in rats is associated with altered nitric oxide synthase activity in neural tissue. J. Neurol. Sci. *138*, 14–20.

Choi, Y.B., Tenneti, L., Le, D.A., Ortiz, J., Bai, G., Chen, H.S., and Lipton, S.A. (2000). Molecular basis of NMDA receptor-coupled ion channel modulation by S-nitrosylation. Nat. Neurosci. *3*, 15–21.

Christopherson, K.S., Hillier, B.J., Lim, W.A., and Bredt, D.S. (1999). PSD-95 Assembles a Ternary Complex with the N-Methyl-D-aspartic Acid Receptor and a Bivalent Neuronal NO Synthase PDZ Domain. J. Biol. Chem. *274*, 27467–27473.

Chuang, R.S., Jaffe, H., Cribbs, L., Perez-Reyes, E., and Swartz, K.J. (1998). Inhibition of T-type voltage-gated calcium channels by a new scorpion toxin. Nat. Neurosci. *1*, 668–674.

Clapham, D.E. (2007). Calcium Signaling. Cell *131*, 1047–1058.

Cohen, C.J., McCarthy, R.T., Barrett, P.Q., and Rasmussen, H. (1988). Ca channels in adrenal glomerulosa cells: K^+ and angiotensin II increase T-type Ca channel current. Proc. Natl. Acad. Sci. U.S.A. *85*, 2412–2416.

Cohen, N.A., Brenman, J.E., Snyder, S.H., and Bredt, D.S. (1996). Binding of the inward rectifier K+ channel Kir 2.3 to PSD-95 is regulated by protein kinase A phosphorylation. Neuron *17*, 759–767.

Comunanza, V., Carbone, E., Marcantoni, A., Sher, E., and Ursu, D. (2011). Calcium-dependent inhibition of T-type calcium channels by TRPV1 activation in rat sensory neurons. Pflugers Arch. *462*, 709–722.

Contreras, D. (2006). The Role of T-Channels in the Generation of Thalamocortical Rhythms. CNS & Neurological Disorders - Drug Targets *5*, 571–585.

Coulter, D.A., Huguenard, J.R., and Prince, D.A. (1989). Calcium currents in rat thalamocortical relay neurones: kinetic properties of the transient, low-threshold current. J. Physiol. (Lond.) *414*, 587–604.

Craig, P.J., Beattie, R.E., Folly, E.A., Banerjee, M.D., Reeves, M.B., Priestley, J.V., Carney, S.L., Sher, E., Perez-Reyes, E., and Volsen, S.G. (1999). Distribution of the voltage-dependent calcium channel alpha1G subunit mRNA and protein throughout the mature rat brain. Eur. J. Neurosci. *11*, 2949–2964.

Cribbs, L.L. (2010). T-type calcium channel expression and function in the diseased heart. Channels (Austin) *4*, 447–452.

Cribbs, L.L., Lee, J.-H., Yang, J., Satin, J., Zhang, Y., Daud, A., Barclay, J., Williamson, M.P., Fox, M., Rees, M., et al. (1998). Cloning and characterization of alpha1H from human heart, a member of the T-Type Ca^{2+} channel gene family. Circ Res *83*, 103–109.

Cribbs, L.L., Martin, B.L., Schroder, E.A., Keller, B.B., Delisle, B.P., and Satin, J. (2001). Identification of the T-Type calcium channel ($Ca_v3.1d$) in developing mouse heart. Circ Res *88*, 403–407.

Crunelli, V., and Leresche, N. (2002). Childhood absence epilepsy: genes, channels, neurons and networks. Nature Reviews Neuroscience *3*, 371–382.

Crunelli, V., Lightowler, S., and Pollard, C.E. (1989). A T-type Ca^{2+} current underlies low-threshold Ca^{2+} potentials in cells of the cat and rat lateral geniculate nucleus. J. Physiol. (Lond.) *413*, 543–561.

Crunelli, V., Toth, T.I., Cope, D.W., Blethyn, K., and Hughes, S.W. (2005). The "window" T-type calcium current in brain dynamics of different behavioural states. J Physiol (Lond) *562*, 121–129.

Currie, K.P.M. (2010). Inhibition of Ca^{2+} Channels and Adrenal Catecholamine Release by G Protein Coupled Receptors. Cell Mol Neurobiol *30*, 1201–1208.

D'Ascenzo, M., Martinotti, G., Azzena, G.B., and Grassi, C. (2002). cGMP/protein kinase G-dependent inhibition of N-type Ca^{2+} channels induced by nitric oxide in human neuroblastoma IMR32 cells. J. Neurosci. *22*, 7485–7492.

Dableh, L.J., and Henry, J.L. (2011). The selective neuronal nitric oxide synthase inhibitor 7-nitroindazole has acute analgesic but not cumulative effects in a rat model of peripheral neuropathy. J Pain Res *4*, 85–90.

Dai, C., Liang, D., Li, H., Sasaki, M., Dawson, T.M., and Dawson, V.L. (2010). Functional Identification of Neuroprotective Molecules. PLoS ONE *5*, e15008.

Darszon, A., López-Martínez, P., Acevedo, J.J., Hernández-Cruz, A., and Treviño, C.L. (2006). T-type Ca^{2+} channels in sperm function. Cell Calcium *40*, 241–252.

David, L.S., Garcia, E., Cain, S.M., Thau, E., Tyson, J.R., and Snutch, T.P. (2010). Splice-variant changes of the $Ca_v3.2$ T-type calcium channel mediate voltage-dependent facilitation and associate with cardiac hypertrophy and development. Channels (Austin) *4*, 375–389.

Davis, B.J. (1991). NADPH-diaphorase activity in the olfactory system of the hamster and rat. J. Comp. Neurol *314*, 493–511.

Dawson, V.L., Dawson, T.M., Bartley, D.A., Uhl, G.R., and Snyder, S.H. (1993). Mechanisms of nitric oxide-mediated neurotoxicity in primary brain cultures. J. Neurosci. *13*, 2651–2661.

Dawson, V.L., Dawson, T.M., London, E.D., Bredt, D.S., and Snyder, S.H. (1991). Nitric oxide mediates glutamate neurotoxicity in primary cortical cultures. Proc. Natl. Acad. Sci. U.S.A. *88*, 6368–6371.

Dawson, V.L., Kizushi, V.M., Huang, P.L., Snyder, S.H., and Dawson, T.M. (1996). Resistance to neurotoxicity in cortical cultures from neuronal nitric oxide synthase-deficient mice. J. Neurosci. *16*, 2479–2487.

DeFelipe, J. (1993). A study of NADPH diaphorase-positive axonal plexuses in the human temporal cortex. Brain Res. *615*, 342–346.

Dejours, P.J. (1962). Chemoreflexes in breathing. Physiol. Rev *42*, 335–358.

Dejours, P.J. (1988). Respiration in Water and Air: Adaptions Regulations Evolution (New York: Elsevier Science Ltd).

DePuy, S.D., Yao, J., Hu, C., McIntire, W., Bidaud, I., Lory, P., Rastinejad, F., Gonzalez, C., Garrison, J.C., and Barrett, P.Q. (2006). The molecular basis for T-type Ca^{2+} channel inhibition by G protein beta2{gamma}2 subunits. PNAS *103*, 14590–14595.

Deschenes, M., Roy, J.P., and Steriade, M. (1982). Thalamic bursting mechanism: an inward slow current revealed by membrane hyperpolarization. Brain Research *239*, 289–293.

Dinerman, J.L., Steiner, J.P., Dawson, T.M., Dawson, V., and Snyder, S.H. (1994). Cyclic nucleotide dependent phosphorylation of neuronal nitric oxide synthase inhibits catalytic activity. Neuropharmacology *33*, 1245–1251.

Dogrul, A., Gardell, L.R., Ossipov, M.H., Tulunay, F.C., Lai, J., and Porreca, F. (2003). Reversal of experimental neuropathic pain by T-type calcium channel blockers. Pain *105*, 159–168.

Dolphin, A.C., Wyatt, C.N., Richards, J., Beattie, R.E., Craig, P., Lee, J.H., Cribbs, L.L., Volsen, S.G., and Perez-Reyes, E. (1999). The effect of alpha2-delta and other accessory subunits on expression and properties of the calcium channel alpha1G. J. Physiol. (Lond.) *519 Pt 1*, 35–45.

Domek-Łopacińska, K., and Strosznajder, J.B. (2005). Cyclic GMP metabolism and its role in brain physiology. J. Physiol. Pharmacol. *56 Suppl 2*, 15–34.

Dong, H., Zhang, P., Song, I., Petralia, R.S., Liao, D., and Huganir, R.L. (1999). Characterization of the glutamate receptor-interacting proteins GRIP1 and GRIP2. J. Neurosci. *19*, 6930–6941.

Doyle, D.A., Lee, A., Lewis, J., Kim, E., Sheng, M., and MacKinnon, R. (1996). Crystal structures of a complexed and peptide-free membrane protein-binding domain: molecular basis of peptide recognition by PDZ. Cell *85*, 1067–1076.

Draper, M.H., and Weidmann, S. (1951). Cardiac resting and action potentials recorded with an intracellular electrode. J. Physiol. (Lond.) *115*, 74–94.

Dreyfus, F.M., Tscherter, A., Errington, A.C., Renger, J.J., Shin, H.-S., Uebele, V.N., Crunelli, V., Lambert, R.C., and Leresche, N. (2010). Selective T-type calcium channel block in thalamic neurons reveals channel redundancy and physiological impact of I_T window. J. Neurosci. *30*, 99–109.

Drolet, P., Bilodeau, L., Chorvatova, A., Laflamme, L., Gallo-Payet, N., and Payet, M.D. (1997). Inhibition of the T-type Ca^{2+} current by the dopamine D1 receptor in rat adrenal glomerulosa cells: requirement of the combined action of the G betagamma protein subunit and cyclic adenosine 3',5'-monophosphate. Mol. Endocrinol. *11*, 503–514.

Dubel, S.J., Altier, C., Chaumont, S., Lory, P., Bourinet, E., and Nargeot, J. (2004). Plasma membrane expression of T-type calcium channel alpha(1) subunits is modulated by high voltage-activated auxiliary subunits. J. Biol. Chem *279*, 29263–29269.

Dubel, S.J., Starr, T.V.B., Hell, J., Ahlijanian, M.K., Enyeart, J.J., Catterall, W.A., and Snutch, T.P. (1992). Molecular Cloning of the {alpha}-1 Subunit of an {omega}-Conotoxin-Sensitive Calcium Channel. PNAS *89*, 5058–5062.

Eckert, D.J., Jordan, A.S., Merchia, P., and Malhotra, A. (2007). Central Sleep Apnea* Pathophysiology and Treatment. Chest *131*, 595–607.

Edgerton, G.B., Blumenthal, K.M., and Hanck, D.A. (2010). Inhibition of the activation pathway of the T-type calcium channel Ca(V)3.1 by ProTxII. Toxicon *56*, 624–636.

Emerick, M.C., Stein, R., Kunze, R., McNulty, M.M., Regan, M.R., Hanck, D.A., and Agnew, W.S. (2006). Profiling the array of Ca(v)3.1 variants from the human T-type calcium channel gene CACNA1G: alternative structures, developmental expression, and biophysical variations. Proteins *64*, 320–342.

Ertel, E.A., Campbell, K.P., Harpold, M.M., Hofmann, F., Mori, Y., Perez-Reyes, E., Schwartz, A., Snutch, T.P., Tanabe, T., Birnbaumer, L., et al. (2000). Nomenclature of voltage-gated calcium channels. Neuron *25*, 533–535.

Fatt, P., and Ginsborg, B.L. (1958). The ionic requirements for the production of action potentials in crustacean muscle fibres. J. Physiol. (Lond.) *142*, 516–543.

Fatt, P., and Katz, B. (1951). An analysis of the end-plate potential recorded with an intracellular electrode. J. Physiol. (Lond.) *115*, 320–370.

Fatt, P., and Katz, B. (1953a). The effect of inhibitory nerve impulses on a crustacean muscle fibre. J. Physiol. (Lond.) *121*, 374–389.

Fatt, P., and Katz, B. (1953b). The electrical properties of crustacean muscle fibres. J. Physiol. (Lond.) *120*, 171–204.

Fawell, S., Seery, J., Daikh, Y., Moore, C., Chen, L.L., Pepinsky, B., and Barsoum, J. (1994). Tat-mediated delivery of heterologous proteins into cells. Proc. Natl. Acad. Sci. U.S.A *91*, 664–668.

Fedulova, S.A., Kostyuk, P.G., and Veselovsky, N.S. (1985). Two types of calcium channels in the somatic membrane of new-born rat dorsal root ganglion neurones. J. Physiol. (Lond.) *359*, 431–446.

Fern, R.J., Hahm, M.S., Lu, H.K., Liu, L.P., Gorelick, F.S., and Barrett, P.Q. (1995). Ca^{2+}/calmodulin-dependent protein kinase II activation and regulation of adrenal glomerulosa Ca^{2+} signaling. Am. J. Physiol. *269*, F751–760.

Ferriero, D.M., Holtzman, D.M., Black, S.M., and Sheldon, R.A. (1996). Neonatal mice lacking neuronal nitric oxide synthase are less vulnerable to hypoxic-ischemic injury. Neurobiol. Dis. *3*, 64–71.

Fleckenstein, A. (1983). History of calcium antagonists. Circ. Res. *52*, I3–16.

Freeze, B.S., McNulty, M.M., and Hanck, D.A. (2006). State-dependent verapamil block of the cloned human Ca(v)3.1 T-type Ca^{2+} channel. Mol. Pharmacol. *70*, 718–726.

Fujita, Y., Mynlieff, M., Dirksen, R.T., Kim, M.S., Niidome, T., Nakai, J., Friedrich, T., Iwabe, N., Miyata, T., and Furuichi, T. (1993). Primary structure and functional expression of the omega-conotoxin-sensitive N-type calcium channel from rabbit brain. Neuron *10*, 585–598.

Fukuto, J.M., Wallace, G.C., Hszieh, R., and Chaudhuri, G. (1992). Chemical oxidation of N-hydroxyguanidine compounds. Release of nitric oxide, nitroxyl and possible relationship to the mechanism of biological nitric oxide generation. Biochem. Pharmacol. *43*, 607–613.

Galiñanes, M., and Matata, B.M. (2002). Protein nitration is predominantly mediated by a peroxynitrite-dependent pathway in cultured human leucocytes. Biochem. J. *367*, 467–473.

Gao, Y., and Strowbridge, B.W. (2009). Long-term plasticity of excitatory inputs to granule cells in the rat olfactory bulb. Nat Neurosci *12*, 731–733.

Garthwaite, J. (2005). Dynamics of cellular NO-cGMP signaling. Front. Biosci. *10*, 1868–1880.

Gee, S.H., Quenneville, S., Lombardo, C.R., and Chabot, J. (2000). Single-Amino Acid Substitutions Alter the Specificity and Affinity of PDZ Domains for Their Ligands. Biochemistry *39*, 14638–14646.

George, M.J., and Shibata, E.F. (1995). Regulation of calcium-activated potassium channels by S-nitrosothiol compounds and cyclic guanosine monophosphate in rabbit coronary artery myocytes. J. Investig. Med. *43*, 451–458.

Giancippoli, A., Novara, M., De Luca, A., Baldelli, P., Marcantoni, A., Carbone, E., and Carabelli, V. (2006). Low-threshold exocytosis induced by cAMP-recruited $Ca_v3.2$ (alpha1H) channels in rat chromaffin cells. Biophys. J. *90*, 1830–1841.

Golowasch, J., Thomas, G., Taylor, A.L., Patel, A., Pineda, A., Khalil, C., and Nadim, F. (2009). Membrane capacitance measurements revisited: dependence of capacitance value on measurement method in nonisopotential neurons. Journal of Neurophysiology *102*, 2161 – 2175.

Gonzalez, C., Almaraz, L., Obeso, A., and Rigual, R. (1994). Carotid body chemoreceptors: from natural stimuli to sensory discharges. Physiol. Rev *74*, 829–898.

Gozal, D., Gozal, E., Gozal, Y.M., and Torres, J.E. (1996a). Nitric oxide synthase isoforms and peripheral chemoreceptor stimulation in conscious rats. Neuroreport *7*, 1145–1148.

Gozal, D., Torres, J.E., Gozal, Y.M., and Littwin, S.M. (1996b). Effect of nitric oxide synthase inhibition on cardiorespiratory responses in the conscious rat. Journal of Applied Physiology *81*, 2068 –2077.

Granik, V.G., and Grigor'ev, N.B. (2002). Nitric oxide synthase inhibitors: biology and chemistry. Russian Chemical Bulletin *51*, 1973–1995.

Grassi, C., D'Ascenzo, M., Valente, A., and Battista Azzena, G. (1999). Ca^{2+} channel inhibition induced by nitric oxide in rat insulinoma RINm5F cells. Pflugers Arch. *437*, 241–247.

Green, M., and Loewenstein, P.M. (1988). Autonomous functional domains of chemically synthesized human immunodeficiency virus tat trans-activator protein. Cell *55*, 1179–1188.

Grimes, P.A., Lahiri, S., Stone, R., Mokashi, A., and Chug, D. (1994). Nitric oxide synthase occurs in neurons and nerve fibers of the carotid body. Adv. Exp. Med. Biol *360*, 221–224.

Guan, Y., Yaster, M., Raja, S.N., and Tao, Y.-X. (2007). Genetic knockout and pharmacologic inhibition of neuronal nitric oxide synthase attenuate nerve injury-induced mechanical hypersensitivity in mice. Mol Pain *3*, 29.

Guix, F.X., Uribesalgo, I., Coma, M., and Munoz, F.J. (2005). The physiology and pathophysiology of nitric oxide in the brain. Progress in Neurobiology *76*, 126–152.

Haedo, R.J., and Golowasch, J. (2006). Ionic mechanism underlying recovery of rhythmic activity in adult isolated neurons. J. Neurophysiol. *96*, 1860–1876.

Hagiwara, S., Ozawa, S., and Sand, O. (1975). Voltage clamp analysis of two inward current mechanisms in the egg cell membrane of a starfish. J. Gen. Physiol. *65*, 617–644.

Hall, C.N., and Garthwaite, J. (2006). Inactivation of nitric oxide by rat cerebellar slices. J. Physiol. (Lond.) *577*, 549–567.

Hansen, P.B., Jensen, B.L., Andreasen, D., and Skott, O. (2001). Differential expression of T- and L-Type voltage-dependent calcium channels in renal resistance vessels. Circ Res *89*, 630–638.

Hao, J.X., and Xu, X.J. (1996). Treatment of a chronic allodynia-like response in spinally injured rats: effects of systemically administered nitric oxide synthase inhibitors. Pain *66*, 313–319.

Hardingham, N., and Fox, K.. (2006). The role of nitric oxide and GluR1 in presynaptic and postsynaptic components of neocortical potentiation. J. Neurosci. *26*, 7395–7404.

Haxhiu, M.A., Chang, C.H., Dreshaj, I.A., Erokwu, B., Prabhakar, N.R., and Cherniack, N.S. (1995). Nitric oxide and ventilatory response to hypoxia. Respiration Physiology *101*, 257–266.

Heafield, M.T.E. (2000). Managing status epilepticus. BMJ *320*, 953–954.

Herlitze, S., and Mark, M.D. (2005). Distribution and targeting mechanisms of voltage activated Ca^{2+} channels. Voltage-Gated calcium Channels 113–140.

Heron, S.E., Phillips, H.A., Mulley, J.C., Mazarib, A., Neufeld, M.Y., Berkovic, S.F., and Scheffer, I.E. (2004). Genetic variation of CACNA1H in idiopathic generalized epilepsy. Annals of Neurology *55*, 595–596.

Hildebrand, M.E., David, L.S., Hamid, J., Mulatz, K.J., Garcia, E., Zamponi, G.W., and Snutch, T.P. (2007). Selective inhibition of $Ca_v3.3$ T-type calcium channels by Galphaq/11-coupled muscarinic acetylcholine receptors. J. Biol. Chem *282*, 21043–21055.

Hildebrand, M.E., Isope, P., Miyazaki, T., Nakaya, T., Garcia, E., Feltz, A., Schneider, T., Hescheler, J., Kano, M., Sakimura, K., et al. (2009). Functional coupling between mGluR1 and $Ca_v3.1$ T-type calcium channels contributes to parallel fiber-induced fast calcium signaling within Purkinje cell dendritic spines. J. Neurosci *29*, 9668–9682.

Hildebrand, M.E., and Snutch, T.P. (2006). Contributions of T-Type Calcium Channels to the Pathophysiology of Pain Signaling. Drug Discovery Today: Disease Mechanisms *3*, 335–341.

Hill, J., Chan, S.-A., Kuri, B., and Smith, C. (2011). Pituitary adenylate cyclase-activating peptide (PACAP) recruits low voltage-activated T-type calcium influx under acute sympathetic stimulation in mouse adrenal chromaffin cells. J. Biol. Chem. *286*, 42459–42469.

Hillier, B.J., Christopherson, K.S., Prehoda, K.E., Bredt, D.S., and Lim, W.A. (1999). Unexpected modes of PDZ domain scaffolding revealed by structure of nNOS-syntrophin complex. Science *284*, 812–815.

Hodgkin, A.L., and Huxley, A.F. (1945). Resting and action potentials in single nerve fibres. J. Physiol. (Lond.) *104*, 176–195.

Hodgkin, A.L., and Katz, B. (1949). The effect of sodium ions on the electrical activity of giant axon of the squid. J. Physiol. (Lond.) *108*, 37–77.

Hodgkin, A.L., and Keynes, R.D. (1957). Movements of labelled calcium in squid giant axons. J. Physiol. (Lond.) *138*, 253–281.

Hofmann, F., Bernhard, D., Lukowski, R., and Weinmeister, P. (2009). cGMP regulated protein kinases (cGK). Handb Exp Pharmacol 137–162.

Hofmann, F., Biel, M., and Flockerzi, V. (1994). Molecular basis for Ca^{2+} channel diversity. Annu. Rev. Neurosci. *17*, 399–418.

Hölscher, C., McGlinchey, L., Anwyl, R., and Rowan, M.J. (1996). 7-Nitro indazole, a selective neuronal nitric oxide synthase inhibitor in vivo, impairs spatial learning in the rat. Learn. Mem. *2*, 267–278.

Hosey, M.M., Chien, A.J., and Puri, T.S. (1996). Structure and regulation of L-type calcium channels a current assessment of the properties and roles of channel subunits. Trends Cardiovasc. Med. *6*, 265–273.

Hsueh, Y.P., Kim, E., and Sheng, M. (1997). Disulfide-linked head-to-head multimerization in the mechanism of ion channel clustering by PSD-95. Neuron *18*, 803–814.

Hsueh, Y.P., and Sheng, M. (1999). Requirement of N-terminal cysteines of PSD-95 for PSD-95 multimerization and ternary complex formation, but not for binding to potassium channel Kv1.4. J. Biol. Chem. *274*, 532–536.

Hu, C., Depuy, S.D., Yao, J., McIntire, W.E., and Barrett, P.Q. (2009). Protein kinase A activity controls the regulation of T-type $Ca_v3.2$ channels by Gbetagamma dimers. J. Biol. Chem *284*, 7465–7473.

Huang, B., Qin, D., Deng, L., Boutjdir, M., and E1-Sherif, N. (2000). Reexpression of T-type Ca^{2+} channel gene and current in post-infarction remodeled rat left ventricle. Cardiovasc. Res. *46*, 442–449.

Hughes, S.W., Cope, D.W., Tóth, T.I., Williams, S.R., and Crunelli, V. (1999). All thalamocortical neurones possess a T-type Ca^{2+} "window" current that enables the expression of bistability-mediated activities. J. Physiol. (Lond.) *517 (Pt 3)*, 805–815.

Huguenard, J.R. (1996). Low-threshold calcium currents in central nervous system neurons. Annu. Rev. Physiol *58*, 329–348.

Huguenard, J.R., and Prince, D.A. (1992). A novel T-type current underlies prolonged Ca^{2+}-dependent burst firing in GABAergic neurons of rat thalamic reticular nucleus. J. Neurosci. *12*, 3804–3817.

Hui, A., Ellinor, P.T., Krizanova, O., Wang, J.-D., Diebold, R.J., and Schwartz, A. (1991). Molecular cloning of multiple subtypes of a novel rat brain isoform of the α1 subunit of the voltage-dependent calcium channel. Neuron *7*, 35–44.

Hung, A.Y., and Sheng, M. (2002). PDZ Domains: Structural Modules for Protein Complex Assembly. J. Biol. Chem. *277*, 5699–5702.

Hurshman, A.R., Krebs, C., Edmondson, D.E., and Marletta, M.A. (2003). Ability of tetrahydrobiopterin analogues to support catalysis by inducible nitric oxide synthase: formation of a pterin radical is required for enzyme activity. Biochemistry *42*, 13287–13303.

Huxley, A.F., and Stampfli, R. (1951). Effect of potassium and sodium on resting and action potentials of single myelinated nerve fibers. J. Physiol. (Lond.) *112*, 496–508.

Iftinca, M.C. (2011). Neuronal T-type calcium channels: what's new? Iftinca: T-type channel regulation. J Med Life *4*, 126–138.

Iftinca, M.C., Hamid, J., Chen, L., Varela, D., Tadayonnejad, R., Altier, C., Turner, R.W., and Zamponi, G.W. (2007). Regulation of T-type calcium channels by Rho-associated kinase. Nat. Neurosci. *10*, 854–860.

Iftinca, M.C., and Zamponi, G.W. (2009). Regulation of neuronal T-type calcium channels. Trends Pharmacol. Sci. *30*, 32–40.

Ignarro, L.J. (1989). Endothelium-derived nitric oxide: actions and properties. FASEB J. *3*, 31–36.

Islam, M.S. (2011). Transient Receptor Potential Channels (Springer).

Ivanina, T., Blumenstein, Y., Shistik, E., Barzilai, R., and Dascal, N. (2000). Modulation of L-type Ca^{2+} channels by gbeta gamma and calmodulin via interactions with N and C termini of alpha 1C. J. Biol. Chem. *275*, 39846–39854.

Iwasaki, S., Chihara, Y., Komuta, Y., Ito, K., and Sahara, Y. (2008). Low-voltage-activated potassium channels underlie the regulation of intrinsic firing properties of rat vestibular ganglion cells. J. Neurophysiol. *100*, 2192–2204.

Jacky, J.P. (1978). A plethysmograph for long-term measurements of ventilation in unrestrained animals. J Appl Physiol *45*, 644–647.

Jacky, J.P. (1980). Barometric measurement of tidal volume: effects of pattern and nasal temperature. J Appl Physiol *49*, 319–325.

Jacoby, S., Sims, R.E., and Hartell, N.A. (2001). Nitric oxide is required for the induction and heterosynaptic spread of long-term potentiation in rat cerebellar slices. J. Physiol. (Lond.) *535*, 825–839.

Jacus, M.O., Uebele, V.N., Renger, J.J., and Todorovic, S.M. (2012). Presynaptic $Ca_V3.2$ channels regulate excitatory neurotransmission in nociceptive dorsal horn neurons. J. Neurosci. *32*, 9374–9382.

Jaffrey, S.R., Erdjument-Bromage, H., Ferris, C.D., Tempst, P., and Snyder, S.H. (2001). Protein S-nitrosylation: a physiological signal for neuronal nitric oxide. Nat. Cell Biol. *3*, 193–197.

Jaffrey, S.R., Snowman, A.M., Eliasson, M.J.L., Cohen, N.A., and Snyder, S.H. (1998). CAPON: A Protein Associated with Neuronal Nitric Oxide Synthase that Regulates Its Interactions with PSD95. Neuron *20*, 115–124.

Jagannathan, S., Punt, E.L., Gu, Y., Arnoult, C., Sakkas, D., Barratt, C.L.R., and Publicover, S.J. (2002). Identification and localization of T-Type voltage-operated calcium channel subunits in human male germ cells EXPRESSION OF MULTIPLE ISOFORMS. J. Biol. Chem. *277*, 8449–8456.

Jagodic, M.M., Pathirathna, S., Nelson, M.T., Mancuso, S., Joksovic, P.M., Rosenberg, E.R., Bayliss, D.A., Jevtovic-Todorovic, V., and Todorovic, S.M. (2007). Cell-specific alterations of T-type calcium current in painful diabetic neuropathy enhance excitability of sensory neurons. J. Neurosci *27*, 3305–3316.

Jahnsen, H., and Llinás, R. (1984). Ionic basis for the electro-responsiveness and oscillatory properties of guinea-pig thalamic neurones in vitro. The Journal of Physiology *349*, 227–247.

Jang, J.H., Kim, D.-W., Sang Nam, T., Se Paik, K., and Leem, J.W. (2004). Peripheral glutamate receptors contribute to mechanical hyperalgesia in a neuropathic pain model of the rat. Neuroscience *128*, 169–176.

Janssens, S.P., Shimouchi, A., Quertermous, T., Bloch, D.B., and Bloch, K.D. (1992). Cloning and expression of a cDNA encoding human endothelium-derived relaxing factor/nitric oxide synthase. J. Biol. Chem. *267*, 14519–14522.

Jay, S.D., Ellis, S.B., McCue, A.F., Williams, M.E., Vedvick, T.S., Harpold, M.M., and Campbell, K.P. (1990). Primary structure of the gamma subunit of the DHP-sensitive calcium channel from skeletal muscle. Science *248*, 490–492.

Jevtovic-Todorovic, V., and Todorovic, S.M. (2006). The role of peripheral T-type calcium channels in pain transmission. Cell Calcium *40*, 197–203.

Jimenez, C., Bourinet, E., Leuranguer, V., Sylvain, R., Snutch, T.P., and Nargeot, J. (2000). Determinants of voltage-dependent inactivation affect Mibefradil block of calcium channels. Neuropharmacology *39*, 1–10.

Joksovic, P.M., Bayliss, D.A., and Todorovic, S.M. (2005). Different kinetic properties of two T-type Ca^{2+} currents of rat reticular thalamic neurones and their modulation by enflurane. J. Physiol. (Lond.) *566*, 125–142.

Joksovic, P.M., Doctor, A., Gaston, B., and Todorovic, S.M. (2007). Functional regulation of T-type calcium channels by s-nitrosothiols in the rat thalamus. J. Neurophysiol *97*, 2712–2721.

Joksovic, P.M., Nelson, M.T., Jevtovic-Todorovic, V., Patel, M.K., Perez-Reyes, E., Campbell, K.P., Chen, C.-C., and Todorovic, S.M. (2006). $Ca_V3.2$ is the major molecular

substrate for redox regulation of T-type Ca^{2+} channels in the rat and mouse thalamus. J Physiol (Lond) *574*, 415–430.

Joseph, V., and Pequignot, J.-M. (2009). Breathing at high altitude. Cell. Mol. Life Sci. *66*, 3565–3573.

Kaba, H., and Huang, G.-Z. (2005). Long-term potentiation in the accessory olfactory bulb: A mechanism for olfactory learning. Chem. Senses *30*, i150–151.

Kaku, T. (2003). The gating and conductance properties of $Ca_v3.2$ Low-voltage-activated T-Type calcium channels. Japanese Journal of Physiology *53*, 165–172.

Kandel, E.R., Schwartz, J.H., and Jessell, T.M. (2000). The Perception of Pain. Principles of Neural Science *(New York: McGraw-Hill)*, 472–491.

Kaneda, M., Wakamori, M., Ito, C., and Akaike, N. (1990). Low-threshold calcium current in isolated Purkinje cell bodies of rat cerebellum. J. Neurophysiol. *63*, 1046–1051.

Kang, H.-W., Park, J.-Y., Jeong, S.-W., Kim, J.-A., Moon, H.-J., Perez-Reyes, E., and Lee, J.-H. (2006). A molecular determinant of nickel inhibition in $Ca_v3.2$ T-type calcium channels. J. Biol. Chem. *281*, 4823–4830.

Katz, B., and Miledi, R. (1967). A study of synaptic transmission in the absence of nerve impulses. J. Physiol. (Lond.) *192*, 407–436.

Katz, B., and Miledi, R. (1970). Further study of the role of calcium in synaptic transmission. J. Physiol. (Lond.) *207*, 789–801.

Kaupp, U.B., and Seifert, R. (2002). Cyclic nucleotide-gated ion channels. Physiol. Rev. *82*, 769–824.

Kawai, F., and Miyachi, E. (2001). Enhancement by T-Type Ca^{2+} currents of odor sensitivity in olfactory receptor cells. J. Neurosci. *21*, 144RC.

Keith, D., and El-Husseini, A. (2008). Excitation control: Balancing PSD-95 function at the synapse. Front Mol Neurosci *1*, 4.

Khorkova, O., and Golowasch, J. (2007). Neuromodulators, not activity, control coordinated expression of ionic currents. J. Neurosci. *27*, 8709–8718.

Khosravani, H., and Zamponi, G.W. (2006). Voltage-gated calcium channels and idiopathic generalized epilepsies. Physiol. Rev. *86*, 941–966.

Kim, D., Park, D., Choi, S., Lee, S., Sun, M., Kim, C., and Shin, H.-S. (2003). Thalamic control of visceral nociception mediated by T-type Ca^{2+} channels. Science *302*, 117–119.

Kim, D., Song, I., Keum, S., Lee, T., Jeong, M.J., Kim, S.S., McEnery, M.W., and Shin, H.-S. (2001). Lack of the burst firing of thalamocortical relay neurons and resistance to absence seizures in mice lacking alpha(1G) T-type Ca^{2+} channels. Neuron *31*, 35–45.

Kim, E., Niethammer, M., Rothschild, A., Jan, Y.N., and Sheng, M. (1995). Clustering of Shaker-type K^+ channels by interaction with a family of membrane-associated guanylate kinases. Nature *378*, 85–88.

Kim, J.-A., Park, J.-Y., Kang, H.-W., Huh, S.-U., Jeong, S.-W., and Lee, J.-H. (2006). Augmentation of $Ca_v3.2$ T-type Calcium Channel Activity by cAMP-dependent Protein Kinase A. J Pharmacol Exp Ther jpet.106.101402.

Kim, K.H., Kim, J.-I., Han, J.A., Choe, M.-A., and Ahn, J.-H. (2011). Upregulation of neuronal nitric oxide synthase in the periphery promotes pain hypersensitivity after peripheral nerve injury. Neuroscience *190*, 367–378.

Kim, M.S., Morii, T., Sun, L.X., Imoto, K., and Mori, Y. (1993). Structural determinants of ion selectivity in brain calcium channel. FEBS Lett. *318*, 145–148.

Kim, T., Choi, J., Kim, S., Kwon, O., Nah, S.-Y., Han, Y.-S., and Rhim, H. (2004). The biochemical activation of T-type Ca^{2+} channels in HEK293 cells stably expressing alpha1G and Kir2.1 subunits. Biochemical and Biophysical Research Communications *324*, 401–408.

Kim, Y., Park, M.K., Uhm, D.-Y., and Chung, S. (2007). Modulation of T-type Ca^{2+} channels by corticotropin-releasing factor through protein kinase C pathway in MN9D dopaminergic cells. Biochem. Biophys. Res. Commun. *358*, 796–801.

Kinjo, N., Skinner, R.D., and Powell, E.W. (1989). A study of NADPH-diaphorase positive septohippocampal neurons in rat. Neurosci. Res *7*, 154–158.

Kissner, R., Nauser, T., Bugnon, P., Lye, P.G., and Koppenol, W.H. (1997). Formation and properties of peroxynitrite as studied by laser flash photolysis, high-pressure stopped-flow technique, and pulse radiolysis. Chem. Res. Toxicol. *10*, 1285–1292.

Kleppisch, T., and Feil, R. (2009). cGMP signalling in the mammalian brain: role in synaptic plasticity and behaviour. Handb Exp Pharmacol 549–579.

Kline, D.D., Overholt, J.L., and Prabhakar, N.R. (2002). Mutant mice deficient in NOS-1 exhibit attenuated long-term facilitation and short-term potentiation in breathing. J. Physiol. (Lond.) *539*, 309–315.

Kline, D.D., Ramirez-Navarro, A., and Kunze, D.L. (2007). Adaptive depression in synaptic transmission in the nucleus of the solitary tract after in vivo chronic intermittent hypoxia: evidence for homeostatic plasticity. J. Neurosci *27*, 4663–4673.

Kline, D.D., Yang, T., Huang, P.L., and Prabhakar, N.R. (1998). Altered respiratory responses to hypoxia in mutant mice deficient in neuronal nitric oxide synthase. J. Physiol. (Lond.) *511 (Pt 1)*, 273–287.

Kline, D.D., Yang, T., Premkumar, D.R., Thomas, A.J., and Prabhakar, N.R. (2000). Blunted respiratory responses to hypoxia in mutant mice deficient in nitric oxide synthase-3. J. Appl. Physiol *88*, 1496–1508.

Klöckner, U., Lee, J.H., Cribbs, L.L., Daud, A., Hescheler, J., Pereverzev, A., Perez-Reyes, E., and Schneider, T. (1999). Comparison of the Ca2 + currents induced by expression of three cloned alpha1 subunits, alpha1G, alpha1H and alpha1I, of low-voltage-activated T-type Ca^{2+} channels. Eur. J. Neurosci. *11*, 4171–4178.

Koch, W.J., Ellinor, P.T., and Schwartz, A. (1990). cDNA cloning of a dihydropyridine-sensitive calcium channel from rat aorta. Evidence for the existence of alternatively spliced forms. J. Biol. Chem. *265*, 17786–17791.

Kolesnikov, Y.A., Chereshnev, I., Criesta, M., Pan, Y.-X., and Pasternak, G.W. (2009). Opposing actions of neuronal nitric oxide synthase isoforms in formalin-induced pain in mice. Brain Res. *1289*, 14–21.

Kolesnikov, Y.A., Pick, C.G., Ciszewska, G., and Pasternak, G.W. (1993). Blockade of tolerance to morphine but not to kappa opioids by a nitric oxide synthase inhibitor. Proc. Natl. Acad. Sci. U.S.A. *90*, 5162–5166.

Kornau, H.C., Schenker, L.T., Kennedy, M.B., and Seeburg, P.H. (1995). Domain interaction between NMDA receptor subunits and the postsynaptic density protein PSD-95. Science *269*, 1737–1740.

Kowall, N.W., Beal, M.F., Ferrante, R.J., and Martin, J.B. (1985). Topography of nicotinamide adenine dinucleotide phosphate-diaphorase staining neurons in rat striatum. Neurosci. Lett *59*, 61–66.

Koylu, E.O., Kanit, L., Taskiran, D., Dagci, T., Balkan, B., and Pogun, S. (2005). Effects of nitric oxide synthase inhibition on spatial discrimination learning and central DA2 and mACh receptors. Pharmacol. Biochem. Behav. *81*, 32–40.

Kozlov, A.S., McKenna, F., Lee, J.H., Cribbs, L.L., Perez-Reyes, E., Feltz, A., and Lambert, R.C. (1999). Distinct kinetics of cloned T-type Ca2 + channels lead to differential Ca2 + entry and frequency-dependence during mock action potentials. Eur. J. Neurosci. *11*, 4149–4158.

Krahe, R., and Gabbiani, F. (2004). Burst firing in sensory systems. Nat Rev Neurosci *5*, 13–23.

Kraus, R.L., Li, Y., Jovanovska, A., and Renger, J.J. (2007). Trazodone inhibits T-type calcium channels. Neuropharmacology *53*, 308–317.

Krumenacker, J.S., Hanafy, K.A., and Murad, F. (2004). Regulation of nitric oxide and soluble guanylyl cyclase. Brain Research Bulletin *62*, 505–515.

Kurejová, M., Lacinová, L., Pavlovicová, M., Eschbach, M., and Klugbauer, N. (2007). The effect of the outermost basic residues in the S4 segments of the $Ca_v3.1$ T-type calcium channel on channel gating. Pflugers Arch. *455*, 527–539.

Lam, A.D., Chikina, M.D., McNulty, M.M., Glaaser, I.W., and Hanck, D.A. (2005). Role of Domain IV/S4 outermost arginines in gating of T-type calcium channels. Pflugers Arch. *451*, 349–361.

Lamas, S., Marsden, P.A., Li, G.K., Tempst, P., and Michel, T. (1992). Endothelial nitric oxide synthase: molecular cloning and characterization of a distinct constitutive enzyme isoform. Proc. Natl. Acad. Sci. U.S.A. *89*, 6348–6352.

Lancaster, J.R.J. (1994). Simulation of the diffusion and reaction of endogenously produced nitric oxide. Proc. Natl. Acad. Sci. U.S.A. *91*, 8137–8141.

Lee, H.-J., and Zheng, J.J. (2010). PDZ domains and their binding partners: structure, specificity, and modification. Cell Commun Signal *8*, 8.

Lee, J.-H., Daud, A.N., Cribbs, L.L., Lacerda, A.E., Pereverzev, A., Klockner, U., Schneider, T., and Perez-Reyes, E. (1999a). Cloning and expression of a novel member of the low voltage-activated T-Type calcium channel family. J. Neurosci. *19*, 1912–1921.

Lee, J.-H., Gomora, J.C., Cribbs, L.L., and Perez-Reyes, E. (1999b). Nickel block of three cloned T-Type calcium channels: low concentrations selectively block alpha 1H. Biophys. J. *77*, 3034–3042.

Lee, J.-H., Kim, E.-G., Park, B.-G., Kim, K.-H., Cha, S.-K., Kong, I.D., Lee, J.-W., and Jeong, S.-W. (2002). Identification of T-type alpha1H Ca^{2+} channels ($Ca_v3.2$) in major pelvic ganglion neurons. J. Neurophysiol *87*, 2844–2850.

Leigh, P.N. (1990). Distribution of NADPH-diaphoase positive cells in the rat brain. Comp Biochem Physiol *97C*, 259–264.

Letts, V.A., Felix, R., Biddlecome, G.H., Arikkath, J., Mahaffey, C.L., Valenzuela, A., Bartlett, F.S., 2nd, Mori, Y., Campbell, K.P., and Frankel, W.N. (1998). The mouse stargazer gene encodes a neuronal Ca^{2+}-channel gamma subunit. Nat. Genet. *19*, 340–347.

Levitsky, K.L., and López-Barneo, J. (2009). Developmental change of T-type Ca^{2+} channel expression and its role in rat chromaffin cell responsiveness to acute hypoxia. J. Physiol. (Lond.) *587*, 1917–1929.

Li, H., and Poulos, T.L. (2005). Structure-function studies on nitric oxide synthases. J Inorg Biochem *99*, 293–305.

Li, Y., Liu, S., Lu, F., Zhang, T., Chen, H., Wu, S., and Zhuang, H. (2009). A role of functional T-type Ca^{2+} channel in hepatocellular carcinoma cell proliferation. Oncol. Rep. *22*, 1229–1235.

Liu, X., Miller, M.J., Joshi, M.S., Sadowska-Krowicka, H., Clark, D.A., and Lancaster, J.R.J. (1998). Diffusion-limited reaction of free nitric oxide with erythrocytes. J. Biol. Chem. *273*, 18709–18713.

Llinás, R., and Jahnsen, H. (1982). Electrophysiology of mammalian thalamic neurones in vitro. Nature *297*, 406–408.

Llinás, R., Sugimori, M., Hillman, D.E., and Cherksey, B. (1992). Distribution and functional significance of the P-type, voltage-dependent Ca^{2+} channels in the mammalian central nervous system. Trends Neurosci. *15*, 351–355.

Llinás, R., Sugimori, M., Lin, J.W., and Cherksey, B. (1989). Blocking and isolation of a calcium channel from neurons in mammals and cephalopods utilizing a toxin fraction (FTX) from funnel-web spider poison. Proc. Natl. Acad. Sci. U.S.A. *86*, 1689–1693.

Llinás, R., and Yarom, Y. (1981). Electrophysiology of mammalian inferior olivary neurones in vitro. Different types of voltage-dependent ionic conductances. J. Physiol. (Lond.) *315*, 549–567.

Lory, P., Ophoff, R.A., and Nahmias, J. (1997). Towards a unified nomenclature describing voltage-gated calcium channel genes. Hum. Genet. *100*, 149–150.

Lowenstein, C.J., Alley, E.W., Raval, P., Snowman, A.M., Snyder, S.H., Russell, S.W., and Murphy, W.J. (1993). Macrophage nitric oxide synthase gene: two upstream regions mediate induction by interferon gamma and lipopolysaccharide. Proc. Natl. Acad. Sci. U.S.A. *90*, 9730–9734.

Lu, H.K., Fern, R.J., Nee, J.J.., and Barrett, P.Q. (1994). Ca^{2+}-dependent activation of T-type Ca^{2+} channels by calmodulin-dependent protein kinase II. Am. J. Physiol. *267*, F183–189.

Lu, W., and Ziff, E.B. (2005). PICK1 interacts with ABP/GRIP to regulate AMPA receptor trafficking. Neuron *47*, 407–421.

Luo, Z.D., Chaplan, S.R., Scott, B.P., Cizkova, D., Calcutt, N.A., and Yaksh, T.L. (1999). Neuronal nitric oxide synthase mRNA upregulation in rat sensory neurons after spinal nerve ligation: lack of a role in allodynia development. J. Neurosci. *19*, 9201–9208.

Lyons, C.R., Orloff, G.J., and Cunningham, J.M. (1992). Molecular cloning and functional expression of an inducible nitric oxide synthase from a murine macrophage cell line. J. Biol. Chem. *267*, 6370–6374.

Ma, S., Abboud, F.M., and Felder, R.B. (1995). Effects of L-arginine-derived nitric oxide synthesis on neuronal activity in nucleus tractus solitarius. Am. J. Physiol *268*, R487–491.

Magee, T., Fuentes, A.M., Garban, H., Rajavashisth, T., Marquez, D., Rodriguez, J.A., Rajfer, J., and Gonzalez-Cadavid, N.F. (1996). Cloning of a novel neuronal nitric oxide synthase expressed in penis and lower urinary tract. Biochem. Biophys. Res. Commun. *226*, 145–151.

Malan, A. (1973). Ventilation measured by body plethysmography in hibernating mammals and in poikilotherms. Respir Physiol *17*, 32–44.

Malinski, T., Bailey, F., Zhang, Z.G., and Chopp, M. (1993). Nitric oxide measured by a porphyrinic microsensor in rat brain after transient middle cerebral artery occlusion. J. Cereb. Blood Flow Metab. *13*, 355–358.

Mangoni, M.E., Traboulsie, A., Leoni, A.-L., Couette, B., Marger, L., Le Quang, K., Kupfer, E., Cohen-Solal, A., Vilar, J., Shin, H.-S., et al. (2006). Bradycardia and slowing of the atrioventricular conduction in mice lacking $Ca_v3.1$/alpha1G T-type calcium channels. Circ. Res. *98*, 1422–1430.

Manzoni, O., Prezeau, L., Marin, P., Deshager, S., Bockaert, J., and Fagni, L. (1992). Nitric oxide-induced blockade of NMDA receptors. Neuron *8*, 653–662.

Markandeya, Y.S., Fahey, J.M., Pluteanu, F., Cribbs, L.L., and Balijepalli, R.C. (2011). Caveolin-3 regulates protein kinase A modulation of the $Ca_v3.2$ (alpha1H) T-type Ca^{2+} channels. J. Biol. Chem. *286*, 2433–2444.

Marshall, H.E., and Stamler, J.S. (2001). Inhibition of NF-kappa B by S-nitrosylation. Biochemistry *40*, 1688–1693.

Martin, R.L., Lee, J.H., Cribbs, L.L., Perez-Reyes, E., and Hanck, D.A. (2000). Mibefradil block of cloned T-type calcium channels. J. Pharmacol. Exp. Ther. *295*, 302–308.

Martínez, M.L., Heredia, M.P., and Delgado, C. (1999). Expression of T-type Ca^{2+} channels in ventricular cells from hypertrophied rat hearts. J. Mol. Cell. Cardiol. *31*, 1617–1625.

Matteson, D.R., and Armstrong, C.M. (1986). Properties of two types of calcium channels in clonal pituitary cells. J. Gen. Physiol. *87*, 161–182.

Mayer, B. (1995). Biochemistry and molecular pharamacology of nitric oxide synthases. In NItric Oxide in the Nervous System, (San Diego: Academic Press), pp. 21–42.

McCauley, A.K., Meyer, G.A., and Godwin, D.W. (2002). Developmental regulation of brain nitric oxide synthase expression in the ferret thalamic reticular nucleus. Neuroscience Letters *320*, 151–155.

McCleskey, E.W., Fox, A.P., Feldman, D.H., Cruz, L.J., Olivera, B.M., Tsien, R.W., and Yoshikami, D. (1987). Omega-conotoxin: direct and persistent blockade of specific types of calcium channels in neurons but not muscle. Proc. Natl. Acad. Sci. U.S.A. *84*, 4327–4331.

McCobb, D.P., and Beam, K.G. (1991). Action potential waveform voltage-clamp commands reveal striking differences in calcium entry via low and high voltage activated calcium channels. Neuron *7*, 119–127.

McDonald, T.F., Pelzer, S., Trautwein, W., and Pelzer, D.J. (1994). Regulation and modulation of calcium channels in cardiac, skeletal, and smooth muscle cells. Physiol. Rev. *74*, 365–507.

McKay, B.E. (2006). Ca_v3 T-type calcium channel isoforms differentially distribute to somatic and dendrtic compartments in rat central neurons. European Journal of Neuroscience *24*, 2581–2594.

McRory, J.E., Santi, C.M., Hamming, K.S.C., Mezeyova, J., Sutton, K.G., Baillie, D.L., Stea, A., and Snutch, T.P. (2001). Molecular and functional characterization of a family of rat brain T-type calcium channels. J. Biol. Chem. *276*, 3999–4011.

Meller, S.T., Pechman, P.S., Gebhart, G.F., and Maves, T.J. (1992). Nitric oxide mediates the thermal hyperalgesia produced in a model of neuropathic pain in the rat. Neuroscience *50*, 7–10.

Meyer, G., and González-Hernández, T. (1993). Developmental changes in layer I of the human neocortex during prenatal life: a DiI-tracing and AChE and NADPH-d histochemistry study. J. Comp. Neurol. *338*, 317–336.

Meyer, G., Gonzalez-Hernandez, T., Galindo-Mireles, D., Castañeyra-Perdomo, A., and Ferres-Torres, R. (1991). The efferent projections of neurons in the white matter of different cortical areas of the adult rat. Anat. Embryol *184*, 99–102.

Mikami, A., Imoto, K., Tanabe, T., Niidome, T., Mori, Y., Takeshima, H., Narumiya, S., and Numa, S. (1989). Primary structure and functional expression of the cardiac dihydropyridine-sensitive calcium channel. Nature *340*, 230–233.

Mintz, I.M., Venema, V.J., Swiderek, K.M., Lee, T.D., Bean, B.P., and Adams, M.E. (1992). P-type calcium channels blocked by the spider toxin omega-Aga-IVA. Nature *355*, 827–829.

Mizukawa, K. (1989). Distribution of reduced-nictoinamide-adenine-dinucleotide-phosphate diaphorase-positive cells and fibers in the cat central nervous system. Journal of Comparative Neurology *279*,.

Mizukawa, K., Vincent, S.R., McGeer, P.L., and McGeer, E.G. (1988). Reduced nicotinamide adenine dinucleotide phosphate (NADPH)-diaphorase-positive neurons in cat cerebral white matter. Brain Res. *461*, 274–281.

Mlinar, B., Biagi, B.A., and Enyeart, J.J. (1993). Voltage-gated transient currents in bovine adrenal fasciculata cells. I. T-type Ca^{2+} current. J. Gen. Physiol. *102*, 217–237.

Moilanen, E., and Vapaatalo, H. (1995). Nitric oxide in inflammation and immune response. Ann. Med. *27*, 359–367.

Monteil, A., Chemin, J., Bourinet, E., Mennessier, G., Lory, P., and Nargeot, J. (2000a). Molecular and functional properties of the human alpha(1G) subunit that forms T-type calcium channels. J. Biol. Chem. *275*, 6090–6100.

Monteil, A., Chemin, J., Leuranguer, V., Altier, C., Mennessier, G., Bourinet, E., Lory, P., and Nargeot, J. (2000b). Specific properties of T-type calcium channels generated by the human alpha 1I subunit. J. Biol. Chem. *275*, 16530–16535.

Mori, Y., Friedrich, T., Kim, M.S., Mikami, A., Nakai, J., Ruth, P., Bosse, E., Hofmann, F., Flockerzi, V., and Furuichi, T. (1991). Primary structure and functional expression from complementary DNA of a brain calcium channel. Nature *350*, 398–402.

Murphy, M.E., and Sies, H. (1991). Reversible conversion of nitroxyl anion to nitric oxide by superoxide dismutase. Proc. Natl. Acad. Sci. U.S.A. *88*, 10860–10864.

Na, H.S., Choi, S., Kim, J., Park, J., and Shin, H.-S. (2008). Attenuated neuropathic pain in $Ca_v3.1$ null mice. Mol. Cells *25*, 242–246.

Nakane, M., Schmidt, H.H., Pollock, J.S., Förstermann, U., and Murad, F. (1993). Cloned human brain nitric oxide synthase is highly expressed in skeletal muscle. FEBS Lett. *316*, 175–180.

Nastuk, W.L., and Hodgkin, A.L. (1950). The electrical activity of single muscle fibres. J Cell Comp Physl 39–73.

Nathan, C.F., and Hibbs, J.B.J. (1991). Role of nitric oxide synthesis in macrophage antimicrobial activity. Curr. Opin. Immunol. *3*, 65–70.

Naylor, M.J., Rancourt, D.E., and Bech-Hansen, N.T. (2000). Isolation and characterization of a calcium channel gene, Cacna1f, the murine orthologue of the gene for incomplete X-linked congenital stationary night blindness. Genomics *66*, 324–327.

Nelson, M.T., Joksovic, P.M., Perez-Reyes, E., and Todorovic, S.M. (2005). The endogenous redox agent L-cysteine induces T-Type Ca^{2+} channel-dependent sensitization of a novel subpopulation of rat peripheral nociceptors. J. Neurosci. *25*, 8766–8775.

Nelson, M.T., Joksovic, P.M., Su, P., Kang, H.-W., Van Deusen, A., Baumgart, J.P., David, L.S., Snutch, T.P., Barrett, P.Q., Lee, J.-H., et al. (2007a). Molecular mechanisms of subtype-specific inhibition of neuronal T-Type calcium channels by ascorbate. J. Neurosci. *27*, 12577–12583.

Nelson, M.T., Woo, J., Kang, H.-W., Vitko, I., Barrett, P.Q., Perez-Reyes, E., Lee, J.-H., Shin, H.-S., and Todorovic, S.M. (2007b). Reducing agents sensitize C-Type nociceptors by relieving high-affinity zinc inhibition of T-Type calcium channels. J. Neurosci. *27*, 8250–8260.

Newcomb, R., Szoke, B., Palma, A., Wang, G., Chen, X.H., Hopkins, W., Cong, R., Miller, J., Urge, L., Tarczy-Hornoch, K., et al. (1998). Selective peptide antagonist of the class E calcium channel from the venom of the tarantula Hysterocrates gigas. Biochemistry *37*, 15353–15362.

Newman, D.K., Hoffman, S., Kotamraju, S., Zhao, T., Wakim, B., Kalyanaraman, B., and Newman, P.J. (2002). Nitration of PECAM-1 ITIM tyrosines abrogates phosphorylation and SHP-2 binding. Biochem. Biophys. Res. Commun. *296*, 1171–1179.

Niethammer, M., Kim, E., and Sheng, M. (1996). Interaction between the C terminus of NMDA receptor subunits and multiple members of the PSD-95 family of membrane-associated guanylate kinases. J. Neurosci. *16*, 2157–2163.

Niethammer, M., Valtschanoff, J.G., Kapoor, T.M., Allison, D.W., Weinberg, R.J., Craig, A.M., and Sheng, M. (1998). CRIPT, a novel postsynaptic protein that binds to the third PDZ domain of PSD-95/SAP90. Neuron *20*, 693–707.

Niidome, T., Kim, M.S., Friedrich, T., and Mori, Y. (1992). Molecular cloning and characterization of a novel calcium channel from rabbit brain. FEBS Lett. *308*, 7–13.

Niwa, N., Yasui, K., Opthof, T., Takemura, H., Shimizu, A., Horiba, M., Lee, J.-K., Honjo, H., Kamiya, K., and Kodama, I. (2004). $Ca_V3.2$ subunit underlies the functional T-type Ca^{2+} channel in murine hearts during the embryonic period. Am. J. Physiol. Heart Circ. Physiol. *286*, H2257–2263.

Novara, M., Baldelli, P., Cavallari, D., Carabelli, V., Giancippoli, A., and Carbone, E. (2004). Exposure to cAMP and beta-adrenergic stimulation recruits Ca_v3 T-type channels in rat chromaffin cells through Epac cAMP-receptor proteins. J. Physiol. (Lond.) *558*, 433–449.

Nowycky, M.C., Fox, A.P., and Tsien, R.W. (1985). Three types of neuronal calcium channel with different calcium agonist sensitivity. Nature *316*, 440–443.

Nuss, H.B., and Houser, S.R. (1993). T-type Ca^{2+} current is expressed in hypertrophied adult feline left ventricular myocytes. Circ. Res. *73*, 777–782.

O'Donnell, V.B., Chumley, P.H., Hogg, N., Bloodsworth, A., Darley-Usmar, V.M., and Freeman, B.A. (1997). Nitric oxide inhibition of lipid peroxidation: kinetics of reaction with lipid peroxyl radicals and comparison with alpha-tocopherol. Biochemistry *36*, 15216–15223.

Ogasawara, H., Doi, T., Doya, K., and Kawato, M. (2007). Nitric oxide regulates input specificity of long-term depression and context dependence of cerebellar learning. PLoS Comput. Biol. *3*, e179.

Ogawa, H., Mizusawa, A., Kikuchi, Y., Hida, W., Miki, H., and Shirato, K. (1995). Nitric oxide as a retrograde messenger in the nucleus tractus solitarii of rats during hypoxia. J. Physiol. (Lond.) *486 (Pt 2)*, 495–504.

Ogura, T., Yokoyama, T., Fujisawa, H., Kurashima, Y., and Esumi, H. (1993). Structural diversity of neuronal nitric oxide synthase mRNA in the nervous system. Biochem. Biophys. Res. Commun. *193*, 1014–1022.

Ohkubo, T., Yamazaki, J., and Kitamura, K. (2010). Tarantula toxin ProTx-I differentiates between human T-type voltage-gated Ca^{2+} Channels $Ca_v3.1$ and $Ca_v3.2$. J. Pharmacol. Sci. *112*, 452–458.

Olivera, B.M., Rivier, J., Scott, J.K., Hillyard, D.R., and Cruz, L.J. (1991). Conotoxins. J. Biol. Chem. *266*, 22067–22070.

Orestes, P., Bojadzic, D., Lee, J., Leach, E., Salajegheh, R., Digruccio, M.R., Nelson, M.T., and Todorovic, S.M. (2011). Free radical signalling underlies inhibition of $Ca_v3.2$ T-type calcium channels by nitrous oxide in the pain pathway. J. Physiol. (Lond.) *589*, 135–148.

Palmer, R.M., Ferrige, A.G., and Moncada, S. (1987). Nitric oxide release accounts for the biological activity of endothelium-derived relaxing factor. Nature *327*, 524–526.

Pan, Z.H., Hu, H.J., Perring, P., and Andrade, R. (2001). T-type Ca^{2+} channels mediate neurotransmitter release in retinal bipolar cells. Neuron *32*, 89–98.

Park, J.-Y., Jeong, S.-W., Perez-Reyes, E., and Lee, J.-H. (2003). Modulation of Ca(v)3.2 T-type Ca^{2+} channels by protein kinase C. FEBS Lett. *547*, 37–42.

Park, J.-Y., Kang, H.-W., Moon, H.-J., Huh, S.-U., Jeong, S.-W., Soldatov, N.M., and Lee, J.-H. (2006). Activation of protein kinase C augments T-type Ca^{2+} channel activity without changing channel surface density. J. Physiol. (Lond.) *577*, 513–523.

Park, Y.-G., Park, H.-Y., Lee, C.J., Choi, S., Jo, S., Choi, H., Kim, Y.-H., Shin, H.-S., Llinas, R.R., and Kim, D. (2010). Ca(V)3.1 is a tremor rhythm pacemaker in the inferior olive. Proc. Natl. Acad. Sci. U.S.A. *107*, 10731–10736.

Peloquin, J.B., Khosravani, H., Barr, W., Bladen, C., Evans, R., Mezeyova, J., Parker, D., Snutch, T.P., McRory, J.E., and Zamponi, G.W. (2006). Functional analysis of $Ca_v3.2$ T-type calcium channel mutations linked to childhood absence epilepsy. Epilepsia *47*, 655–658.

Perez-Reyes, E. (2003). Molecular physiology of low-voltage-activated T-type calcium channels. Physiol. Rev. *83*, 117–161.

Perez-Reyes, E., Cribbs, L.L., Daud, A., Lacerda, A.E., Barclay, J., Williamson, M.P., Fox, M., Rees, M., and Lee, J.H. (1998). Molecular characterization of a neuronal low-voltage-activated T-type calcium channel. Nature *391*, 896–900.

Persechini, A., and Stemmer, P.M. (2002). Calmodulin is a limiting factor in the cell. Trends Cardiovasc. Med. *12*, 32–37.

Phillips, K.G., Hardingham, N.R., and Fox, K. (2008). Postsynaptic action potentials are required for nitric-oxide-dependent long-term potentiation in CA1 neurons of adult GluR1 knock-out and wild-type mice. J. Neurosci. *28*, 14031–14041.

Plummer, M.R., Logothetis, D.E., and Hess, P. (1989). Elementary properties and pharmacological sensitivities of calcium channels in mammalian peripheral neurons. Neuron *2*, 1453–1463.

Pluteanu, F., and Cribbs, L.L. (2009). T-type calcium channels are regulated by hypoxia/reoxygenation in ventricular myocytes. Am. J. Physiol. Heart Circ. Physiol. *297*, H1304–1313.

Potter, L.R. (2011). Guanylyl cyclase structure, function and regulation. Cell. Signal. *23*, 1921–1926.

Powell, K.L., Cain, S.M., Ng, C., Sirdesai, S., David, L.S., Kyi, M., Garcia, E., Tyson, J.R., Reid, C.A., Bahlo, M., et al. (2009). A $Ca_v3.2$ T-type calcium channel point mutation has splice-variant-specific effects on function and segregates with seizure expression in a polygenic rat model of absence epilepsy. J. Neurosci *29*, 371–380.

Prabhakar, N.R. (1999). NO and CO as second messengers in oxygen sensing in the carotid body. Respir Physiol *115*, 161–168.

Qiu, D.-L., and Knöpfel, T. (2007). An NMDA receptor/nitric oxide cascade in presynaptic parallel fiber-Purkinje neuron long-term potentiation. J. Neurosci. *27*, 3408–3415.

Ramirez, J.M., and Richter, D.W. (1996). The neuronal mechanisms of respiratory rhythm generation. Curr. Opin. Neurobiol. *6*, 817–825.

Randall, A.D., and Tsien, R.W. (1995). Pharmacological dissection of multiple types of Ca^{2+} channel currents in rat cerebellar granule neurons. J. Neurosci. *15*, 2995–3012.

Randall, A.D., and Tsien, R.W. (1997). Contrasting biophysical and pharmacological properties of T-type and R-type calcium channels. Neuropharmacology *36*, 879–893.

Rangel, A., Sánchez-Armass, S., and Meza, U. (2010). Protein kinase C-mediated inhibition of recombinant T-type $Ca_v3.2$ channels by neurokinin 1 receptors. Mol. Pharmacol. *77*, 202–210.

Reuter, H. (1967). The dependence of slow inward current in Purkinje fibres on the extracellular calcium-concentration. J. Physiol. (Lond.) *192*, 479–492.

Richards, D.A., Guatimosim, C., Rizzoli, S.O., and Betz, W.J. (2003). Synaptic Vesicle Pools at the Frog Neuromuscular Junction. Neuron *39*, 529–541.

Riefler, G.M., and Firestein, B.L. (2001). Binding of neuronal nitric-oxide synthase (nNOS) to carboxyl-terminal-binding protein (CtBP) changes the localization of CtBP from the nucleus to the cytosol. A NOVEL FUNCTION FOR TARGETING BY THE PDZ DOMAIN OF nNOS. J. Biol. Chem. *276*, 48262–48268.

Roche, A.K., Cook, M., Wilcox, G.L., and Kajander, K.C. (1996). A nitric oxide synthesis inhibitor (L-NAME) reduces licking behavior and Fos-labeling in the spinal cord of rats during formalin-induced inflammation. Pain *66*, 331–341.

Ruth, P., Röhrkasten, A., Biel, M., Bosse, E., Regulla, S., Meyer, H.E., Flockerzi, V., and Hofmann, F. (1989). Primary structure of the beta subunit of the DHP-sensitive calcium channel from skeletal muscle. Science *245*, 1115–1118.

Samuni, A., Aronovitch, J., Godinger, D., Chevion, M., and Czapski, G. (1983). On the cytotoxicity of vitamin C and metal ions. A site-specific Fenton mechanism. Eur. J. Biochem. *137*, 119–124.

Santoni, G., Santoni, M., and Nabissi, M. (2012). Functional role of T-type calcium channels in tumour growth and progression: prospective in cancer therapy. Br. J. Pharmacol. *166*, 1244–1246.

Sather, W.A. (2005). Selective permeability of voltage-gated calcium channels. Voltage-Gated calcium Channels 205–218.

Satoh, R., Nakabayashi, Y., and Kano, M. (1991). Pharmacological properties of two types of calcium channel in embryonic chick skeletal muscle cells in culture. Neurosci. Lett. *122*, 233–236.

Sattler, R., Xiong, Z., Lu, W.-Y., Hafner, M., MacDonald, J.F., and Tymianski, M. (1999). Specific coupling of NMDA receptor activation to nitric oxide neurotoxicity by PSD-95 protein. Science *284*, 1845–1848.

Schaible, H.-G., and Richter, F. (2004). Pathophysiology of pain. Langenbeck's Archives of Surgery *389*, 237–243.

Schepens, J., Cuppen, E., Wieringa, B., and Hendriks, W. (1997). The neuronal nitric oxide synthase PDZ motif binds to -G(D,E)XV* carboxyterminal sequences. FEBS Letters *409*, 53–56.

Schöneich, C. (2000). Mechanisms of metal-catalyzed oxidation of histidine to 2-oxo-histidine in peptides and proteins. Journal of Pharmaceutical and Biomedical Analysis *21*, 1093–1097.

Schrier, A.D., Wang, H., Talley, E.M., Perez-Reyes, E., and Barrett, P.Q. (2001). alpha1H T-type Ca^{2+} channel is the predominant subtype expressed in bovine and rat zona glomerulosa. Am. J. Physiol., Cell Physiol. *280*, C265–272.

Schwarz, P.M., Kleinert, H., and Förstermann, U. (1999). Potential functional significance of brain-type and muscle-type nitric oxide synthase I expressed in adventitia and media of rat aorta. Arterioscler. Thromb. Vasc. Biol. *19*, 2584–2590.

Schwarze, S.R., Ho, A., Vocero-Akbani, A., and Dowdy, S.F. (1999). In vivo protein transduction: delivery of a biologically active protein into the mouse. Science *285*, 1569–1572.

Scroggs, R.S., and Fox, A.P. (1992). Calcium current variation between acutely isolated adult rat dorsal root ganglion neurons of different size. J. Physiol. (Lond.) *445*, 639–658.

Serrano, J.R., Perez-Reyes, E., and Jones, S.W. (1999). State-dependent inactivation of the alpha1G T-type calcium channel. J. Gen. Physiol. *114*, 185–201.

Sessa, W.C., Harrison, J.K., Barber, C.M., Zeng, D., Durieux, M.E., D'Angelo, D.D., Lynch, K.R., and Peach, M.J. (1992). Molecular cloning and expression of a cDNA encoding endothelial cell nitric oxide synthase. J. Biol. Chem. *267*, 15274–15276.

Sheng, M., and Sala, C. (2001). PDZ domains and the organization of supramolecular complexes. Annual Review of Neuroscience *24*, 1–29.

Shin, J.H., and Linden, D.J. (2005). An NMDA receptor/nitric oxide cascade is involved in cerebellar LTD but is not localized to the parallel fiber terminal. J. Neurophysiol. *94*, 4281–4289.

Shipe, W.D., Barrow, J.C., Yang, Z.-Q., Lindsley, C.W., Yang, F.V., Schlegel, K.-A.S., Shu, Y., Rittle, K.E., Bock, M.G., Hartman, G.D., et al. (2008). Design, synthesis, and evaluation of a novel 4-aminomethyl-4-fluoropiperidine as a T-type Ca^{2+} channel antagonist. J. Med. Chem. *51*, 3692–3695.

Sidach, S.S., and Mintz, I.M. (2002). Kurtoxin, a gating modifier of neuronal high- and low-threshold ca channels. J. Neurosci. *22*, 2023–2034.

Silvagno, F., Xia, H., and Bredt, D.S. (1996). Neuronal nitric-oxide synthase-mu, an alternatively spliced isoform expressed in differentiated skeletal muscle. J. Biol. Chem. *271*, 11204–11208.

Smith, E.M., Sorota, S., Kim, H.M., McKittrick, B.A., Nechuta, T.L., Bennett, C., Knutson, C., Burnett, D.A., Kieselgof, J., Tan, Z., et al. (2010). T-type calcium channel blockers: spiro-piperidine azetidines and azetidinones-optimization, design and synthesis. Bioorg. Med. Chem. Lett. *20*, 4602–4606.

Smith, J.C., Abdala, A.P.L., Rybak, I.A., and Paton, J.F.R. (2009). Structural and functional architecture of respiratory networks in the mammalian brainstem. Philos Trans R Soc Lond B Biol Sci *364*, 2577–2587.

Snutch, T.P., Leonard, J.P., Gilbert, M.M., Lester, H.A., and Davidson, N. (1990). Rat brain expresses a heterogeneous family of calcium channels. Proc. Natl. Acad. Sci. U.S.A. *87*, 3391–3395.

Snutch, T.P., Peloquin, J., Mathews, E., and McRory, J.E. (2005). molecular properties of voltage-gated calcium channels. In Voltage-Gated Calcium Channels, (Kluwer Academic), pp. 61–94.

Snutch, T.P., Tomlinson, W.J., Leonard, J.P., and Gilbert, M.M. (1991). Distinct calcium channels are generated by alternative splicing and are differentially expressed in the mammalian CNS. Neuron *7*, 45–57.

Son, W.-Y., Han, C.-T., Lee, J.-H., Jung, K.-Y., Lee, H.-M., and Choo, Y.-K. (2002). Developmental expression patterns of alpha1H T-type Ca^{2+} channels during spermatogenesis and organogenesis in mice. Dev. Growth Differ. *44*, 181–190.

Songyang, Z., Fanning, A.S., Fu, C., Xu, J., Marfatia, S.M., Chishti, A.H., Crompton, A., Chan, A.C., Anderson, J.M., and Cantley, L.C. (1997). Recognition of unique carboxyl-terminal motifs by distinct PDZ domains. Science *275*, 73–77.

Soong, T.W., DeMaria, C.D., Alvania, R.S., Zweifel, L.S., Liang, M.C., Mittman, S., Agnew, W.S., and Yue, D.T. (2002). Systematic identification of splice variants in human P/Q-Type channel $alpha_1$2.1 subunits: implications for current density and Ca^{2+}-dependent inactivation. J. Neurosci. *22*, 10142–10152.

Soong, T.W., Stea, A., Hodson, C.D., Dubel, S.J., Vincent, S.R., and Snutch, T.P. (1993). Structure and functional expression of a member of the low voltage-activated calcium channel family. Science *260*, 1133–1136.

Souvannakitti, D., Nanduri, J., Yuan, G., Kumar, G.K., Fox, A.P., and Prabhakar, N.R. (2010). NADPH oxidase-dependent regulation of T-type Ca^{2+} channels and ryanodine receptors mediate the augmented exocytosis of catecholamines from intermittent hypoxia-treated neonatal rat chromaffin cells. J. Neurosci. *30*, 10763–10772.

Springall, D.R., Riveros-Moreno, V., Buttery, L., Suburo, A., Bishop, A.E., Merrett, M., Moncada, S., and Polak, J.M. (1992). Immunological detection of nitric oxide synthase(s) in human tissues using heterologous antibodies suggesting different isoforms. Histochemistry *98*, 259–266.

Srivastava, S., Osten, P., Vilim, F.S., Khatri, L., Inman, G., States, B., Daly, C., DeSouza, S., Abagyan, R., Valtschanoff, J.G., et al. (1998). Novel anchorage of GluR2/3 to the postsynaptic density by the AMPA receptor-binding protein ABP. Neuron *21*, 581–591.

Stadtman, E.R. (1991). Ascorbic acid and oxidative inactivation of proteins. Am. J. Clin. Nutr. *54*, 1125S–1128S.

Starr, T.V.B., Prystay, W., and Snutch, T.P. (1991). Primary structure of a calcium channel that is highly expressed in the rat cerebellum. PNAS *88*, 5621–5625.

Stea, A., Tomlinson, W.J., Soong, T.W., Bourinet, E., Dubel, S.J., Vincent, S.R., and Snutch, T.P. (1994). Localization and functional properties of a rat brain alpha1A calcium channel reflect similarities to neuronal Q- and P-Type channels. PNAS *91*, 10576–10580.

Steel, J.H., Terenghi, G., Chung, J.M., Na, H.S., Carlton, S.M., and Polak, J.M. (1994). Increased nitric oxide synthase immunoreactivity in rat dorsal root ganglia in a neuropathic pain model. Neurosci. Lett. *169*, 81–84.

Steriade, M. (2005). Sleep, epilepsy and thalamic reticular inhibitory neurons. Trends in Neurosciences *28*, 317–324.

Stricker, N.L., Christopherson, K.S., Yi, B.A., Schatz, P.J., Raab, R.W., Dawes, G., Bassett, D.E.J., Bredt, D.S., and Li, M. (1997). PDZ domain of neuronal nitric oxide synthase recognizes novel C-terminal peptide sequences. Nat Biotechnol. *15*, 336–342.

Strom, T.M., Nyakatura, G., Apfelstedt-Sylla, E., Hellebrand, H., Lorenz, B., Weber, B.H., Wutz, K., Gutwillinger, N., Rüther, K., Drescher, B., et al. (1998). An L-type calcium-channel gene mutated in incomplete X-linked congenital stationary night blindness. Nat. Genet. *19*, 260–263.

Su, H. (2002). Upregulation of a T-Type Ca^{2+} Channel Causes a Long-Lasting Modification of Neuronal Firing Mode after Status Epilepticus. J. Neurosci. *22*, 3645–3655.

Subramanian, S., Erokwu, B., Han, F., Dick, T.E., and Strohl, K.P. (2002). L-NAME differentially alters ventilatory behavior in Sprague-Dawley and Brown Norway rats. J Appl Physiol *93*, 984–989.

Sugaya, K., and McKinney, M. (1994). Nitric oxide synthase gene expression in cholinergic neurons in the rat brain examined by combined immunocytochemistry and in situ hybridization histochemistry. Brain Res. Mol. Brain Res *23*, 111–125.

Summers, B.A., Overholt, J.L., and Prabhakar, N.R. (1999). Nitric oxide inhibits L-type Ca^{2+} current in glomus cells of the rabbit carotid body via a cGMP-independent mechanism. J. Neurophysiol. *81*, 1449–1457.

Sun, H.-S., Hui, K., Lee, D.W.K., and Feng, Z.-P. (2007). Z^{2+} sensitivity of high- and low-voltage activated calcium channels. Biophys. J. biophysj.106.103333.

Susswein, A.J., Katzoff, A., Miller, N., and Hurwitz, I. (2004). Nitric oxide and memory. Neuroscientist *10*, 153–162.

Swandulla, D., and Armstrong, C.M. (1988). Fast-deactivating calcium channels in chick sensory neurons. J. Gen. Physiol. *92*, 197–218.

Takahashi, M., MJ, S., JF, J., BFX, R., and Catterall, W.W. (1987). Subunit structure of dihydropyridine-sensitive calcium channels from skeletal muscle. Proc. Natl. Acad. Sci. *84*, 5478–5482.

Talavera, K., and Nilius, B. (2006). Biophysics and structure-function relationship of T-type Ca^{2+} channels. Cell Calcium *40*, 97–114.

Talavera, K., Staes, M., Janssens, A., Klugbauer, N., Droogmans, G., Hofmann, F., and Nilius, B. (2001). Aspartate residues of the Glu-Glu-Asp-Asp (EEDD) pore locus control selectivity and permeation of the T-type Ca^{2+} channel alpha(1G). J. Biol. Chem. *276*, 45628–45635.

Talley, E.M., Cribbs, L.L., Lee, J.-H., Daud, A., Perez-Reyes, E., and Bayliss, D.A. (1999). Differential distribution of three members of a gene family encoding low voltage-activated (T-Type) calcium channels. J. Neurosci. *19*, 1895–1911.

Tanabe, T., Takeshima, H., Mikami, A., Flockerzi, V., Takahashi, H., Kangawa, K., Kojima, M., Matsuo, H., Hirose, T., and Numa, S. (1987). Primary structure of the receptor for calcium channel blockers from skeletal muscle. Nature *328*, 313–318.

Tao, F., Su, Q., and Johns, R.A. (2008). Cell-permeable peptide Tat-PSD-95 PDZ2 inhibits chronic inflammatory pain behaviors in mice. Mol Ther *16*, 1776–1782.

Taqatqeh, F., Mergia, E., Neitz, A., Eysel, U.T., Koesling, D., and Mittmann, T. (2009). More than a retrograde messenger: nitric oxide needs two cGMP pathways to induce hippocampal long-term potentiation. J. Neurosci. *29*, 9344–9350.

Tian, Y., Kongsuphol, P., Hug, M., Ousingsawat, J., Witzgall, R., Schreiber, R., and Kunzelmann, K. (2011). Calmodulin-dependent activation of the epithelial calcium-dependent chloride channel TMEM16A. FASEB J. *25*, 1058–1068.

Tochio, H., Mok, Y.-K., Zhang, Q., Kan, H.-M., Bredt, D.S., and Zhang, M. (2000). Formation of nNOS/PSD-95 PDZ dimer requires a preformed [beta]-finger structure from the nNOS PDZ domain. Journal of Molecular Biology *303*, 359–370.

Tochio, H., Zhang, Q., Mandal, P., Li, M., and Zhang, M. (1999). Solution structure of the extended neuronal nitric oxide synthase PDZ domain complexed with an associated peptide. Nat Struct Mol Biol *6*, 417–421.

Todorovic, S.M., Jevtovic-Todorovic, V., Mennerick, S., Perez-Reyes, E., and Zorumski, C.F. (2001a). $Ca_v3.2$ channel is a molecular substrate for inhibition of T-Type calcium currents in rat sensory neurons by nitrous oxide. Mol Pharmacol *60*, 603–610.

Todorovic, S.M., Jevtovic-Todorovic, V., Meyenburg, A., Mennerick, S., Perez-Reyes, E., Romano, C., Olney, J.W., and Zorumski, C.F. (2001b). Redox modulation of T-Type calcium channels in rat peripheral nociceptors. Neuron *31*, 75–85.

Todorovic, S.M., Meyenburg, A., and Jevtovic-Todorovic, V. (2002). Mechanical and thermal antinociception in rats following systemic administration of mibefradil, a T-type calcium channel blocker. Brain Res. *951*, 336–340.

Todorovic, S.M., Meyenburg, A., and Jevtovic-Todorovic, V. (2004). Redox modulation of peripheral T-type Ca^{2+} channels in vivo: alteration of nerve injury-induced thermal hyperalgesia. Pain *109*, 328–339.

Topinka, J.R., and Bredt, D.S. (1998). N-Terminal palmitoylation of PSD-95 regulates association with cell membranes and interaction with K^+ channel $K_v1.4$. Neuron *20*, 125–134.

Tozer, A.J.B., Forsythe, I.D., and Steinert, J.R. (2012). Nitric oxide signalling augments neuronal voltage-gated L-type (Ca(v)1) and P/q-type (Ca(v)2.1) channels in the mouse medial nucleus of the trapezoid body. PLoS ONE *7*, e32256.

Traboulsie, A., Chemin, J., Chevalier, M., Quignard, J.-F., Nargeot, J., and Lory, P. (2006). Subunit-specific modulation of T-type calcium channels by Zinc. J Physiol (Lond) jphysiol.2006.114496.

Trejo, J. (2005). Internal PDZ ligands: novel endocytic recycling motifs for G protein-coupled receptors. Mol. Pharmacol. *67*, 1388–1390.

Tringham, E., Powell, K.L., Cain, S.M., Kuplast, K., Mezeyova, J., Weerapura, M., Eduljee, C., Jiang, X., Smith, P., Morrison, J.-L., et al. (2012). T-type calcium channel blockers that attenuate thalamic burst firing and suppress absence seizures. Sci Transl Med *4*, 121ra19.

Tsien, R.W., and Barrett, C.F. (2005). A brief history of calcium channel discovery. Voltage-Gated calcium Channels *(New York: Kluwer Academic)*, 27–47.

US National Library of Medicine/National Institutes of Health PubMed.

Vagenende, V., Yap, M.G.S., and Trout, B.L. (2009). Mechanisms of protein stabilization and prevention of protein aggregation by glycerol. Biochemistry *48*, 11084–11096.

Valdés, V., Mosqueira, M., Rey, S., Del Rio, R., and Iturriaga, R. (2003). Inhibitory effects of NO on carotid body: contribution of neural and endothelial nitric oxide synthase isoforms. American Journal of Physiology - Lung Cellular and Molecular Physiology *284*, L57 –L68.

Vassort, G., Talavera, K., and Alvarez, J.L. (2006). Role of T-type Ca^{2+} channels in the heart. Cell Calcium *40*, 205–220.

Viana, F., Van den Bosch, L., Missiaen, L., Vandenberghe, W., Droogmans, G., Nilius, B., and Robberecht, W. (1997). Mibefradil (Ro 40-5967) blocks multiple types of voltage-gated calcium channels in cultured rat spinal motoneurones. Cell Calcium *22*, 299–311.

Vincent, S.R. (1992). Neurons that say NO. TINS *15*, 108–113.

Vincent, S.R. (1994). Nitric Oxide: A Radical Neurotransmitter in the central nervous system. Prog Neur *42*, 129–160.

Vincent, S.R. (1995a). Localization of nitric oxide neurons in the central nervous system. In NItric Oxide in the Nervous System, (San Diego: Academic Press), pp. 83–96.

Vincent, S.R. (1995b). Nitric Oxide in the Nervous System: Neuroscience Perspectives (San Diego: Academic Press).

Vincent, S.R., and Kimura, H. (1992). Histochemical mapping of nitric oxide synthase in the rat brain. Neuroscience *46*, 755–784.

Vitko, I., Bidaud, I., Arias, J.M., Mezghrani, A., Lory, P., and Perez-Reyes, E. (2007). The I-II loop controls plasma membrane expression and gating of $Ca_v3.2$ T-Type Ca^{2+} channels: A paradigm for childhood absence epilepsy mutations. J. Neurosci. *27*, 322–330.

Wang, X., and Robinson, P.J. (1997). Cyclic GMP-dependent protein kinase and cellular signaling in the nervous system. J. Neurochem. *68*, 443–456.

Wang, Z.Z., Bredt, D.S., Fidone, S.J., and Stensaas, L.J. (1993). Neurons synthesizing nitric oxide innervate the mammalian carotid body. J. Comp. Neurol *336*, 419–432.

Wang, Z.Z., Dinger, B.G., Stensaas, L.J., and Fidone, S.J. (1995a). The role of nitric oxide in carotid chemoreception. Biol. Signals *4*, 109–116.

Wang, Z.Z., Stensaas, L.J., Bredt, D.S., Dinger, B.G., and Fidone, S.J. (1994). Mechanisms of carotid body inhibition. Adv. Exp. Med. Biol. *360*, 229–235.

Wang, Z.Z., Stensaas, L.J., Dinger, B.G., and Fidone, S.J. (1995b). Nitric oxide mediates chemoreceptor inhibition in the cat carotid body. Neuroscience *65*, 217–229.

Welker, H.A., Wiltshire, H., and Bullingham, R. (1998). Clinical pharmacokinetics of mibefradil. Clin Pharmacokinet *35*, 405–423.

Welsby, P.J., Wang, H., Wolfe, J.T., Colbran, R.J., Johnson, M.L., and Barrett, P.Q. (2003). A mechanism for the direct regulation of T-type calcium channels by Ca^{2+}/calmodulin-dependent kinase II. J. Neurosci *23*, 10116–10121.

White, G., Lovinger, D.M., and Weight, F.F. (1989). Transient low-threshold Ca^{2+} current triggers burst firing through an afterdepolarizing potential in an adult mammalian neuron. Proc. Natl. Acad. Sci. U.S.A. *86*, 6802–6806.

Williams, M.E., Brust, P.F., Feldman, D.H., Patthi, S., Simerson, S., Maroufi, A., McCue, A.F., Veliçelebi, G., Ellis, S.B., and Harpold, M.M. (1992a). Structure and functional expression of an omega-conotoxin-sensitive human N-type calcium channel. Science *257*, 389–395.

Williams, M.E., Feldman, D.H., McCue, A.F., Brenner, R., Velicelebi, G., Ellis, S.B., and Harpold, M.M. (1992b). Structure and functional expression of alpha 1, alpha 2, and beta subunits of a novel human neuronal calcium channel subtype. Neuron *8*, 71–84.

Williams, M.E., Washburn, M.S., Hans, M., Urrutia, A., Brust, P.F., Prodanovich, P., Harpold, M.M., and Stauderman, K.A. (1999). Structure and functional characterization of a novel human low-voltage activated calcium channel. J. Neurochem. *72*, 791–799.

Williams, S.R., Tóth, T.I., Turner, J.P., Hughes, S.W., and Crunelli, V. (1997). The "window" component of the low threshold Ca^{2+} current produces input signal amplification and bistability in cat and rat thalamocortical neurones. J. Physiol. (Lond.) *505 (Pt 3)*, 689–705.

Wolfe, J.T., Wang, H., Howard, J., Garrison, J.C., and Barrett, P.Q. (2003). T-type calcium channel regulation by specific G-protein betagamma subunits. Nature *424*, 209–213.

Wolfe, J.T., Wang, H., Perez-Reyes, E., and Barrett, P.Q. (2002). Stimulation of recombinant Ca(v)3.2, T-type, Ca^{2+} channel currents by CaMKIIgamma(C). J. Physiol. (Lond.) *538*, 343–355.

Woo, H.M., Lee, Y.S., Roh, E.J., Seo, S.H., Song, C.M., Chung, H.J., Pae, A.N., and Shin, K.J. (2011). Synthesis and biological evaluation of 4-piperidinecarboxylate and 4-piperidinecyanide derivatives for T-type calcium channel blockers. Bioorg. Med. Chem. Lett. *21*, 5910–5915.

Wood, J., and Garthwaite, J. (1994). Models of the diffusional spread of nitric oxide: implications for neural nitric oxide signalling and its pharmacological properties. Neuropharmacology *33*, 1235–1244.

Xie, Q.W., Whisnant, R., and Nathan, C. (1993). Promoter of the mouse gene encoding calcium-independent nitric oxide synthase confers inducibility by interferon gamma and bacterial lipopolysaccharide. J. Exp. Med. *177*, 1779–1784.

Xu, K.Y., Huso, D.L., Dawson, T.M., Bredt, D.S., and Becker, L.C. (1999). Nitric oxide synthase in cardiac sarcoplasmic reticulum. Proc. Natl. Acad. Sci. U.S.A. *96*, 657–662.

Yang, Z.Q., Barrow, J.C., Shipe, W.D., Schlegel, K.-A.S., Shu, Y., Yang, F.V., Lindsley, C.W., Rittle, K.E., Bock, M.G., Hartman, G.D., et al. (2008). Discovery of 1,4-substituted piperidines as potent and selective inhibitors of T-type calcium channels. J. Med. Chem. *51*, 6471–6477.

Yao, J., Davies, L.A., Howard, J.D., Adney, S.K., Welsby, P.J., Howell, N., Carey, R.M., Colbran, R.J., and Barrett, P.Q. (2006). Molecular basis for the modulation of native T-type Ca^{2+} channels in vivo by Ca^{2+}/calmodulin-dependent protein kinase II. J. Clin. Invest. *116*, 2403–2412.

Yoon, Y.W., Sung, B., and Chung, J.M. (1998). Nitric oxide mediates behavioral signs of neuropathic pain in an experimental rat model. Neuroreport *9*, 367–372.

Yoshikami, D., Bagabaldo, Z., and Olivera, B.M. (1989). The inhibitory effects of omega-conotoxins on Ca channels and synapses. Ann. N. Y. Acad. Sci. *560*, 230–248.

Yoshimura, N., Seki, S., and De Groat, W.C. (2001). Nitric oxide modulates Ca^{2+} channels in dorsal root ganglion neurons innervating rat urinary bladder. J. Neurophysiol. *86*, 304–311.

Yu, F.H., Yarov-Yarovoy, V., Gutman, G.A., and Catterall, W.A. (2005). Overview of molecular relationships in the voltage-gated ion channel superfamily. (57), pp. 387–395.

Yunker, A.M.R. (2003). Modulation and pharmacology of low voltage-activated ("T-Type") calcium channels. Journal of Bioenergetics and Biomembranes *35*, 577–598.

Zaccolo, M., and Movsesian, M.A. (2007). cAMP and cGMP signaling cross-talk: role of phosphodiesterases and implications for cardiac pathophysiology. Circ. Res. *100*, 1569–1578.

Zamponi, G.W., Bourinet, E., and Snutch, T.P. (1996). Nickel block of a family of neuronal calcium channels: Subtype- and subunit-dependent action at multiple sites. Journal of Membrane Biology *151*, 77–90.

Zamponi, G.W., Lory, P., and Perez-Reyes, E. (2009). Role of voltage-gated calcium channels in epilepsy. Pflugers Arch.

Zhang, C., Bosch, M.A., Rick, E.A., Kelly, M.J., and Rønnekleiv, O.K. (2009). 17Beta-estradiol regulation of T-type calcium channels in gonadotropin-releasing hormone neurons. J. Neurosci. *29*, 10552–10562.

Zhang, Y., Zhang, J., Jiang, D., Zhang, D., Qian, Z., Liu, C., and Tao, J. (2012). Inhibition of T-type Ca^{2+} channels by endostatin attenuates human glioblastoma cell proliferation and migration. Br. J. Pharmacol. *166*, 1247–1260.

Zhao, Y., Brandish, P.E., DiValentin, M., Schelvis, J.P., Babcock, G.T., and Marletta, M.A. (2000). Inhibition of soluble guanylate cyclase by ODQ. Biochemistry *39*, 10848–10854.

Zhuang, H., Bhattacharjee, A., Hu, F., Zhang, M., Goswami, T., Wang, L., Wu, S., Berggren, P.O., and Li, M. (2000). Cloning of a T-type Ca^{2+} channel isoform in insulin-secreting cells. Diabetes *49*, 59–64.

Appendix 1. Selective Inhibition of $Ca_v3.3$ T-type Calcium Channels by G□q/11-coupled Muscarinic Acetylcholine Receptor.
Original reference: Hildebrand, M.E., David, L.S., Hamid, J., Mulatz, K.J., Garcia, E., Zamponi, G.W., and Snutch, T.P. (2007). Selective inhibition of $Ca_v3.3$ T-type calcium channels by Galphaq/11-coupled muscarinic acetylcholine receptors. J. Biol. Chem *282*, 21043–21055

THE JOURNAL OF BIOLOGICAL CHEMISTRY VOL. 282, NO. 29, pp. 21043–21055, July 20, 2007
© 2007 by The American Society for Biochemistry and Molecular Biology, Inc. Printed in the U.S.A.

Selective Inhibition of Cav3.3 T-type Calcium Channels by $G\alpha_{q/11}$-coupled Muscarinic Acetylcholine Receptors*

Received for publication, December 26, 2006, and in revised form, April 19, 2007 Published, JBC Papers in Press, May 29, 2007, DOI 10.1074/jbc.M611809200

Michael E. Hildebrand[‡], Laurence S. David[‡], Jawed Hamid[§], Kirk Mulatz[‡], Esperanza Garcia[‡], Gerald W. Zamponi[§], and Terrance P. Snutch[‡1]

From the [‡]Michael Smith Laboratories, University of British Columbia, Vancouver, British Columbia V6T 1Z4 and the [§]Hotchkiss Brain Institute, University of Calgary, Calgary, Alberta T2N 4N1, Canada

T-type calcium channels play critical roles in controlling neuronal excitability, including the generation of complex spiking patterns and the modulation of synaptic plasticity, although the mechanisms and extent to which T-type Ca^{2+} channels are modulated by G-protein-coupled receptors (GPCRs) remain largely unexplored. To examine specific interactions between T-type Ca^{2+} channel subtypes and muscarinic acetylcholine receptors (mAChRs), the Cav3.1 (α_{1G}), Cav3.2 (α_{1H}), and Cav3.3 (α_{1I}) T-type Ca^{2+} channels were co-expressed with the M1 $G\alpha_{q/11}$-coupled mAChR. Perforated patch recordings demonstrate that activation of M1 receptors has a strong inhibitory effect on Cav3.3 T-type Ca^{2+} currents but either no effect or a moderate stimulating effect on Cav3.1 and Cav3.2 peak current amplitudes. This differential modulation was observed for both rat and human T-type Ca^{2+} channel variants. The inhibition of Cav3.3 channels by M1 receptors is reversible, use-independent, and associated with a concomitant increase in inactivation kinetics. Loss-of-function experiments with genetically encoded antagonists of $G\alpha$ and $G\beta\gamma$ proteins and gain-of-function experiments with genetically encoded $G\alpha$ subtypes indicate that M1 receptor-mediated inhibition of Cav3.3 occurs through $G\alpha_{q/11}$. This is supported by experiments showing that activation of the M3 and M5 $G\alpha_{q/11}$-coupled mAChRs also causes inhibition of Cav3.3 currents, although $G\alpha_i$-coupled mAChRs (M2 and M4) have no effect. Examining Cav3.1-Cav3.3 chimeric channels demonstrates that two distinct regions of the Cav3.3 channel are necessary and sufficient for complete M1 receptor-mediated channel inhibition and represent novel sites not previously implicated in T-type channel modulation.

T-type calcium channels play critical roles in shaping the electrical, chemical, and plastic properties of neurons throughout the central and peripheral nervous systems. In thalamic reticular and relay neurons, T-type channels are involved in rhythmic rebound burst firing and spindle waves associated with slow-wave sleep (1–5). Studies on knock-out mice and a rat model of absence epilepsy indicate that altering T-type activity within thalamic cells can contribute to pathological conditions such as sleep disorders and epilepsy (1–5). Certain human epilepsies appear to be associated with T-type Ca^{2+} channel point mutations conferring channel gain-of-function phenotype (6–9). T-type channels also play crucial roles in dendritic integration and Ca^{2+} spiking in hippocampal pyramidal cells (10, 11). Within the olfactory bulb, T-type channels are implicated in modulating Ca^{2+} transients and synaptic release at dendrodendritic synapses (12, 13). In the periphery, antisense oligonucleotides and pharmacological approaches have implicated T-type channels in contributing to both acute and chronic nociceptive behaviors (14, 15).

Previous studies have identified three main subtypes of T-type Ca^{2+} channel α_1 subunits (Cav3.1/α_{1G}, Cav3.2/α_{1H} and Cav3.3/α_{1I}) and characterized their voltage-dependent, kinetic, and pharmacological properties (16–21). Cav3.1 and Cav3.2 channels display "typical" T-type properties, including relatively small conductance, fast activation and inactivation kinetics, and slow deactivation kinetics, whereas Cav3.3 channels uniquely display a larger conductance, much slower activation and inactivation kinetics, as well as faster deactivation kinetics (17, 19). Some of the distinct biophysical properties associated with Cav3.3 T-type currents have been observed in certain populations of native T-type currents (4, 17, 19, 22). The biophysical differences between the T-type channels likely enable them to differentially shape and modulate firing patterns, with the more slowly inactivating Cav3.3 currents able to produce longer bursts of spikes and tonic firing patterns (17, 23, 24).

Although the basic properties of both cloned and native T-type channels have now been largely characterized, there remains relatively little information concerning their modulation by GPCR[2]-linked pathways. Neurotransmitters such as acetylcholine have been shown to either attenuate or stimulate low threshold Ca^{2+} currents depending on the type of native cells examined, and sometimes multiple forms of modulation

* This work was supported in part by operating grants from the Canadian Institutes for Health Research and Canada Research Tier 1 Chairs (to T. P. S. and G. W. Z.) a fellowship from the Heart and Stroke Foundation of Canada, and trainee fellowships from the Natural Sciences and Engineering Research Council of Canada and Michael Smith Foundation for Health Research (to M. E. H.). The costs of publication of this article were defrayed in part by the payment of page charges. This article must therefore be hereby marked "*advertisement*" in accordance with 18 U.S.C. Section 1734 solely to indicate this fact.

[1] To whom correspondence should be addressed: Michael Smith Laboratories, University of British Columbia, 2185 East Mall, Vancouver, British Columbia V6T 1Z4, Canada. Tel.: 604-822-6968; Fax: 604-822-6470; E-mail: snutch@msl.ubc.ca.

[2] The abbreviations used are: GPCR, G-protein coupled receptor; mAChR, muscarinic acetylcholine receptor; pEGFP, enhanced green fluorescent protein; WT, wild type; $PI(4,5)P_2$, phosphatidylinositol 4,5-biphosphate; CCh, carbachol; PLC, phospholipase C; PKC, protein kinase C; BAPTA-AM, 1,2-bis(2-aminophenoxy)ethane-*N*,*N*,*N*′,*N*′-tetraacetic acid-acetoxymethyl ester.

Downloaded from www.jbc.org at Univ of Ottawa - OCUL on September 28, 2012

can be observed within the same cell type (25–29). Multiple T-type Ca^{2+} channel subtypes are expressed in most native cells (30, 31), although pharmacological tools with the specificity needed to separate these currents have not been generated. In this regard, the description of the modulation of specific T-type Ca^{2+} channels in heterologous systems will provide insights crucial toward further investigations within native systems. This approach is also well suited for GPCR studies as most neurotransmitters activate multiple receptor subtypes in neurons.

Within thalamic reticular, hippocampal pyramidal, and olfactory granule cells, there is evidence for the expression of both T-type Ca^{2+} channels and $G\alpha_{q/11}$-coupled muscarinic acetylcholine receptors (mAChRs) (25, 30–36). As both T-type Ca^{2+} currents and mAChRs have been independently shown to play important physiological roles within these cell types, their functional coupling could be relevant to a number of neuronal processes. Here we studied the modulatory effects of mAChRs on the three main subtypes of low threshold T-type Ca^{2+} channels expressed in the mammalian nervous system. We found the selective modulation of Cav3.3 Ca^{2+} channels by $G\alpha_{q/11}$-coupled mAChRs and combined pharmacological, genetic, and chimeric channel approaches to examine the G-protein-mediated pathway and structural regions responsible for the distinct Cav3.3 signaling characteristics.

EXPERIMENTAL PROCEDURES

Molecular Biology—Human Cav3.1–Cav3.3 T-type Ca^{2+} channel α_1 subunit chimeras were constructed as described in detail by Hamid *et al.* (37).

Cell Culture and Transfection—Human embryonic kidney cells (HEK 293H, Invitrogen) were grown in standard Dulbecco's modified Eagle's medium (10% fetal bovine serum and 50 units/ml penicillin/streptomycin) to ~80% confluence and maintained at 37 °C in a humidified incubator with 95% atmosphere and 5% CO_2. The generation of stable T-type cell lines (in HEK 293, tsa-201) expressing rat brain Cav3.1, Cav3.2, or Cav3.3 α_1 subunits has been described previously (16). Stable cell lines were transiently transfected with human muscarinic M1, M2, M3, M4, or M5 cDNAs (all in pcDNA3.1) using Lipofectamine (Invitrogen). As a reporter for transfection, all transient transfections included co-transfection with either CD8 or pEGFP marker plasmids at a 1:0.25 molar ratio compared with receptor and/or channel plasmid DNA, unless otherwise indicated. Lipofectamine-mediated transfections used 1–1.25 μg of DNA/35-mm dish and 5 μl of Lipofectamine/dish. In G-protein experiments, stable Cav3.3 cells were co-transfected with M1 receptors and equal amounts of either MAS-GRK3ct (in pcDNA3.1), $G\alpha_t$ (in pcDNA3.1), or RGS2 (in pEGFP) using Lipofectamine. Only MAS-GRK3ct and $G\alpha_t$ transfections required co-transfection with marker plasmids as RGS2 expression could be directly detected with fluorescence. In $G\alpha$ transfection experiments, stable Cav3.3 cells were transfected with constitutively active mutants of $G\alpha_q$, $G\alpha_{11}$, or $G\alpha_{13}$ ($G\alpha_{q\text{-}Q209L}$, $G\alpha_{11\text{-}Q209L}$, and $G\alpha_{13\text{-}Q226L}$, respectively, all in pcDNA3.1) using Lipofectamine. Twelve to 18 h after transfection, the medium was changed from Opti-MEM I to regular Dulbecco's modified Eagle's medium, and cells were transferred to a 28 °C incubator. The M1 to M5, $G\alpha_{q\text{-}Q209L}$, $G\alpha_{11\text{-}Q209L}$, and $G\alpha_{13\text{-}Q226L}$ cDNAs were all obtained from the UMR cDNA Resource Center (Rolla, MO), and the RGS2 and MAS-GRK3ct constructs were a generous gift from Dr. Brett Adams.

In separate experiments, HEK 293H cells were co-transfected with M1 and wild type (WT) or chimeric human Cav3.1 or Cav3.3 channels using standard Ca^{2+} phosphate transfection with 2 μg of total cDNA/dish, 0.15 to 0.4 μg of channel cDNA/dish, and 0.2 μg of M1 cDNA/dish. In a subset of these experiments involving co-transfection of WT Cav3.3 and M1, either 200 μM di-C8 $PI(4,5)P_2$ (Echelon Biosciences Inc., Salt Lake City, UT) or 50 μg/ml $PI(4,5)P_2$ IgG_{2b} antibody (~1:30 dilution) (Assay Designs, Ann Arbor, MI) was included in the internal solution to explore the role of $PI(4,5)P_2$ signaling. As the $PI(4,5)P_2$ antibody was supplied in a phosphate-buffered saline solution containing 10% calf serum and 0.05% sodium azide, the control Cav3.3 + M1 cells were recorded in an internal solution containing a 1:30 dilution of phosphate-buffered saline with 10% fetal bovine serum and 0.05% sodium azide. Electrophysiological recordings for all experiments were performed 24–48 h after transfection. Transiently transfected cells were selected for CD8 or pEGFP expression using either adherence of Dynabeads (Dynal, Great Neck, NY) or fluorescence of EGFP under UV light.

Electrophysiological Recordings and Analysis—Macroscopic currents were recorded using the perforated patch clamp technique to reduce current rundown and to preserve cytoplasmic signaling pathways. The external recording solution contained (in mM) 2 $CaCl_2$, 1 $MgCl_2$, 10 HEPES, 40 tetraethylammonium chloride, 92 CsCl, 10 glucose, pH 7.4, and the internal pipette solution contained (in mM) 120 Cs^+ methanesulfonate, 11 EGTA, 10 HEPES, 2 $MgCl_2$, 75–100 μM β-escin, pH 7.2. For these perforated patch recordings, experimental recording did not begin until the series resistance was below 20 megohms and constant, as measured by amplifier compensation. Whole-cell recordings were used for the transiently transfected WT or chimeric human Cav3.1 and Cav3.3 channel experiments as well as the $G\alpha$ transfection experiments. The internal solution for these recordings contained (in mM) 120 Cs^+ methanesulfonate, 11 EGTA, 10 HEPES, 2 $MgCl_2$, 4 Mg-ATP, 0.3 sodium GTP. Macroscopic currents were recorded using Axopatch 200A and 200B amplifiers (Axon Instruments, Foster City, CA), controlled and monitored with Pentium 4 personal computers running pClamp software version 9 (Axon Instruments). Patch pipettes (borosilicate glass BF150-86-10; Sutter Instruments, Novato, CA) were pulled using a Sutter P-87 puller and polished with a Narishige (Tokyo, Japan) microforge, with typical resistances of 3–6 megohms when filled with internal solution. The bath was connected to the ground via a 3 M KCl agar bridge.

Data were low-pass filtered at 2 kHz using the built-in Bessel filter of the amplifier, with sampling at 10 kHz. The amplifier was also used for capacitance and series resistance compensation between 70 and 85% on every cell. Leak subtraction of capacitance and leakage current was performed on-line using a P/5 protocol or else performed with Clampfit (Axon Instruments) during off-line analysis. Figures and fittings utilized the software program Microcal Origin (version

Downloaded from www.jbc.org at Univ of Ottawa - OCUL on September 28, 2012

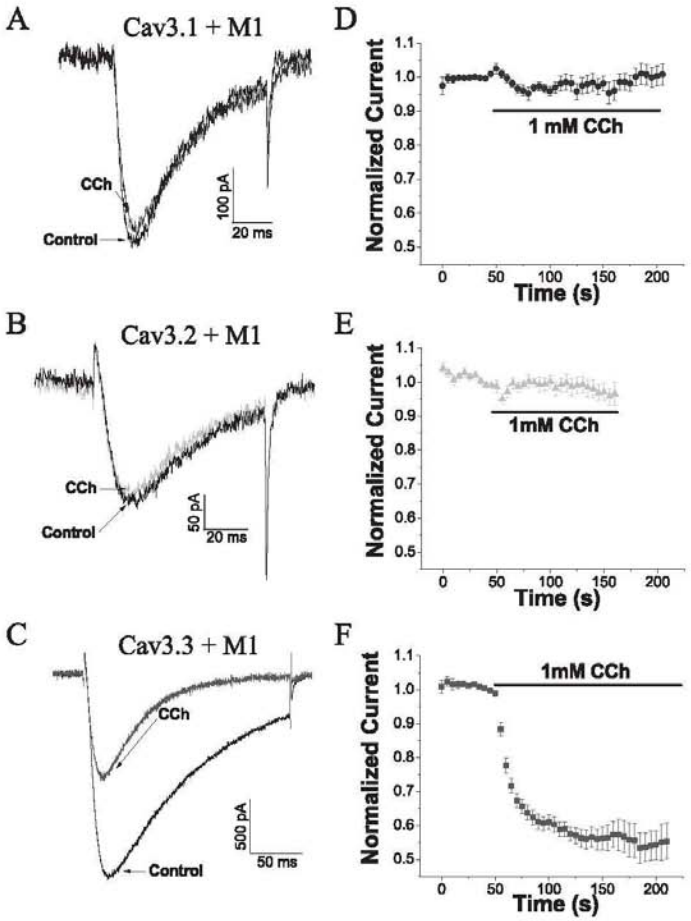

FIGURE 1. **T-type Ca^{2+} channels are differentially modulated by M1 receptors.** *A* and *B*, representative perforated patch current traces during depolarizing pulses from −110 to −30 mV demonstrating no effect on Cav3.1 currents (*A*) and Cav3.2 currents (*B*) when M1 is activated with 1 mM CCh. *D* and *E*, normalized peak current levels during perfusion of control recording solution (2 mM Ca^{2+}) followed by 1 mM CCh for Cav3.1 (+M1) currents (*D*) and Cav3.2 (+M1) currents (*E*). Perfusion of CCh usually had no effect on Cav3.1 peak current amplitudes (−2.1 ± 2.0%, n = 18) and Cav3.2 peak current amplitudes (−0.1 ± 2.3%, n = 17). *C*, representative perforated patch current traces during depolarizing pulses from −110 to −40 mV showing inhibition of Cav3.3 currents by M1. *F*, normalized peak current levels during perfusion of control recording solution (2 mM Ca^{2+}) followed by 1 mM CCh for Cav3.3 (+M1) currents. Perfusion of CCh caused a 45% (± 2%, n = 34) decrease in Cav3.3 currents. All data points correspond to mean ± S.E.

7.5, Northampton, MA). All recordings were performed at room temperature (20–22 °C).

The voltage dependence of activation for Cav3.1, Cav3.2, and Cav3.3 currents was measured by a series of 100–220-ms depolarizing pulses applied from a holding potential of −110 mV to membrane potentials from −80 to +10 mV, increasing at 5-mV increments, with 2 s between pulses. The potential that elicited peak currents ("peak potential" ranging from −45 to −25 mV) was obtained from this protocol and used in subsequent protocols. Series resistance was also monitored with a 5-ms depolarizing pulse to −105 mV immediately before the test pulse to ensure that this variable was relatively constant, and any changes in peak current levels were not because of significant changes in series resistance. Effects of saturating concentrations of mAChR agonist (1 mM CCh) on stable T-type currents were then investigated using steps to peak potential every 5 s (0.2 Hz) from a holding potential of −110 mV. These depolarizing steps were 80 ms in duration for Cav3.1 and Cav3.2 and 200 ms in duration for Cav3.3. The −140-mV prepulse protocol for Cav3.3 included a 1-s prepulse to −140 mV to remove any accumulated channel inactivation. To quantify the percent of channel inhibition, stimulation, or washout during CCh or control solution perfusion, the peak current magnitude at equilibrium was averaged (2–5 values). When distinct effects were observed (*i.e.* stimulation *versus* no effect of M1 on Cav3.1 currents), all cells displaying a >10% modulating effect with a clear exponential time course were grouped into one group, while the rest of the cells were grouped into the "no effect" group.

Current-voltage relationships were fitted with the modified Boltzmann equation, $I = (G_{max} \times (V_m - E_{rev}))/(1 + \exp(\{V_m - V_{0.5a}\}/k_a))$, where V_m is the test potential; $V_{0.5a}$ is the half-activation potential; E_{rev} is the extrapolated reversal potential; G_{max} is the maximum slope conductance, and k_a reflects the slope of the activation curve. Data from CCh concentration-response studies were fitted with the equation, $y = ((A_1 - A_2)/\{1 + (x/x_0)^P\} + A_2)$, where A_1 is initial amplitude (=0) and A_2 is final block value; x_0 is IC_{50} (concentration causing 50% inhibition of currents), and P gives a measure of the steepness of the curve. The activation and inactivation rates during steps to peak potential were well described by single exponential curves to give τ_{act} and τ_{inact} values, respectively. Statistical significance was tested with Student's t tests with significance being determined at a confidence interval of $p < 0.02$.

Solutions, Drugs, and Perfusion—A 25 mM stock of β-escin (in distilled H_2O) was prepared fresh, with dilution to working stocks in intracellular solution. Carbachol (CCh) was added directly to the extracellular recording solution. Wortmannin, okadaic acid, genistein, and H9 were all obtained from Tocris

Downloaded from www.jbc.org at Univ of Ottawa - OCUL on September 28, 2012

TABLE 1
Effects of receptor activation on T-type channel kinetic and voltage-dependent properties

	2 mM Ca^{2+} control			1 mM carbachol		
	τ_{act}	τ_{inact}	V_{50act}	τ_{act}	τ_{inact}	V_{50act}
	ms	*ms*	*mV*	*ms*	*ms*	*mV*
Cav3.3 + M1*(inhibition)	6.0 ± 0.4, $n = 27$	86 ± 6, $n = 27$	−51 ± 2, $n = 13$	4.1 ± 0.3, $n = 27^a$	31 ± 2, $n = 27^a$	−49 ± 1, $n = 13$
Human Cav3.3 + M1(whole-cell; inhibition)	9.7 ± 0.8, $n = 10$	117 ± 6, $n = 10$	−44 ± 1, $n = 4$	5.4 ± 0.6, $n = 10^a$	41 ± 5, $n = 10^a$	−47 ± 1, $n = 4$
Cav3.3 + M2(no effect)	6.1 ± 0.7, $n = 10$	81 ± 9, $n = 10$	−53 ± 3, $n = 4$	5.5 ± 0.7, $n = 10$	76 ± 9, $n = 10$	−52 ± 3, $n = 4$
Cav3.3 + M3(inhibition)	9.5 ± 0.9, $n = 9$	104 ± 13, $n = 9$	−53 ± 4, $n = 4$	6.2 ± 0.6, $n = 9^b$	56 ± 6, $n = 8^b$	−50 ± 4, $n = 4$
Cav3.3 + M4(no effect)	6.7 ± 0.9, $n = 6$	110 ± 18, $n = 6$	−50 ± 1, $n = 5$	6.0 ± 0.9, $n = 6$	101 ± 16, $n = 6$	−51 ± 2, $n = 5$
Cav3.3 + M5(inhibition)	8.6 ± 0.9, $n = 6$	127 ± 23, $n = 7$	−48 ± 1, $n = 5$	5.6 ± 0.6, $n = 6$	49 ± 6, $n = 7^b$	−45 ± 1, $n = 5$
Cav3.3 + Control Plasmid	6.0 ± 0.4, $n = 5$	78 ± 13, $n = 5$		5.2 ± 0.2, $n = 5$	71 ± 12, $n = 5$	
Cav3.1 + M1(no effect)	2.3 ± 0.2, $n = 17$	19 ± 2, $n = 17$	−36 ± 2, $n = 17$	2.1 ± 0.2, $n = 17$	17 ± 1, $n = 17$	−39 ± 3, $n = 11$
Human Cav3.1 + M1(whole-cell; no effect)	2.0 ± 0.4, $n = 9$	14 ± 1, $n = 9$	−42 ± 2, $n = 6$	1.2 ± 0.1, $n = 9$	13 ± 1, $n = 9$	−51 ± 3, $n = 4$
Cav3.2 + M1(no effect)	4.7 ± 0.2, $n = 16$	36 ± 2, $n = 15$	−42 ± 1, $n = 7$	4.3 ± 0.2, $n = 16$	34 ± 2, $n = 15$	−40 ± 2, $n = 7$

[a] $p < 0.001$.
[b] $p < 0.02$.

Cookson (Ellisville, MO). (R_p)-cAMP was obtained from BioMol International (Plymouth Meeting, PA). BAPTA-AM was obtained from Molecular Probes (Eugene, OR). Unless otherwise stated, all other drugs were obtained from Sigma. Drugs were dissolved in either distilled H_2O or Me_2SO, according to manufacturer's solubility data. The highest concentration of Me_2SO in the recording solution did not exceed 0.1%, a concentration that did not detectably affect T-type properties (data not shown). Gravity-driven perfusion occurred at a rate of ~400 μl/min, and the outputs of the manifold were placed within close proximity of the cell, resulting in the cell being bathed in new solutions with minimal delay (within 1 s).

RESULTS

Muscarinic M1 Receptors Selectively Inhibit Cav3.3 T-type Ca^{2+} Channels—To investigate the potential for T-type Ca^{2+} channel modulation by mAChRs, we transiently transfected HEK cell lines stably expressing individual subtypes of recombinant rat brain T-type channels with the human muscarinic M1 receptor. Perforated patch recordings with β-escin demonstrated that activation of M1 with 1 mM CCh caused a rapid (<30 s) and robust inhibition of exogenously expressed rat brain Cav3.3 T-type channel peak currents (−45 ± 2%, $n = 34$) (Fig. 1, *C* and *F*). Only a small subpopulation of stable Cav3.3 cells (<10%) was not affected by CCh application (likely representing cells untransfected with the M1 receptor).

Activation of M1 with 1 mM CCh had no significant effect ($p > 0.05$) on the voltage dependence of Cav3.3 currents but significantly increased both the rates of activation and inactivation ($p < 0.001$; Table 1). In contrast to the clear inhibition of Cav3.3 T-type currents, activation of M1 receptors with 1 mM CCh largely had no effect on the peak current amplitude of either rat brain Cav3.1(−2.1 ± 2.0%, $n = 18$) or Cav3.2 channels (−0.1 ± 2.3%, $n = 17$) (Fig. 1, *A, B, D,* and *E*). In a small subset of both Cav3.1 and Cav3.2 currents we noted a stimulation induced by M1 activation (Cav3.1 = 35 ± 12%, $n = 4$; Cav3.2 = 36 ± 12%, $n = 5$), with a slower time course to equilibrium of greater than 1 min ($n = 3$ and $n = 4$, respectively). For the prevalent null effect on Cav3.1 and Cav3.2 currents, 1 mM CCh application had no significant effect on channel activation and inactivation kinetics or the voltage dependence of activation ($p > 0.05$; Table 1).

Different Cav3.3 T-type channel isoforms with distinct carboxyl termini have been identified from both the rat and human brain (17, 19, 21, 38). To test whether inhibition of the Cav3.3 channel by M1 receptors was restricted to the rat brain short carboxyl-terminal isoform (17), we also examined the longer human Cav3.3 isoform (21) transiently co-transfected into HEK cells with the M1 receptor. Similar to that for the shorter rat brain isoform, application of 1 mM CCh resulted in significant inhibition of the human Cav3.3 peak current amplitude (−28 ± 2%, $n = 15$) and also significantly increased activation and inactivation kinetics ($p < 0.001$; Fig. 5*A*; Table 1). Additionally, similar to that for the rat Cav3.1 T-type channel, application of 1 mM CCh to HEK cells co-transfected with the human Cav3.1 channel and M1 receptor had no significant effect on peak current amplitude (−0.3 ± 2.0%, $n = 9$) or channel kinetics (for 100% cells tested; $p > 0.05$; Fig. 7*B*; Table 1). Overall, the differential modulation of T-type Ca^{2+} channel subtypes mediated by M1 receptors was consistent across both rat and human recombinant T-type channels.

Muscarinic M1 Receptors Dose-dependently Modulate Cav3.3 Biophysical Properties—Perforated patch recordings on stable rat Cav3.3 cells transiently transfected with M1 receptors revealed that the CCh-induced inhibition of peak current levels was reversible over a time course of about 2 min ($n = 13$; Fig. 2, *A* and *B*). As previously mentioned, activation of M1 receptors with 1 mM CCh caused a significant ($p < 0.001$) increase in inactivation kinetics (control, $\tau_{inact} = 86 \pm 6$, $n = 27$; 1 mM CCh, $\tau_{inact} = 31 \pm 2$, $n = 27$). Along with peak current inhibition, the CCh-induced increase in Cav3.3 inactivation kinetics was reversible (Fig. 2, *A* and *C*). Both the M1 receptor-induced inhibition of Cav3.3 peak currents and the increased inactivation rate would be predicted to reduce the total amount of Ca^{2+} flowing through Cav3.3 T-type channels during a cellular depolarization. The effect of M1 receptor activation on total Ca^{2+} influx was determined by integrating the area over Cav3.3 current traces during 200-ms depolarizing pulses to peak potential before and after 1 mM CCh application. Normalizing these Ca^{2+} influx values to control levels showed a 77 ± 2% ($n = 20$) reduction in Ca^{2+} influx mediated by M1 receptor activation (Fig. 2*D*).

As activation of M1 receptors increases the kinetics of Cav3.3 activation and inactivation, it is possible that this signaling pathway modulates Cav3.3 function via acting upon the open and/or inactivated states. A protocol that involved perfusion of 1 mM CCh for 50 s (time to reach normal inhibition equilib-

Downloaded from www.jbc.org at Univ of Ottawa - OCUL on September 28, 2012

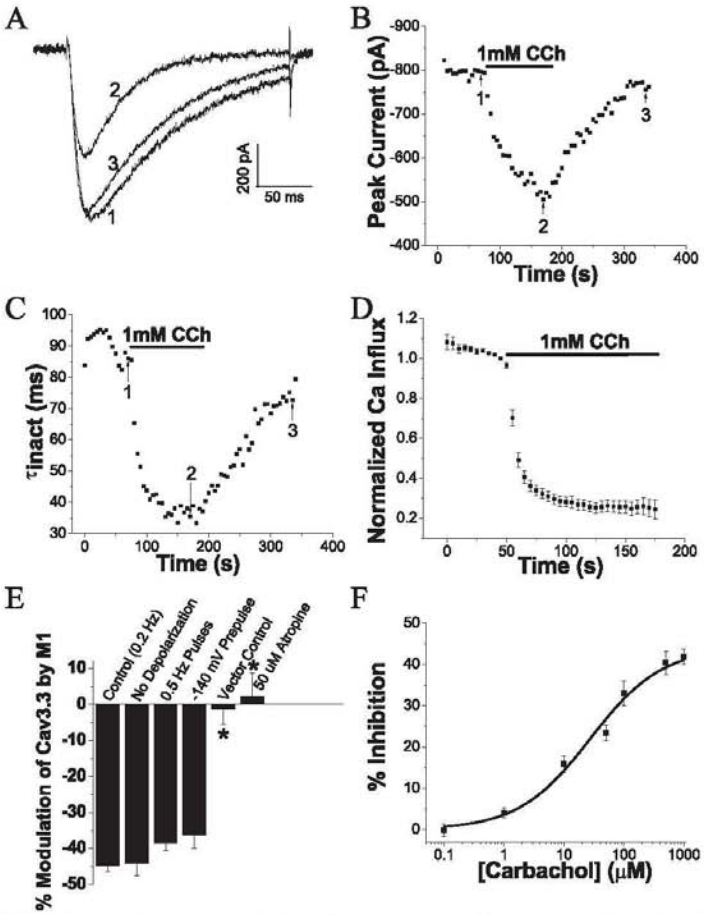

FIGURE 2. **Mechanistic properties of inhibition of Cav3.3 currents by M1 receptors.** *A*, inhibition of Cav3.3 channels by M1 is reversible. Representative Cav3.3 perforated patch current traces during depolarizing pulses from −110 to −40 mV before (*trace 1*), during (*trace 2*), and after (*trace 3*) perfusion of 1 mM CCh. Note the increase in inactivation kinetics when CCh is applied (Table 1). *B*, plot of peak current amplitude (for same cell as in *A*) showing the rate of inhibition by 1 mM CCh perfusion and the rate of washout, with the selected traces from *A* (*traces 1–3*) labeled. *C*, application of 1 mM CCh increases Cav3.3 inactivation kinetics in a reversible manner. The inactivating component of every trace from *B* was fit with an exponential equation to give τ_{inact}. *D*, application of 1 mM CCh dramatically reduces the amount of Ca^{2+} influx through Cav3.3 channels. The effects of M1 activation on normalized Ca^{2+} influx is shown for all Cav3.3 cells. Perfusion of 1 mM CCh caused a 77% (± 2%, $n = 20$) decrease in Ca^{2+} influx. *E*, inhibition of Cav3.3 currents by 1 mM CCh occurs through M1 receptors. Control experiments show elimination of the inhibition because of 1 mM CCh when a muscarinic antagonist (50 μM atropine) is co-applied or when a control vector (pBluescript) is transfected instead of M1. A lack of depolarizing test pulses during initial CCh perfusion, increase in test pulse frequency to 0.5 Hz, or a hyperpolarizing prepulse to −140 mV for 1 s had no significant ($p > 0.02$) effect on the magnitude of Cav3.3 inhibition by M1. * indicates significance at $p < 0.001$ compared with control (0.2 Hz). *F*, CCh inhibited Cav3.3 currents in a dose-dependent manner. CCh concentration *versus* percentage block data were fit with a Hill equation, and the IC_{50} for CCh inhibition of Cav3.3 currents was 27 μM. All data points correspond to mean ± S.E.

rium) in the absence of test pulses, followed by regular 0.2-Hz test pulses to peak potential, examined whether the M1 receptor-mediated inhibitory effect is use-dependent. Fig. 2*E* shows that this "no depolarization" protocol displayed the same level of inhibition of Cav3.3 currents observed in the regular 0.2-Hz experiments, indicating that M1 effects on Cav3.3 are use-independent. Increasing the test pulse frequency to 0.5 Hz also caused no significant ($p > 0.05$) change in the level of Cav3.3 inhibition, indicating that the M1 effects on Cav3.3 are also frequency-independent (Fig. 2*E*). Another possibility is that M1 receptor activation inhibits Cav3.3 currents by shifting steady-state inactivation to more hyperpolarized potentials, reducing the proportion of channels available (in the closed state) to open at the holding potential of −110 mV. A protocol with a 1-s prepulse to −140 mV to remove accumulated channel inactivation demonstrated no significant ($p > 0.05$) difference in inhibition compared with the control protocol, suggesting that the inhibitory effect is not because of changes in the steady-state inactivation of Cav3.3 channels (Fig. 2*E*).

Control experiments with mock transfections of an empty control vector or with a preincubated mAChR antagonist (atropine) demonstrated that the CCh-induced inhibition of Cav3.3 currents is mediated specifically via the transfected M1 receptor (Fig. 2*E*). Testing the effects of varying concentrations of CCh on stable Cav3.3 cells with transfected M1 receptors revealed that the inhibitory effect is dose-dependent (Fig. 2*F*). The IC_{50} for inhibition of Cav3.3 currents by CCh = 27 μM, consistent with that reported for phosphatidylinositol hydrolysis triggered by M1 receptor activation in both HEK 293 and Chinese hamster ovary cells (39, 40).

Inhibition of Cav3.3 Channels by M1 Receptors Requires $G\alpha_{q/11}$—The inhibitory effect of M1 receptor activation on Cav3.3 currents could occur either through Gβγ- or Gα-mediated processes. To test for the involvement of Gβγ, a membrane-targeted version of the carboxyl terminus of β-arrestin kinase, MAS-GRK3ct (41), was co-transfected with M1 receptors into the stable Cav3.3 HEK cell line. Control experiments showed that the MAS-GRK3ct construct was able to completely abolish the well described Gβγ-dependent inhibition of N-type Ca^{2+} channels (data not shown). MAS-GRK3ct only partially

Downloaded from www.jbc.org at Univ of Ottawa - OCUL on September 28, 2012

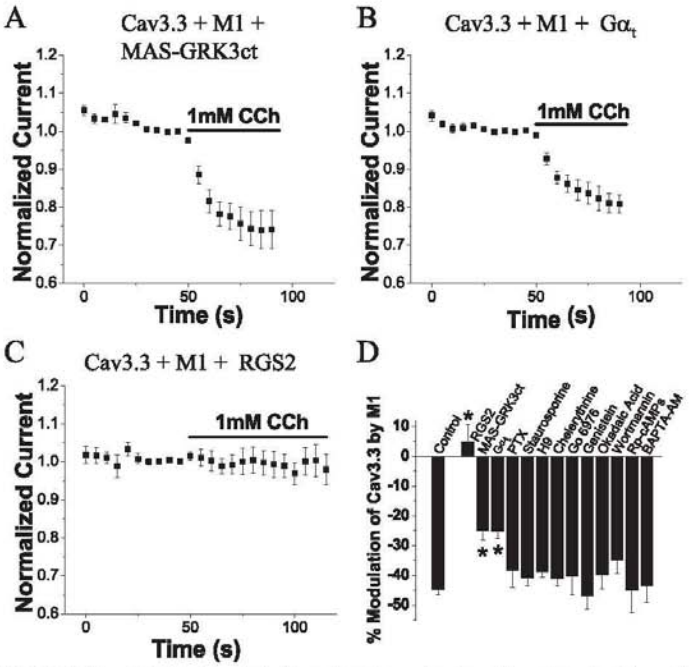

FIGURE 3. **Inhibition of Cav3.3 channels by M1 requires $G\alpha_{q/11}$ signaling.** *A*, in perforated patch recordings of Cav3.3 stable cells co-transfected with M1 and a membrane targeted form of the carboxyl terminus of β-arrestin kinase that sequesters active Gβγ subunits (MAS-GRK3ct), application of 1 mM CCh caused inhibition of Cav3.3 currents (−24.8 ± 3.4%, $n = 10$). *B*, similarly, inhibition by perfusion of 1 mM CCh was observed for Cav3.3 cells co-transfected with the Gβγ buffer $G\alpha_{transducin}$ ($G\alpha_t$) and M1 (−25.1% ± 2.5%, $n = 10$). *C*, in perforated patch recordings of Cav3.3 cells co-transfected with M1 and RGS2 (antagonist of active $G\alpha_{q/11}$ subunits), application of 1 mM CCh predominantly had no effect (1 ± 5%, $n = 7$) on Cav3.3 currents. *D*, *bar graph* comparing various genetic and pharmacological manipulations to control conditions where stable Cav3.3 cells are transfected with M1 and inhibited by 1 mM CCh. Inhibitors of serine/threonine kinases (500 nM staurosporine, $n = 7$; 50 μM H9, $n = 6$), PKC (10 μM chelerythrine, $n = 5$; 500 nM Go 6976, $n = 6$), tyrosine kinases (10 μM genistein, $n = 7$), phosphatases (100 nM okadaic acid, $n = 6$), phosphoinositide 3-kinases (200 nM wortmannin, $n = 7$), PTX-sensitive Gα proteins (0.5 μg/ml PTX, $n = 6$), cAMP (10 μM (R_p)-cAMP, $n = 5$), and internal Ca^{2+} (10 μM BAPTA-AM, $n = 5$) had no significant effect ($p > 0.02$) on the inhibition of Cav3.3 currents by M1. RGS2, MAS-GRK3ct, and $G\alpha_t$ ($p < 0.001$) caused a significant elimination or reduction in the inhibition of Cav3.3 currents by M1. All data points correspond to mean ± S.E. * indicates significance at $p < 0.001$ compared with control.

reduced M1-mediated Cav3.3 current inhibition (−24.8 ± 3.4%, $n = 10$) in most cells, suggesting that inhibition is distinct from the previously reported pure Gβγ-mediated inhibition of N- and P/Q-type and Cav3.2 Ca^{2+} channels (42, 43) (Fig. 3, *A* and *D*). A smaller subset of MAS-GRK3ct co-transfected cells displayed no exponential inhibitory effect (−9.3 ± 3.0%, $n = 7$). Co-expression of transducin ($G\alpha_t$), which also buffers Gβγ signaling (41), caused the same reduction in M1-mediated inhibition of Cav3.3 currents (−25.1 ± 2.5%, $n = 10$), with a small number of cells not being inhibited at all (7.0 ± 10.1%, $n = 3$) (Fig. 3, *B* and *D*).

In contrast to the partial effect of Gβγ signaling antagonists, co-expression of the regulator of G-protein signaling 2 (RGS2), an effector antagonist for $G\alpha_{q/11}$ (44), completely prevented the M1 receptor-induced inhibition of Cav3.3 currents for all cells examined. In perforated patch recordings of Cav3.3 cells co-transfected with M1 and RGS2, application of 1 mM CCh either had no effect (Fig. 3, *C* and *D*; 1% ± 5%, $n = 7$) or caused a stimulation of Cav3.3 currents (30% ± 9%, $n = 5$). RGS2 has been thoroughly characterized and shown to be a selective GTPase-activating protein for $G\alpha_q$/$G\alpha_{11}$, but not for other Gα proteins (44), and is an effector antagonist that does not block the Gβγ-mediated inhibition of R-type Ca^{2+} channels (45).

Constitutively Active $G\alpha_{q/11}$ Proteins Modulate Cav3.3 T-type Ca^{2+} Channels—To further test whether active $G\alpha_{q/11}$ G-proteins are sufficient to produce inhibition of Cav3.3 currents, stable Cav3.3 cells were transiently transfected with various constitutively active Gα subunit constructs. These constructs contain missense mutations that confer constitutive activity by reducing GTPase activity. If $G\alpha_{q/11}$ is the downstream signal of M1 receptor activation mediating the effects on Cav3.3 currents, then it is hypothesized that activation of the co-expressed $G\alpha_q$ or $G\alpha_{11}$ mutants by dialysis of GTP would cause a reduction in current amplitude and an increase in inactivation kinetics. Similar to a study that analyzed inhibition of KCNQ2/KCNQ3 channels by $G\alpha_{q/11}$ (46), we used constitutively active $G\alpha_q$ ($G\alpha_{q\text{-}Q209L}$) and $G\alpha_{11}$ ($G\alpha_{11\text{-}Q209L}$) mutants to test for the hypothesized effect and a constitutively active Gα protein ($G\alpha_{13\text{-}Q226L}$) that does not couple to the same downstream effectors (PLC) as a negative control. We also performed controls wherein empty vectors were transfected. By comparing traces 30 s after forming the whole-cell configuration with traces 2 min after whole-cell in Fig. 4, *A–D*, we found that dialysis of the cell with the GTP-containing pipette internal solution caused both a significant reduction in peak current levels and an increase in inactivation kinetics only for the $G\alpha_{q\text{-}Q209L}$ and $G\alpha_{11\text{-}Q209L}$ transfections. The ratio of peak current levels at 2 min divided by the peak current levels at 30 s was significantly reduced ($p < 0.001$) for $G\alpha_{q\text{-}Q209L}$ ($n = 16$) and $G\alpha_{11\text{-}Q209L}$ ($n = 15$) compared with the control transfection ($n = 18$), whereas the $G\alpha_{13\text{-}Q226L}$ ($n = 17$) transfection current ratio was not significantly altered (($p > 0.05$), Fig. 4*E*). The rates of inactivation (τ_{inact}) were determined during depolarizing steps from −110 to −30 mV for all transfection types. The τ_{inact} was significantly faster ($p < 0.001$) for $G\alpha_{q\text{-}Q209L}$ and $G\alpha_{11\text{-}Q209L}$

Downloaded from www.jbc.org at Univ of Ottawa - OCUL on September 28, 2012

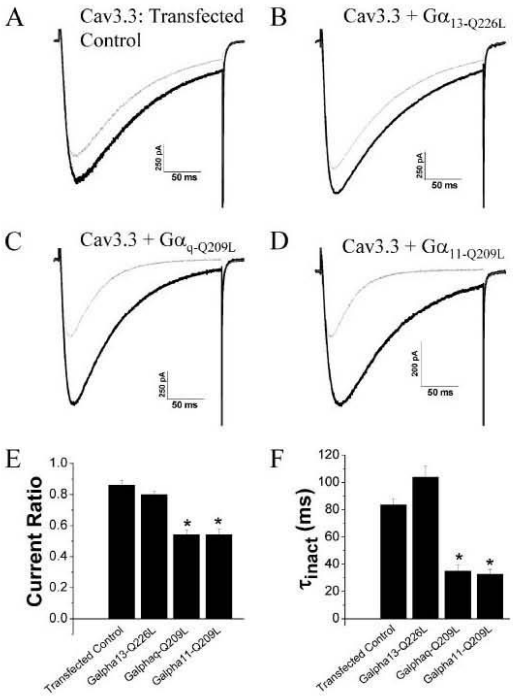

FIGURE 4. **The $G\alpha_{q/11}$ subtypes of $G\alpha$ proteins specifically cause inhibition of Cav3.3 currents.** *A–D*, representative whole-cell current traces of stable Cav3.3 cells transfected with various control or $G\alpha$ plasmids during depolarizing steps from −110 to −30 mV. Traces were obtained 30 s (*black*) and 2 min (*gray*) after the whole-cell conformation was formed, using an internal solution that contained 4 mM ATP and 0.3 mM GTP. The stable Cav3.3 cells were mock-transfected with empty plasmid (*A*) or transfected with the constitutively active forms (lack of GTPase activity) of $G\alpha$ proteins as follows: $G\alpha_{13\text{-}Q226L}$ (*B*), $G\alpha_{q\text{-}Q209L}$ (*C*), $G\alpha_{11\text{-}Q209L}$ (*D*). *E*, $G\alpha_{q\text{-}Q209L}$ and $G\alpha_{11\text{-}Q209L}$ cause a time-dependent reduction in Cav3.3 current magnitude. The peak current levels at 2 min were divided by the peak current levels at 30 s to determine the level of inhibition because of internal solution dialysis for the various types of transfected Cav3.3 cells, as described above. The Cav3.3 currents co-transfected with $G\alpha_{q\text{-}Q209L}$ and $G\alpha_{11\text{-}Q209L}$ had a significant ($p < 0.001$) reduction in current ratio compared with the control transfection, whereas the $G\alpha_{13\text{-}Q226L}$ transfection caused no significant change ($p > 0.05$). *F*, rate of inactivation (τ_{inact}) was determined during depolarizing steps from −110 to −30 mV for all transfection types. The τ_{inact} was significantly ($p < 0.001$) faster for $G\alpha_{q\text{-}Q209L}$ and $G\alpha_{11\text{-}Q209L}$ compared with control transfections, whereas the τ_{inact} was not significantly ($p > 0.02$) different for $G\alpha_{13\text{-}Q226L}$. All data points correspond to mean ± S.E. * indicates significance at $p < 0.001$ compared with transfected control.

compared with control transfections, whereas the τ_{inact} was not significantly different for $G\alpha_{13\text{-}Q226L}$ ($p > 0.02$; Fig. 4*F*).

$G\alpha_{q/11}$ Inhibits Cav3.3 Channels through an Unidentified Nonclassical Pathway—The active GTP-bound form of $G\alpha_{q/11}$ causes the activation of PLC, which then produces inositol 1,4,5-trisphosphate- and diacylglycerol/PKC-mediated signals. Various pharmacological antagonists were used to investigate the role of potential cellular signals downstream of $G\alpha_{q/11}$. Specific inhibitors of PKC, including 10 μM chelerythrine ($n = 5$) and 500 nM Go 6976 ($n = 6$), had no significant ($p > 0.05$) effect on the M1-mediated inhibition of Cav3.3 currents (Fig. 3*D*). To ensure pharmacological activity of these antagonists, the PKC-mediated stimulation of Cav3.2 channels by 300 nM phorbol 12-myristate 13-acetate (65 ± 17%, $n = 7$; see Ref 47) was shown to be significantly ($p < 0.02$) abolished by both 10 μM chelerythrine (−15 ± 6%, $n = 5$) and 500 nM Go 6976 (3 ± 5%, $n = 5$) (data not shown). Inhibitors of serine/threonine kinases (500 nM staurosporine, $n = 7$; 50 μM H9, $n = 6$), tyrosine kinases (10 μM genistein, $n = 7$), phosphatases (100 nM okadaic acid, $n = 6$), phosphoinositide 3-kinases (200 nM wortmannin, $n = 7$), pertussis toxin-sensitive $G\alpha$ proteins (0.5 μg/ml pertussis toxin, $n = 6$), cAMP (10 μM (R_p)-cAMP, $n = 5$), and internal Ca^{2+} (10 μM BAPTA-AM, $n = 5$) also had no significant effect ($p > 0.02$) on the inhibition of Cav3.3 currents by M1 receptors (Fig. 3*D*). In this regard, classical $G\alpha_{q/11}$ downstream effectors such as PKC, cAMP-dependent protein kinase, and increased cytosolic Ca^{2+} concentration appear not to be directly involved in the M1 receptor-mediated inhibition of Cav3.3 T-type Ca^{2+} currents. Phospholipase C activity has been shown recently to directly inhibit voltage-gated ion channels through the depletion of membrane $PI(4,5)P_2$ levels, which are thought to stabilize active channels in the membrane (48). Dialyzing cells with a $PI(4,5)P_2$ antibody (50 μg/ml) to reduce available $PI(4,5)P_2$ levels had no significant effect ($p > 0.05$) on the M1 receptor-mediated inhibition of Cav3.3 currents (Fig. 5, *B* and *D*). Similarly, dialyzing cells with synthetic $PI(4,5)P_2$ (200 μM di-C8 $PI(4,5)P_2$) to saturate membrane $PI(4,5)P_2$ levels also had no significant effect ($p > 0.05$) on M1 receptor-mediated inhibition of Cav3.3 currents (Fig. 5, *C* and *D*). As a positive control for di-C8 $PI(4,5)P_2$ activity and as previously shown (49), dialysis of 200 μM di-C8 $PI(4,5)P_2$ into HEK 293 cells stably expressing HERG K^+ channels caused a significant ($p < 0.02$) stimulation of K^+ channel currents ($n = 8$) compared with control recordings ($n = 5$; data not shown). Taken together, these results indicate that inhibition of Cav3.3 by M1 receptors occurs either directly through $G\alpha_{q/11}$ or a downstream pathway that is independent of $PI(4,5)P_2$ metabolism and other classical effectors.

$G\alpha_{q/11}$-coupled Muscarinic Receptors Selectively Inhibit Cav3.3 Channels—If inhibition of Cav3.3 T-type Ca^{2+} channels by M1 receptors is primarily dependent on $G\alpha_{q/11}$ signaling, then all $G\alpha_q/G\alpha_{11}$-coupled mAChRs should similarly inhibit Cav3.3 currents, whereas $G\alpha_i$-coupled mAChRs should have no effect. Indeed, activation of co-expressed $G\alpha_i$-coupled M2 and M4 receptors with 1 mM CCh had no effect on Cav3.3 current amplitude (M2 = −4 ± 2%, $n = 11$; M4 = −4 ± 3%, $n = 8$) or kinetics (Fig. 6, *A*, *C*, *E*, and *G*; Table 1). In contrast, upon transfection of either the $G\alpha_q/G\alpha_{11}$-coupled M3 or M5 receptor subtypes into stable Cav3.3 cells, perforated patch recordings revealed a significant CCh-mediated inhibition (M3 = −25 ± 3%, $n = 10$; M5 = −31 ± 3%, $n = 10$) as well as a concomitant increase in both activation and inactivation kinetics (Fig. 6, *B*, *D*, *F*, and *H*; Table 1). Overall, experiments with genetically encoded antagonists of $G\alpha_{q/11}$ (RGS2) and $G\beta\gamma$ (MAS-GRK3ct) and genetically encoded $G\alpha$ subtypes, as well as inhibition experiments with various mAChRs, all support the assertion that inhibition of Cav3.3 channels by mAChRs specifically occurs through $G\alpha_{q/11}$.

Downloaded from www.jbc.org at Univ of Ottawa - OCUL, on September 28, 2012

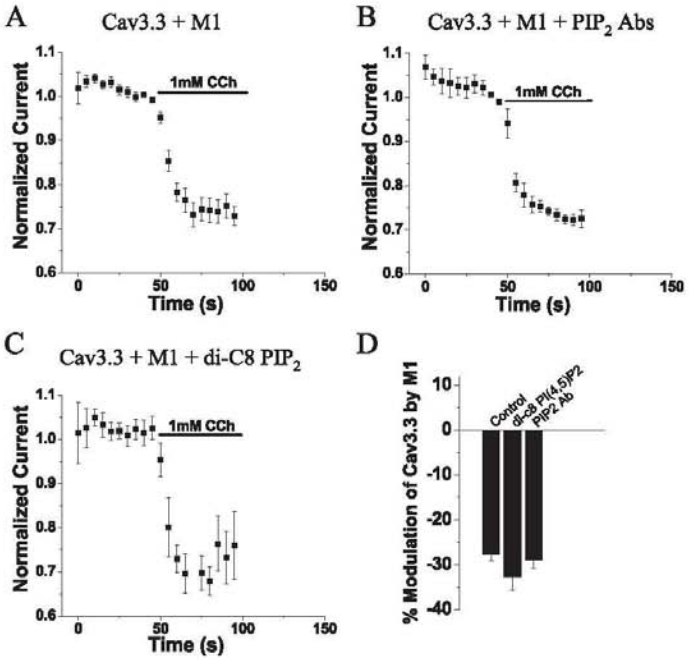

FIGURE 5. **Inhibition of Cav3.3 channels by M1 does not require PI(4,5)P_2 signaling.** *A*, in whole-cell recordings of HEK 293 cells co-transfected with human Cav3.3 and M1, application of 1 mM CCh caused inhibition of Cav3.3 currents (−27.7 ± 1.5%, n = 15). *B*, dialyzing cells with 50 μg/ml PI(4,5)P_2 antibody for 10+ min had no effect on the inhibition of human Cav3.3 currents by M1 receptor activation (−30.8 ± 3.9%, n = 7). *C*, dialyzing cells with 200 μM di-C8 PI(4,5)P_2 for 5+ min had no effect on the inhibition of human Cav3.3 currents by M1 receptor activation (−29.0 ± 1.8%, n = 6). *D*, *bar graph* showing that attenuating PI(4,5)P_2 signaling with either PI(4,5)P_2 antibodies or di-C8 PI(4,5)P_2 had no significant effect ($p > 0.05$) on M1-mediated inhibition compared with whole-cell recordings from control human Cav3.3 + M1 cells.

Two Distinct Cav3.3 Channel Regions Are Involved in M1-mediated Inhibition—Most modulation of Ca^{2+} channels by intracellular signaling pathways involves physical interactions between various effectors and cytoplasmic channel domains (42, 50). Chimeric T-type Ca^{2+} channels between human Cav3.1 and human Cav3.3 were generated to determine the molecular regions of the Cav3.3 channel involved in the M1 receptor-mediated inhibition (Fig. 7). The Cav3.1 and Cav3.3 full-length channels were initially divided into four approximately equal portions, and chimeric channels were constructed using restriction enzyme digestion and religation (see Ref. 37). The four channel portions were named as follows: region 1 = amino terminus + domain I; region 2 = domain I–II linker, domain II + the first 39–63 amino acids of the domain II–III linker; region 3 = remainder of the domain II–III linker + domain III; and region 4 = the domain III–IV linker, domain IV + the carboxyl terminus. Chimeric channel names were assigned based on whether the chimera contained Cav3.1 (G) or Cav3.3 (I) sequence in each of the four regions described (*e.g.* the chimeric Cav3.3 channel that contained region 2 from Cav3.1 is called IGII).

Co-expression of M1 receptors with chimeric GIII and IIGI T-type channels both showed a similar degree of M1 receptor-mediated peak current inhibition compared with that of the inhibition of the WT Cav3.3 channel (IIII) (Fig. 7, *A* and *E*). In contrast, when the IGII chimera was co-transfected with M1 receptors, application of 1 mM CCh resulted in a significantly attenuated degree of inhibition (−5.6 ± 2.1%, n = 11, ($p < 0.001$)) compared with the wild type IIII channel (−26.9 ± 2.3%, n = 9; Fig. 7*E*). Interestingly, although the chimeric IGII channels exhibited lowered M1 receptor-mediated inhibition, they still possessed significantly increased inactivation kinetics ($p < 0.001$; Table 2). Finally, although the IIIG chimeric channels showed similar degree of M1 receptor-mediated peak current inhibition compared with the wild type IIII, the rate of inhibition was notably slower (not shown). The changes in the rate of inhibition for IIIG and the significant decrease in the amount of inhibition for IGII suggested that both regions 2 and 4 might be involved in the M1-induced inhibition of Cav3.3 channels. To explore this, a double chimera (IGIG) was co-transfected into HEK cells with M1 receptors. Fig. 7, *C* and *E*, shows that the inhibiting effect of 1 mM CCh application on peak current amplitude was completely abolished for the IGIG chimera (0.9 ± 2.5%, n = 8). Activation of M1 with 1 mM CCh still caused a significant increase ($p < 0.001$) in the inactivation kinetics of IGIG, but the τ_{inact} decreased by less than 25% for IGIG, and it decreased by 40–65% for all the single chimeric and wild type Cav3.3 channels (Table 2).

The chimeric channel loss-of-function experiments indicate that both regions 2 and 4 are involved in the M1-mediated inhibition of current amplitude and increase in inactivation kinetics of Cav3.3 currents. In gain-of-function experiments, substitution of either region 2 (GIGG) or region 4 (GGGI) into the Cav3.1 channel resulted in 1 mM CCh-induced inhibition (GIGG = −14.3 ± 0.8%, n = 7; GGGI = −9.1 ± 2.6%, n = 9) that was significantly different ($p < 0.001$ and $p < 0.02$, respectively) when compared with GGGG (−0.3 ± 2.2%, n = 9; Fig. 7, *B* and *E*; Table 2). In contrast, inclusion of either region 1 or region 3 of Cav3.3 into Cav3.1 resulted in no significant change ($p > 0.05$) in M1-mediated inhibition when compared with GGGG (Fig. 7*E*). Although both GIGG and GGGI were inhibited by M1, the level of inhibition was significantly lower ($p < 0.001$) than the inhibition of IIII by M1 (Fig. 7*E*). When the effect of 1 mM CCh application on GIGI current amplitude was tested, M1 activation was found to produce a significant level of

Downloaded from www.jbc.org at Univ of Ottawa - OCUL on September 28, 2012

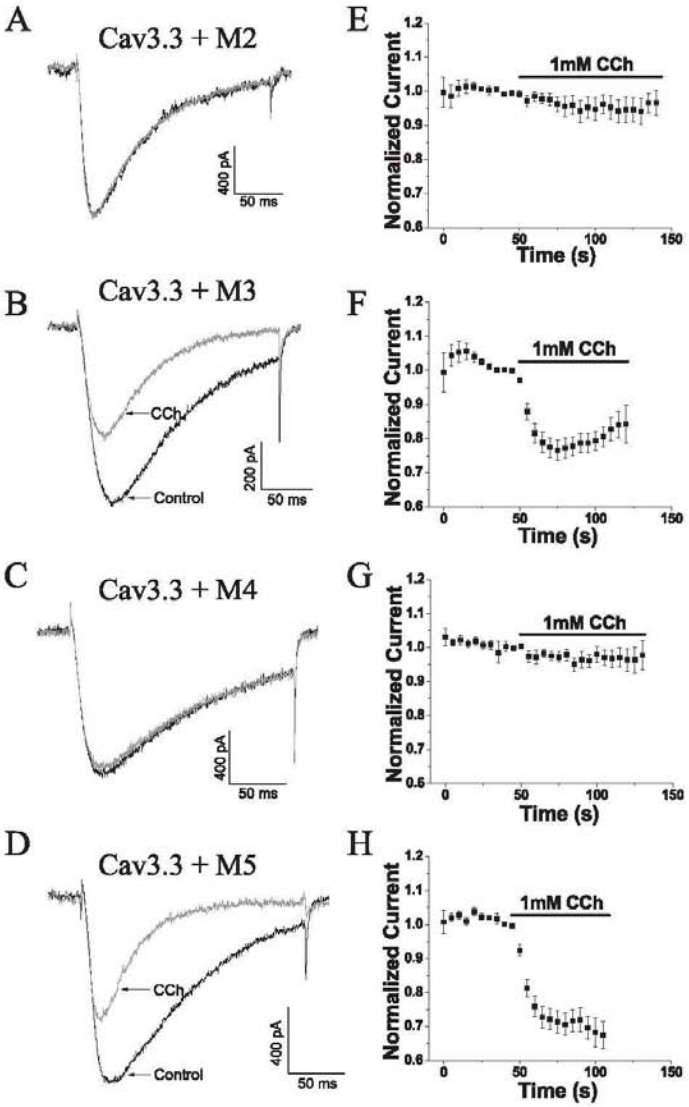

FIGURE 6. **Inhibition of Cav3.3 currents occurs specifically through $G\alpha_{q/11}$-coupled muscarinic receptors.** *A* and *C*, representative perforated patch current traces during depolarizing pulses from −110 to −40 mV showing no effect on Cav3.3 currents by the $G\alpha_i$-coupled M2 and M4 receptors, respectively. Traces during control perfusion and perfusion of 1 mM CCh are indistinguishable, and CCh application had no significant effect on channel kinetics (Table 1). *E* and *G*, averaged time course of normalized peak current levels during perfusion of control recording solution (2 mM Ca^{2+}) followed by 1 mM CCh for Cav3.3 (+M2/M4) currents. Perfusion of CCh had no effect on Cav3.3 currents for M2 (*E*; −4 ± 2%, $n = 11$) and M4 (*G*; −4 ± 3%, $n = 8$) receptors. *B* and *D*, representative perforated patch current traces during depolarizing pulses from −110 to −40 mV showing inhibition of Cav3.3 currents by the $G\alpha_{q/11}$-coupled M3 and M5 receptors, respectively. Activating the receptors with 1 mM CCh also significantly ($p < 0.02$) increased channel kinetics (Table 1). *F* and *H*, averaged time course of normalized peak current levels during perfusion of control recording solution (2 mM Ca^{2+}) followed by 1 mM CCh for Cav3.3 plus either M3 or M5 receptors. Perfusion of CCh caused a 25 ± 3% decrease ($n = 10$) of Cav3.3 currents with co-transfected M3 receptors (*F*) and a 31 ± 3% decrease ($n = 10$) of Cav3.3 currents with co-transfected M5 receptors. Only a small number of cells ($n = 2$ for both M3 and M5) were not inhibited by CCh. All data points correspond to mean ± S.E.

GIGI inhibition (−25.1 ± 2.4%, $n = 11$; $p < 0.001$) compared with GGGG that was not significantly ($p > 0.05$) different from the inhibition of IIII (Fig. 7, *A*, *B*, *D*, and *E*). Application of 1 mM CCh also significantly increased ($p < 0.001$) the rate of inactivation for the GIGI Cav3.1 chimera but not for GIGG, GGGI, or the other Cav3.1 single chimeras (Table 2). Overall, the combined substitution of regions 2 and 4 from the Cav3.3 channel into the Cav3.1 channel completely restores M1-induced inhibition together with the associated increase in channel inactivation kinetics.

DISCUSSION

In this study we systematically explored the effects of activated muscarinic GPCRs on the three main T-type Ca^{2+} channel isoforms expressed in the mammalian nervous system, and we report for the first time the differential modulation between a G-protein signaling pathway and Cav3.3 T-type Ca^{2+} channels. Most studies on T-type Ca^{2+} channel modulation have involved the Cav3.2 (α_{1H}) subtype, revealing specific modulatory responses to $G\beta_2\gamma$, CAMKII, and redox modulation that are not observed for the Cav3.1 and Cav3.3 T-type Ca^{2+} channel isoforms (42, 51, 52). The exclusive inhibition of Cav3.3 channels by $G\alpha_{q/11}$-coupled mAChRs is the first example of specific GPCR-mediated modulation of a T-type Ca^{2+} channel subtype other than for Cav3.2.

Differential Effects of mAChRs on T-type Ca^{2+} Channel Isoforms—Examination of the literature shows that activation of mAChRs can result in multiple effects on native T-type Ca^{2+} currents, including causing stimulation (26, 27, 53), inhibition (28), or having no effect (54). Given the heterogeneous nature of native low threshold Ca^{2+} currents, without investigating interactions between specific mAChR gene products and specific T-type Ca^{2+} channel isoforms, the published differences in modulation

Downloaded from www.jbc.org at Univ of Ottawa - OCUL on September 28, 2012

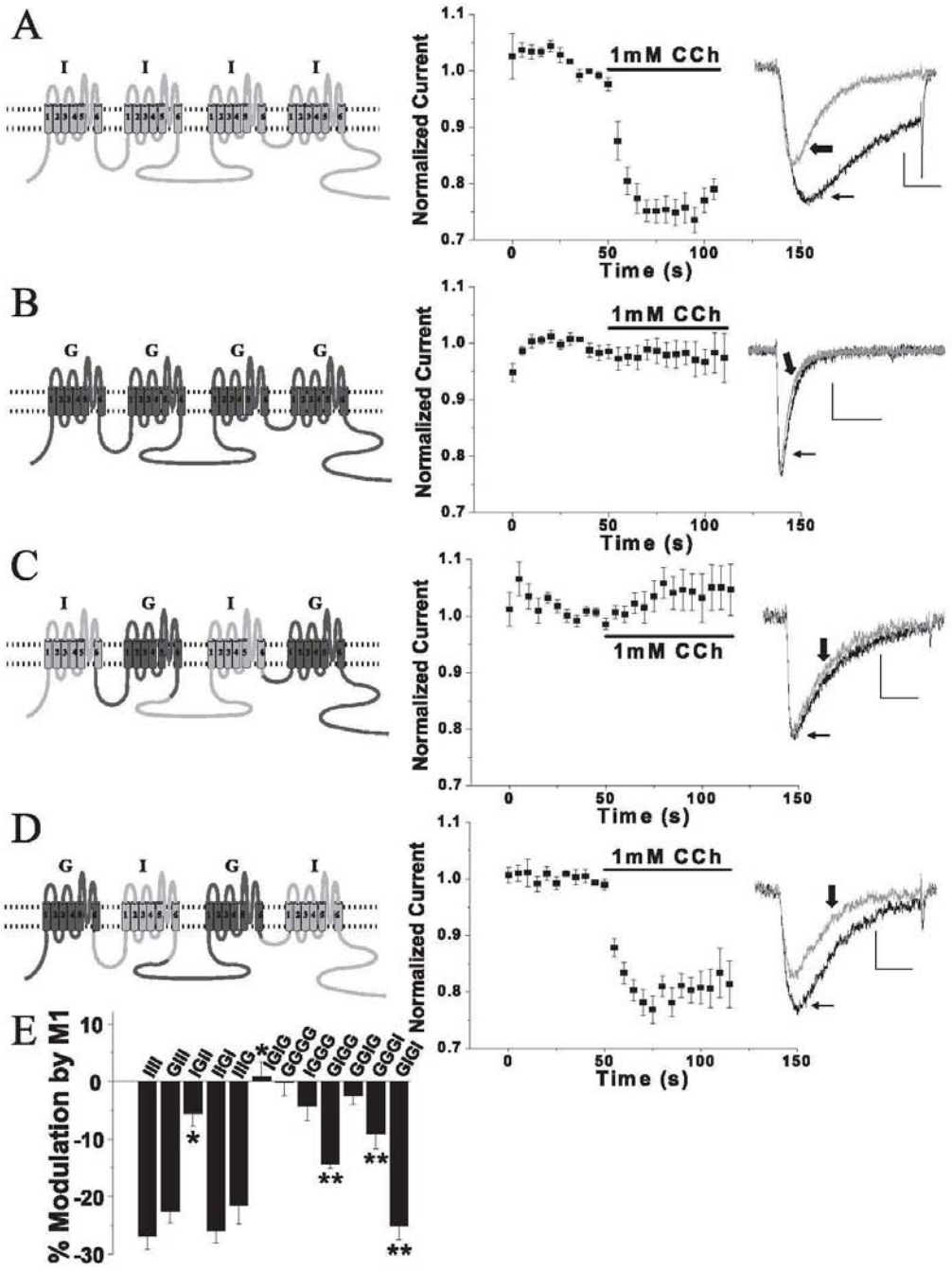

Downloaded from www.jbc.org at Univ of Ottawa - OCUL on September 28, 2012

TABLE 2
Effects of M1 receptor activation on chimeric T-type channel inactivation kinetics

	IIII	IGII	IIIG	IGIG	GGGG	GIGG	GGGI	GIGI
Control $-\tau_{inact}$ (ms)	$117 \pm 6, n = 10$	$86 \pm 7, n = 11$	$103 \pm 11, n = 10$	$62 \pm 2, n = 8$	$14 \pm 1, n = 9$	$20 \pm 1, n = 9$	$38 \pm 3, n = 8$	$58 \pm 2, n = 10$
1 mM CCh $-\tau_{inact}$ (ms)	$41 \pm 5, n = 10^a$	$43 \pm 3, n = 11^a$	$58 \pm 4, n = 10^b$	$47 \pm 3, n = 8^b$	$13 \pm 1, n = 9$	$17 \pm 2, n = 7$	$32 \pm 2, n = 8$	$38 \pm 1, n = 10^a$

[a] $p < 0.001$.
[b] $p < 0.02$.

are nearly impossible to interpret. Our results using exogenous expression of cloned T-type Ca^{2+} channels indicates that M1 receptor activation has a robust inhibitory effect on Cav3.3 currents and has either no effect or a small stimulation on both Cav3.1 and Cav3.2 currents. Similarly, experiments examining native Cav3.2 Ca^{2+} channels in NIH3T3 cells transiently transfected with mAChRs demonstrated that M1 receptor activation had either no effect or a stimulatory effect if a PKC inhibitor was applied (27). Active $G\beta_2\gamma$ subunits have been shown to specifically inhibit Cav3.2 currents (42, 55), and the lack of inhibition of Cav3.2 channels by M1 receptors in our study is likely because of the absence of any functional coupling between M1 receptors and $G\beta_2$ proteins (56). We also found that all $G\alpha_{q/11}$-coupled mAChR subtypes (M1, M3, and M5) cause attenuation of Cav3.3 currents, whereas $G\alpha_i$-coupled M2 and M4 receptors had no effect on Cav3.3 currents. Thus it is likely that any *stimulation* of T-type Ca^{2+} currents by mAChRs in native systems does not involve Cav3.3 channels. Experiments testing the effects of recombinant M2–M5 receptors on the Cav3.2 and Cav3.1 Ca^{2+} channel isoforms in a heterologous system are required to further facilitate the possibility of interactions between these T-type channels and mAChRs.

Functional Effects of M1 Receptor Activation on Cav3.3 Currents—Activation of M1 receptors dramatically altered Cav3.3 currents by both reversibly attenuating peak current levels and increasing the rate of inactivation, resulting in a significant reduction in the influx of Ca^{2+}. The relationship between these effects was explored using both structural channel chimeras and classical gating property studies. In chimeric studies (see below), the activation of M1 receptors primarily caused an increase in inactivation kinetics of the IGII chimera and, conversely, primarily a decrease in peak current levels for the GIGG chimera. Both this isolation of the two specific M1 receptor-mediated effects and the gating results discussed below suggest that the effects of M1 on current amplitude and inactivation kinetics are complementary but distinct phenomena. For gating studies, reduction of Cav3.3 current magnitude by M1 receptor activation was equally robust when the Cav3.3 channels were held in various states including: 1) during a prolonged hyperpolarization with no test depolarizations (channels mostly in closed state); 2) after a strong hyperpolarizing prepulse to −140 mV; and 3) during 200-ms test depolarizations to peak potential at 0.2 and 0.5 Hz. Combining this lack of use dependence with the observed reduction in peak current amplitude and the increase in activation and inactivation kinetics indicates that all states of the Cav3.3 channel are subject to modulation by M1 receptor activation. The acceleration of Cav3.3 channel kinetics by M1 receptor activation also supports the hypothesis that modulation affects channel biophysical properties and not channel density via internalization, which has recently been shown to occur for the voltage-independent, GPCR-mediated inhibition of N-type Ca^{2+} channels on a relatively fast time scale (57). Physiologically, the combined decrease in Cav3.3 peak currents and the increased activation and inactivation kinetics would be predicted to alter neuronal firing patterns and perhaps eliminate rhythmic oscillations (23, 58). In support of this notion, the concomitant reduction in peak current and increase in inactivation kinetics of Cav3.3 currents triggered by anandamide have been shown to completely eliminate the sustained, rhythmic Cav3.3 current during an action potential voltage clamp experiment with an oscillating thalamic waveform (59).

Signal Transduction Pathway of M1 Receptor-mediated Cav3.3 Inhibition—Use of genetically encoded antagonists of $G\beta\gamma$ (MAS-GRK3ct and $G\alpha_t$) and $G\alpha_{q/11}$ (RGS2) demonstrated that $G\beta\gamma$ may partially contribute to the M1-mediated inhibition of Cav3.3 currents, whereas $G\alpha_{q/11}$ is absolutely required for complete inhibition. The potential involvement of both $G\alpha_{q/11}$ and $G\beta\gamma$ in a nonclassical, voltage-independent mechanism of Ca^{2+} channel inhibition by mAChRs has been described previously for HVA Ca^{2+} channels. In rat superior cervical ganglion sympathetic neurons, application of a muscarinic agonist causes the voltage-independent inhibition of endogenous N-type Ca^{2+} channels that is abolished by co-expression of RGS2, $G\alpha_t$, or MAS-GRK3ct and exhibits a time course similar to the Cav3.3 inhibition reported here (41). As $G\beta\gamma$ is a cofactor for PLCβ activity, a possible explanation is that sequestering $G\beta\gamma$ reduces PLCβ activity (60). Although $G\beta\gamma$ may potentiate the inhibitory effect of M1 receptor activation, transfection of constitutively active $G\alpha_{q/11}$ mutants into

FIGURE 7. **Regions II and IV of human Cav3.3 channels are required and appear sufficient for M1-mediated inhibition.** *A–D, left,* schematic diagrams of the various chimeric channels that were co-transfected into HEK cells with M1. The lighter transmembrane domains and intra/extracellular regions correspond to Cav3.3 (*labeled I*) sequences, whereas the darker transmembrane domains and intra/extracellular regions correspond to Cav3.1 (*labeled G*) sequences. *Middle,* effect of activating M1 receptors with 1 mM CCh on the normalized peak current levels of chimeric channel types shown to the *left*. Inclusion of Cav3.1 sequence at regions II and IV (*C*) eliminated M1-mediated inhibition and attenuated the effect on inactivation kinetics, whereas inclusion of Cav3.3 sequence at regions II and IV (*D*) restored M1-mediated inhibition to a level that was not significantly ($p > 0.05$) different from IIII inhibition levels (see Table 1). *Right, insets* include chimeric whole-cell current traces during depolarizing pulses from −110 mV to peak potential before (*line arrow*) and after (*block arrow*) application of 1 mM CCh. *Traces* are representative of the various chimeras in terms of activation and inactivation kinetics as well as magnitude of inhibition. For *inset scale bars*, $x = 50$ ms and $y = 100$ pA. *E,* histogram where GIII, IGII, IIGI, IIIG, and IGIG inhibition values were statistically compared with the IIII control, and IGGG, GIGG, GGIG, and GGGI values were compared with the GGGG control, and the GIGI value was compared with both the IIII and GGGG controls. * indicates significant difference (<0.02) compared with IIII inhibition, and ** indicates a significant difference ($p < 0.02$) compared with GGGG modulation levels. All data points correspond to mean ± S.E.

Downloaded from www.jbc.org at Univ of Ottawa - OCUL on September 28, 2012

stable Cav3.3 cells demonstrated that active $G\alpha_{q/11}$ alone is sufficient to induce the inhibition of Cav3.3 currents. In support of this notion, only $G\alpha_{q/11}$-coupled mAChRs (M1, M3, and M5) inhibited Cav3.3 currents, whereas $G\alpha_i$-coupled M2 and M4 receptors that activate $G\beta\gamma$ signaling have no effect on Cav3.3 currents. Unlike that reported for the attenuation of Cav3.2 channels by $G\beta_2\gamma$, this novel form of T-type Ca^{2+} channel inhibition involves the $G\alpha_{q/11}$ subunit and also affects channel kinetics. This inhibitory mechanism for the Cav3.3 T-type isoform may be applicable to all $G\alpha_{q/11}$-coupled receptors as we have also found a similar inhibition of Cav3.3 channels by $mGluR_{1a}$ receptors (61).

Pharmacological antagonists eliminated the potential involvement of various intracellular signals downstream of $G\alpha_{q/11}$ activation that may be involved in the inhibition of Cav3.3 by M1 receptor activation. Abolishing the activity of PKC, serine/threonine kinases (including cAMP-dependent protein kinase), tyrosine kinases, phosphatases, phosphoinositide 3-kinases, and intracellular Ca^{2+} signaling all had no effect on inhibition. This profile of M1/$G\alpha_{q/11}$-mediated Ca^{2+} channel inhibition resistant to common antagonists of cytoplasmic signaling is not unique and has been reported for the inhibition of L-type channels by $G\alpha_q$-coupled M1/3/5 receptors in HEK cells (62). Like the inhibition of Cav3.3 via M1 receptors, this inhibition is voltage-independent, relatively slow kinetically (τ_{on} = 13 s), and insensitive to antagonists of protein kinases and protein phosphatases (62).

A more recent explanation for the $G\alpha_{q/11}$-mediated inhibition of ion channels, including voltage-gated K^+ channels and HVA Ca^{2+} channels, has emerged wherein channel activity is suppressed through the depletion of membrane $PI(4,5)P_2$ levels via PLC activity (46, 63, 64). In these studies, $G\alpha_{q/11}$-mediated inhibition was shown to be inhibited via dialysis of synthetic $PI(4,5)P_2$ or a $PI(4,5)P_2$-specific antibody into the cytoplasm. In our experiments, adding di-C8 $PI(4,5)P_2$ or the $PI(4,5)P_2$ antibody into the internal pipette solution and dialyzing cells for up to 25 min had no significant effect on M1-mediated inhibition of Cav3.3 channels, suggestive of another to-be-defined mechanism whereby $G\alpha_{q/11}$ signaling causes the inhibition of voltage-gated ion channels. Further biophysical and biochemical experiments are required to clarify the nature of the intracellular messengers and/or scaffolding proteins that can modulate Cav3.3 T-type Ca^{2+} channels and also whether $G\alpha_{q/11}$ can interact directly with the channel through a novel mechanism.

$G\alpha_{q/11}$-mediated Inhibition of Cav3.3 Involves Two Discrete Channel Regions—Replacing both regions 2 and 4 in the Cav3.3 channel with the corresponding Cav3.1 T-type Ca^{2+} channel sequences abrogated both the M1 receptor-mediated peak current inhibition and concomitant increase in inactivation kinetics. Conversely, substituting regions 2 and 4 from Cav3.3 into Cav3.1 conferred M1 receptor-mediated inhibition and increased inactivation kinetics. These data suggest that regions 2 and 4 of the Cav3.3 channel are both necessary and sufficient to recapitulate M1 receptor-mediated channel modulation. Region 2 of the Cav3.1 and Cav3.3 sequence contains the highly divergent domain I–II linker, the highly conserved domain II, and 39–63 amino acids of the domain II–III linker, and region 4 contains most of the III–IV linker, the highly conserved domain IV, and the highly divergent carboxyl terminus. Based on their putatively intracellular regions and their high divergence between the two T-type isoforms, the I–II linker, proximal region of the II–III linker, the III–IV linker, and the carboxyl terminus are all candidates for modulation sites within regions 2 and 4. Interestingly, the only identified sites of alternative splicing within the rat and human Cav3.3 channel occur both in the I–II linker and the carboxyl-terminal regions (38, 65). The effects of these splicing variations on the biophysical properties (activation kinetics) of the human Cav3.3 channel are interdependent rather than additive, suggesting a possible direct interaction between the I–II linker and carboxyl terminus that affects channel kinetics (24). Both the human and rat Cav3.3 channels inhibited by M1 receptor activation in our study lack exon 9 located in the I–II linker, whereas both the rat and human Cav3.1 channels have a 10-amino acid insertion in this region in a manner similar to that for the +exon 9 Cav3.3 splice variant. Thus, several observations suggest that the I–II linker may be a target region in the inhibition of Cav3.3 by M1, and some evidence points to a possible role for the carboxyl terminus. However, as multiple structural determinants contribute to the slow inactivation kinetics of Cav3.3 compared with Cav3.1 in a nearly additive manner (37), and M1 activation dramatically speeds up Cav3.3 inactivation kinetics, it is also possible that multiple intracellular loci within regions 2 and 4 of the Cav3.3 channel may be involved in the M1-mediated effect.

In summary, we find that activation of known $G\alpha_{q/11}$-coupled mAChRs results in the selective inhibition of Cav3.3 T-type Ca^{2+} currents with a concomitant increase in inactivation kinetics. The $G\alpha_{q/11}$-mediated signaling pathway appears to be mediated via two disparate regions of the Cav3.3 channel. Functional interactions between mAChRs and Cav3.3 Ca^{2+} channels could potentially impact firing patterns of various cell types, including thalamic nRT cells. Biophysical and pharmacological evidence suggests that primarily Cav3.3 channels compose dendritic T-type currents in nRT cells (22), whereas immunostaining suggests the presence of M3 receptors in these cells (33). This raises the possibility that the inhibition of Cav3.3 T-type Ca^{2+} channels by M3 receptors in the dendrites of nRT cells could be involved in cholinergic modulation of thalamic firing patterns.

Acknowledgments—We thank Dr. Brett Adams for the kind gifts of MAS-GRK3ct and EGFP-RGS2 and Drs. Aaron Beedle, Arnaud Monteil, and Philippe Lory for the human Cav3.1 and Cav3.3 channels used in the chimeric channel experiments. We also thank Dr. Colin Thacker, Tracy Evans, Paul Adams, and Dr. John Tyson for molecular biology support, Diana Janke and Dr. David Parker for providing stable cell lines, and to Dr. Philippe Isope for comments on the manuscript.

REFERENCES

1. Anderson, M. P., Mochizuki, T., Xie, J., Fischler, W., Manger, J. P., Talley, E. M., Scammell, T. E., and Tonegawa, S. (2005) *Proc. Natl. Acad. Sci. U. S. A.* **102**, 1743–1748
2. Kim, D., Song, I., Keum, S., Lee, T., Jeong, M. J., Kim, S. S., McEnery, M. W., and Shin, H. S. (2001) *Neuron* **31**, 35–45
3. Destexhe, A., and Sejnowski, T. J. (2003) *Physiol. Rev.* **83**, 1401–1453

Downloaded from www.jbc.org at Univ of Ottawa - OCUL on September 28, 2012

4. Huguenard, J. R., and Prince, D. A. (1992) *J. Neurosci.* **12,** 3804–3817
5. Tsakiridou, E., Bertollini, L., de Curtis, M., Avanzini, G., and Pape, H. C. (1995) *J. Neurosci.* **15,** 3110–3117
6. Peloquin, J. B., Khosravani, H., Barr, W., Bladen, C., Evans, R., Mezeyova, J., Parker, D., Snutch, T. P., McRory, J. E., and Zamponi, G. W. (2006) *Epilepsia* **47,** 655–658
7. Khosravani, H., Bladen, C., Parker, D. B., Snutch, T. P., McRory, J. E., and Zamponi, G. W. (2005) *Ann. Neurol.* **57,** 745–749
8. Khosravani, H., Altier, C., Simms, B., Hamming, K. S., Snutch, T. P., Mezeyova, J., McRory, J. E., and Zamponi, G. W. (2004) *J. Biol. Chem.* **279,** 9681–9684
9. Vitko, I., Chen, Y., Arias, J. M., Shen, Y., Wu, X. R., and Perez-Reyes, E. (2005) *J. Neurosci.* **25,** 4844–4855
10. Thompson, S. M., and Wong, R. K. (1991) *J. Physiol. (Lond.)* **439,** 671–689
11. Christie, B. R., Eliot, L. S., Ito, K., Miyakawa, H., and Johnston, D. (1995) *J. Neurophysiol.* **73,** 2553–2557
12. Egger, V., Svoboda, K., and Mainen, Z. F. (2005) *J. Neurosci.* **25,** 3521–3530
13. Egger, V., Svoboda, K., and Mainen, Z. F. (2003) *J. Neurosci.* **23,** 7551–7558
14. Hildebrand, M. E., and Snutch, T. P. (2006) *Drug Discov. Today* **3,** 335–341
15. Bourinet, E., Alloui, A., Monteil, A., Barrere, C., Couette, B., Poirot, O., Pages, A., McRory, J., Snutch, T. P., Eschalier, A., and Nargeot, J. (2005) *EMBO J.* **24,** 315–324
16. Santi, C. M., Cayabyab, F. S., Sutton, K. G., McRory, J. E., Mezeyova, J., Hamming, K. S., Parker, D., Stea, A., and Snutch, T. P. (2002) *J. Neurosci.* **22,** 396–403
17. McRory, J. E., Santi, C. M., Hamming, K. S., Mezeyova, J., Sutton, K. G., Baillie, D. L., Stea, A., and Snutch, T. P. (2001) *J. Biol. Chem.* **276,** 3999–4011
18. Cribbs, L. L., Lee, J. H., Yang, J., Satin, J., Zhang, Y., Daud, A., Barclay, J., Williamson, M. P., Fox, M., Rees, M., and Perez-Reyes, E. (1998) *Circ. Res.* **83,** 103–109
19. Lee, J. H., Daud, A. N., Cribbs, L. L., Lacerda, A. E., Pereverzev, A., Klockner, U., Schneider, T., and Perez-Reyes, E. (1999) *J. Neurosci.* **19,** 1912–1921
20. Perez-Reyes, E., Cribbs, L. L., Daud, A., Lacerda, A. E., Barclay, J., Williamson, M. P., Fox, M., Rees, M., and Lee, J. H. (1998) *Nature* **391,** 896–900
21. Monteil, A., Chemin, J., Leuranguer, V., Altier, C., Mennessier, G., Bourinet, E., Lory, P., and Nargeot, J. (2000) *J. Biol. Chem.* **275,** 16530–16535
22. Joksovic, P. M., Bayliss, D. A., and Todorovic, S. M. (2005) *J. Physiol. (Lond.)* **566,** 125–142
23. Chevalier, M., Lory, P., Mironneau, C., Macrez, N., and Quignard, J. F. (2006) *Eur. J. Neurosci.* **23,** 2321–2329
24. Murbartian, J., Arias, J. M., and Perez-Reyes, E. (2004) *J. Neurophysiol.* **92,** 3399–3407
25. Castillo, P. E., Carleton, A., Vincent, J. D., and Lledo, P. M. (1999) *J. Neurosci.* **19,** 9180–9191
26. Fraser, D. D., and MacVicar, B. A. (1991) *J. Neurosci.* **11,** 2812–2820
27. Pemberton, K. E., Hill-Eubanks, L. J., and Jones, S. V. (2000) *Pfluegers Arch.* **440,** 452–461
28. Wan, X., Desilets, M., Soboloff, J., Morris, C., and Tsang, B. K. (1996) *Endocrinology* **137,** 2514–2521
29. Chemin, J., Traboulsie, A., and Lory, P. (2006) *Cell Calcium* **40,** 121–134
30. Talley, E. M., Cribbs, L. L., Lee, J. H., Daud, A., Perez-Reyes, E., and Bayliss, D. A. (1999) *J. Neurosci.* **19,** 1895–1911
31. Yunker, A. M., Sharp, A. H., Sundarraj, S., Ranganathan, V., Copeland, T. D., and McEnery, M. W. (2003) *Neuroscience* **117,** 321–335
32. Plummer, K. L., Manning, K. A., Levey, A. I., Rees, H. D., and Uhlrich, D. J. (1999) *J. Comp. Neurol.* **404,** 408–425
33. Levey, A. I., Edmunds, S. M., Heilman, C. J., Desmond, T. J., and Frey, K. A. (1994) *Neuroscience* **63,** 207–221
34. Wei, J., Walton, E. A., Milici, A., and Buccafusco, J. J. (1994) *J. Neurochem.* **63,** 815–821
35. Levey, A. I., Edmunds, S. M., Koliatsos, V., Wiley, R. G., and Heilman, C. J. (1995) *J. Neurosci.* **15,** 4077–4092
36. McKay, B. E., McRory, J. E., Molineux, M. L., Hamid, J., Snutch, T. P., Zamponi, G. W., and Turner, R. W. (2006) *Eur. J. Neurosci.* **24,** 2581–2594
37. Hamid, J., Peloquin, J. B., Monteil, A., and Zamponi, G. W. (2006) *Neuroscience* **143,** 717–728
38. Murbartian, J., Arias, J. M., Lee, J. H., Gomora, J. C., and Perez-Reyes, E. (2002) *FEBS Lett.* **528,** 272–278
39. Hogger, P., Shockley, M. S., Lameh, J., and Sadee, W. (1995) *J. Biol. Chem.* **270,** 7405–7410
40. Schwarz, R. D., Davis, R. E., Jaen, J. C., Spencer, C. J., Tecle, H., and Thomas, A. J. (1993) *Life Sci.* **52,** 465–472
41. Kammermeier, P. J., Ruiz-Velasco, V., and Ikeda, S. R. (2000) *J. Neurosci.* **20,** 5623–5629
42. Wolfe, J. T., Wang, H., Howard, J., Garrison, J. C., and Barrett, P. Q. (2003) *Nature* **424,** 209–213
43. Dolphin, A. C. (2003) *Pharmacol. Rev.* **55,** 607–627
44. Heximer, S. P., Watson, N., Linder, M. E., Blumer, K. J., and Hepler, J. R. (1997) *Proc. Natl. Acad. Sci. U. S. A.* **94,** 14389–14393
45. Melliti, K., Meza, U., and Adams, B. (2000) *J. Neurosci.* **20,** 7167–7173
46. Suh, B. C., Horowitz, L. F., Hirdes, W., Mackie, K., and Hille, B. (2004) *J. Gen. Physiol.* **123,** 663–683
47. Park, J. Y., Kang, H. W., Moon, H. J., Huh, S. U., Jeong, S. W., Soldatov, N. M., and Lee, J. H. (2006) *J. Physiol. (Lond.)* **577,** 513–523
48. Suh, B. C., and Hille, B. (2005) *Curr. Opin. Neurobiol.* **15,** 370–378
49. Bian, J., Cui, J., and McDonald, T. V. (2001) *Circ. Res.* **89,** 1168–1176
50. Zamponi, G. W., and Snutch, T. P. (2002) *Mol. Interv.* **2,** 476–478
51. Joksovic, P., Nelson, M., Jevtovic-Todorovic, V., Patel, M., Perez-Reyes, E., Campbell, K., Chen, C. C., and Todorovic, S. (2006) *J. Physiol. (Lond.)* **574,** 415–430
52. Welsby, P. J., Wang, H., Wolfe, J. T., Colbran, R. J., Johnson, M. L., and Barrett, P. Q. (2003) *J. Neurosci.* **23,** 10116–10121
53. Fisher, R., and Johnston, D. (1990) *J. Neurophysiol.* **64,** 1291–1302
54. Allen, T. G., and Brown, D. A. (1993) *J. Physiol. (Lond.)* **466,** 173–189
55. Depuy, S. D., Yao, I., Hu, C., McIntire, W., Bidaud, I., Lory, P., Rastinejad, F., Gonzalez, C., Garrison, J. C., and Barrett, P. Q. (2006) *Proc. Natl. Acad. Sci. U. S. A.* **103,** 14590–14595
56. Dippel, E., Kalkbrenner, F., Wittig, B., and Schultz, G. (1996) *Proc. Natl. Acad. Sci. U. S. A.* **93,** 1391–1396
57. Tombler, E., Cabanilla, N. J., Carman, P., Permaul, N., Hall, J. I., Richman, R. W., Lee, J., Rodriguez, J., Felsenfeld, D. P., Hennigan, R. F., and Diverse-Pierluissi, M. A. (2006) *J. Biol. Chem.* **281,** 1827–1839
58. Chemin, J., Monteil, A., Perez-Reyes, E., Bourinet, E., Nargeot, J., and Lory, P. (2002) *J. Physiol. (Lond.)* **540,** 3–14
59. Chemin, J., Monteil, A., Perez-Reyes, E., Nargeot, J., and Lory, P. (2001) *EMBO J.* **20,** 7033–7040
60. Rhee, S. G., and Bae, Y. S. (1997) *J. Biol. Chem.* **272,** 15045–15048
61. Hildebrand, M. E., David, L. S., and Snutch, T. P. (2005) *Biophysical Society 49th Annual Meeting, Long Beach, CA, February 12–16, 2005,* abstr. 1346-Pos, Biophysical Society, Bethesda
62. Bannister, R. A., Melliti, K., and Adams, B. A. (2002) *Biophys. J.* **83,** 3256–3267
63. Wu, L., Bauer, C. S., Zhen, X. G., Xie, C., and Yang, J. (2002) *Nature* **419,** 947–952
64. Gamper, N., Reznikov, V., Yamada, Y., Yang, J., and Shapiro, M. S. (2004) *J. Neurosci.* **24,** 10980–10992
65. Mittman, S., Guo, J., Emerick, M. C., and Agnew, W. S. (1999) *Neurosci. Lett.* **269,** 121–124

Downloaded from www.jbc.org at Univ of Ottawa - OCUL on September 28, 2012

Appendix 2. $Ca_V2.1$ P/Q-type calcium channel alternative splicing affects the functional impact of familial hemiplegic migraine mutations.
Original reference:
Adams, P.J., Garcia, E., David, L.S., Mulatz, K.J., Spacey, S.D., and Snutch, T.P. (2009). Ca(V)2.1 P/Q-type calcium channel alternative splicing affects the functional impact of familial hemiplegic migraine mutations: implications for calcium channelopathies. Channels (Austin) *3*, 110–121.

[Channels 3:2, 110-121; March/April 2009]; ©2009 Landes Bioscience

Research Paper

$Ca_V2.1$ P/Q-type calcium channel alternative splicing affects the functional impact of familial hemiplegic migraine mutations

Implications for calcium channelopathies

Paul J. Adams,[1] Esperanza Garcia,[1] Laurence S. David,[1] Kirk J. Mulatz,[1] Sian D. Spacey[1,2] and Terrance P. Snutch[1,*]

[1]Michael Smith Laboratories; and [2]Division of Neurology; University of British Columbia; Vancouver, BC CA

Key words: calcium channel, P/Q-type, familial hemiplegic migraine, alternative splicing

Alternative splicing is known to generate multiple functionally distinct calcium channel variants that exhibit unique spatial and temporal expression patterns. In humans, naturally occurring mutations in genes encoding calcium channel pore forming α_1-subunits are associated with several severe hereditary disorders although it remains to be described whether there exists any relationship between the physiological effects of these mutations and calcium channel splice variation. In the present study, we systematically compare the biophysical effects of three type-1 familial hemiplegic migraine (FHM-1) mutations in two predominant splice variants of the neuronal $Ca_V2.1$ P/Q-type channel. All three FHM-1 mutations cause a greater hyperpolarizing shift in voltage-dependent properties when expressed in the short carboxyl terminus variant ($Ca_V2.1$ Δ47) compared to the long variant ($Ca_V2.1$ +47). Furthermore, the FHM-1 mutations also exhibit differential splice variant-specific effects on recovery from inactivation and accumulation of inactivation during tonic and burst firing. Our findings provide important insight concerning the role of calcium channel alternatively spliced variants and the molecular pathophysiology of FHM-1 and potentially of other calcium channelopathies.

Introduction

Voltage-gated calcium channels are important in many normal physiological processes including muscle contraction, neurotransmitter release, regulation of calcium-dependent enzymes and gene expression (reviewed in ref. 1). It is therefore perhaps not surprising that naturally occurring mutations in calcium channel genes have been implicated in a number of severe human diseases. Since the first mutation in a calcium channel was identified,[2,3] over 150 individual mutations have now been reported in five of the ten genes encoding calcium channel pore forming α_1-subunits (Ca_V) and are associated with nine distinguishable disorders ("calcium channelopathies"). Over the past decade studies using recombinant channels in various expression systems have shown that many of these mutations have significant positive or negative effects on channel gating and/or expression levels, while others result in non-functional channels or have dominant negative effects (reviewed in ref. 4). It is noteworthy that the effects of mutations on channel function have thus far only been tested in a small subset of known calcium channel variants and a direct comparison of how mutations affect channel alternative splice variants has been largely unexplored.

It has been predicted that the ten genes encoding Ca_V subunits have the potential to generate thousands of functionally distinct splice variants.[5,6] Indeed, isolation and characterization of some variants has shown that alternative splicing can be a means to obtain specialized calcium channel function and to optimize calcium signalling regionally, temporally and under altered environmental conditions (reviewed in refs. 6–8). It is evident that mutations directly at a splice-site or in an alternate exon can have effects on pre-mRNA splicing and/or affect a subset of splice variants expressing alternate exons.[9-12] However, the majority of identified mutations associated with calcium channelopathies are missense mutations in coding sequences other than splice-sites and alternate exons (reviewed in ref. 4). Whether channel splice variants have different functional responses to disease-causing missense mutations has not been directly explored. We hypothesized that point mutations associated with calcium channelopathies might have splice-variant specific effects with important implications for both understanding disease pathophysiology and also towards interpreting results obtained from heterologous studies using recombinant channels.

Familial Hemiplegic Migraine (FHM) is an autosomal dominant subtype of migraine characterized by an aura of hemiplegia that is associated with at least one other aura symptom such as hemianopsia, hemisensory deficit or aphasia.[13,14] Approximately 20 missense mutations associated with FHM have been identified in the CACNA1A gene[15] (called FHM-1) which encodes the

*Correspondence to: Terrance P. Snutch; Michael Smith Laboratories; University of British Columbia; Rm 219-2185 East Mall; Vancouver, BC V6T 1Z4 CA; Tel.: 604.822.6968; Fax: 604.822.6470; Email: snutch@msl.ubc.ca

Submitted: 01/23/09; Accepted: 01/23/09

Previously published online as a *Channels* E-publication:
http://www.landesbioscience.com/journals/channels/article/7932

n

α_1 subunit ($Ca_V2.1$; α_{1A}) of the P/Q-type voltage-gated calcium channel. P/Q-type calcium channels are abundantly expressed throughout mammalian brain and spinal cord where they mediate calcium influx essential for neurotransmitter release, calcium-mediated second messenger signalling and calcium-dependent gene transcription.[16-20] The functional consequences of FHM-1 mutations on $Ca_V2.1$ P/Q-type channel properties have been investigated in heterologous *Xenopus* oocyte and mammalian expression systems, and more recently in neurons and whole brains of FHM-1 mutant R192Q and S218L knock-in mice.[21-28] While there have been some noted discrepancies reported, in both heterologous and knock-in mice systems there is a general demonstrated trend for FHM-1 mutations to exhibit gain-of-function properties: increased channel availability and increased calcium influx at lower membrane potentials resulting in a greater susceptibility to the cortical spreading depression (CSD) thought to be the underlying mechanism of aura.[21,22,27,29-31]

There are seven identified alternatively spliced sites within the $Ca_V2.1$ subunit gene and the various splice variants exhibit distinct biophysical characteristics, calcium-dependent properties, pharmacological sensitivities and subtype-specific temporal and regional localizations in human brain.[16,32-35] However, it is not known whether the functional impact of FHM-1 mutations is similar amongst the different $Ca_V2.1$ splice variants or whether alternative splicing contributes to the spatial and temporal nature of the FHM-1 phenotype. The carboxyl terminus of $Ca_V2.1$ channels is known to affect several physiological processes and alternative splicing in this region confers functional changes in channel properties.[16,32,35-38] The most substantial changes induced by alternative splicing in the C-terminus of $Ca_V2.1$ channels results from the use of an alternative three prime acceptor site in the intron upstream of the last exon, exon 47.[32,36,39,40] Alternative splicing at exon 47 introduces a frame-shift resulting in a stop codon at the beginning of exon 47. As a result, P/Q-type channels can be of either the short form (isoform 1; $Ca_V2.1$ (Δ47)) or the long form (isoform 2; $Ca_V2.1$ (+47)). The voltage-dependent and kinetic properties of the $Ca_V2.1$ (+47) and $Ca_V2.1$ (Δ47) splice variants and their relative contributions concerning FHM-1 mutations has not been explored.

In the present study we compared the biophysical properties of wild-type (WT) $Ca_V2.1$ (+47) and $Ca_V2.1$ (Δ47) P/Q-type channel splice variants and also explored the effects of three FHM-1 mutations introduced into the two variants. We investigated two mutations, K1336E and R192Q, that are associated with an FHM-1 phenotype of pure hemiplegia and migraine without any other neurological symptoms.[14,15] We further investigated the S218L FHM-1 mutation which is associated with a severe clinical phenotype wherein typical FHM-1 attacks induced by minor head trauma are often followed by a delayed cerebral edema, fever, stupor and sometimes coma (fatal in one reported instance).[41-43] We find that the two P/Q-type channel carboxyl tail splice variants exhibit functionally distinct properties and also that the three FHM-1 mutations have differential splice-dependent effects on voltage-dependent and kinetic properties. We discuss the potential importance of the splice-variant differential effects in the context of FHM-1 pathophysiology as well as the implications for other calcium channelopathies.

Results

$Ca_V2.1$ (+47) and $Ca_V2.1$ (Δ47) variants are expressed in human cortex. Mutations in the P/Q-type channel $Ca_V2.1$ subunit underlie FHM-1 and the current consensus is that initiation of migraine attacks is in the cortex, however the expression of splice variants has not yet been described in the human cortex . In order to determine whether the $Ca_V2.1$ (+47) and $Ca_V2.1$ (Δ47) variants are expressed in human cortex we utilized RT-PCR to amplify a ~1.1 Kb carboxyl terminal fragment of $Ca_V2.1$ from adult human cortex RNA using oligonucleotide primers that recognize both carboxyl alternatively spliced variants in a non-biased manner. The PCR products were subsequently re-amplified using splice-variant specific primers. Figure 1 shows that the $Ca_V2.1$ (+47) and $Ca_V2.1$ (Δ47) splice variants are both expressed in human cortex. To determine their relative proportions, the human cortical $Ca_V2.1$ carboxyl terminal PCR products were sub-cloned and individual cDNAs analyzed using splice-variant specific primers and direct DNA sequencing. From the 53 cDNA clones analyzed we determined that the $Ca_V2.1$ (+47) and $Ca_V2.1$ (Δ47) splice variants were present in whole cortex in relative proportions of 79% and 21%, respectively.

All subsequent biophysical analyses were performed using human long $Ca_V2.1$ (+47) and short $Ca_V2.1$ (Δ47) splice-variant cDNA clones with either WT or FHM-1 mutant K1336E, R192Q or S218L changes introduced (see Fig. 1A for the location of the FHM-1 mutations).

FHM-1 mutations exhibit differential effects on the voltage-dependent properties of $Ca_V2.1$ splice variants. Whole cell current analysis of transiently transfected cells showed that the WT $Ca_V2.1$ (Δ47) and WT $Ca_V2.1$ (+47) variants possess similar membrane potentials at which half the channels are activated (V_{50act} = -14.02 ± 1.49, and -15.08 ± 1.20, respectively) and similar membrane potentials at which half of the channels are inactivated ($V_{50inact}$ = -58.20 ± 2.04, and -62.07 ± 1.87, respectively; see Table 1 and Fig. 2). The K1336E, R192Q and S218L mutations have been previously reported to cause a hyperpolarizing shift in the current-voltage relationship relative to WT $Ca_V2.1$ channels.[24,26,27,29,46] Examining the FHM-1 mutations in the P/Q-type +47 and Δ47 carboxyl tail splice variants we found differential effects. The K1336E $Ca_V2.1$ (+47) and R192Q $Ca_V2.1$ (+47) channels both exhibited a small but significant shift in V_{50act} relative to WT $Ca_V2.1$ (+47) channels (-21.53 ± 1.35 and -19.11 ± 1.11 vs. -15.08 ± 1.20, respectively; $p < 0.05$; ANOVA), while the S218L mutation had no significant affect on $Ca_V2.1$ (+47) channels relative to WT (Table 1 and Fig. 2). In contrast, all three FHM-1 mutations caused large significant hyperpolarizing shifts in V_{50act} when expressed in $Ca_V2.1$ (Δ47) variant channels ($p < 0.001$; ANOVA; Table 1 and Fig. 2). Similar differential splice-dependent effects of the FHM-1 mutations were apparent in examining $V_{50inact}$. Figure 2 shows that the R192Q and S218L mutations resulted in large (~15–17 mV) hyperpolarizing shifts in $V_{50inact}$ in the $Ca_V2.1$ (Δ47) variant relative to WT $Ca_V2.1$ (Δ47) channels ($p < 0.001$; ANOVA), while

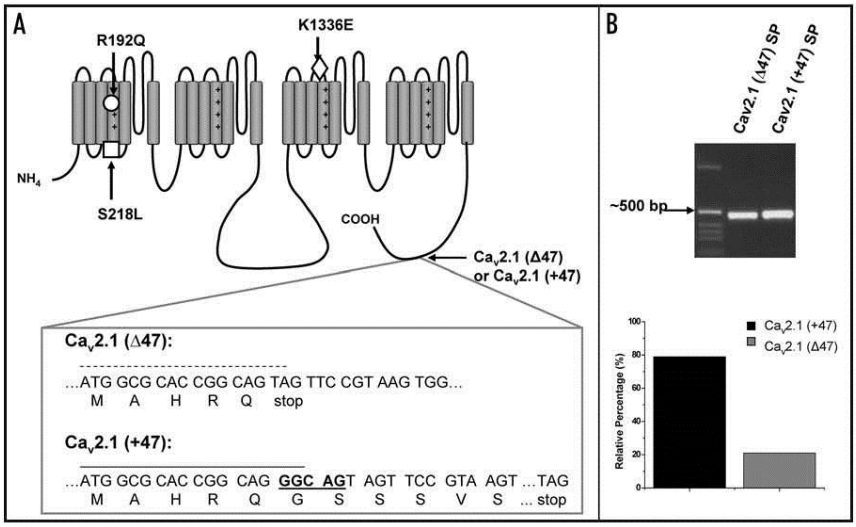

Figure 1. Human P/Q-type calcium channel topology and splice-variant expression in human cortex. (A) schematic showing the location of the three FHM-1 mutations and the carboxyl terminal splice site in the human $Ca_V2.1$ channel. In the box below the channel diagram are partial sequences of the $Ca_V2.1$ (+47) and $Ca_V2.1$ (Δ47) variants at the exon 46/exon 47 boundary. The pentanucleotide insertion is shown in bold for the $Ca_V2.1$ (+47) variant. (B) the last ~1 Kb of the $Ca_V2.1$ carboxyl terminus was amplified from human cortical RNA and purified. Subsequently, splice-variant specific forward primers (SP) designed to exclusively bind either $Ca_V2.1$ (Δ47) or $Ca_V2.1$ (+47) transcripts were used in PCR reactions to generate an ~500 bp fragment from the purified carboxyl fragments; $Ca_V2.1$ (Δ47)-SP and $Ca_V2.1$ (+47)-SP, respectively (dotted line is above the sequence that $Ca_V2.1$ (Δ47)-SP binds and the solid line is above the sequence that $Ca_V2.1$ (+47)-SP binds in (A). Both splice-variant specific primers generated the expected product from the carboxyl PCR fragment of the $Ca_V2.1$ cDNA obtained from human cortex, verifying both $Ca_V2.1$ (Δ47) or $Ca_V2.1$ (+47) are present in human cortex. Products were verified by direct DNA sequencing and determined to be in relative proportions of 79% $Ca_V2.1$ (+47) and 21% $Ca_V2.1$ (Δ47) (bar graph); for protocol details see Materials and Methods.

these same two FHM-1 mutations had a smaller effects on $Ca_V2.1$ (+47) variant channels ($p < 0.05$; ANOVA; Table 1). Interestingly, the K1336E mutation did not cause a significant change in $V_{50inact}$ in either splice variant. Overall, these data indicate that the impact of individual FHM-1 mutations on P/Q-type channel gating properties is differentially affected by the nature of the splice-variant background in which the mutation is expressed.

FHM-1 mutations exhibit differential effects on recovery from inactivation of $Ca_V2.1$ splice variants. Analysis of WT $Ca_V2.1$ (Δ47) and $Ca_V2.1$ (+47) variants showed different rates of recovery from inactivation for these P/Q-type channel splice variants. WT $Ca_V2.1$ (Δ47) channels exhibit faster rates of recovery ($\tau_1 = 0.67 \pm 0.11$ and $\tau_2 = 3.08 \pm 0.61$) than the $Ca_V2.1$ (+47) variant channels ($\tau_1 = 0.76 \pm 0.21$ and $\tau_2 = 3.39 \pm 0.84$). As a result, $Ca_V2.1$ (Δ47) channels show a significantly higher percentage of channels recovered at 7.5 seconds after inactivation relative to $Ca_V2.1$ (+47) channels (89.0 ± 1.8 vs. 77.3 ± 3.8 %, respectively; $p < 0.05$; ANOVA) (Fig. 3 and Table 2).

Examining the effects of FHM-1 mutations in the $Ca_V2.1$ (Δ47) background, Figure 3 shows that the K1336E $Ca_V2.1$ (Δ47) and R192Q $Ca_V2.1$ (Δ47) variants exhibit a significant decrease in current recovered at 7.5 seconds relative to WT $Ca_V2.1$ (Δ47) channels (70.4 ± 3.7% and 83.3 ± 2.3% vs. 89.0 ± 1.8 %, respectively; $p < 0.05$; ANOVA). Contrastingly, K1336E $Ca_V2.1$ (+47) and R192Q $Ca_V2.1$ (+47) channels showed increases in recovery relative to WT $Ca_V2.1$ (+47) channels (86.8 ± 1.7 and 87.0 ± 2.0 vs. 77.3 ± 3.8 %, respectively; $p < 0.05$; ANOVA) (Fig. 3 and Table 2). The S218L mutation was found to increase the recovery in both splice variants, however, only the S218L $Ca_V2.1$ (+47) channels showed a significant increase in recovery relative to WT $Ca_V2.1$ (+47) channels at 7.5 seconds (94.7 ± 1.5 vs. 77.3 ± 3.8 %, respectively; $p < 0.001$; ANOVA) (Fig. 3 and Table 2).

Overall, in agreement with previous reports,[24,27] we observed that both the K1336E and S218L mutations can cause significant changes to recovery from inactivation and show for the first time that the R192Q mutation also changes recovery from inactivation. Importantly, we also show that the quantitative effects of the FHM-1 mutations on channel function are dependant upon the nature of the $Ca_V2.1$ splice variant. We also note that the differential effects of the mutations resulted in significant changes to the functional distinction observed between the two WT channel variants; that is, while the WT $Ca_V2.1$ (Δ47) channel variant recovered significantly faster than the WT $Ca_V2.1$ (+47) channel variant, the K1336E $Ca_V2.1$ (Δ47) channels recovered significantly slower

Table 1 Mean values for voltage-dependent activation and inactivation parameters

	V_{50} Activation (mV)	k Activation	τ_{act} (msec)	V_{50} Inactivation (mV)	k Inactivation
$Ca_V2.1$ (Δ47) Wild-type	-14.02 ± 1.49 (n = 16)	4.82 ± 0.27	1.42 ± 0.09	-58.20 ± 2.04 (n = 21)	7.03 ± 0.29
$Ca_V2.1$ (Δ47) K1336E	-24.12 ± 1.33# (n = 10)	2.80 ± 0.20#	1.16 ± 0.21	-62.27 ± 1.81 (n = 7)	7.23 ± 0.45
$Ca_V2.1$ (Δ47) R192Q	-20.84 ± 0.94# (n = 16)	4.30 ± 0.19	1.31 ± 0.07	-73.41 ± 3.15# (n = 11)	7.58 ± 0.57
$Ca_V2.1$ (Δ47) S218L	-24.10 ± 1.15# (n = 9)	5.53 ± 0.39	0.97 ± 0.11*	-75.07 ± 3.96# (n = 10)	6.34 ± 0.62
$Ca_V2.1$ (+47) Wild-type	-15.08 ± 1.20 (n = 16)	4.33 ± 0.24	1.28 ± 0.07	-62.07 ± 1.87 (n = 16)	6.85 ± 0.38
$Ca_V2.1$ (+47) K1336E	-21.53 ± 1.35* (n = 9)	3.10 ± 0.18*	1.33 ± 0.10	-65.02 ± 1.87 (n = 8)	8.39 ± 0.78
$Ca_V2.1$ (+47) R192Q	-19.11 ± 1.11* (n = 16)	4.79 ± 0.26	1.43 ± 0.10	-70.27 ± 2.36* (n = 16)	7.19 ± 0.47
$Ca_V2.1$ (+47) S218L	-18.08 ± 1.28 (n = 11)	6.26 ± 0.31#	1.06 ± 0.08*	-72.54 ± 1.70* (n = 9)	5.92 ± 0.37

The voltage at which half of the channels are in the activated state (V_{50act}) and inactivated state ($V_{50inact}$), and the steepness of the curves for activation (k_{act}) and inactivation (k_{inact}) were obtained by fitting the data with the Boltzmann equation for the indicated number of cells in parentheses. The kinetics of activation (τ_{act}) were obtained by fitting the maximum current trace from the IV curves with a single exponential. Asterisks (*) and number signs (#) indicate significant difference relative to wild-type with p-values less than either 0.05 or 0.001 (one-way ANOVA), respectively.

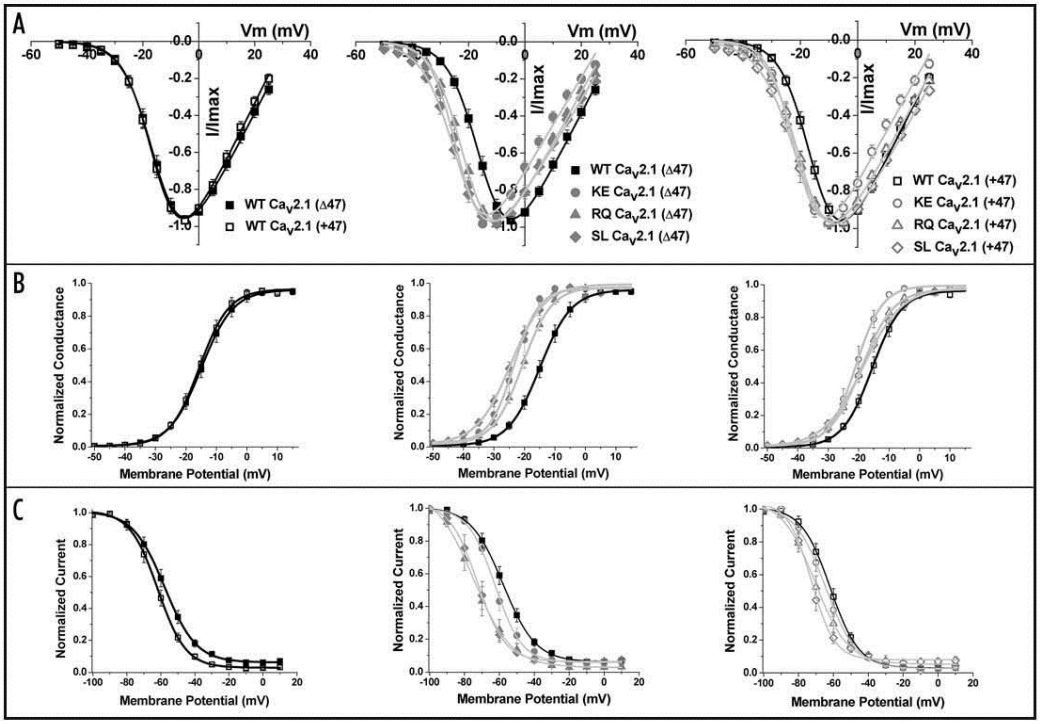

Figure 2. FHM-1 mutations differentially affect voltage-dependent properties of $Ca_V2.1$ (Δ47) and $Ca_V2.1$ (+47) P/Q-type variants. (A) shows the comparison between current-voltage relationships (IV-curves) for wild-type (WT; black squares), FHM-1 mutant K1336E (KE; grey circles), R192Q (RQ; grey triangles) and S218L (SL; grey diamond) in both the short $Ca_V2.1$ (Δ47) (filled symbols) and long $Ca_V2.1$ (+47) (open symbols) C-terminus splice variants. IV curves for all constructs were determined from currents evoked during 90 ms square pulse depolarizations shown between -50 mV and +20 mV from a holding potential of -90 mV. (B) conductance values were calculated from IV curves to obtain activation curves. (C) steady-state inactivation curves were generated using a standard protocol in which 5 s prepulse holdings of -100 to +10 mV were elicited prior to the 80 ms, 0 mV test pulse from a holding of -120 mV. Normalized current evoked during the test pulse is plotted vs. prepulse membrane potential. For complete statistics see Table 1 and for details of protocols see Methods.

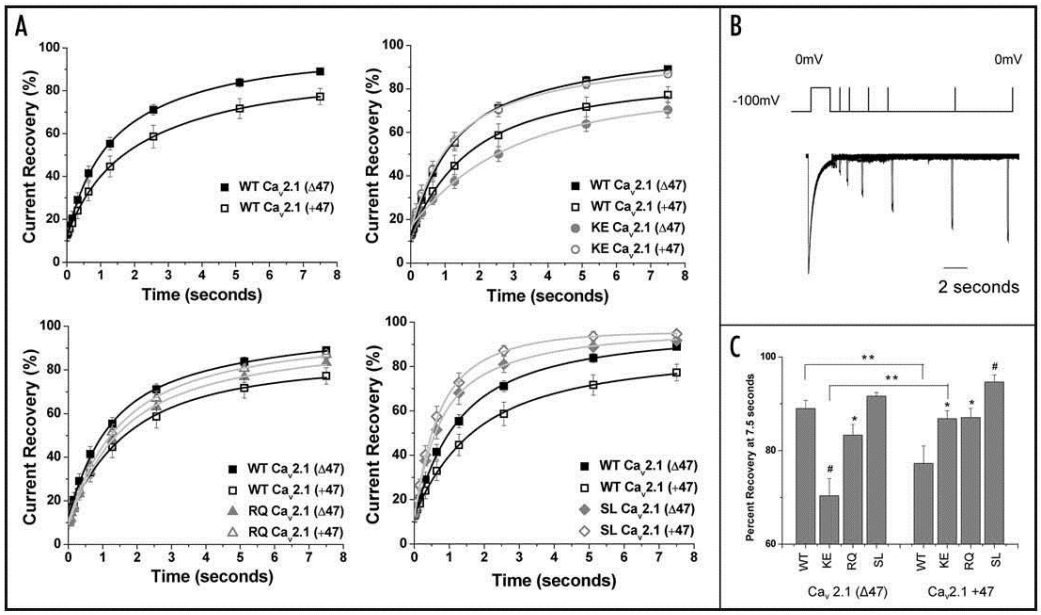

Figure 3. Wild-type and FHM-1 mutant Ca$_V$2.1 (Δ47) and Ca$_V$2.1 (+47) variants exhibit different rates of recovery from inactivation. (A) graphs show percentage of the current recovered vs. time given to recover for all WT and FHM-1 mutated constructs. Recovery from inactivation was examined for wild-type (WT; black squares), FHM-1 mutant K1336E (KE; grey circles), R192Q (RQ; grey triangles) and S218L (SL; grey diamond) in both the short Ca$_V$2.1 (Δ47) (filled symbols) and long Ca$_V$2.1 (+47) (open symbols) C-terminus splice variants. (B) shows a representative (WT) trace (transient currents removed for clarity) and the two pulse protocol used. The protocol consists of a 2 second, 0 mV prepulse followed by a 50 ms, 0 mV test pulse elicited after inter-pulse intervals between 10 ms and 7.5 seconds. Time constants were determined by fitting the average values for percent recovery with a single exponential or double exponential (values shown in Table 2). (C) bar graph shows percent recovery at 7.5 seconds for all WT and FHM-1 mutant clones studied. Single asterisks and number signs indicate significant difference between mutant and wild-type of the same variant with p-values less than either 0.05 or 0.001 (one-way ANOVA), respectively. Double asterisks indicate significant difference between the Δ47 and +47 variants containing the same sequence (i.e., WT or mutant) with p-value less than 0.05 (one-way ANOVA).

than K1336E Ca$_V$2.1 (+47) channels. In addition, the R192Q and S218L mutations altered recovery such that the R192Q Ca$_V$2.1 (Δ47) and R192Q Ca$_V$2.1 (+47) channels and S218L Ca$_V$2.1 (Δ47) and S218L Ca$_V$2.1 (+47) channels were not functionally distinct in this parameter (Fig. 3 and Table 2).

FHM-1 mutations exhibit differential effects on inactivation of Ca$_V$2.1 splice variants during tonic depolarization. WT Ca$_V$2.1 (+47) and Ca$_V$2.1 (Δ47) variants exhibit functional differences with regard to accumulation of inactivation during short (3.5 msec) 25 Hz repetitive stimulations (Fig. 4). While Ca$_V$2.1 (Δ47) variant channels showed 95.0 ± 1.4% of current remaining at the end of 25 pulses, Ca$_V$2.1 (+47) variant channels had 90.0 ± 0.9% ($p < 0.05$; ANOVA) (Fig. 4C).

All three FHM-1 mutations examined significantly altered accumulation of inactivation (Fig. 4A); however, again the effects were contingent on the nature of the Ca$_V$2.1 variant in which mutations were expressed. The K1336E Ca$_V$2.1 (Δ47) and K1336E Ca$_V$2.1 (+47) channels had a significant increase in accumulation of inactivation and thus a lower percent of current remaining at the end of 25 pulses relative to WT Ca$_V$2.1 (Δ47) and WT Ca$_V$2.1 (+47) (88.0 ± 2.2% and 84.0 ± 1.7% vs. 95.0 ± 1.4 and 90.0 ± 0.9%, respectively; $p < 0.05$; ANOVA) (Fig. 4C). The changes were such that the K1336E Ca$_V$2.1 (+47) and K1336E Ca$_V$2.1 (Δ47) variants had similar current remaining at the end of the repetitive stimulation and thus lacked the clear functional distinction observed between the WT channel variants.

In the context of the Ca$_V$2.1 (Δ47) variant background the R192Q mutation caused a significant increase in accumulation of inactivation relative to WT Ca$_V$2.1 (Δ47) (current remaining at end of the 25 pulses = 90.0 ± 1.6% vs. 95.0 ± 1.4%: $p < 0.05$; ANOVA). In contrast, R192Q Ca$_V$2.1 (+47) channels were similar to WT Ca$_V$2.1 (+47) channels (92 ± 1.3% vs. 90 ± 0.9%) (Fig. 4C). Similar to K1336E channels, the R192Q Ca$_V$2.1 (Δ47) and R192Q Ca$_V$2.1 (+47) channel variants lacked the clear functional distinction observed between the WT variants for this property.

The S218L mutation showed a large and significant increase in accumulation of inactivation and thus a lower percent of current remaining at the end of 25 pulses relative to both the WT $Ca_V2.1$ (Δ47) and $Ca_V2.1$ (+47) channel variants (81 ± 2.5% and 77 ± 1.7% vs. 95 ± 1.4 and 90 ± 0.9%, respectively; $p < 0.05$; ANOVA). Similar to that for R192Q and K1336E, a further overall effect of the S218L mutation is to decrease the relative difference in current remaining observed between WT $Ca_V2.1$ (Δ47) and $Ca_V2.1$ (+47) variant channels.

FHM-1 mutations exhibit differential effects on inactivation of $Ca_V2.1$ splice variants during bursts of depolarization. In addition to tonic depolarizations, neurons experience various frequencies of burst firing in which brief periods of tonic firing are interspersed with silent periods as the membrane potential drops below threshold.[47-51] During the tonic firing periods P/Q-type channels will inactivate and during silent periods they will have the opportunity to recover from inactivation. Based upon the above noted splice-variant changes in accumulation of inactivation and recovery from inactivation, we predicted that bursts of depolarization would also differentially affect WT and FHM-1 mutated $Ca_V2.1$ (+47) and $Ca_V2.1$ (Δ47) variant channels.

Figure 5 shows that WT $Ca_V2.1$ (+47) and $Ca_V2.1$ (Δ47) variants exhibit significant differences in the amount of current remaining at the end of five 25 Hz bursts given at 3.5 Hz. Current through the WT $Ca_V2.1$ (+47) variant decayed to 73 ± 3.4% by the end of the fifth burst while current through the WT $Ca_V2.1$ (Δ47) variant decayed to 88 ± 3.6% ($p < 0.05$; ANOVA) (Fig. 5C). The increased inactivation during the depolarizations and the reduced recovery from inactivation of WT $Ca_V2.1$ (+47) variants discussed above likely contributed to the overall 15% decrease in current relative to the WT $Ca_V2.1$ (Δ47) variant.

Figure 5 shows that during burst firing the K1336E mutation in the $Ca_V2.1$ (Δ47) variant background results in an overall lower percentage of current remaining at the end of five bursts (70 ± 4.9% vs. 88 ± 3.6%, respectively; $p < 0.05$; ANOVA) (Fig. 5C), likely resulting from the increased accumulation of inactivation and slowed recovery from inactivation of K1336E $Ca_V2.1$ (Δ47) channels relative to WT $Ca_V2.1$ (Δ47) (see Figs. 3 and 4). Contrastingly, the K1336E mutation in the $Ca_V2.1$ (+47) variant background did not show significant current decay relative to WT, likely due to the fact that although the K1336E $Ca_V2.1$ (+47) variant channels exhibit a small increase in accumulation of inactivation during tonic stimulation (Fig. 4), they also possess an increased rate of recovery from inactivation (Fig. 3A). We note that unlike WT channel variants, the K1336E $Ca_V2.1$ (+47) and K1336E $Ca_V2.1$ (Δ47) variants did not differ significantly relative to one another.

Similar to that for the K1336E mutation in the Δ47 background, examination of burst firing effects on the R192Q mutation showed an increase in current decay during burst firing relative to WT $Ca_V2.1$ (Δ47) channels (70 ± 3.6% vs. 88 ± 3.6% current remaining, respectively; $p < 0.05$; ANOVA) (Fig. 5C). In contrast, the R192Q mutation in the +47 background resulted in a higher degree of current remaining compared to WT $Ca_V2.1$ (+47) channels (83 ± 2.7% vs. 73 ± 3.4% current remaining, respectively; $p < 0.05$; ANOVA). This may reflect the fact that R192Q $Ca_V2.1$ (+47) channels exhibit increased recovery from inactivation (see Fig. 3). We note that an overall effect concerning current decay during burst firing is for R192Q $Ca_V2.1$ (+47) channels to behave more similar to that for the WT Δ47 channels and for R192Q $Ca_V2.1$ (Δ47) channels to behave more similar to those of the WT +47 variant.

Similar to that for the K1336E mutation, the S218L mutation only caused a significant current decay during the burst firing in the $Ca_V2.1$ (Δ47) variant background (73.0 ± 4.0% vs. 88.0 ± 3.6% current remaining at the end of five bursts, respectively; $p < 0.05$; ANOVA). Presumably, although the S218L mutation increased accumulation of inactivation substantially in both splice variants (see Fig. 4), S218L $Ca_V2.1$ (+47) channels had a larger increase in the rate of recovery from inactivation (Fig. 3) which likely slowed overall accumulation of inactivation during the burst firing. The S218L $Ca_V2.1$ (+47) and S218L $Ca_V2.1$ (Δ47) variants did not differ significantly relative to one another.

Table 2 Time constant values and recovery from inactivation

	τ_1 (Fast) (msec)	τ_2 (Slow) (msec)	% Recovery at 7.5 seconds
$Ca_V2.1$ (Δ47) Wild-type	0.67 ± 0.11	3.08 ± 0.61	89.0 ± 1.8 (n = 5)
$Ca_V2.1$ (Δ47) K1336E	2.89 ± 0.12	N.A.	70.4 ± 3.7# (n = 8)
$Ca_V2.1$ (Δ47) R192Q	0.91 ± 0.19	4.97 ± 2.65	83.3 ± 2.3* (n = 7)
$Ca_V2.1$ (Δ47) S218L	0.617 ± 0.10	2.71 ± 1.18	91.6 ± 0.8 (n = 5)
$Ca_V2.1$ (+47) Wild-type	0.76 ± 0.21	3.39 ± 0.84	77.3 ± 3.8** (n = 7)
$Ca_V2.1$ (+47) K1336E	0.54 ± 0.13	2.67 ± 0.53	86.8 ± 1.7* (n = 5)
$Ca_V2.1$ (+47) R192Q	1.08 ± 0.20	5.78 ± 4.96	87.0 ± 2.0* (n = 6)
$Ca_V2.1$ (+47) S218L	0.50 ± 0.12	1.71 ± 0.59	94.7 ± 1.5# (n = 5)

Time constants were determined by fitting the average percent recovery with a double exponential for all constructs except the $Ca_V2.1$ (Δ47) K1336E which was best fit with a single exponential. Percent recovery is a measure of the percentage of current evoked during the test pulse, given at 7.5 seconds after the prepulse, relative to the maximum current evoked during the prepulse. Asterisks and number signs indicate significant difference between mutant and wild-type of the same variant with p-values less than either 0.05 or 0.001 (one-way ANOVA), respectively. Double asterisks indicate significant difference between the $Ca_V2.1$ Δ47 and +47 variants containing the same sequence (i.e. WT or mutant) with p-value less than 0.05 (one-way ANOVA). Number of cells recorded for each done is indicated in parenthesis. N.A. = not applicable.

Discussion

We report here that FHM-1 missense mutations confer differential effects on the biophysical properties of the $Ca_V2.1$ (+47) and $Ca_V2.1$ (Δ47) P/Q-type channel splice variants. Although the current-voltage relationships and steady-state properties of the two WT P/Q-type splice variants are similar, all three

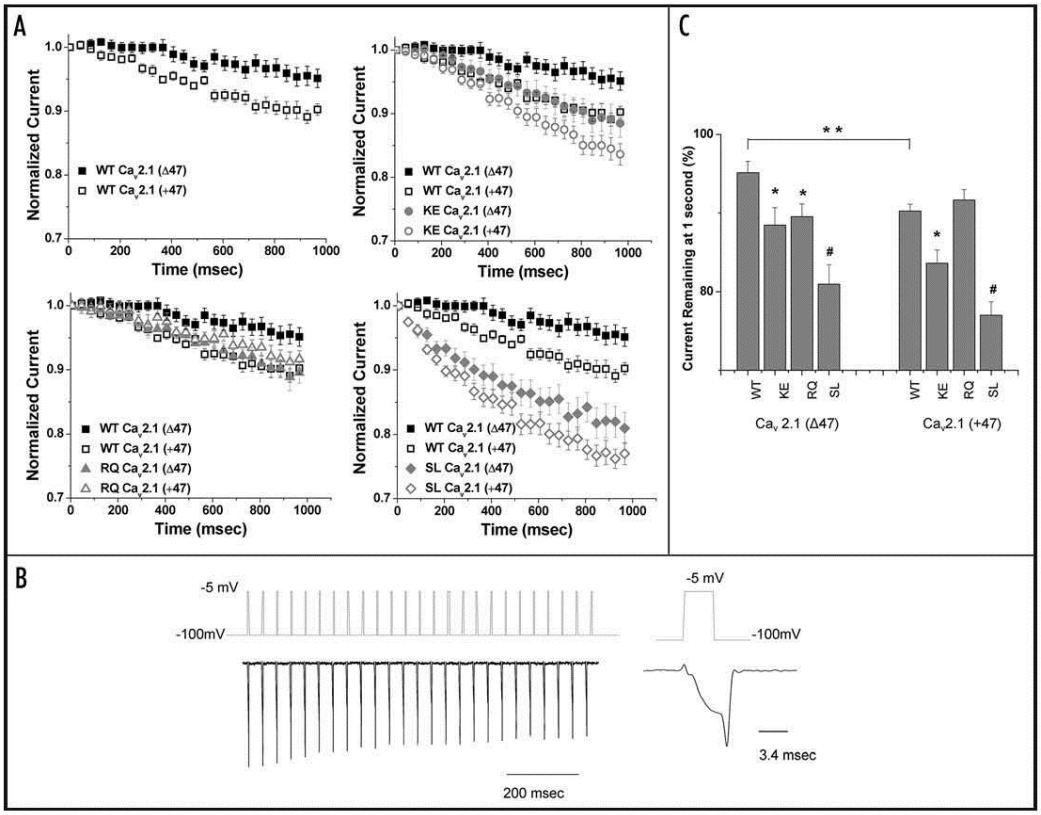

Figure 4. Wild-type and FHM-1 mutant $Ca_V2.1$ (Δ47) and $Ca_V2.1$ (+47) variants exhibit different current decay during 25 Hz tonic depolarizations. (A) graphs show normalized current remaining vs. time after initial onset of depolarizations. Current decay was measured for wild-type (WT; black squares), FHM-1 mutant K1336E (KE; grey circles), R192Q (RQ; grey triangles) and S218L (SL; grey diamond) in both the short $Ca_V2.1$ (Δ47) (filled symbols) and long $Ca_V2.1$ (+47) (open symbols) C-terminus splice variants. (B) to investigate current decay during repetitive stimulations we used 25 square pulses from a holding of -100 mV to a depolarizing potential of -5 mV for a duration of 3.4 ms. The test pulses were given at a rate of 25 Hz. Representative current trace and pulse protocol indicated at bottom (capacitive transients were compensated using a P/4 protocol), with single current response enlarged. (C) bar graph shows the percent of current remaining at the end of 25 pulses for each clone. Single asterisks and number signs indicate significant difference between mutant and wild-type of the same variant with p-values less than either 0.05 or 0.001 (one-way ANOVA), respectively. Double asterisks indicate significant difference between the Δ47 and +47 variants containing the same sequence (i.e., WT or mutant) with p-value less than 0.05 (one-way ANOVA). Number of cells recorded for WT $Ca_V2.1$ (Δ47) (n = 14), WT $Ca_V2.1$ (+47) (n = 13), KE $Ca_V2.1$ (Δ47) (n = 15), KE $Ca_V2.1$ (+47) (n = 18), RQ $Ca_V2.1$ (Δ47) (n = 17), RQ $Ca_V2.1$ (+47) (n = 15), SL $Ca_V2.1$ (Δ47) (n =15), SL $Ca_V2.1$ (+47) (n = 14).

FHM-1 mutations exhibited a greater hyperpolarizing shift when expressed in the $Ca_V2.1$ (Δ47) variant compared to the $Ca_V2.1$ (+47) variant (Fig. 2). In addition, we show for the first time that WT $Ca_V2.1$ (Δ47) and WT $Ca_V2.1$ (+47) variants have both different kinetics of recovery from inactivation and accumulation of inactivation during tonic depolarization that are likely relevant to the differential response of channel variants during bursts of depolarization (Figs. 3–5). It is known that $Ca_V2.1$ channels in different states possess alternative modes of gating that are reflected in biophysical properties at the whole cell current level.[52,53] Furthermore, it has been shown that alternative splicing in the EF-hand region of the $Ca_V2.1$ carboxyl terminus can shift gating modes.[54] It is therefore possible that WT $Ca_V2.1$ (Δ47) and WT $Ca_V2.1$ (+47) variants also have distinct gating modes that respond differently to FHM-1 mutations which are localized near voltage sensor regions (e.g., R192Q, S218L,

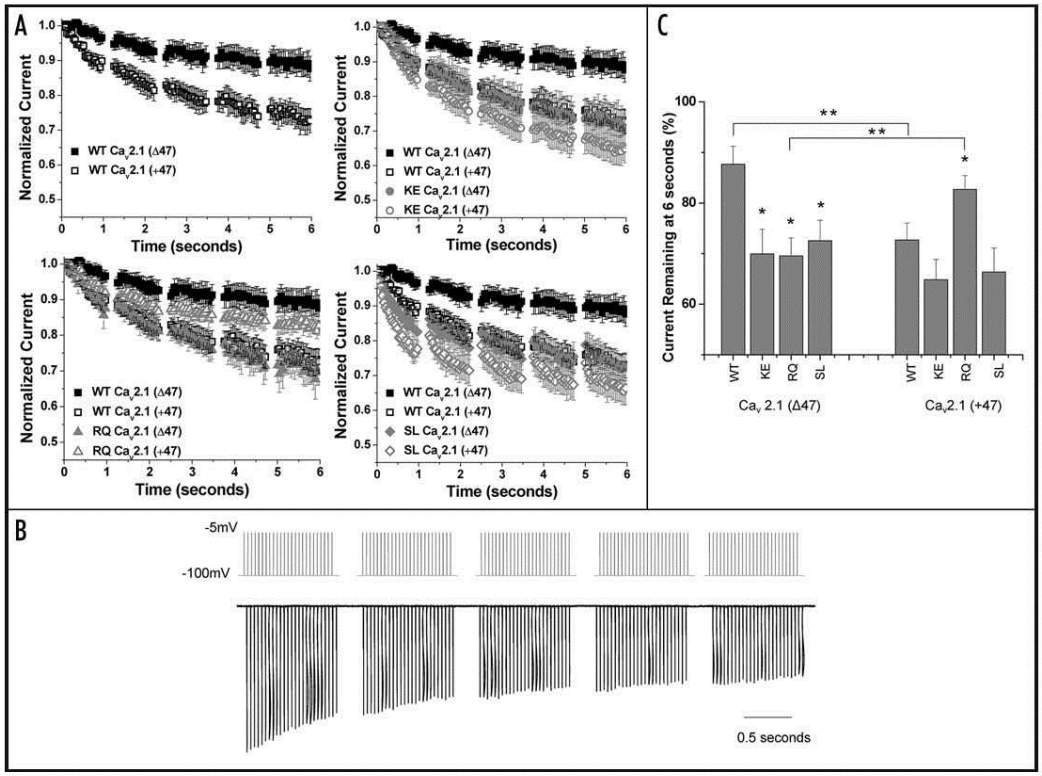

Figure 5. Wild-type and FHM-1 mutant $Ca_V2.1$ (Δ47) and $Ca_V2.1$ (+47) variants exhibit different current decay during bursts of depolarizations. (A) graphs show normalized current remaining vs. time after initial onset of depolarizations. Current decay was measured for wild-type (WT; black squares), FHM-1 mutant K1336E (KE; grey circles), R192Q (RQ; grey triangles) and S218L (SL; grey diamond) in both the short $Ca_V2.1$ (Δ47) (filled symbols) and long $Ca_V2.1$ (+47) (open symbols) C-terminus splice variants. (B) to investigate current decay during bursts of repetitive stimulations we used five bursts of 25 square pulses to -5 mV for 3.4 msec from a holding of -100 mV; bursts given at 290 msec intervals (3.5 Hz burst firing). Each burst contained 25 pulses at a rate of 25 Hz. Representative current trace indicated at bottom (capacitive transients were compensated using a P/4 protocol). (C) bar graph shows the percent of current remaining at the end of 6 seconds for each clone. Single asterisks and number signs indicate significant difference between mutant and wild-type of the same variant with p-values less than either 0.05 or 0.001 (one-way ANOVA), respectively. Double asterisks indicate significant difference between the $Ca_V2.1$ Δ47 and +47 variants containing the same sequence (i.e., WT or mutant) with p-value less than 0.05 (one-way ANOVA). Number of cells recorded for WT $Ca_V2.1$ (Δ47) (n = 8), WT $Ca_V2.1$ (+47) (n = 7), KE $Ca_V2.1$ (Δ47) (n = 8), KE $Ca_V2.1$ (+47) (n = 10), RQ $Ca_V2.1$ (Δ47) (n = 9), RQ $Ca_V2.1$ (+47) (n = 7), SL $Ca_V2.1$ (Δ47) (n =8), SL $Ca_V2.1$ (+47) (n = 8).

K1336E). Detailed single channel analyses would be required to fully explore this hypothesis.

Our findings provide the first suggestion for a potential role of P/Q-type channel alternative splicing in FHM-1 pathophysiology and raise the notion that even though $Ca_V2.1$ channels are widely expressed in the central and peripheral nervous systems, point mutations can have greater or lesser functional affects on specific splice variants. Although the mechanism of FHM-1 pathophysiology is not completely resolved, the current opinion is that the migraine usually initiates with aura due to CSD, which leads to headache pain through activation of the trigeminovascular pain pathway.[55,56] In this regard, specific $Ca_V2.1$ variants within the cortex may have important roles in the onset of migraine attacks.

We show that the $Ca_V2.1$ (Δ47) and $Ca_V2.1$ (+47) variants are both expressed in whole human cortex (Fig. 1B), and that the three FHM-1 mutations all cause a greater hyperpolarizing shift in the voltage-dependence of activation in $Ca_V2.1$ (Δ47) channels relative to that for $Ca_V2.1$ (+47) variant channels. A hyperpolarizing shift in P/Q-type channel activation has been suggested as an underlying mechanism of increased susceptibility to CSD and the initiation

of migraine.[22,57] CSD begins within small domains of the cortex and propagates outward from a focal point. Our data supports the notion that $Ca_V2.1$ splice variants with greater sensitivity to hyperpolarizing shifts in the voltage-dependence of activation (e.g., $Ca_V2.1$ (Δ47), could result in cortical regions with greater susceptibility to CSD and migraine initiation. Conversely, the effects of FHM-1 mutations on other $Ca_V2.1$ splice variants (e.g., $Ca_V2.1$ (+47)), expressed elsewhere in the cortex or other brain regions may be below the threshold to initiate CSD and/or other pathological effects. Future exploration of the exact regional and cellular distributions of these and other $Ca_V2.1$ splice variants within the cortex and throughout the human brain using in situ hybridization and/or RT-PCR analyses will be necessary to fully understand the role of $Ca_V2.1$ splice variants in FHM-1 pathology.

Our results examining tonic and burst firing patterns also suggests the possibility of differential effects of FHM-1 mutations on P/Q-type channel splice variants under different firing conditions. This is most clearly seen with the S218L mutation in the $Ca_V2.1$ (+47) variant; during tonic depolarization current decay is significantly faster relative to WT, yet during burst firing the S218L $Ca_V2.1$ (+47) variant has similar current decay to WT channels after five bursts, likely due to rapid recovery from inactivation (see Figs. 4 and 5). On the other hand, in $Ca_V2.1$ (Δ47) variant channels the S218L mutation has significant effects on current decay under both tonic and burst firing conditions. Interestingly, certain initiating factors of FHM-1 attacks such as emotional stress[14] are known to alter neuronal firing patterns in the brain.[58,59] Although the exact firing conditions directly associated with precipitating factors of migraine are unknown, the episodic nature of the FHM-1 phenotype may in part be associated with changes in neuronal firing pattern and/or frequency that could be relevant to specific $Ca_V2.1$ splice variants expressed in localized brain regions.

It is likely that there exists a complex relationship between channel missense mutations and disease mechanism. While we show alternative splicing at a single $Ca_V2.1$ splice-site can determine the functional impact of FHM-1 mutations, we recognize that across the entire brain many additional factors are likely to be involved in ultimately defining disease pathophysiology. These likely include the expression of multiple splice P/Q-type variants with distinct combinations of alternative splicing as well as the interaction with different auxiliary subunits[27] and other structural and regulatory proteins. Nonetheless, our results demonstrate the relevance of alternative splicing as an important factor in considering underlying disease molecular mechanisms and also the need for a comprehensive understanding of the splice-variant profile of $Ca_V2.1$ channels across brain regions and developmental stages as they might relate to FHM-1 pathology.

While in the present report we show that individual FHM-1 mutations can have differential effects on the biophysical properties of the short and long P/Q-type channel splice variants, we predict this phenomenon is likely relevant to both other FHM-1 mutations and $Ca_V2.1$ variants and also to other types of Ca_V channels and calcium channelopathies.[61] Understanding the differential effects of channelopathy mutations on ion channel splice variants is likely to be important for interpreting results obtained in both heterologous and native systems, as well as for making inferences concerning disease mechanisms and phenotypes. Mutations in the $Ca_V1.1$ L-type channel are associated with hypokalemic periodic paralysis, the $Ca_V1.2$ L-type with Timothy syndrome, the $Ca_V1.4$ L-type with incomplete X-linked congenital stationary night blindness and X-linked cone-rod dystrophy, and the $Ca_V3.2$ T-type with idiopathic generalized epilepsy and autism spectrum disorder (reviewed in ref. 4). Similar to FHM-1, many of these disorders exhibit phenotypes with episodic and/or developmentally specific attributes localized to a subset of regions or tissues that express the respective channels, and like $Ca_V2.1$, these channels also undergo alternative splicing that generates functionally distinct channel variants (reviewed in refs. 6 and 7). The identification of specific Ca_V splice variants involved in disease pathophysiology may also provide the opportunity for targeted therapeutic approaches. For example, while the $Ca_V2.2$ N-type channels have a central role in nociceptive signalling, distinct $Ca_V2.2$ splice variants are involved in the transmission of specific types of pain and has led to new strategies for splice variant-specific targeting in pain therapy.[60]

Methods

Site-directed mutagenesis. Standard PCR-based in vitro mutagenesis was performed using the Pfu Turbo DNA Polymerase (Stratagene, La Jolla, CA), 10 mM dNTPs (Invitrogen) and paired forward and reverse mutagenesis primers.[44] The human $Ca_V2.1$ long (+47) (isoform 2) (NCBI accession number NM_023035.1) cloned in pcDNA 3.1 Zeo (+) was used as the source for the generation of the WT short human $Ca_V2.1$ (Δ47) (isoform 1) cDNA (the other known six splice sites are: Δ10A, 16+/17+, -VEA, -NP, EFa, 43+/44+). Paired forward and reverse primers were designed to adhere to the C-terminus of the $Ca_V2.1$ isoform 2 at the exon 46/47 boundary nucleotide number 6784 and removed the GGCAG pentanucleotide sequence creating the premature stop in exon 47 ($Ca_V2.1$ (Δ47)). Both $Ca_V2.1$ splice variant cDNAs were used in site-directed mutagenesis reactions to generate human $Ca_V2.1$ K1336E, R192Q and S218L mutants in the short and long variants; paired forward and reverse primers were designed to convert codon 1336 from AAA to GAA, codon 192 from CGG to CAG, and codon 218 from TCG to TTA. The integrity of all constructs generated through site-directed mutagenesis were verified by direct DNA sequencing.

Cell culture and transfection. Human embryonic kidney (HEK 293) cells were grown in standard Dulbecco's modified Eagle's medium supplemented with 10% fetal bovine serum (heat inactivated) and 50 U/ml penicillin-50ug/ml streptomycin. Cells were incubated at 37°C in a humidified incubator with 95% atmosphere and 5% CO_2 and grown to 8–15% confluency for transfection. HEK 293 cells were transiently transfected with either WT human $Ca_V2.1$ (Δ47) or $Ca_V2.1$ (+47), or mutant K1336E $Ca_V2.1$ (Δ47), R192Q $Ca_V2.1$ (Δ47), S218L $Ca_V2.1$ (Δ47) or K1336E $Ca_V2.1$ (+47), R192Q $Ca_V2.1$ (+47), S218L $Ca_V2.1$ (+47) in combination with calcium channel auxiliary subunits β_4, $\alpha_2\delta$-1, and the CD8 marker plasmid in a 1:1:1:0.25 molar ratio using Lipofectamine (Invitrogen, La Jolla, CA). To ensure accurate

comparisons, transfections were performed at the same time and electrophysiological recordings alternated within the same day for all channel types.

Electrophysiological recordings. On the second day after transfection, macroscopic Ba^{2+} currents where recorded at room temperature using the whole-cell patch-clamp technique.[45] The internal pipette solution used contained 105 mM CsCl, 25 mM TEACl, 1 mM $CaCl_2$, 11 mM EGTA, 10 mM HEPES and 5 mM ATP (pH 7.2 with CsOH); external: 5 mM $BaCl_2$, 1 mM $MgCl_2$, 10 mM HEPES, 40 mM TEACl, 10 mM glucose and 87.5 mM CsCl (pH 7.4 with TEAOH). Patch pipettes (borosilicate glass BF150-86-10; Sutter Instrument Company, Novato, CA) were made using a horizontal puller (P-87; Sutter Instruments Company) and fire polished using a microforge (Narishige, Tokyo, Japan), with resistances typically of 3 to 5 MΩ when containing internal solution. External solution bath was connected to ground with a 3 M KCl agar bridge. Whole cell currents were recorded and filtered at 2–5 kHz bandwidth using an Axopatch 200A amplifier monitored and stored on a personal computer running pClamp software package version 9. Sampling frequencies were between 2 and 10 kHz. Recordings were analyzed using Clampfit 9 and figures, fittings and statistics (ANOVA) were made using the software program Origin version 7.5 (OriginLab Corp., Northampton, MA). Data are represented as mean ± standard error (S.E.).

Recording protocols and data analysis. Current-voltage relationships were determined by measured currents obtained using a series of 90 millisecond depolarization pulses applied from a holding potential of -90 mV to membrane potentials from -50 mV to +45 mV, increasing by 5 mV increments. Current-voltage relationships were fitted, and IV curves generated, using a modified Boltzmann equation:

$$I = (Gmax*(V_m - E_r))/(1 + \exp((V_m - V_{50})/k))$$

where Gmax is the maximum slope conductance, Vm is the test potential, E_r is the extrapolated reversal potential, V_{50} is the half-activation potential, and k reflects the slope of the activation curve. Activation curves were constructed by calculating conductance from the IV curves and plotting the normalized conductance as a function of the membrane potential. The data were fit with the Boltzmann equation:

$$G/Gmax = A2 + (A1 - A2)/(1 + \exp((V_m - V_{50})/k))$$

where A1 is minimum normalized conductance, A2 is maximum normalized conductance, V_m is the test potential, V_{50} is the half-activation potential, and k reflects the slope of the activation curve (goodness of fit had R^2 values ≥ 0.998).

Voltage-dependence of inactivation was analyzed using depolarizations to 0 mV for 80 ms following 5 s prepulses ranging from -100 to +10 mV at 10mV increments (holding potential of -120 mV). Steady state inactivation curves were constructed by plotting the maximum normalized current during the test pulse as a function of the prepulse potential. The data were fit with the Boltzmann equation:

$$I/Imax = A2 + (A1 - A2)/ (1 + \exp((V_m - V_{50})/k))$$

where A1 is minimum normalized current, A2 is the maximum normalized current, Vm is the test potential, V_{50} is the half-inactivation potential, and k reflects the slope of the inactivation curve (goodness of fit had R^2 values ≥ 0.998).

The kinetics of activation (τ_{act}) were determined from currents obtained from the IV protocol. Current traces were fit with a standard single exponential equation: $I = A*\exp(-t/\tau)$, where A is the amplitude of the current, and τ is the time constant.

Recovery from inactivation was determined using a double-pulse protocol. The first depolarization was to 0 mV for 2 s (the prepulse), followed by a return to the holding potential of -100 mV for variable lengths between 10 ms and 7.5 s. At the end of the variable repolarization period, a second 0 mV (the test pulse) was given for 50 ms. The time interval between sweeps was a total of 1 minute to ensure maximum recovery between sweeps. All traces were normalized to the maximum current during the prepulse for each sweep. The peak current from the test pulse was plotted as a percentage of maximum prepulse current vs. repolarization time. Average traces were fit with either a single or double exponential equation (goodness of fit had R^2 values ≥0.998).

Current decay during a tonic depolarization was examined using a 25 Hz train of 25 square pulses from a holding of -100 mV to a depolarizing potential of -5 mV for 3.4 ms. Current decay curves were generated by plotting normalized maximum current during the test pulses as a function of the time of pulse onset. Current decay during bursts of depolarization was examined using square pulses to -5 mV for 3.4 msec from a holding of -100 mV. Five bursts were given with 290 msec intervals (3.5 burst firing). Each burst contained 25 pulses at a rate of 25 Hz. Current decay curves were generated by plotting normalized maximum current during the test pulses as a function of the time of pulse onset.

RT-PCR of $Ca_V2.1$ carboxyl-terminal region from human cortex RNA. Prior to reverse transcription, 1 ug total RNA from human cortex (Clontech; 636561) was treated with 1X DNase I reaction buffer and 1 unit DNase I (Invitrogen) in a final volume adjusted to 10 uL using sterile DEPC-treated H_2O. Following a 15-minute incubation period at room temperature, the reaction was inactivated by adding 1 uL of 25 mM EDTA and heating at 65°C for 10 minutes. cDNA synthesis was performed using Superscript II Reverse Transcriptase (Invitrogen) following manufacturer's instructions with slight modification. A ~1.1-Kb nucleotide fragment of the carboxyl end of the $Ca_V2.1$ channel was amplified from the human cortex cDNA using standard PCR. The reaction mixture consisted of 3% DMSO, 1X Phusion enzyme buffer, 0.4 pmol/uL of forward and reverse primers, 0.2 mM dNTPs, 1 uL of cortex cDNA, and 1 unit of Phusion enzyme in a final volume of 25 uL. The forward primer (5'GGC ACA TGG AGT CCG GAA CA 3') corresponds to nucleotide position 6130 and the reverse primer (5'GGT AGT AGC CAT GGT GCC3') to nucleotide position 7211 of the human $Ca_V2.1$ α_1 subunit (NCBI accession number NM_023035.1). The cycling profile included an initial activation step of 98°C for 30 s

followed by 30 cycles of 98°C for 30 s, 65°C for 30 s, 72°C for 2.5 minutes and a final extension period of 72°C for 10 minutes. As positive controls, the same PCR reaction was performed on human $Ca_V2.1$ (Δ47) and $Ca_V2.1$ (+47) cDNA plasmids to demonstrate unbiased amplification. PCR reactions using primers for tubulin were used to verify the success of RT reactions. As negative controls, identical PCR reactions without template and containing no RT were performed. To analyze individual $Ca_V2.1$ amplified carboxyl terminal transcripts, PCR products were ligated into pGEMT-Easy (Promega) and then transformed into competent XL-1 *E.coli* bacterial cells. Bacteria containing PCR inserts were identified by blue-white screening and collected and subject to $Ca_V2.1$ (Δ47) and $Ca_V2.1$ (+47) specific PCR reactions. The reverse primer (5'GGT AGT AGC CAT GGT GCC3') was used for both $Ca_V2.1$ (Δ47) and $Ca_V2.1$ (+47) specific PCR reactions. Forward primer (5'ATG GCG CAC CGG CAG TA3') and (5'CAT GGC GCA CCG GCA GGG3') were designed to specifically amplify $Ca_V2.1$ (Δ47) and $Ca_V2.1$ (+47), respectively. All PCR products were run on a 1% agarose gel. In determining the percentage of each variants, only colonies positive for $Ca_V2.1$ (Δ47) and negative for $Ca_V2.1$ (+47), and visa versa, were included and ambiguous results discarded. Direct DNA sequence determination of several representative clones confirmed both the veracity of the splice-variant specific PCR reactions and the identity of the cloned PCR products.

Acknowledgements

This work was funded by operating grant #10677 from the Canadian Institutes of Health Research (CIHR) and a Tier 1 Canada Research Chair in Biotechnology and Genomics-Neurobiology to Terrance P. Snutch, an operating grant from the National Ataxia Foundation and a salary award from the Vancouver Coastal Health Authority to Sian D. Spacey, graduate fellowships from the Michael Smith Foundation for Health Research to Paul J. Adams and Kirk J. Mulatz, and a doctoral fellowship from the Heart and Stroke Foundation of Canada to Laurence S. David. We thank Dr. David Parker and Luke Materek for providing the wild-type isoform 2 $Ca_V2.1$ human cDNA and Ms. Alexi Millman for protocol optimization.

References

1. Catterall WA. Structure and regulation of voltage-gated Ca^{2+} channels. Annu Rev Cell Dev Biol 2000; 16:521-55.
2. Ptacek LJ, Tawil R, Griggs RC, Engel AG, Layzer RB, Kwiecinski H, et al. Dihydropyridine receptor mutations cause hypokalemic periodic paralysis. Cell 1994; 77:863-8.
3. Fontaine B, Vale-Santos J, Jurkat-Rott K, Reboul J, Plassart E, Rime CS, et al. Mapping of the hypokalaemic periodic paralysis (HypoPP) locus to chromosome 1q31-32 in three European families. Nat Genet 1994; 6:267-72.
4. Adams PJ, Snutch TP. Calcium channelopathies: voltage-gated calcium channels. Subcell Biochem 2007; 45:215-51.
5. Emerick MC, Stein R, Kunze R, McNulty MM, Regan MR, Hanck DA, Agnew WS. Profiling the array of $Ca_V3.1$ variants from the human T-type calcium channel gene CACNA1G: alternative structures, developmental expression and biophysical variations. Proteins 2006; 64:320-42.
6. Lipscombe D, Castiglioni AJ. Alternative Splicing in Voltage Gated Calcium Channels. In: McDonough SI, ed. Calcium Channel Pharmacology. Kluwer Academic/Plenum Publishers 2004; 369-409.
7. Lipscombe D, Pan JQ, Gray AC. Functional diversity in neuronal voltage-gated calcium channels by alternative splicing of $Ca_V\alpha_1$. Mol Neurobiol 2002; 26:21-44.
8. Gray AC, Raingo J, Lipscombe D. Neuronal calcium channels: splicing for optimal performance. Cell Calcium 2007; 42:409-17.
9. Splawski I, Timothy KW, Sharpe LM, Decher N, Kumar P, Bloise R, et al. $Ca_V1.2$ calcium channel dysfunction causes a multisystem disorder including arrhythmia and autism. Cell 2004; 119:19-31.
10. Splawski I, Timothy KW, Decher N, Kumar P, Sachse FB, Beggs AH, et al. Severe arrhythmia disorder caused by cardiac L-type calcium channel mutations. Proc Natl Acad Sci USA 2005; 102:8089-96.
11. Graves TD, Imbrici P, Kors EE, Terwindt GM, Eunson LH, Frants RR, et al. Premature stop codons in a facilitating EF-hand splice variant of $Ca_V2.1$ cause episodic ataxia type 2. Neurobiol Dis 2008; 32:10-5.
12. Zhuchenko O, Bailey J, Bonnen P, Ashizawa T, Stockton DW, Amos C, et al. Autosomal dominant cerebellar ataxia (SCA6) associated with small polyglutamine expansions in the alpha 1A-voltage-dependent calcium channel. Nat Genet 1997; 15:62-9.
13. Thomsen LL, Eriksen MK, Roemer SF, Andersen I, Olesen J, Russell MB. A population-based study of familial hemiplegic migraine suggests revised diagnostic criteria. Brain 2002; 125:1379-91.
14. Ducros A, Denier C, Joutel A, Cecillon M, Lescoat C, Vahedi K, et al. The clinical spectrum of familial hemiplegic migraine associated with mutations in a neuronal calcium channel. N Engl J Med 2001; 345:17-24.
15. Ophoff RA, Terwindt GM, Vergouwe MN, van Eijk R, Oefner PJ, Hoffman SM, et al. Familial hemiplegic migraine and episodic ataxia type-2 are caused by mutations in the Ca^{2+} channel gene CACNL1A4. Cell 1996; 87:543-52.
16. Bourinet E, Soong TW, Sutton K, Slaymaker S, Mathews E, Monteil A, et al. Splicing of alpha 1A subunit gene generates phenotypic variants of P- and Q-type calcium channels. Nat Neurosci 1999; 2:407-15.
17. Starr TV, Prystay W, Snutch TP. Primary structure of a calcium channel that is highly expressed in the rat cerebellum. Proc Natl Acad Sci USA 1991; 88:5621-5.
18. Westenbroek RE, Sakurai T, Elliott EM, Hell JW, Starr TV, Snutch TP, Catterall WA. Immunochemical identification and subcellular distribution of the alpha 1A subunits of brain calcium channels. J Neurosci 1995; 15:6403-18.
19. Takahashi T, Momiyama A. Different types of calcium channels mediate central synaptic transmission. Nature 1993; 366:156-8.
20. Sutton KG, McRory JE, Guthrie H, Murphy TH, Snutch TP. P/Q-type calcium channels mediate the activity-dependent feedback of syntaxin-1A. Nature 1999; 401:800-4.
21. Hans M, Luvisetto S, Williams ME, Spagnolo M, Urrutia A, Tottene A, et al. Functional consequences of mutations in the human alpha1A calcium channel subunit linked to familial hemiplegic migraine. J Neurosci 1999; 19:1610-9.
22. van den Maagdenberg AM, Pietrobon D, Pizzorusso T, Kaja S, Broos LA, Cesetti T, et al. A Cacna1a knockin migraine mouse model with increased susceptibility to cortical spreading depression. Neuron 2004; 41:701-10.
23. Tottene A, Fellin T, Pagnutti S, Luvisetto S, Striessnig J, Fletcher C, Pietrobon D. Familial hemiplegic migraine mutations increase Ca^{2+} influx through single human $Ca_V2.1$ channels and decrease maximal $Ca_V2.1$ current density in neurons. Proc Natl Acad Sci USA 2002; 99:13284-9.
24. Tottene A, Pivotto F, Fellin T, Cesetti T, van den Maagdenberg AM, Pietrobon D. Specific kinetic alterations of human $Ca_V2.1$ calcium channels produced by mutation S218L causing familial hemiplegic migraine and delayed cerebral edema and coma after minor head trauma. J Biol Chem 2005; 280:17678-86.
25. Tottene ASM, Frants RR, Ferrari M, van den Maagdenberg AMJ, Pietrobon D. Gain-Of-Function Of $Ca_V2.1$ Calcium Channels Leads To Increased Excitatory Synaptic Transmission In Microcultures Of Cortical Neurons From Cacna1a Knock-In Mice With The R192Q Familial Hemiplegic Migraine Mutation. Abstract Viewer/Itinerary Planner Washington, DC: Society for Neuroscience 2005; Online 2005.
26. Cao YQ, Tsien RW. Effects of familial hemiplegic migraine type 1 mutations on neuronal P/Q-type Ca^{2+} channel activity and inhibitory synaptic transmission. Proc Natl Acad Sci USA 2005; 102:2590-5.
27. Mullner C, Broos LA, van den Maagdenberg AM, Striessnig J. Familial hemiplegic migraine type 1 mutations K1336E, W1684R and V1696I alter $Ca_V2.1$ Ca^{2+} channel gating: evidence for beta-subunit isoform-specific effects. J Biol Chem 2004; 279:51844-50.
28. Kraus RL, Sinnegger MJ, Koschak A, Glossmann H, Stenirri S, Carrera P, Striessnig J. Three new familial hemiplegic migraine mutants affect P/Q-type Ca^{2+} channel kinetics. J Biol Chem 2000; 275:9239-43.
29. Melliti K, Grabner M, Seabrook GR. The familial hemiplegic migraine mutation R192Q reduces G-protein-mediated inhibition of P/Q-type ($Ca_V2.1$) calcium channels expressed in human embryonic kidney cells. J Physiol 2003; 546:337-47.
30. Gherardini LVDMA, Van De Ven RCG, Ferrari MD, Frants RR, Pietrobon D, Pizzorusso T. Increased susceptibility to cortical spreading depression in knockin mice carrying the S218L mutation of human $Ca_V2.1$ calcium channels: a new model for in vivo study of familial hemiplegic migraine type 1 (FHM1). Poster: Federation of European Neuroscience Societies Forum, Vienna Austria 2006.
31. Kraus RL, Sinnegger MJ, Glossmann H, Hering S, Striessnig J. Familial hemiplegic migraine mutations change alpha1A Ca^{2+} channel kinetics. J Biol Chem 1998; 273:5586-90.

32. Soong TW, DeMaria CD, Alvania RS, Zweifel LS, Liang MC, Mittman S, et al. Systematic identification of splice variants in human P/Q-type channel alpha1(2.1) subunits: implications for current density and Ca^{2+}-dependent inactivation. J Neurosci 2002; 22:10142-52.
33. Chang SY, Yong TF, Yu CY, Liang MC, Pletnikova O, Troncoso J, et al. Age and gender-dependent alternative splicing of P/Q-type calcium channel EF-hand. Neuroscience 2007; 145:1026-36.
34. Timmermann DB, Westenbroek RE, Schousboe A, Catterall WA. Distribution of high-voltage-activated calcium channels in cultured gamma-aminobutyric acidergic neurons from mouse cerebral cortex. J Neurosci Res 2002; 67:48-61.
35. Chaudhuri D, Chang SY, DeMaria CD, Alvania RS, Soong TW, Yue DT. Alternative splicing as a molecular switch for Ca^{2+}/calmodulin-dependent facilitation of P/Q-type Ca^{2+} channels. J Neurosci 2004; 24:6334-42.
36. Krovetz HS, Helton TD, Crews AL, Horne WA. C-Terminal alternative splicing changes the gating properties of a human spinal cord calcium channel alpha 1A subunit. J Neurosci 2000; 20:7564-70.
37. Restituito S, Thompson RM, Eliet J, Raike RS, Riedl M, Charnet P, Gomez CM. The polyglutamine expansion in spinocerebellar ataxia type 6 causes a β subunit-specific enhanced activation of P/Q-type calcium channels in *Xenopus* oocytes. J Neurosci 2000; 20:6394-403.
38. Maximov A, Sudhof TC, Bezprozvanny I. Association of neuronal calcium channels with modular adaptor proteins. J Biol Chem 1999; 274:24453-6.
39. Mori Y, Friedrich T, Kim MS, Mikami A, Nakai J, Ruth P, et al. Primary structure and functional expression from complementary DNA of a brain calcium channel. Nature 1991; 350:398-402.
40. Hans M, Urrutia A, Deal C, Brust PF, Stauderman K, Ellis SB, et al. Structural elements in domain IV that influence biophysical and pharmacological properties of human alpha1A-containing high-voltage-activated calcium channels. Biophys J 1999; 76:1384-400.
41. Fitzsimons RB, Wolfenden WH. Migraine coma. Meningitic migraine with cerebral oedema associated with a new form of autosomal dominant cerebellar ataxia. Brain 1985; 108:555-77.
42. Kors EE, Terwindt GM, Vermeulen FL, Fitzsimons RB, Jardine PE, Heywood P, et al. Delayed cerebral edema and fatal coma after minor head trauma: role of the CACNA1A calcium channel subunit gene and relationship with familial hemiplegic migraine. Ann Neurol 2001; 49:753-60.
43. Chan YC, Burgunder JM, Wilder-Smith E, Chew SE, Lam-Mok-Sing KM, Sharma V, Ong BK. Electroencephalographic changes and seizures in familial hemiplegic migraine patients with the CACNA1A gene S218L mutation. J Clin Neurosci 2008; 15:891-4.
44. Zoller MJ, Smith M. Oligonucleotide-directed mutagenesis: a simple method using two oligonucleotide primers and a single-stranded DNA template. DNA 1984; 3:479-88.
45. Hamill OP, Marty A, Neher E, Sakmann B, Sigworth FJ. Improved patch-clamp techniques for high-resolution current recording from cells and cell-free membrane patches. Pflugers Arch 1981; 391:85-100.
46. Weiss N, Sandoval A, Felix R, Van den Maagdenberg A, De Waard M. The S218L familial hemiplegic migraine mutation promotes deinhibition of $Ca_v2.1$ calcium channels during direct G-protein regulation. Pflugers Arch 2008; 457:315-26.
47. Womack M, Khodakhah K. Active contribution of dendrites to the tonic and trimodal patterns of activity in cerebellar Purkinje neurons. J Neurosci 2002; 22:10603-12.
48. Fernandez FR, Engbers JD, Turner RW. Firing dynamics of cerebellar purkinje cells. J Neurophysiol 2007; 98:278-94.
49. Shin SL, Rotter S, Aertsen A, De Schutter E. Stochastic description of complex and simple spike firing in cerebellar Purkinje cells. Eur J Neurosci 2007; 25:785-94.
50. McCormick DA, Connors BW, Lighthall JW, Prince DA. Comparative electrophysiology of pyramidal and sparsely spiny stellate neurons of the neocortex. J Neurophysiol 1985; 54:782-806.
51. Brumberg JC. Firing pattern modulation by oscillatory input in supragranular pyramidal neurons. Neuroscience 2002; 114:239-46.
52. Fellin T, Luvisetto S, Spagnolo M, Pietrobon D. Modal gating of human $Ca_v2.1$ (P/Q-type) calcium channels: II. The b mode and reversible uncoupling of inactivation. J Gen Physiol 2004; 124:463-74.
53. Luvisetto S, Fellin T, Spagnolo M, Hivert B, Brust PF, Harpold MM, et al. Modal gating of human $Ca_v2.1$ (P/Q-type) calcium channels: I. The slow and the fast gating modes and their modulation by beta subunits. J Gen Physiol 2004; 124:445-61.
54. Chaudhuri D, Issa JB, Yue DT. Elementary mechanisms producing facilitation of $Ca_v2.1$ (P/Q-type) channels. J Gen Physiol 2007; 129:385-401.
55. Bolay H, Reuter U, Dunn AK, Huang Z, Boas DA, Moskowitz MA. Intrinsic brain activity triggers trigeminal meningeal afferents in a migraine model. Nat Med 2002; 8:136-42.
56. Pietrobon D. Migraine: new molecular mechanisms. Neuroscientist 2005; 11:373-86.
57. Pietrobon D. Familial hemiplegic migraine. Neurotherapeutics 2007; 4:274-84.
58. Weiss JM, Simson PE. Neurochemical and electrophysiological events underlying stress-induced depression in an animal model. Adv Exp Med Biol 1988; 245:425-40.
59. McEwen BS. Physiology and neurobiology of stress and adaptation: central role of the brain. Physiol Rev 2007; 87:873-904.
60. Altier C, Dale CS, Kisilevsky AE, Chapman K, Castiglioni AJ, Matthews EA, et al. Differential role of N-type calcium channel splice isoforms in pain. J Neurosci 2007; 27:6363-73.
61. Powell KL, Cain SM, Ng C, Sirdesai S, David LS, Kyi M, Garcia E, Tyson JR, Reid CA, Bahlo M, Foote SJ, Snutch TP, O'Brien TJ. A $Ca_v3.2$ T-type calcium channel point mutation has splice-variant-specific effects on function and segregates with seizure expression in a polygenic rat model of absence epilepsy. J Neurosci 2009; 29:371-80.

Appendix 3. Amyotrophic lateral sclerosis-immunoglobulins selectively interact with neuromuscular junctions expressing P/Q-type calcium channels.
Original reference:
Gonzalez, L.E., Kotler, M.L., Vattino, L.G., Conti, E., Reisin, R.C., Mulatz, K.J., Snutch, T.P., and Uchitel, O.D. (2011). Amyotrophic lateral sclerosis-immunoglobulins selectively interact with neuromuscular junctions expressing P/Q-type calcium channels. J. Neurochem. *119*, 826–838.

Journal of Neurochemistry JNC
JOURNAL OF NEUROCHEMISTRY | 2011 | 119 | 826–838 doi: 10.1111/j.1471-4159.2011.07462.x

ORIGINAL ARTICLE

Amyotrophic lateral sclerosis–immunoglobulins selectively interact with neuromuscular junctions expressing P/Q–type calcium channels

Laura E. Gonzalez,*† Mónica L. Kotler,† Lucas G. Vattino,* Eugenia Conti,‡ Ricardo C. Reisin,‡ Kirk J. Mulatz,§ Terrance P. Snutch§ and Osvaldo D. Uchitel*

*Departamento de Fisiología, Biología Molecular y Celular, Facultad de Ciencias Exactas y Naturales, IFIBYNE-CONICET, UBA, Argentina
†Departamento de Química Biológica, Facultad de Ciencias Exactas y Naturales, UBA, Argentina
‡Servicio de Neurología, Hospital Británico, Argentina
§Michael Smith Laboratories, University of British Columbia, Vancouver, Canada

Abstract
Amyotrophic lateral sclerosis (ALS) is a fatal neurodegenerative disease characterized by a gradual loss of motoneurons. The majority of ALS cases are associated with a sporadic form whose etiology is unknown. Several pieces of evidence favor autoimmunity as a potential contributor to sporadic ALS pathology. To gain understanding concerning possible antigens interacting with IgGs from sporadic ALS patients (ALS–IgGs), we studied immunoreactivity against neuromuscular junction (NMJ), spinal cord and cerebellum of mice with and without the $Ca_V2.1$ pore-forming subunit of the P/Q-type voltage-gated calcium (Ca^{2+}) channel. ALS–IgGs showed a strong reactivity against NMJs of wild-type diaphragms. ALS–IgGs also increased muscle miniature end-plate potential frequency, suggesting a functional role for ALS–IgGs on synaptic signaling. In support, in mice lacking the $Ca_V2.1$ subunit ALS–IgGs showed significantly reduced NMJ immunoreactivity and did not alter spontaneous acetylcholine release. This difference in reactivity was absent when comparing N-type Ca^{2+} channel wild-type or null mice. These results are particularly relevant because motoneurons are known to be early pathogenic targets in ALS. Our findings add further evidence supporting autoimmunity as one of the possible mechanisms contributing to ALS pathology. They also suggest that serum autoantibodies in a subset of ALS patients would interact with NMJ proteins down-regulated when P/Q-type channels are absent.
Keywords: amyotrophic lateral sclerosis, autoantibodies, autoimmunity, calcium channels.
J. Neurochem. (2011) **119**, 826–838.

ORIGINAL ARTICLE

Amyotrophic lateral sclerosis (ALS) is a neurodegenerative disorder characterized by progressive neuromuscular dysfunction and decrease in the number of upper and lower motoneurons (Mulder 1982). Clinical manifestations include fatigue, fasciculations, spasticity, hyperreflexia, weakness and muscle atrophy, ultimately leading to paralysis and death (Rowland 1998). Currently, there are no effective treatments to either stop or delay ALS progression.

Approximately 10% of patients present a familiar form of the disorder (fALS) characterized molecularly by underlying mutations in several different genes (Valdmanis *et al.* 2009). The remaining ALS cases (~90%) are sporadic (sALS) and of unknown etiology. Different hypotheses have been

Received June 11, 2011; revised manuscript received August 25, 2011; accepted August 25, 2011.
Address correspondence and reprint requests to Osvaldo D. Uchitel, Laboratorio de Fisiología y Biología Molecular, Facultad de Ciencias Exactas y Naturales, Universidad de Buenos Aires, Ciudad Universitaria, pabellón 2, piso 2, C1428EHA, Ciudad Autónoma de Buenos Aires, Argentina. E-mail: odu@fbmc.fcen.uba.ar

Abbreviations used: ALS, amyotrophic lateral sclerosis; ANOVA, analysis of variance; BSA, bovine serum albumin; Ca^{2+}, calcium; DC, disease control; DMEM, Dulbecco's modified Eagle's medium; fALS, familiar ALS; HC, healthy control; HCl, chlorhydric acid; HEK, human embryonic kidney; MEPP, miniature end-plate potential; NMJ, neuromuscular junction; PBS, phosphate-buffered saline; RN, Ringer's normal solution; sALS, sporadic ALS; SDS, sodium dodecylsulfate; TMR, tetramethylrhodamine; WT, wild-type.

© 2011 The Authors

proposed to explain sALS pathogenesis, including antibody-mediated autoimmunity (Appel *et al.* 1993; Pagani *et al.* 2006), glutamate excitotoxicity (Rothstein *et al.* 1992; Van Den Bosch *et al.* 2006), oxidative damage (Bowling *et al.* 1993; Niebroj-Dobosz *et al.* 2004) and neurofilament aggregation (Xu *et al.* 1993; Mendonca *et al.* 2005). There is considerable evidence supporting immune-mediated mechanisms in motoneuronal degeneration. First, autoimmune disorders have been demonstrated in ALS patients (Appel *et al.* 1986) along with serum antibodies against gangliosides (Pestronk *et al.* 1989), neurofilaments (Couratier *et al.* 1998) and voltage-dependent calcium (Ca^{2+}) channels (Smith *et al.* 1992). Secondly, spinal inflammatory infiltrates have been detected in ALS patients (Engelhardt and Appel 1990; Troost *et al.* 1990), as well as IgGs in endoplasmic reticulum of spinal and cortical motoneurons (Engelhardt and Appel 1990). However, the presence and pathophysiological relevance of autoantibodies remains controversial (Drachman and Kuncl 1989; Drachman *et al.* 1995; Arsac *et al.* 1996).

In guinea pigs' spinal cords, upper and lower motoneuron injury was observed when they were inoculated with bovine spinal homogenates (Engelhardt *et al.* 1990; Xu *et al.* 2009), resembling human ALS with regard to the presence of IgGs within motoneurons and inflammatory cells (Appel *et al.* 1991). Additionally, passive transfer of IgGs from immunized animals (Appel *et al.* 1991) or ALS patients (Uchitel *et al.* 1992b) can induce neuromuscular dysfunction in injected mice. In the latter instance, human IgGs were subsequently detected at motoneuronal soma and nerve terminals (Fratantoni *et al.* 1996; Engelhardt *et al.* 2005).

In vitro studies have shown that ALS–IgGs can induce apoptosis in spinal cord cultures and motoneuron cell lines, presumably by increasing intracellular Ca^{2+} concentration (Smith *et al.* 1994; Demestre *et al.* 2005). At neuromuscular junctions (NMJs), pre-incubation with ALS–IgGs stimulates spontaneous and asynchronous synaptic activity (Uchitel *et al.* 1988, 1992b; Pagani *et al.* 2006), Ca^{2+} influx (Mosier *et al.* 1995) and signaling pathways leading to Ca^{2+} release from intracellular stores (Pagani *et al.* 2006).

In all of these processes, an involvement of NMJ Ca^{2+} channels has been established. At NMJs evoked-transmitter release in response to Ca^{2+} influx is mediated mainly by P/Q-type Ca^{2+} channels (encoded by the $Ca_V2.1$ subunit; Protti *et al.* 1991; Starr *et al.* 1991; Uchitel *et al.* 1992a; Stea *et al.* 1994; Katz *et al.* 1997). Furthermore, the presence of L-type channels at motor end-plates (Urbano and Uchitel 1999) has been attributed to modulation of fast acetylcholine vesicle recycling (Perissinotti *et al.* 2008). Finally, N-type Ca^{2+} activity is critical for synaptic transmission early during development and in $Ca_V2.1$-lacking animals (Rosato Siri and Uchitel 1999; Urbano *et al.* 2003).

Given the proposed interaction between ALS–IgGs and Ca^{2+} channels (Llinas *et al.* 1993; Smith *et al.* 1994; Carter and Mynlieff 2003; Pagani *et al.* 2006), we evaluated the IgG reactivity effects in mouse models of genetic deletion of the $Ca_V2.1$ (P/Q-type; Bourinet *et al.* 1999) and $Ca_V2.2$ (N-type; Dubel *et al.* 1992) subunits. Our results suggest that NMJ antigens recognized by ALS–IgGs require the presence of P/Q-type channels, although the $Ca_V2.1$ subunit itself does not seem to be the major antigen.

Materials and methods

Animal genotyping

Determination of mice genotype was performed by multiplex PCR using mice tail biopsies. DNA samples were purified with DNeasy Tissue Kit (Qiagen Inc., Valencia, CA, USA) after tissue digestion with proteinase K (2 mg/mL) for 15 h at 56°C. Primers used for genotyping were:

$Ca_V2.1$ forward: 5′-CCAGCTTGAGTGGCCGCAGCACACG-3′
$Ca_V2.1^{+/+}$ reverse: 5′-ATAATAAGTCACCTCTGGTTCTAAAG-3′
$Ca_V2.1^{-/-}$ reverse: 5′-CTGACTAGGGGAGGAGTAGAAG-3′
$Ca_V2.2$ forward: 5′-TGGCACCTTATGCCTTGCACGGTGCCTGCG-3′
$Ca_V2.2^{+/+}$ reverse: 5′-GGTCGAGATGGCTTGCGGGACCCGTTGGGA-3′
$Ca_V2.2^{-/-}$ reverse: 5′-GCCTGCTTGCCGAATATCATGGTGGAAAAT-3′

The following amplification protocol was used:

$Ca_V2.1$ genotyping:
95°C for 3 min
95°C for 30 s, 55°C for 30 s, 72°C for 30 s (35 cycles)
72°C for 5 min
$Ca_V2.2$ genotyping:
94°C for 2 min
94°C for 20 s, 58°C for 20 s, 72°C for 40 s (35 cycles)
72°C for 7 min

PCR products were subjected to electrophoresis in a 1% (wt/vol) agarose gel containing ethidium bromide and bands analyzed according to their expected size: 240 bp for $Ca_V2.1^{+/+}$, 390 bp for $Ca_V2.1^{-/-}$, 460 bp for $Ca_V2.2^{+/+}$ and 580 bp for $Ca_V2.2^{-/-}$.

Human serum samples

Patients were diagnosed with sporadic ALS according to El Escorial criteria (Brooks 1994). All participating individuals provided written consent to take part in the study and the applied protocol was approved by the Institutional Review Board of the Hospital Británico of Buenos Aires. Age at diagnosis ranged from 59 to 76 (mean: 64.6 years) and the sex ratio was 6 : 2 (M : F). Six patients had spinal onset while the rest showed bulbar onset. All of the clinical parameters evaluated in each ALS patient (ALS Functional Rating and Norris Scales) had similar values (Table 1). Exclusion of genetic forms of ALS was based upon family history.

Disease controls (DC; $n = 7$; 4 females; mean age: 56.0 years) comprised people with Lambert-Eaton myasthenic syndrome (an autoimmune disorder against voltage-dependent Ca^{2+} channels, DC1), myasthenia gravis (an autoimmune disease against acetylcholine receptors, DC2), Charcot-Marie-Tooth (a purely genetic motoneuron disease involving myelin sheath destruction, DC3), fALS (DC4-6) and multifocal motor neuropathy with conduction block (an autoimmune disease against myelin sheath, DC7).

© 2011 The Authors

Table 1 Clinical parameters of sporadic ALS patients

Patient	Age (years)	Sex	ALS	VFC	Scores		Progression time (months)
					ALSFR[a]	Norris[b]	
ALS1	66	M	Definite	Abnormal	22	49	4
ALS2	70	F	Definite	Normal	NA	NA	12
ALS3	67	M	Definite	Normal	33	68	12
ALS4	62	M	Probable	Abnormal	32	38	18
ALS5	70	F	Definite	Normal	30	73	30
ALS6	77	M	Possible	Abnormal	35	71	60
ALS7	59	M	Definite	Normal	27	80	18
ALS8	67	M	Definite	Normal	28	59	24

VFC, vital force capacity; ALSFR, ALS functional rating; M, male; F, female; NA, not available.
[a]ALSFR Score ranges from 0 (pathological) to 40 (normal).
[b]Norris Score ranges from 0 (pathological) to 99 (normal).

Healthy controls (HC) consisted of three subjects with no evidence of neurological diseases (two females, mean age: 36.7 years). Blood samples were collected at the time of clinical evaluation. Serum was separated by centrifugation and stored at −80°C until purification.

IgG purification

All of the procedure was performed at 4°C. Serum samples were centrifuged at 12 000 *g* for 10 min and the supernatant subjected to ammonium sulfate fractionation to a final salt concentration of 50% (wt/vol). The solution was stirred for 60 min and centrifuged at 12 000 *g* for 30 min. The resulting pellet was resuspended in phosphate buffer (20 mM pH 7.0) and dialyzed against the same solution for 16 h using a 12-kDa pore cellulose membrane. IgG isolation was performed by affinity chromatography employing a ProteinG-Agarose column and 20 mM phosphate buffer as washing buffer. IgGs were eluted with glycine (0.1 M pH 2.7) and then acid-neutralized with Tris–HCl (1.0 M pH 9.0). The isolated fractions were subsequently dialyzed against phosphate-buffered saline (PBS; 10 mM phosphate buffer, 150 mM NaCl, 3 mM KCl pH 7.4) for 5 h. IgG concentrations were estimated by absorbance analysis at 280 nm, taking into consideration the human IgG molar absorptivity coefficient. Testing of purified fractions was performed by electrophoresis in 10% (wt/vol) sodium dodecylsulfate (SDS)-polyacrylamide gels and subsequent staining with Coomassie blue. Aliquots were stored at −20°C.

Animal handling

Animals were treated in accordance with national guidelines for the humane treatment of laboratory animals from University of Buenos Aires, which are comparable to those of the USA National Institutes of Health. All possible efforts were made to reduce the number of animals used and any suffering/discomfort.

For all the experiments, tissue was extracted from three different mice strains: Swiss (males, P > 30), $Ca_V2.1$-null strain sv129 (males and females, P16-P23) and $Ca_V2.2$-null strain C57BL/6 (males, P18). Both null strains were kindly provided by Dr Shin Hee-Sup (Korea Institute of Science and Technology, Seoul, Republic of Korea).

Intracellular recordings

Mice were anesthetized with an intraperitoneal overdose of 2% (wt/vol) tribromoethanol (0.3 mL/10 g body weight), exsanguinated and killed by beheading. Diaphragm muscle dissections were carried out in a Sylgard-covered Petri dish (Dow Corning, Midland, MI, USA) containing Ringer's normal solution (RN; 137 mM NaCl, 5 mM KCl, 2 mM $CaCl_2$, 1 mM $MgSO_4$, 12 mM $NaHCO_3$, 1 mM Na_2HPO_4 and 11 mM glucose pH 7.2–7.4), continuously bubbled with 95% O_2/5% CO_2. All procedures were carried out at room temperature (20–23°C) except as otherwise stated.

Phrenic nerve-muscle preparations were dissected and placed in a 1 mL volume recording chamber and incubated for 4 h in a humidified atmosphere with purified IgGs from either ALS patients or control subjects. IgGs were diluted in RN to a final concentration of 0.4 mg/mL. Either the right or left hemi-diaphragm was randomly used to test immunoglobulins.

Miniature end-plate potentials (MEPP) frequency was determined in the absence of tetrodotoxin (spontaneous activity), before and after the incubation period, using intracellular recordings (glass microelectrodes filled with 3.0 M KCl, 20–30 MΩ). Recordings of 2–5 min duration were randomly acquired from a maximum of 15 fibers from a minimum of 3 mice. Acquisition procedures were performed as previously described (Pagani *et al.* 2006). Data were stored on disk for further computer analysis using appropriate software (Axoscope 9.0 and Clampfit 9.0, Axon Instruments, Foster City, CA, USA). SigmaPlot 10.0 integrated with SigmaStat 3.5 (Systat Software Inc., Chicago, IL, USA) was used to compare and plot the data.

Neuromuscular junction immunofluorescence

Diaphragm dissection was performed as described above. Dissected muscles were fixed at 4°C in 4% (wt/vol) paraformaldehyde, permeabilized with 1% (vol/vol) Triton-X-100 and cryopreserved in 30% (wt/vol) sucrose. Optimum cutting temperature 4583 Tissue-Tek (Sakura, Tokyo, Japan) was employed as inclusion medium to generate 40-μm thick sections in a cryostat (ETR2248, Reichert-Jung, Bensheim, Germany), which were then mounted on gelatin-coated slides and stored at −20°C. To reduce background signal from muscle fibers, diaphragms were tangentially sliced and consequently, NMJs rarely showed the usual pretzel-like shape.

© 2011 The Authors

Tissue preparations were permeabilized with Triton-X100 0.05% (vol/vol) and subsequently blocked for 30 min in 3% (wt/vol) bovine serum albumin (BSA) and 5% (vol/vol) normal goat serum. Incubation with purified IgGs from ALS patients or control subjects at the appropriate dilutions (1 : 10 to 1 : 100) was performed for 16–20 h at 4°C in PBS containing 3% BSA, 0.1 M L-lysine and 0.075% (vol/vol) Triton X-100. Binding of the primary antibody was revealed by using a goat anti-human IgG coupled to fluorescein-isothiocyanate at a 1 : 2000 dilution. Co-staining with tetramethyl-rhodamine (TMR)-conjugated α-bungarotoxin (0.25 μg/mL) allowed us to identify NMJs through its high affinity for the post-synaptic nicotinic acetylcholine receptors. After extensive washing with PBS, sections were mounted in PBS-glycerol (1 : 1), covered with coverslips and sealed with nail polish. To check for non-specific binding and autofluorescence, controls were performed by omission of α-bungarotoxin, primary (isotype control) or secondary antibody.

Spinal cord, brain and cerebellum immunofluorescence

Tribromoethanol-anesthetized mice were transcardially perfused with PBS followed by 4% (wt/vol) paraformaldehyde-4% (wt/vol) sucrose after loss of both toe pitch and pupil-closing reflexes. After dissection of whole brain, cerebellum and spinal cord, tissue samples were additionally fixed in the same solution for 2–4 h at 4°C. Sections of 150 μm were obtained with an Integraslice 7550PSDS vibrating microslicer (Campden Instruments, Loughborough, UK) and subsequently permeabilized with 1% (vol/vol) Triton X-100 for 30 min. Incubation with purified IgGs from ALS patients or control subjects at a concentration of 0.2 mg/mL was performed for 16–20 h at 4°C in PBS containing 3% BSA (wt/vol), 0.1 M L-lysine and 0.075% (vol/vol) Triton X-100. Binding of primary antibody was detected using a goat anti-human IgG conjugated to fluorescein-isothiocyanate (1 : 2000 dilution). For spinal cord immunolabeling, thoracic and lumbar sections were analyzed because of the large size of cells in these regions. Lower motoneurons were detected by their morphology and localization at the ventral horn. The cortical primary motor area in slices was identified using a mouse brain atlas (Paxinos and Franklin 2001), while motoneurons were localized by size and shape. Purkinje neurons were recognized within cerebellar sections by means of their distinctive morphology. Subsequent distinction of molecular and granular cell layers was performed. In some cases, counter-staining with propidium iodide (3 μM, 60 min) was employed to distinguish different cellular populations by their morphology. In fixed tissues, propidium iodide stains citoplasm and nucleus due to its general affinity for nucleic acids.

Immunofluorescence analysis and image processing

Immunofluorescence staining was assessed using a FV300 confocal fluorescence microscope (Olympus Optical Co., Tokyo, Japan) equipped with an image acquisition system and Fluoview 3.3 software (Olympus Optical Co.). Sequential scanning of slices with Argon (λ: 488 nm) and Helium-Neon (λ: 543 nm) lasers was performed to reduce bleed-through of the fluorescence signal. Laser intensity as well as voltage, gain and offset configuration of each photomultiplier were kept constant for each experiment. An Olympus 60× oil-immersion PlanApo objective (numerical aperture: 1.4) was employed for analysis of coverslipped NMJ cryosections, whereas thick slices were kept in a Petri dish with PBS and photographed with an Olympus 60× water-immersion LUMplanFL objective (numerical aperture: 0.9), while immobilized with a slice hold-down device. Stacks of 10 confocal planes (1-μm interval) were acquired for each channel and subsequently analyzed with ImageJ 1.42 software (National Institutes of Health, Bethesda, MD, USA). Fluorescence intensity quantification was carried out by measuring mean grey values of at least 15 cells or NMJs from two to three different animals, after background subtraction. In the case of muscle preparations, the regions of interest were chosen based on the α-bungarotoxin signal. Mean gray values for each sample were normalized to the isotype control.

Cell culture and transfection/induction

Human embryonic kidney 293 (HEK293) cells [passage 18–26, American Type Culture Collection (ATCC) number CRL-1573] were maintained by serial passages in 75-cm^2 culture flasks. Cells were grown in Dulbecco's Modified Eagle's Medium containing 4 mM L-glutamine, 4.5 g/L glucose, 4 mg/L pyridoxine-HCl and 110 mL/L sodium pyruvate, supplemented with 10% heat-inactivated fetal bovine serum at 37°C in a humidified incubator with 5% CO_2 and 95% air. Sub-culturing of cells was performed with 0.25% trypsin-EDTA, followed by protease inactivation with Dulbecco's modified Eagle's medium containing fetal bovine serum and reseeding into 25-cm^2 culture flasks. Cultures at ~50% confluency were used for transfection experiments using Lipofectamine 2000 (Invitrogen, Carlsbad, CA, USA) following the manufacturer's instructions. Full-length human $Ca_V2.1$, and rat β_{2a} and $\alpha_2\delta_2$ cDNAs were contained in pcDNA3.1Zeo(+) (Invitrogen). Approximately 36 h post-transfection cells were processed for immunoprecipitation and/or western blot experiments.

Culturing of HEK293-derived T-rex 293 cells (passage 9–12) stably expressing the P/Q-type channel subunits was essentially the same as described above, except for the addition of 1% non-essential amino acids and, 24 h prior to induction, the addition of induction/selection agents Blasticidine (10 μg/mL), Zeocin (200 μg/mL) and Hygromycin B (150 μg/mL). In these cells, the pcDNA5/TO vector (Invitrogen) containing a tetracycline-responsive element was used to drive expression of the full-length $Ca_V2.1$ subunit, whereas the auxiliary subunits β_{2a} and $\alpha_2\delta_2$ were expressed in pBudCE4.1 (Invitrogen). Cells were lysed 48 h after induction with Tetracycline (1.5 μg/mL).

Crude membrane fraction preparation

Mouse cerebellum was disrupted with a glass-Teflon homogenizer in 4°C buffer containing 0.32 M sucrose in 50 mM Tris–HCl (pH 7.4). Homogenates were centrifuged at 1950 *g* for 10 min at 4°C and the resulting supernatant was spun down at 24 500 *g* for 20 min at 4°C. Pellets were resuspended in radio immunoprecipitation assay buffer (50 mM Tris–HCl buffer pH 8.0, 150 mM NaCl, 1% NP-40, 0.1% SDS and 0.5% sodium deoxycholate) with protease inhibitors (10 μM EDTA, 2 mM phenylmethylsulfonyl fluoride, 10 μg/mL aprotinin, 100 μM leupeptin, and 1 μg/mL pepstatin). Protein concentrations were determined by the Bradford (1976) assay.

Immunoprecipitation assay

Two-hundred micrograms of proteins were incubated overnight with ALS–IgGs (4 μg) and 60 μL of Protein G Plus-agarose beads (Santa

© 2011 The Authors

Cruz Biotechnology, Santa Cruz, California, USA), in a mixing rotor at 4°C. Beads were then washed with NP-40-containing lysis buffer (50 mM Tris-HCl buffer pH 7.4, 0.5% NP-40, 150 mM NaCl and 50 mM EDTA) and protein complexes interacting with the antibodies eluted with Laemmli buffer (62.5 mM Tris-HCl buffer pH 6.8, 2% SDS, 0.01% bromophenol blue, 2% β-mercaptoethanol and 10% glycerol) supplemented with protease inhibitors. Immunoprecipitates were analyzed by electrophoresis followed by western blot. An aliquot of the lysate originally used for each assay was run in parallel to check for the presence of the analyzed proteins (input), as well as a control by omission of antibodies (beads).

Gel electrophoresis and western blot

Western blots were performed according to standard procedures. In brief, cells were resuspended in Laemmli buffer containing protease inhibitors and mechanically disrupted using needles of decreasing internal diameter (26–29 G). Proteins were resolved by 4–12% Nu-polyacrylamide gradient gel electrophoresis (Nu-PAGE) and transferred onto nitrocellulose membranes (Amersham Hybond ECL; GE Healthcare, Piscataway, NJ, USA). Non-specific binding was blocked by 2% non-fat powdered milk in PBS containing 0.2% Tween-20 for 60 min at 20–23°C. Membranes were incubated overnight at 4°C with primary antibodies as described in Results, followed by addition of horseradish peroxidase-conjugated secondary antibodies. All antibodies were diluted in PBS containing 0.2% Tween-20 with 2% non-fat powdered milk. Immunoreactive bands were detected by chemiluminescence using horseradish peroxidase-conjugated secondary antibodies and a Supersignal Chemi-Luminescence detection kit (Pierce, Rockford, IL, USA) following the manufacturer's instructions.

Statistical analysis

Results are expressed and plotted as mean ± standard error of the mean (SEM) values. Experimental differences between groups were analyzed by the Mann–Whitney Rank Sum test or two-way analysis of variance (ANOVA) followed by Student–Newman–Keuls post-test where appropriate, with SigmaStat 3.5 software (Systat Software Inc.). A p-value of less than 0.05 was considered as statistically significant.

Materials

Tribromoethanol was purchased from Aldrich (Milwaukee, WI, USA). BSA, normal goat serum, TMR-tagged α-bungarotoxin and other chemicals were analytical grade and obtained from Sigma (St Louis, MO, USA). Goat anti-human secondary antibody (catalog number 1201-0081) was obtained from Cappel (Organon Teknika Corp., Arnhem, The Netherlands) whereas HiTrap ProteinG-Agarose columns were from GE Healthcare Bio-Sciences AB (Uppsala, Sweden).

Results

ALS–IgGs increased neuromuscular spontaneous synaptic activity and were able to bind to mouse neuromuscular junctions

To determine whether ALS–IgGs from our set of patients were able to modify MEPP frequency, we incubated diaphragm muscle preparations and analyzed spontaneous acetylcholine release using intracellular recordings. Figure 1 shows that 63% of the ALS patients tested (five of eight) possessed serum antibodies that significantly increased the frequency of MEPPs in mouse diaphragm from a resting state of ~30 MEPPs/min to a 2- to 5-fold increase (Rank Sum test, $p < 0.05$ comparing initial and final frequency). The enhanced effect on MEPPs was completely absent in experiments using any of RN, healthy or disease control IgGs (Rank Sum test, $p > 0.05$ comparing initial and final frequencies). This lack of effect was also observed in the three remaining ALS–IgGs, which were unable to raise spontaneous synaptic activity above basal levels (Rank Sum test, $p > 0.05$ comparing initial and final frequencies).

To gain a better understanding of the sites of action of the reactive antibodies, we performed indirect immunofluo-

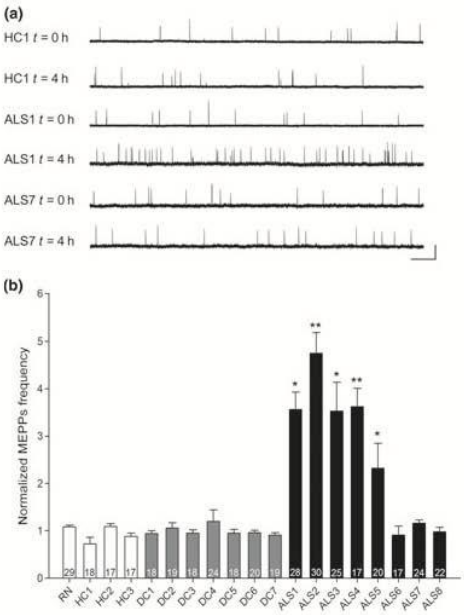

Fig. 1 MEPPs recordings of Swiss mice (P > 30) diaphragm preparations. Muscles were incubated with RN or with purified IgGs from ALS patients (ALS), healthy (HC) or disease controls (DC). (a) Representative intracellular recordings acquired before ($t = 0$ h) or after ($t = 4$ h) IgG incubation. Bar: 1 mV, 2 s. (b) MEPPs frequency quantification relative to the beginning of the experiment. Statistically significant differences after incubation time were detected by Rank Sum test. *$p < 0.05$ and **$p < 0.001$ compared with initial MEPP frequency. Numbers inside bars indicate the number of NMJs studied in each experimental condition.

© 2011 The Authors

rescence using IgGs from ALS or control individuals as primary antibodies, and α-bungarotoxin coupled to TMR as a post-synaptic marker of NMJs. Of note, Figs 2 and 3 show that the same set of five ALS–IgGs that produced synaptic potentiation also presented strong immunoreactivity against wild-type (WT) mouse diaphragm NMJs. Fluorescence intensities ranged from 3 to 22 times higher than those found for control subjects (Fig. 3, Rank Sum test, $p < 0.05$ comparing ALS and HCs). Conversely, NMJ reactivity for the remaining ALS–IgGs was not significantly different from healthy control samples (Rank Sum test, $p > 0.05$ comparing ALS and HCs). Although most of the control samples remained within non-specific binding levels, two of six disease controls also gave a positive result in this immunolabeling assay (Rank Sum test, $p < 0.01$ comparing disease samples and HCs). These sera belonged to patients with known autoimmune diseases directed against NMJ components, such as Lambert-Eaton myasthenic syndrome (DC1) and myasthenia gravis (DC2). A further aspect worth noting is the lack of electrophysiological effect and NMJ binding in all of the fALS samples tested (DC4-6; Figs 1b and 3).

ALS–IgGs reactivity towards $Ca_V2.1^{-/-}$ and $Ca_V2.2^{-/-}$ mouse neuromuscular junctions

We started evaluating whether the presence or absence of P/Q-type and N-type α_1 subunits affected ALS–IgGs reactivity. As shown in Fig. 4a, ALS–IgGs reactivity was almost completely absent when diaphragm muscles from animals null for the P/Q-type $Ca_V2.1$ subunit were examined (two-way ANOVA followed by Student–Newman-Keuls post-test, $p < 0.001$ comparing WT and null animals). In the $Ca_V2.1^{-/-}$ animals, fluorescence intensity values were not statistically different from those obtained using control IgGs (Fig. 4b, two-way ANOVA followed by Student–Newman–Keuls post-test, $p > 0.05$ comparing ALS–IgGs and healthy control IgGs). In contrast, antibodies from the disease controls which showed affinity for WT NMJs (DC1 and DC2, Fig. 3) exhibited strong affinity to sections from both WT and $Ca_V2.1$-null animals (Fig. 4b, two-way ANOVA followed by Student–Newman–Keuls post-test, $p > 0.05$ comparing WT and $Ca_V2.1^{-/-}$ animals).

In contrast to that for the P/Q-type channel, there was no difference in ALS–IgGs immunoreactivity in mice either WT or null for the N-type $Ca_V2.2$ Ca^{2+} channel subunit. Figure 5 shows that interaction of most ALS antibodies with NMJs was present at similar levels for both genotypes (two-way ANOVA followed by Student–Newman–Keuls post-test, $p > 0.05$ comparing WT and null muscles), except for ALS2 and ALS7 which displayed a small but significant decrease and increase in NMJ immunolabeling, respectively (two-way ANOVA followed by Student–Newman–Keuls post-

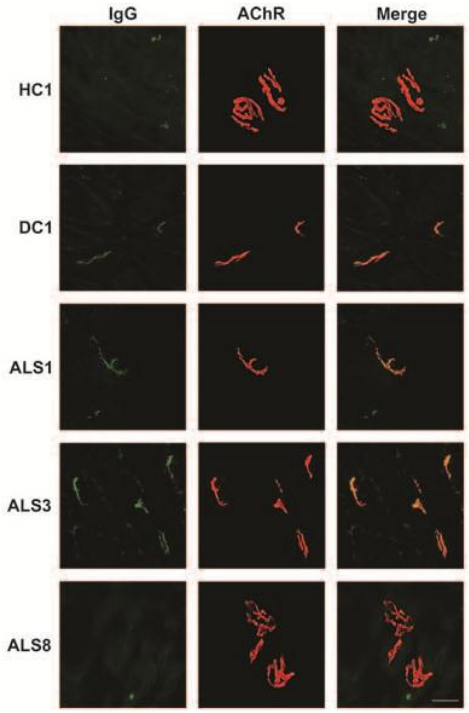

Fig. 2 Immunofluorescence of Swiss mice (P > 30) diaphragm sections (40 µm) incubated with purified IgGs from HC, DC or ALS. Visualization of the primary antibody was performed by anti-human IgG coupled to FITC. Alpha-bungarotoxin tagged with TMR was used as a post-synaptic marker of NMJs (AChR, acetylcholine receptor). Pictures in the last column show superimposed images. Bar: 25 µm.

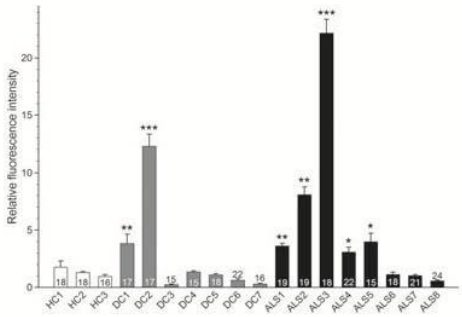

Fig. 3 Fluorescence intensity quantification of Swiss mice (P > 30) diaphragm sections incubated with purified IgGs from HC, DC or ALS. Data are normalized to isotype control. Statistical analysis was performed by Rank Sum test. *$p < 0.05$, **$p < 0.01$ and ***$p < 0.001$ compared with HCs. Figures inside bars indicate the number of NMJs studied in each experimental condition ($N = 7$ animals).

© 2011 The Authors

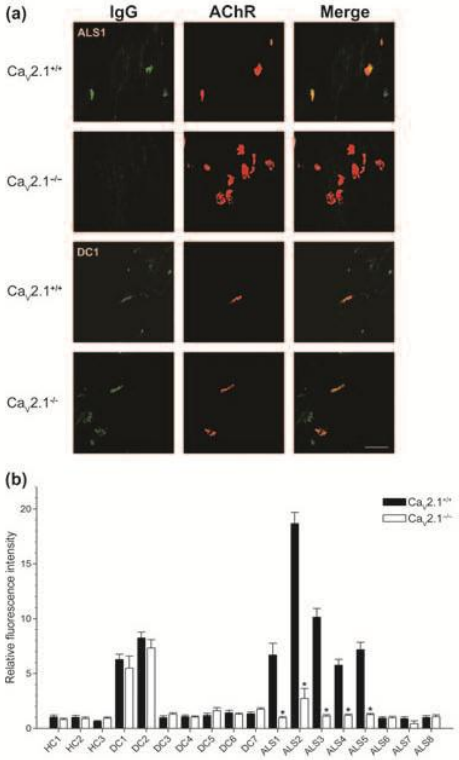

Fig. 4 Diaphragm sections (40 μm) from WT or $Ca_V2.1^{-/-}$ mice (P16-23), incubated with purified IgGs from HC, DC or ALS. Presence of primary antibody was determined as previously described. (a) Representative confocal micrographs of NMJ. The smaller size of end-plates compared with Fig. 2 is due to the younger age of animals. Bar: 25 μm. (b) Fluorescence intensity determinations normalized to isotype control. Statistical analysis between WT and $Ca_V2.1$-null muscles was performed by two-way ANOVA. *$p < 0.001$ compared with WT. The number of NMJs studied in each experimental condition varied between 16 and 30 ($N = 5$ animals).

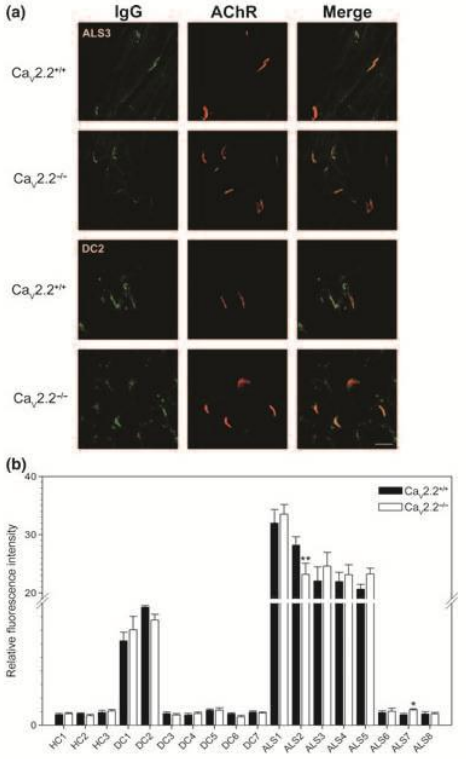

Fig. 5 Immunofluorescence of diaphragm sections (40 μm) from WT or $Ca_V2.2^{-/-}$ mice (P18), incubated with purified IgGs from HC, DC or ALS. Visualization of primary antibody was performed as previously described. (a) Representative NMJ pictures. The smaller size of end-plates compared with Fig. 2 is due to the younger age of animals. Bar: 25 μm. (b) Fluorescence intensity quantification normalized to isotype control. Statistical analysis between WT and $Ca_V2.2$-null muscles was performed by two-way ANOVA. *$p < 0.05$ and **$p < 0.01$ compared with WT. The number of NMJs studied in each experimental condition varied between 15 and 25 ($N = 4$ animals).

test, $p < 0.01$ for ALS2 and $p < 0.05$ for ALS7, comparing WT and null muscles). Additionally, neither of the disease controls that reacted against WT end-plates (DC1 and DC2) exhibited any difference in immunoreactivity in N-type $Ca_V2.2$-null samples (Fig. 5b, two-way ANOVA followed by Student–Newman–Keuls post-test, $p > 0.05$ comparing WT and null animals).

ALS–IgGs functionality on $Ca_V2.1$-null mice spontaneous neuromuscular activity

To evaluate the functional relevance of the diminished ALS–IgG interaction found for $Ca_V2.1$-null NMJs, we next tested for effects on spontaneous synaptic activity. Because of sample shortage, we could not include in this study all of the ALS–IgGs previously assessed. After a 4-h incubation period, two of four ALS samples (ALS2 and ALS5) were found to significantly increase acetylcholine release in WT diaphragm to frequencies 40–60 times higher than initial values (Fig. 6a and b, two-way ANOVA followed by Student–Newman–Keuls post-test, $p < 0.001$ comparing WT and null mice). Although sv129 mice muscles resulted more sensitive to ALS–IgGs modulatory effects than Swiss mice diaphragms (Fig. 1), it is important to emphasize that both results are essentially in accordance.

© 2011 The Authors

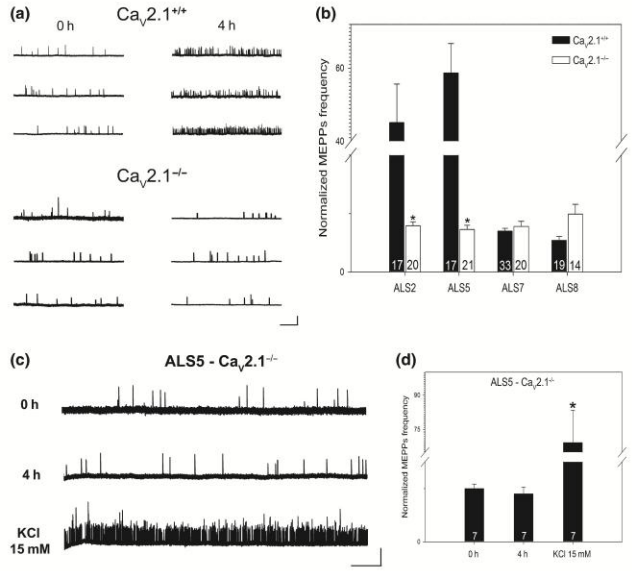

Fig. 6 MEPPs recordings of mouse diaphragm preparations from WT or $Ca_V2.1$-null animals (P16-22). Muscles were incubated with purified IgGs from ALS patients (ALS). (a) Representative intracellular recordings acquired before ($t = 0$ h) or after ($t = 4$ h) IgG incubation (ALS2). Bar: 2 mV, 5 s. (b) MEPPs frequency quantification relative to the beginning of the experiment. Statistically significant differences after incubation time between genotypes were detected by two-way ANOVA. *$p < 0.001$ compared with WT frequency. Figures inside bars indicate the number of NMJs studied in each experimental condition. (c) Representative intracellular recordings of $Ca_V2.1$-null muscles. Tissue was subsequently incubated with ALS5-IgGs for 4 h and a 15 mM-KCl solution for 10 min. Bar: 2 mV, 5 s. (d) MEPPs frequency quantification relative to the beginning of the experiment. Statistically significant differences after treatments were detected by Rank Sum test. *$p < 0.001$ compared with initial and 4-h frequency. Figures inside bars indicate the number of NMJs studied in each experimental condition.

Those antibodies that promoted an increase in NMJ neurotransmitter release were unable to increase MEPPs frequency above initial values in muscles from $Ca_V2.1^{-/-}$ animals (Fig. 6a and b, two-way ANOVA followed by Student–Newman–Keuls post-test, $p > 0.05$ comparing WT and $Ca_V2.1^{-/-}$ mice). However, all the $Ca_V2.1$-null diaphragm preparations retained their ability to respond to a depolarizing stimulus (15 mM KCl) by significantly increasing spontaneous acetylcholine release after a 10-min incubation period (Fig. 6c and d, Rank Sum test, $p < 0.001$ comparing initial, 4-h and KCl frequencies).

CNS: cerebellar, cortical and spinal cord immunolabeling

Immunofluorescence experiments performed on mouse spinal and brain cortical slices showed that the majority of ALS–IgGs (six of eight) had affinity for antigens present in the soma of Purkinje neurons (Figure S1a and b, Rank Sum test, $p < 0.05$ comparing ALS and HCs), as well as for motoneurons located at the spinal ventral horn (Figure S1c and d, Rank Sum test, $p < 0.01$ comparing ALS and HCs). In contrast, no reactivity was observed when healthy control IgGs were examined (Figure S1). Furthermore, when the presence of immunoreactivity was evaluated in slices of primary motor cortex, neither samples from ALS patients nor control subjects exhibited differences compared to non-specific control binding (data not shown).

We next assessed whether antibody interactions with neuronal structures was altered in $Ca_V2.1^{-/-}$ animals. Unlike that for NMJs, the absence of the P/Q-type channel $Ca_V2.1$ subunit did not decrease either cerebellar or spinal cord immunolabeling when compared to WT mice slices (Figure S2; two-way ANOVA followed by Student–Newman–Keuls post-test, $p > 0.05$ comparing WT and null animals). This unexpected result suggests the existence of antigens reactive to ALS–IgGs at peripheral and central synaptic locations that are differentially affected by the expression of intact P/Q-type channels.

Analysis of ALS–IgGs interaction with the P/Q-type Ca^{2+} channel α_1 subunit and other pre-synaptic proteins

Our results indicating that IgGs from a subset of sALS patients strongly react with wild-type mouse NMJs (both by

© 2011 The Authors

immunofluorescence signal and functional effects on MEPP frequency) but not with end-plates from P/Q-type channel-null animals, together with a lack of immunostaining difference across CNS targets in $Ca_V2.1^{-/-}$ versus $Ca_V2.1^{+/+}$ animals, prompted us to more directly evaluate the interactions between ALS–IgGs and P/Q-type Ca^{2+} channels. To this aim we transfected HEK cells with full-length $Ca_V2.1$, β_{2a} and $\alpha_2\delta_2$ cDNAs and analyzed cell lysates by western blot. None of the evaluated ALS–IgG samples exhibited affinity towards the human $Ca_V2.1$ pore-forming or ancillary subunits exogenously expressed in HEK cells (Figure S3a). There was some reactivity towards an unknown protein of molecular weight ~130 kDa (similar to the molecular weight of the $\alpha_2\delta_2$ subunit), although this antigen was also present in non-transfected cells (Figure S3b).

We next attempted to immunoprecipitate exogenously expressed P/Q-type channel subunits with ALS–IgGs. Although the human $Ca_V2.1$ subunit was easily detectable in the original lysate, the ALS–IgGs tested did not exhibit noticeable interaction with the channel (Figure S3c). Similarly negative results were found when performing immunoprecipitation experiments with a HEK293-derived cell line stably expressing the P/Q-type channel subunit complex (Figure S3d and e).

We also evaluated several ALS–IgG samples for reactivity against other pre-synaptic proteins, including synaptotagmin I, syntaxin 1A, synaptophysin and synaptobrevin II, using cerebellar synaptosomal extracts as a protein source for the immunoprecipitation assay. In none of the tested cases we were able to detect an interaction between the analyzed ALS–IgGs and the synaptic components (Figure S3f), although they were all easily detectable either in the input fraction or in the positive controls (PRE).

Discussion

In the present study, we demonstrated the existence of a subpopulation of sALS patients (63% in our sample), whose IgG fractions induced a significant enhancement of spontaneous acetylcholine release (Fig. 1). A similar effect has been postulated to be the consequence of increased intracellular Ca^{2+} at nerve terminals caused by ALS–IgG binding to targets in presynaptic membranes (Uchitel *et al.* 1988, 1992b; Pagani *et al.* 2006). IgGs from the same set of sALS patients also exhibited strong immunolabeling in wild-type mouse NMJs (Figs 2 and 3). Together, our results reinforce those of Pagani *et al.* (2006) who found an association between ALS–IgG binding and electrophysiological effects. From our data, it is also apparent that it is possible to separate sALS patients into two groups; one of which appears to have a strong autoimmune, neuromuscular-related component and that might contribute towards disease neuropathology.

There is a growing body of evidence supporting a role for Ca^{2+}-dependent signaling as an important regulator of cellular dysfunction and death (Appel *et al.* 2001; Orrenius *et al.* 2003). Furthermore, spinal motoneurons are known to be particularly vulnerable to Ca^{2+} imbalance caused by their diminished expression of Ca^{2+}-buffering proteins (Alexianu *et al.* 1994). An increase in intracellular Ca^{2+} levels above a certain threshold is predicted to trigger processes such as calpain activation, protein misfolding-endoplasmic reticulum stress, reactive oxygen species production and glutamate release (Orrenius *et al.* 2003; Smaili *et al.* 2009). The stimulation of any of these pathways via an aberrant rise in intracellular Ca^{2+} concentration could lead to the induction of apoptosis and provide a key link underlying ALS pathology. Additionally, reports documenting an enhancement in Ca^{2+} content of motoneurons and synaptic terminals in mice injected with ALS–IgGs have provided a key connection between Ca^{2+} overload and ALS (Engelhardt *et al.* 1995; Pullen and Humphreys 2000).

The comparison of ALS–IgG reactivity levels against NMJ (Fig. 3) and their potentiator effect on end-plate basal discharge activity (Fig. 1) indicates that both characteristics show a basically similar behavior, even though their sensitivities seem to be moderately different. Apart from differences in the intrinsic sensitivity of each technique employed, the discrepancy might also arrive as a consequence of the presence in some samples of several antibodies capable of interacting with the motor terminals.

The presence of significant levels of immunoreactivity in some disease controls was not unexpected (Figs 2–5 and Figures S1 and S2), as these individuals might have antibodies against proteins involved in synaptic transmission (i.e. voltage-dependent Ca^{2+} channels in DC1 and acetylcholine receptors in DC2). In this way, these samples serve as useful positive controls for the immunohistochemical techniques used to detect autoantibodies in sALS samples. Another important aspect to consider is the complete lack of reactivity in all the fALS samples analyzed (Fig. 3), as well as their inability to affect end-plate spontaneous synaptic activity (Fig. 1b). These results emphasize the specificity of our findings concerning sALS immunoglobulins since it is known that the hereditary form of the disease is clinically indistinguishable from the sporadic variant.

The finding that the IgG sample from DC1 (a Lambert-Eaton myasthenic syndrome patient) exhibited a similar level of interaction with $Ca_V2.1^{+/+}$ and $Ca_V2.1^{-/-}$ end-plates might seem contradictory at first sight, because of the proposed etiology for this disease. However, it should be stressed that this sample might contain antibodies against not only $Ca_V2.1$ Ca^{2+} channels but also $Ca_V2.2$ (Takamori *et al.* 1995; Motomura *et al.* 1997). This latter channel is known to compensate for the lack of P/Q-type channels, both at the functional (Urbano *et al.* 2003) and proteic level (Pagani *et al.* 2004), and therefore could explain the invariability observed in immunostaining.

© 2011 The Authors

To further characterize ALS antibody reactivity against other neuronal substrates possibly relevant to disease pathophysiology, we performed immunofluorescence assays on mouse spinal and brain cortical slices. These neural structures are the site of residence for lower and upper motoneurons, respectively, both of which are important movement effectors. Cerebellar structures were also analyzed since they comprise cells involved in movement coordination and it has been shown that ALS antibodies are capable of modulating P/Q-type Ca^{2+} currents (Llinas *et al.* 1993). We found a broad reactivity pattern for ALS–IgGs in neuronal tissues such as the cerebellum and spinal cord (Figure S1), in which the vast majority of samples analyzed resulted in positive staining. Of note, we could not detect any difference in the reactivity of ALS–IgGs when comparing WT to $Ca_V2.1$-null animals in these regions (Figure S2). These data are in striking contrast to the clear differences detected in immunofluorescence experiments performed on NMJs (Fig. 4), and thus highlight the specificity of the findings for end-plate preparations. Along these lines, we speculate that the antigen(s) responsible for ALS–IgG labeling motor terminals is(are) predominantly expressed in these more peripheral synaptic sites than others such as the cerebellum or spinal ventral horn. However, we cannot exclude the possibility that the presence of the ALS–IgG reactive antigen(s) could be masked by other antigens expressed in the cerebellar or spinal cord neurons and which are more abundant or reactive towards ALS–IgGs. Additionally, the presence in ALS sera of such CNS-reactive antibodies is more likely the consequence of intracellular content exposure caused by neuronal injury, owing to their broad distribution amongst several ALS samples and the lack of correlation with NMJ binding.

As P/Q-type channels are the principal mediators of synaptic transmission in mammalian NMJs (Uchitel *et al.* 1992a; Katz *et al.* 1997) and there is evidence supporting an interaction between ALS–IgGs and Ca^{2+} channels (Llinas *et al.* 1993; Smith *et al.* 1994; Carter and Mynlieff 2003), we analyzed the effects of ALS–IgGs on deleting the $Ca_V2.1$ subunit. Our results showed that the absence of the P/Q-type channel $Ca_V2.1$ subunit produced a significant decrease in ALS–IgG binding to mouse NMJs (Fig. 4), as well as the complete suppression of ALS–IgG-mediated effects on enhancing spontaneous acetylcholine release (Fig. 6). Taken together, these data suggested that a subset of ALS–IgGs interact with either the $Ca_V2.1$ subunit or other protein(s) whose expression in NMJs is dramatically diminished as a consequence of $Ca_V2.1$ subunit deletion. In support of the latter, it is known that $Ca_V2.1$ subunit-null mice exhibit alterations in the expression of other genes besides the $Ca_V2.1$ subunit (Piedras-Renteria *et al.* 2004). Furthermore, other reports suggest that Ca^{2+} influx through P/Q-type channels – and hence, their presence and functionality – might be an important factor relevant to the transcription of synapse-related genes such as the soluble *N*-ethylmaleimide sensitive factor attachment protein receptor (SNARE) protein syntaxin 1A (Sutton *et al.* 1999; Barbado *et al.* 2009).

A microarray analysis of the $Ca_V2.1$ gene (*CACNA1A*) expression profile revealed a seven-fold decrease in $Ca_V2.1$ messenger ribonucleic acid levels in rat extraocular muscle compared with a typical skeletal muscle such as *tibialis anterior* (Fischer *et al.* 2002). The extraocular muscle is well-known for being relatively spared during ALS progression (Leveille *et al.* 1982) and has been reported to be resistant to ALS–IgG NMJ effects in passive transfer experiments (Mosier *et al.* 2000). These studies provide a further important link between P/Q-type channel expression and ALS susceptibility.

Distinct from the above arguments in favor of a direct role of functional P/Q-type channels, our immunoprecipitation and western blot experiments using HEK293 cells expressing cloned P/Q-type channel subunits do not support a direct interaction of ALS–IgGs with the channel complex itself (Figure S3), at least under the conditions analyzed for this study. In support, ALS–IgGs have been shown not to interact with ^{125}I-ω-conotoxin MVIIC-labeled channels (Drachman *et al.* 1995) and also that P/Q-type channel inhibition by ω-agatoxin IVA did not prevent immunoglobulin-induced synaptic potentiation (Pagani *et al.* 2006). Taken together, our results suggest that the protein(s) interacting with ALS–IgGs requires $Ca_V2.1$ expression/activity at the NMJ although it is $Ca_V2.1$-expression independent in other neuronal structures such as the cerebellum and spinal cord.

Another aspect worth noting is the lack of change in antibody binding to $Ca_V2.1^{-/-}$ NMJ for disease control sera compared to WT conditions (Fig. 4b). This invariability in immunostaining adds relevance to ALS–IgG findings by highlighting their specificity towards a selected subset of patients.

N-type Ca^{2+} channel activation has been found to be relevant for the induction of spontaneous synaptic activity by ALS–IgGs (Pagani *et al.* 2006). However, this effect is unlikely the consequence of a direct interaction between antibodies and the $Ca_V2.2$ N-type subunit as the loss of $Ca_V2.2$ did not significantly alter IgG binding of most of the ALS samples at mouse NMJs (Fig. 5). Moreover, it has been shown that in $Ca_V2.1$-null mutant animals, there is a functional compensation in neuromuscular transmission by N-type Ca^{2+} channels (Urbano *et al.* 2003), as well as an increment in channel protein levels (Pagani *et al.* 2004). Therefore, this could explain the significant changes in ALS–IgG immunoreactivity noted here (Fig. 4). Together, these results do not support a direct binding of ALS antibodies to the N-type channel but rather an indirect effect of IgGs on channel activity, for example through a second messenger signaling pathway, as it has been extensively reported for this channel (Lipscombe *et al.* 1989; Werz *et al.* 1993; Martin *et al.* 2006). In fact, Pagani *et al.* (2006) did detect a requirement of phospholipase C, ryanodine receptor and

© 2011 The Authors

inositol triphosphate receptor activation for the ALS–IgG-induced synaptic potentiation to occur.

Several reports have documented the presence of human antibodies at the motoneuronal soma and nerve terminals of mice injected with ALS–IgGs (Fratantoni *et al.* 1996; Engelhardt *et al.* 2005), we speculated it might be the consequence of an interaction between disease antibodies and pre-synaptic components. In order to test this possibility, we assessed by immunoprecipitation experiments ALS–IgGs binding to several pre-synaptic proteins purified from synaptosomal extracts. We found that none of the evaluated ALS samples showed affinity towards proteins present at synaptic terminals, such as synaptotagmin I, syntaxin 1A, synaptophysin and synaptobrevin II, all of which were readily detectable in the original lysates (Figure S3f). Other candidates to test in the future include extracellular matrix molecules, neurotrophins receptors and proteins involved in synaptogenesis and axon guidance, due to their proposed role during neurodegeneration (Dawbarn and Allen 2003; Glas *et al.* 2007; Schmidt *et al.* 2009).

The results in the current work add relevant evidence in favor of autoimmunity as one of the possible mechanisms contributing to ALS pathology. They also suggest for the first time that, as opposed to generally interacting with all central and peripheral P/Q-type Ca^{2+} channels, autoantibodies in the serum of a subset of patients selectively interact with antigens at NMJs. The results also contribute towards further studies aimed at defining the IgGs as biological markers for sALS and in disease pathophysiology.

Acknowledgements

The authors are very grateful to Drs Joaquín Piriz, Francisco Urbano and Carina Weissmann for helpful comments on the manuscript and to María Eugenia Martín for technical assistance. We would also like to thank Drs John Tyson and Esperanza García for assistance with the transfection and immunoprecipitation experiments. We acknowledge the contribution of Dr Shin Hee-Sup for kindly providing the $Ca_V2.1^{-/-}$ and $Ca_V2.2^{-/-}$ mice. This work was supported by the National Agency for Scientific and Technological Promotion (Grant 32113, Argentina). Work in the laboratory of T.P. Snutch was supported by an operating grant from the Canadian Institutes of Health Research and a Tier 1 Canada Research Chair in Biotechnology and Genomics-Neurobiology. The authors declare no conflict of interests.

Supporting information

Additional supporting information may be found in the online version of this article:

Figure S1. Immunofluorescence of Swiss mice (P > 30) cerebellum and spinal cord slides (150 µm) incubated with purified IgGs from HC, DC or ALS.

Figure S2. Immunofluorescence of mouse cerebellum and spinal cord slides (150 µm) from WT or $Ca_V2.1^{-/-}$ mice (P16-23), incubated with purified IgGs from HC, DC or ALS.

Figure S3. Interaction of ALS antibodies with proteins from P/Q-type channel-expressing cells.

As a service to our authors and readers, this journal provides supporting information supplied by the authors. Such materials are peer-reviewed and may be re-organized for online delivery, but are not copy-edited or typeset. Technical support issues arising from supporting information (other than missing files) should be addressed to the authors.

References

Alexianu M. E., Ho B. K., Mohamed A. H., La Bella V., Smith R. G. and Appel S. H. (1994) The role of calcium-binding proteins in selective motoneuron vulnerability in amyotrophic lateral sclerosis. *Ann. Neurol.* **36**, 846–858.

Appel S. H., Stockton-Appel V., Stewart S. S. and Kerman R. H. (1986) Amyotrophic lateral sclerosis: associated clinical disorders and immunological evaluation. *Arch. Neurol.* **43**, 234–238.

Appel S. H., Engelhardt J. I., Garcia J. and Stefani E. (1991) Immunoglobulins from animal model of motor neurons disease and from human amyotrophic lateral sclerosis patients passively transfer physiological abnormalities to the neuromuscular junction. *Proc. Natl Acad. Sci. USA* **88**, 647–651.

Appel S. H., Smith R. G., Englehardt J. I. and Stefani E. (1993) Evidence for autoimmunity in amyotrophic lateral sclerosis. *J. Neurol. Sci.* **118**, 169–174.

Appel S. H., Beers D., Siklos L., Engelhardt J. I. and Mosier D. R. (2001) Calcium: the Darth Vader of ALS. *Amyotroph. Lateral Scler. Other Motor Neuron Disord.* **2**, S47–S54.

Arsac C., Raymond C., Martin-Moutot N., Dargent B., Couraud F., Pouget J. and Seagar M. (1996) Immunoassays fail to detect antibodies against neuronal calcium channels in amyotrophic lateral sclerosis serum. *Ann. Neurol.* **40**, 695–700.

Barbado M., Fablet K., Ronjat M. and De Waard M. (2009) Gene regulation by voltage-dependent calcium channels. *Biochim. Biophys. Acta* **1793**, 1096–1104.

Bourinet E., Soong T. W., Sutton K., Slaymaker S., Mathews E., Monteil A., Zamponi G. W., Nargeot J. and Snutch T. P. (1999) Phenotypic variants of P- and Q-type calcium channels are generated by alternative splicing of the α1A subunit gene. *Nat. Neurosci.* **2**, 407–415.

Bowling A. C., Schulz J. B., Brown R. H. and Beal M. F. (1993) Superoxide dismutase activity, oxidative damage and mitochondrial energy metabolism in familial and sporadic amyotrophic lateral sclerosis. *J. Neurochem.* **61**, 2322–2325.

Bradford M. M. (1976) A rapid and sensitive method for the quantification of microgram of protein utilizing the principle of protein-dye binding. *Anal. Biochem.* **72**, 248–254.

Brooks B. (1994) El Escorial World Federation of Neurology criteria for the diagnosis of amyotrophic lateral sclerosis. Subcommittee on Motor Neuron Diseases/Amyotrophic Lateral Sclerosis of the World Federation of Neurology Research Group on Neuromuscular Diseases and the El Escorial 'Clinical limits of amyotrophic lateral sclerosis' workshop contributors. *J. Neurol. Sci.* **142**, 96–107.

Carter J. R. and Mynlieff M. (2003) Amyotrophic lateral sclerosis patient IgG alters voltage dependence of Ca^{2+} channels in dissociated rat motoneurons. *Neurosci. Lett.* **353**, 221–225.

Couratier P., Yi F. H., Preud'homme J. L., Clavelou P., White A., Sindou P., Vallat J. M. and Jauberteau M. O. (1998) Serum autoantibodies to neurofilament proteins in sporadic amyotrophic lateral sclerosis. *J. Neurol. Sci.* **154**, 137–145.

© 2011 The Authors

Dawbarn D. and Allen S. J. (2003) Neurotrophins and neurodegeneration. *Neuropathol. Appl. Neurobiol.* **29**, 211–230.

Demestre M., Pullen A., Orrell R. W. and Orth M. (2005) ALS-IgG-induced selective motor neurone apoptosis in rat mixed primary spinal cord cultures. *J. Neurochem.* **94**, 268–275.

Drachman D. B. and Kuncl R. W. (1989) Amyotrophic lateral sclerosis: an unconventional autoimmune disease? *Ann. Neurol.* **26**, 269–274.

Drachman D. B., Fishman P. S., Rothstein J. D., Motomura M., Lang B., Vincent A. and Mellits E. D. (1995) Amyotrophic lateral sclerosis: an autoimmune disease? *Adv. Neurol.* **68**, 59–65.

Dubel S. J., Starr T. V. B., Hell J., Ahlijanian M. K., Enjeart J. J., Catterall W. A. and Snutch T. P. (1992) Molecular cloning of the alpha-1 subunit of an omega-conotoxin-sensitive calcium channel. *Proc. Natl Acad. Sci. USA* **89**, 5058–5062.

Engelhardt J. I. and Appel S. H. (1990) IgG reactivity in the spinal cord and motor cortex in amyotrophic lateral sclerosis. *Arch. Neurol.* **47**, 1210–1216.

Engelhardt J. I., Appel S. H. and Killian J. M. (1990) Motor neuron destruction in guinea pigs immunized with bovine spinal cord ventral horn homogenate: experimental autoimmune gray matter disease. *J. Neuroimmunol.* **27**, 21–31.

Engelhardt J. I., Siklós L., Kömüves L., Smith R. G. and Appel S. H. (1995) Antibodies to calcium channels from ALS patients passively transferred to mice selectively increase intracellular calcium and induce ultrastructural changes in motoneurons. *Synapse* **20**(3), 185–99.

Engelhardt J. I., Soos J., Obal I., Vigh L. and Siklos L. (2005) Subcellular localization of IgG from the sera of ALS patients in the nervous system. *Acta Neurol. Scand.* **112**, 126–133.

Fischer M. D., Gorospe J. R., Felder E., Bogdanovich S., Pedrosa F., Ahima R. S., Rubinstein N. A., Hoffman E. P. and Khurana T. S. (2002) Expression profiling reveals metabolic and structural components of extraocular muscles. *Physiol. Genomics* **9**, 71–84.

Fratantoni S. A., Dubrovsky A. L. and Uchitel O. D. (1996) Uptake of immunoglobulin G from amyotrophic lateral sclerosis patients by motor nerve terminals in mice. *J. Neurol. Sci.* **137**, 97–102.

Glas M., Popp B., Angele B., Koedel U., Chahli C., Schmalix W. A., Anneser J. M., Pfisterand H. W. and Lorenzl S. (2007) A role for the urokinase-type plasminogen activator system in amyotrophic lateral sclerosis. *Exp. Neurol.* **207**(2), 350–356.

Katz E., Protti D. A., Ferro P. A., Rosato Siri M. D. and Uchitel O. D. (1997) Effects of Ca^{2+} channel blocker neurotoxins on transmitter release and presynaptic currents at the neuromuscular junction. *Br. J. Pharmacol.* **121**, 1531–1540.

Leveille A. J., Ciernan A. J., Goodwin J. A. and Antel J. (1982) Eye movements in amyotrophic lateral sclerosis. *Arch. Neurol.* **39**, 684–686.

Lipscombe D., Kongsamut S. and Tsien R. W. (1989) Alpha-adrenergic inhibition of sympathetic neurotransmitter release mediated by modulation of N-type calcium-channel gating. *Nature* **340**(6235), 639–642.

Llinas R., Sugimori M., Cherksey B. D., Smith R. G., Delbono O., Stefani E. and Appel S. (1993) IgG from amyotrophic lateral sclerosis patients increases current through P-type calcium channels in mammalian cerebellar Purkinje cells and in isolated channels protein in lipid bilayer. *Proc. Natl Acad. Sci. USA* **90**, 11743–11747.

Martin S. W., Butcher A. J., Berrow N. S., Richards M. W., Paddon R. E., Turner D. J., Dolphin A. C., Sihra T. S. and Fitzgerald E. M. (2006) Phosphorylation sites on calcium channel alpha 1 and beta subunits regulate ERK-dependent modulation of neuronal N-type calcium channels. *Cell Calcium* **39**(3), 275–292.

Mendonca D. M. F., Chimelli L. and Martinez A. M. B. (2005) Quantitative evidence for neurofilament heavy subunit aggregation in motor neurons of spinal cords of patients with Amyotrophic Lateral Sclerosis. *Braz. J. Med. Biol. Res.* **38**, 925–935.

Mosier D. R., Bardelli P. and Delbono O. (1995) Amyotrophic lateral sclerosis immunoglobulins increase Ca^{2+} current in a motor neuron cell line. *Ann. Neurol.* **37**, 102–109.

Mosier D. R., Siklos L. and Appel S. H. (2000) Resistance of extraocular motoneuron terminals to effects of amyotrophic lateral sclerosis sera. *Neurology* **54**, 252–255.

Motomura M., Lang B., Johnston I., Palace J., Vincent A. and Newsom-Davis J. (1997) Incidence of serum anti-P/O-type and anti-N-type calcium channel autoantibodies in the Lambert-Eaton myasthenic syndrome. *J. Neurol. Sci.* **147**(1), 35–42.

Mulder D. W. (1982) Clinical limits of amyotrophic lateral sclerosis. *Adv. Neurol.* **36**, 15–22.

Niebroj-Dobosz I., Dziewulska D. and Kwiecinski H. (2004) Oxidative damage to proteins in the spinal cord in amyotrophic lateral sclerosis. *Folia Neuropathol.* **42**, 151–156.

Orrenius S., Zhivotovsky B. and Nicotera P. (2003) Regulation of cell death: the calcium-apoptosis link. *Nature Rev.* **4**, 552–565.

Pagani M. R., Song M., McEnery M., Qin N., Tsien R. W., Toro L., Stefani E. and Uchitel O. D. (2004) Differential expression of α_1 and β subunits of voltage-dependent Ca^{2+} channel at the neuromuscular junction of normal and P/Q Ca^{2+} channel knockout mouse. *Neuroscience* **123**, 75–85.

Pagani M. R., Reisin R. C. and Uchitel O. D. (2006) Calcium signaling pathways mediating synaptic potentiation triggered by amyotrophic lateral sclerosis IgG in motor nerve terminals. *J. Neurosci.* **26**, 2661–2672.

Paxinos G. and Franklin K. B. J. (2001) *The Mouse Brain in Stereotaxic Coordinates*, 2nd edn. Academic Press, New York.

Perissinotti P. P., Giugovaz-Tropper B. and Uchitel O. D. (2008) L-Type calcium channels are involved in fast endocytosis at the mouse neuromuscular junction. *Eur. J. Neurosci.* **27**, 1333–1344.

Pestronk A., Adams R. N., Cornblath D., Kuncl R. W., Drachman D. B. and Clawson L. (1989) Patterns of serum IgM antibodies to GM1 and GD1a gangliosides in amyotrophic lateral sclerosis. *Ann. Neurol.* **25**, 98–102.

Piedras-Renteria E. S., Pyle J. L., Diehn M., Glickfeld L. L., Harata N. C., Cao Y., Kavalali E. T., Brown P. O. and Tsien R. W. (2004) Presynaptic homeostasis at CNS nerve terminals compensates for lack of a key Ca^{2+} entry pathway. *Proc. Natl Acad. Sci. USA* **101**, 3609–3614.

Protti D. A., Szczupak L., Scornik F. S. and Uchitel O. D. (1991) Effect of omega-conotoxin GVIA on neurotransmitter release at the mouse neuromuscular junction. *Brain Res.* **557**, 336–339.

Pullen A. H. and Humphreys P. (2000) Ultrastructural analysis of spinal motoneurones from mice treated with IgG from ALS patients, healthy individuals, or disease controls. *J. Neurol. Sci.* **180**(1-2), 35–45.

Rosato Siri M. D. and Uchitel O. D. (1999) Calcium channels coupled to neurotransmitter release at neonatal rat neuromuscular junctions. *J. Physiol.* **514**, 533–540.

Rothstein J. D., Martin L. J. and Kuncl R. W. (1992) Decreased glutamate transport by the brain and spinal cord in amyotrophic lateral sclerosis. *N. Engl. J. Med.* **326**, 1464–1468.

Rowland L. P. (1998) Diagnosis of amyotrophic lateral sclerosis. *J. Neurol. Sci.* **160**, S6–S24.

Schmidt E. R. E., Pasterkamp R. J. and van den Berg L. H. (2009) Axon guidance proteins: novel therapeutic targets for ALS? *Prog. Neurobiol.* **88**, 286–301.

Smaili S., Hirata H., Ureshino R. *et al.* (2009) Calcium and cell death signaling in neurodegeneration and aging. *An. Acad. Bras. Cienc.* **81**(3), 467–475.

© 2011 The Authors

Smith R. G., Hamilton S., Hoffman F., Schneider T., Nastainczyk W. and Birnbaumer L. (1992) Serum antibodies to L-type calcium channels in patients with amyotrophic lateral sclerosis. *N. Engl. J. Med.* **327**, 1721–1728.

Smith R. G., Alexianu M. E., Crawford G., Nyormoi O., Stefani E. and Appel S. H. (1994) Cytotoxicity of immunoglobulins from amyotrophic lateral sclerosis patients on a hybrid motoneuron cell line. *Proc. Natl Acad. Sci. USA* **91**, 3393–3397.

Starr T. V. B., Prystay W. and Snutch T. P. (1991) Primary structure of a calcium channel that is highly expressed in the rat cerebellum. *Proc. Natl Acad. Sci. USA* **88**, 5621–5625.

Stea A., Tomlinson W. J., Soong T. W., Bourinet E., Dubel S. J., Vincent S. R. and Snutch T. P. (1994) The localization and functional properties of a rat brain α1A calcium channel reflect similarities to neuronal Q- and P-type channels. *Proc. Natl Acad. Sci. USA* **91**, 10576–10580.

Sutton K. G., McRory J. E., Guthrie H., Murphy T. H. and Snutch T. P. (1999) P/Q-type calcium channels mediate the activity-dependent feedback of syntaxin-1A. *Nature* **401**, 800–804.

Takamori M., Takahashi M., Yasukawa Y., Iwasa K., Nemoto Y., Suenaga A., Nagataki S. and Nakamura T. (1995) Antibodies to recombinant synaptotagmin and calcium channel subtypes in Lambert-Eaton myasthenic syndrome. *J. Neurol. Sci.* **133**(1-2), 95–101.

Troost D., Van Den Ord J. J. and Vianney De Jong J. M. (1990) Immunohistochemical characterization of the inflammatory infiltrate in amyotrophic lateral sclerosis. *Neuropathol. Appl. Neurobiol.* **16**, 401–410.

Uchitel O. D., Appel S. H., Crawford F. and Sczcupak L. (1988) Immunoglobulins from amyotrophic lateral sclerosis patients enhance spontaneous transmitter release from motor-nerve terminals. *Proc. Natl Acad. Sci. USA* **85**, 7371–7374.

Uchitel O. D., Protti D. A., Sanchez V., Cherksey B. D., Sugimori M. and Llinas R. (1992a) P-type voltage-dependent calcium channel mediates presynaptic calcium influx and transmitter release in mammalian synapses. *Proc. Natl Acad. Sci. USA* **89**, 3330–3333.

Uchitel O. D., Scornik F., Protti D. A., Fumberg C. G., Alvarez V. and Appel S. H. (1992b) Long-term neuromuscular dysfunction produced by passive transfer of amyotrophic lateral sclerosis immunoglobulins. *Neurology* **42**, 2175–2180.

Urbano F. J. and Uchitel O. D. (1999) L-type calcium channels unmasked by cell-permeant Ca^{2+}-buffer at mouse motor nerve terminals. *Pflugers Arch.* **437**, 523–528.

Urbano F. J., Piedras-Rentería E. S., Jun K., Shin H. S., Uchitel O. D. and Tsien R. W. (2003) Altered properties of quantal neurotransmitter release at endplates of mice lacking P/Q-type Ca^{2+} channels. *Proc. Natl Acad. Sci. USA* **100**, 3491–3496.

Valdmanis P. N., Daoud H., Dion P. A. and Rouleau G. A. (2009) Recent advances in the genetics of amyotrophic lateral sclerosis. *Curr. Neurol. Neurosci. Rep.* **9**, 198–205.

Van Den Bosch L., Van Damme P., Bogaert E. and Robberecht W. (2006) The role of excitotoxicity in the pathogenesis of amyotrophic lateral sclerosis. *Biochim. Biophys. Acta* **1762**, 1068–1082.

Werz M. A., Elmslie K. S. and Jones S. W. (1993) Phosphorylation enhances inactivation of N-type calcium channel current in bullfrog sympathetic neurons. *Pflugers Arch.* **424**(5-6), 538–545.

Xu Z., Cook L. C., Griffin J. W. and Cleveland D. W. (1993) Increased expression of new filament subunit NF-1 produces morphological alterations that resemble the pathology of human motor neuron disease. *Cell* **73**, 23–33.

Xu L., Guo Y. S., Liu Y. L., Wu S. Y., Yang C., Wu D. X., Wu H. R., Zhang Y. S. and Li C. Y. (2009) Oxidative stress in immune-mediated motoneuron destruction. *Brain Res.* **1302**, 225–232.

© 2011 The Authors